CORE EXCITATION
OF SOME
ORGANOMETALLIC AND ORGANOSILICON MOLECULES

By

Alex T. Wen, B.Sc. (Hons.), M.Sc.

A Thesis
Submitted to the School of Graduate Studies
in Partial Fulfilment of the Requirements
for the Degree
Doctor of Philosophy

McMaster University

March, 1992

CORE EXCITATION
OF SOME
ORGANOMETALLIC AND ORGANOSILICON MOLECULES

DOCTOR OF PHILOSOPHY (1992) **McMASTER UNIVERSITY**
(Chemistry) **Hamilton, Ontario**

TITLE: Core Excitation of Some Organometallic and Organosilicon Molecules

AUTHOR: Alex T. Wen, B.Sc. (Hons.), M.Sc. (Memorial University)

SUPERVISOR: Professor Adam P. Hitchcock, Ph.D., F.C.I.C.

NUMBER OF PAGES: xiv, 209

This thesis is dedicated to the pursuit of scientific knowledge.

ABSTRACT

Inner-shell electron energy-loss spectroscopy (ISEELS) is an electron impact technique for the examination of inner-shell excitation of matter in the soft X-ray energy range between 20 and 1000 eV. It has long been utilized to study the core-excitation spectra of atoms and small organic or inorganic molecules. This thesis demonstrates the extension of such investigations to large organometallic complexes and organosilicon compounds in the gas phase. Measured under low momentum transfer conditions (>2.5 keV impact energy and small scattering angle, $\leq 2^\circ$), where the spectra are dominated by electric-dipole-allowed transitions, ISEELS spectra have been recorded for transition metal carbonyls $Fe(CO)_5$, $Fe_2(CO)_9$ and $Co_2(CO)_8$; metallocenes $Fe(C_5H_5)_2$, CH_2CH-$C_5H_4FeC_5H_5$, C_4H_9-$C_5H_4FeC_5H_5$ and $Co(C_5H_5)_2$; mixed-ligand complexes $C_5H_5TiCl_3$, $C_6H_6Cr(CO)_3$, CH_3-$C_5H_4Mn(CO)_3$, $C_4H_6Fe(CO)_3$, $C_6H_8Fe(CO)_3$, $C_8H_8Fe(CO)_3$ and $C_5H_5Co(CO)_3$; organopolysilanes $(CH_3)_3SiSi(CH_3)_3$ and $Si[Si(CH_3)_3]_4$ as well as related compounds $TiCl_4$, C_5H_6 and $(C_5H_6)_2$. The spectral features have been assigned on the basis of comparison with the spectra of the free ligands and with a few previous studies of related organometallic/organosilicon species, along with extended Hückel molecular orbital calculations. The spectra provide novel insight into how inner-shell excitation spectroscopy reflects the metal-ligand bonding in these complexes and ligand-ligand interaction via the central metal atom. All the O 1s spectra are similar to each other, and the C 1s and metal 2p spectra of related compounds in a series (e.g., carbonyl complexes or metallocene derivatives) also have a similar shape, suggesting similar origins of the spectral features. Small variations through each series have been interpreted in terms of changes in the electronic structure associated with changing substituents. The metal 2p spectra are found to be surprisingly sensitive to the identity of the ligands present in the complexes and/or the character of the metal-ligand bonding. A resonance associated with the Si-Si σ^* antibonding molecular orbital is identified at 102.5 eV in the Si 2p spectra of the two organosilicon compounds.

ACKNOWLEDGEMENTS

I wish to express my gratitude to Dr. A.P. Hitchcock for his knowledge of electron spectroscopy which he has shared so generously as well as for the opportunity, supervision and support he offered. His criticisms and insights made this thesis more readable and the development of concepts more logical. I also wish to acknowledge the other members of my supervisory committee: Dr. G.J. Schrobilgen, Dr. N.H. Werstiuk and Dr. T.A. Wildman for their enthusiasm, endurance and encouragement. Working with Dr. M.J. McGlinchey has been delightful. He was kind and tolerant when I was learning the basics of extended Hückel molecular orbital calculations. I am grateful to him for always being available and willing to give help and suggestions. My special appreciation must be extended to Dr. T. Tyliszczak for his unfailing technical advice and assistance, especially in optimizing the spectrometer and constructing an improved collision cell heater. He, in his quiet way, has to be the best in the business. The collaboration with Dr. E. Rühl at the beginning of this project was valuable. Finally, I would like to thank McMaster University for its financial and spiritual support.

A. T. W.

Hamilton, Ontario
March 1992

TABLE OF CONTENTS

LIST OF FIGURES

LIST OF TABLES

LIST OF ABBREVIATIONS AND SYMBOLS

AO	atomic orbital
BCT	benzene chromium tricarbonyl, $C_6H_6Cr(CO)_3$
Bz	benzene
CB	centrifugal barrier
Cp	cyclopentadienyl, C_5H_5
Cp'	methylcyclopentadienyl, CH_3-C_5H_4
DCS	differential cross section, $d\sigma/d\Omega$
EELS	electron energy loss spectroscopy
EHMO	extended Hückel molecular orbital (theory)
EHT	extended Hückel theory
EICVOM	equivalent ionic core virtual orbital model
ESR	electron spin resonance
ETS	electron transmission spectroscopy
eV	electron volt
GOS	generalized oscillator strength, $f_n(K)$
HDS	hexamethyldisilane, $(CH_3)_3SiSi(CH_3)_3$
HOMO	the highest occupied molecular orbital
ISEELS	inner-shell electron energy loss
IP	ionization potential
IW	inner well
K	transferred momentum
$\mathbf{k}_0$	pre-scattering wavevector of the fast electron
$\mathbf{k}_1$	post-scattering wavevector of the fast electron
LCAO	linear combination of atomic orbitals
LUMO	the lowest unoccupied molecular orbital
MMT	methylcyclopentadienyl manganese tricarbonyl, CH_3-$C_5H_4Mn(CO)_3$
MO	molecular orbital
MS	mass spectroscopy
OS	oscillator strength
OW	outer well
PES	photoelectron spectroscopy
θ	scattering angle
TMS	tetramethylsilane
TTS	tetrakis-(trimethylsilyl)silane, $Si[Si(CH_3)_3]_4$
XPS	X-ray photoelectron spectroscopy

Chapter 1

INTRODUCTION

§1.1 Inner-Shell Electron Energy Loss Spectroscopy

Electron energy loss spectroscopy (EELS) is an electron impact technique that can be employed to study the electronic excited levels of the target. In EELS a fast electron beam with a well-defined energy is passed through a cell containing the target gas (or crosses a molecular beam) and the yield of inelastically-scattered electrons is measured with an electron spectrometer as a function of the energy loss E_n and the scattering angle θ.

Inner-shell electronic excited states of neutral atoms or molecules are created when an inner-shell electron is promoted to an unoccupied valence or Rydberg orbital. The promotion can be induced either by the absorption of X-rays or by the inelastic scattering of fast electrons. The similarity between these two different approaches (under certain conditions) implies that experiments normally performed by X-rays may be carried out with electrons. Indeed, EELS for the study of the excitation of inner-shell electrons in atoms or molecules has proven to be a useful alternative to photoabsorption spectroscopy.[1] The process of inducing an inner-shell transition using a fast electron of impact energy E_0 is

$$\underset{}{M} + \underset{E_0}{e_{inc.}} \dashrightarrow M^* + \underset{(E_0-E_n)}{e_{scat.}} \tag{1.1.1}$$

where M denotes a free atom or molecule. The energy (E_n) lost by the inelastically-scattered electron gives the energy of the transition from the ground to the inner-shell excited state. A wide variety of inner-shell electron energy loss spectra (ISEELS) have been recorded for small molecules during the last two decades,[1-3] which involve excitation of K shell (C, N, O, F, Ne), L shell (Si, P, S, Cl, Ar), M shell (Br, Kr) and N shell (I, Xe) electrons. This has afforded many different and curious distributions of transition probabilities, leading to a greater understanding of the processes occurring in and resulting from core excitation and ionization.

An excellent illustration of ISEELS is the carbon K-shell (1s) spectrum of CO. The energy-loss spectrum obtained by Wight *et al*,[4] with 2.5 keV impact energy and near forward scattering, is quoted in Figure 1.1. The overall energy resolution is approximately 0.5 eV, but this is sufficient to reveal the main features of the spectrum. The most marked aspect of the spectrum is that the lowest energy peak, corresponding to the transition of a 1s electron to the first unoccupied orbital ($2\pi^*$), has an area that is much larger than the sum of the areas of all the other discrete peaks below the ionization threshold. It is noticeable also that the spectrum above the threshold at 296 eV does not have the normal shape seen in the photoionization continua of atoms (see shaded area in Fig. 1.1), but has an additional structure component of large magnitude. There have been two complementary theoretical methods trying to describe the general features of the inner-shell absorption spectra. One is a multiple scattering theory[5] and the other a molecular orbital approach.[6] In the former Dehmer and Dill[5] have explained the oscillator-strength distribution of various features in the N_2 spectrum, a species isoelectronic with CO, in terms of the shape and strength of the effective anisotropic molecular field experienced by the promoted electron. For example, when the ejected electron is in the $2\pi^*$ MO, it has a d-wave ($\ell = 2$) component of angular momentum, the effective potential of which contains a centrifugal barrier arising from the repulsive centrifugal term. This barrier confines the $2\pi^*$ MO to the vicinity of the molecular core (viz. being highly localized) and causes it to have a large overlap with the K-shell 2σ orbital, thus giving the exceptionally high intensity.

According to Dehmer and Dill's model, the anisotropic potential well with a centrifugal barrier can temporarily trap the ejected electron in the region of the molecular core and delay penetration of the continuum wave until sufficiently high kinetic energy has been gained by the escaping electron. Thus, the presence of such

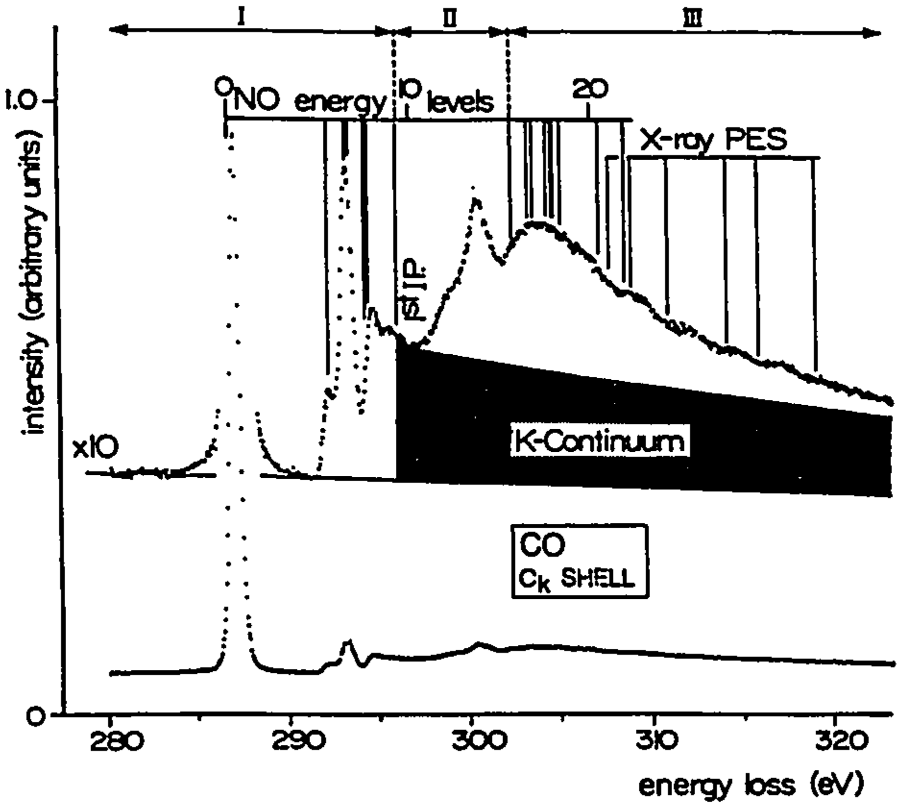

Fig. 1.1 C 1s energy loss spectrum of CO.[4] Energy levels of the equivalent-core molecule NO are indicated.

potential barriers is responsible for the strong resonances below the ionization limit and weak resonances above the limit as well. Such enhanced resonances of core excitation to highly-localized unoccupied MOs seem a fairly common feature in inner-shell EELS and X-ray absorption spectra of many kinds of molecules.[2]

The dynamics of inner-shell processes are characterized by exceedingly short lifetimes and low transition rates with respect to that of valence-shell processes. The general features in the absorption spectra of molecules near inner-shell edges have been classified by van der Wiel[7] as follows:

1]. one or a small number of relatively intense peaks at energies below the edge with, at best, weak Rydberg structure;

2]. features that stand out prominently on a smooth continuum above the ionization threshold;

3]. a weak fine structure extending over hundreds of electron volts into the continuum (normally called extended X-ray absorption fine structure —— EXAFS).

In addition to those gross features inner-shell excitation spectra are usually much easier to comprehend than their valence-shell counterparts owing to the unambiguous assignment of the initial orbital that is an atomic-like, energetically well-isolated core orbital. In contrast, the decisive assignment of the transition in the valence-shell spectra is often troublesome on account of overlapping transitions from the diverse closely-spaced occupied valence MOs. In general, inner-shell excitation from different core levels provides a site-selected probe of the unfilled electronic structure of molecules under investigation since the core hole generated is essentially localized on a single atom. Comparison of the energies and intensities (i.e., transition probabilities or oscillator strengths) of inner-shell excitations between different edges in the same molecules and/or among different molecules can be utilized to map spatial distributions of virtual MOs and facilitate the interpretation of the valence-shell spectra.

The ISEELS studies of CO and N_2 have, besides the spectroscopy of inner-shell transitions, also reinforced the concept of an equivalent core model that had previously been adopted in photoabsorption studies of N_2 by Nakamura *et al.*[8] Wight *et al*[8] showed that the K-shell EELS spectrum of N_2 was indeed very similar to that of NO as was the carbon K-shell EELS spectrum of CO (See Figure 1.1). This model has been used by Wight and Brion[9] to predict the energy levels and even ionization potentials (IP) of the unstable radicals NH_4, H_3O and H_2F from the K-shell EELS spectra of CH_4, NH_3 and H_2O respectively.

Most early studies of inner-shell excitation through ISEELS experiments were focused on small inorganic as well as organic molecules, whose structures and dynamics had been investigated more or less thoroughly by other spectroscopies. Very recently, ISEELS has been used increasingly for the exploration of large molecules, such as model compounds of organic conducting polymers[10] and 3d-transition-element organometallic complexes[11-14] in the gas phase. It is the extension of ISEELS in the direction of organometallic complexes that is the central theme of this thesis.

§1.2 Bonding Interactions in Organometallic Complexes

Organometallic chemistry, one of the most diversified and exciting areas in the chemical sciences, is an extremely active field today. Since the discovery of ferrocene, $Fe(C_5H_5)_2$, in the early 1950s, which gave the main impetus to tie together many previously disparate compounds whose structures and bonding were unclear through the application of bonding theory to organometallic compounds, transition metal chemistry has expanded enormously with the development of metallocenes, metal carbonyls and, more recently, cluster compounds.

All 3d-transition elements in the Periodic Table can form compounds with carbon. A common organometallic compound may be viewed as a ligand that is bound to the 3d element through carbon. The physical and chemical properties of this compound will depend very much on the nature of the element and the bonding between the element and carbon. For instance, 3d-transition elements generally have rather low electronegativities, thus a metal-carbon σ bond, involving a metal atom bonded to a carbon one by a shared pair of electrons, in alkylmetal compounds will be polarized, which makes these compounds very reactive chemically. The placement of electron-withdrawing groups on the carbon atoms in place of hydrogen usually makes these bonds more stable.

Besides the M-C σ bond, many 3d organotransition metal compounds involve another bonding mechanism in which the organic group is bonded to the metal through the electrons in carbon-carbon π bonds. This is the so-called M-C π bond. It has been believed in general that the σ bond in these compounds involves the donation of electron density from an organic ligand to a metal atom while the π bond involves the transfer of electron density in the opposite direction —— from metal to organic ligand, namely, the often-termed back bond. Formation of such a two-component linkage requires both metal and organic moiety to have empty orbitals of appropriate energy/symmetry so as to accept electrons and, electrons in orbitals of suitable energy/symmetry available for donation, leading to the mutual reinforcement of the two components. This confines the metals to transition metals and the organic ligands to divalent carbon species (e.g., CO) or unsaturated hydrocarbons[15] (See Fig. 1.2).

The concept of "backbonding" (or backdonation) and the effect of other ligands on this phenomenon have attracted great research attention. Since electron density is being transferred from metal to an unfilled antibonding orbital of the ligand, bonding theory predicts that this should weaken the strength of the bond in question. In carbon monoxide, for example, the C-O stretching mode has an intense characteristic band at 2150 cm^{-1}. When CO bonds to a 3d transition element as a ligand, the resulting "$d\pi$-$p\pi$ backbond" weakens the C-O bond, causing this band to shift to a lower value [e.g., 2000 cm^{-1} in $Cr(CO)_6$]; the extent of this red shift traditionally serves as an indication of the degree to which this backbonding takes place. For the complexes of unsaturated hydrocarbons this weakening can also be detected through vibrational spectroscopy. The bonding between aromatic hydrocarbons and metal is usually stronger than for simple

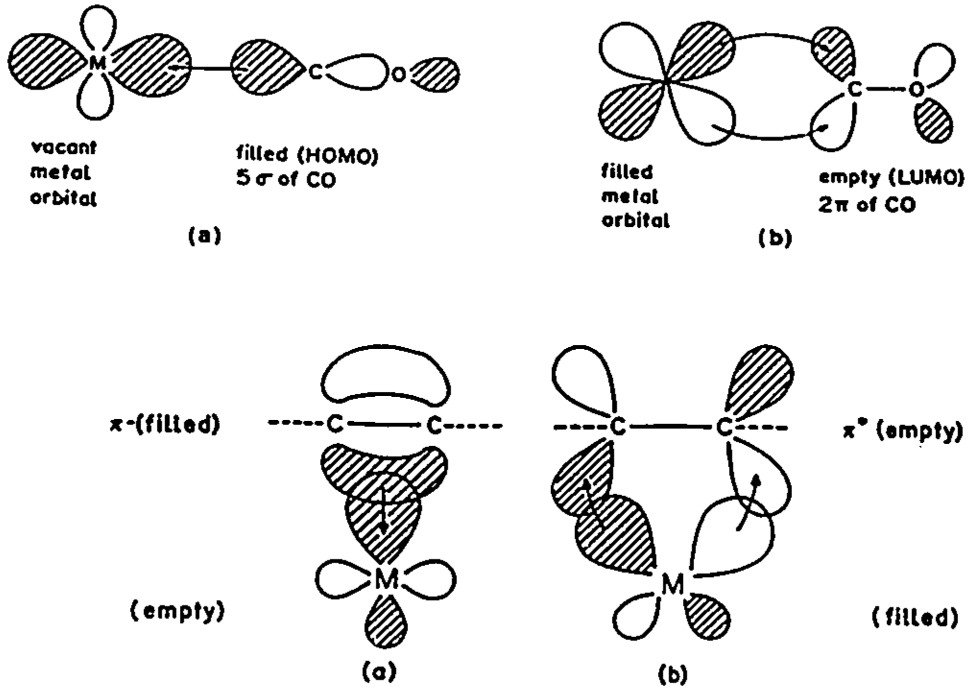

Fig. 1.2 Bonding interactions in a typical transition metal carbonyl complex containing terminal M-CO linkages (upper): (a) σ-donation from 5σ (HOMO) of CO into empty metal orbital directed along M-C-O axis; (b) π-backdonation from filled metal d orbital directed between the axes into 2π (LUMO) of CO. Conventional description of the bonding between a transition metal M and an alkene ligand (lower): (a) Alkene → M σ-donation; (b) M → alkene π-backdonation. The shading indicates the phase of the wave function.

olefins, since delocalized orbitals and more than two electrons are involved in such complexes. The weakened bond (usually double bond) becomes more susceptible to addition reactions in general. It is for this reason that transition metals are used in a wide variety of laboratory and industrial applications as catalysts.

§1.3 Organometallic Chemistry and Spectroscopy

Up until today, the π-backbonding concept has seemingly not been challenged. However, there is still an active debate on which component is more predominant, σ-bonding or π-backbonding, in the formation of these complexes. Apparently, it would be very helpful in answering this question if there is a clear map of the ground-state electronic distribution and frontier levels, occupied as well as unoccupied. Electronic spectroscopies can undoubtedly play a pivotal role in characterizing the electronic structure of this two-component liaison between the metal atom and its ligands. Extensive investigations in this regard have been fostered by, and in turn contributed to, the rapid development of numerous instrumental techniques [vibrational (FTIR, Raman) and/or resonance (NMR, ESR) spectroscopy, mass spectroscopy, X-ray crystallography, photoelectron spectroscopy etc.] for the last two decades. In particular, the 1980s saw a rapidly growing field at the interface of organometallic and physical chemistry, addressing questions of bonding, electronic structure, and reactivity of organometallic complexes. Interest in these issues is reinforced by the promise of metal-containing species for practical applications in areas such as catalysts[16] and microelectronics.[17] Recently, techniques have been developed with the potential for supplying spectroscopic data necessary for a comprehensive study of organometallic complexes. This has come about as experimental physical chemistry has obtained some novel and sophisticated spectroscopic methods for its repertoire.

Inner-shell excitation spectroscopy has special potential in investigating the unoccupied MOs of organometallic molecules, since ISEELS yields information about a whole series of unoccupied MOs both below and above the ionization limit, and hence also about the overall structure of the molecule. As mentioned earlier, the features of the core-to-virtual-valence transitions usually occur well below the Rydberg features and are among the most intense in the inner-shell spectrum on account of better overlap between the core orbital and the localized virtual-valence orbitals with respect to the large and diffuse Rydberg orbitals. This is in sharp contrast to the situation of valence-shell spectra where the transition to virtual-valence and Rydberg levels are much less well separated, and several series of lines overlap and interfere with one another. Furthermore, the core-to-virtual-valence transitions are often enhanced significantly by the occurrence of strong shape resonances owing to interaction between the escaping atomic-like core electron and the anisotropic molecular field.[5] The metal-to-ligand back-donation ($d\pi \rightarrow p\pi$) envisaged in the bonding scheme for the metal carbonyls and other unsaturated complexes involves the unfilled MOs, as receptor orbitals, which correspond to the π^* MOs of free CO and other unsaturated hydrocarbons. If localized π^* and σ^* resonances of the type observed in free ligands also occur in the core excitation spectra of organometallic species, then a study of their energies and transition intensities should provide a sensitive probe of the metal-ligand bonding in various compounds. This in turn could provide helpful insight into reaction mechanisms as well as energetics of complex organometallic transformation. Extension of the ISEELS technique to the study of gas-phase organometallic chemistry has been pioneered by Rühl and Hitchcock[11,13] recently and brought again fresh impetus to the field. Today this study has flourished better than expected.[18,19] It is the bright prospect for the application of ISEELS to organometallic species that inspires this project.

Gas-phase spectroscopies of organometallic complexes have attracted increasing attention in recent years. This is mainly because gas-phase experiments offer a unique opportunity to probe, in the absence of ion-paring effects and any solvation or other possible medium influences, the intrinsic properties/behaviours of metal-ligand bonding and/or ligand-ligand interaction in these complexes. They are an important prerequisite to study the chemistry in the condensed phase. A second major advantage of gas-phase over condensed-phase spectroscopy is that the energy scale is easily and directly referenced to the vacuum level, and the resulting information involves only intramolecular transitions. Thus, gas-phase spectroscopies make possible detailed and high-resolution spectroscopic characterization of organometallic compounds without often-seen spectroscopic-broadening as well as other complicating factors of solution and/or solid state investigations. The principal purpose of this present study is to explore and characterize the electronic structure and bonding of some organometallic complexes in **the gas phase** using the ISEELS technique.

§1.4 How to Study Organometallic Species by ISEELS

Characteristic features of an electron energy loss band are its energy, intensity, width, shape and, sometimes, resolved fine structures in high-resolution EELS spectra (if available). Each feature is sensitive to the electronic structure of the molecule of interest and can furnish information about electron localization on the metal and the ligands, and the antibonding nature of the virtual-valence orbitals. First of all, the inner-shell **excitation** energies are the most significant in light of trends between related molecules. In particular the shift in energy between those electronically or chemically related molecules is a revealing feature of the electronic structure. In some cases, the correlation of energy losses between related molecules simply assists in the assignment of the spectra, such as in the comparison of the energy losses of free ligand molecules with those of organometallic complex molecules. In other cases, the electronic perturbations caused by chemical group substitutions produce identifiable energy shifts that unveil the localized or delocalized character of the electronic states.

Secondly, the **transition intensities** directly indicate the degree of overlap between the atomic-like inner-shell orbital and the virtual valence MOs. Sometimes the relative magnitudes of intensities associated with core excitation to specific antibonding orbitals (e.g., π^* or σ^*) yield information on their abundance in related molecules (e.g., in C_5H_5-H and its dimer[19]). In metallocene ISEELS spectra[13] the band intensity has been used to identify those low-lying energy losses as the metal-3d based MOs. For metal carbonyls, relative oscillator strengths of the C 1s → π^* transition have been considered as a direct measure of the degree of the metal-to-CO backdonation.[14]

In the third place, the **breadth** and **shape** of an energy-loss band are related to factors such as the lifetime of the core hole, orbital relaxation accompanying the inner-shell excitation and simultaneous excitation of vibrational modes in organometallic species, which may be associated with the M-C modes. For transition-metal complexes, observation of resolved vibrational fine structures is often less likely on account of low metal-ligand vibrational frequencies or because several different vibrational progressions are possibly excited by a single inner-shell promotion. In these cases the overlapping vibrational components will blend into a single featureless asymmetric or Gaussian-shaped energy-loss band. The width of the band can provide information on the change in molecular electron-density distribution[12] and the extent of bond distance changes between the ground and excited states in the complexes. This has been observed in the high-resolution ISEELS spectra of some metal carbonyls,[12,20] where the vibrational structure has been resolved for the C 1s → π^* transitions, and the fine structure is seemingly influenced by metal-d → CO-π^* backbanding effects.

In addition, spectral comparison among a series of related complexes offers the opportunity to investigate a particular metal-ligand bonding situation in a variety of electronic environments. A series of related complexes is normally formed by chemical modifications, such as ring methylation and electronegativity perturbations [through electron donating (or electron withdrawing) substituents]. Metal complexes with a variety of ligands are also attractive for studying a wide range of metal-ligand interactions and the trends in bonding as a function of the electron density (or electronegativity) at the central metal, the mobility of charge, and the symmetry about the metal. The dependence on these factors may be assessed by comparing metal systems and/or by altering the type of ligand, which changes the formal d-electron count at the metal without changing the metal itself.

Finally, inner-shell EELS seems particularly suitable for characterizing the electronic effects of ligands on organometallic complexes. This is supported by the ligand-additivity principle which suggests that the inner-shell energy losses associated with a type of ligand (or some MO of it) are relatively independent and/or stable in a certain energy range regardless of the change in electronic environment. This means that (successive) ligand replacements in transition metal species would result in reproducible and systematic (additive) shifts of the core-shell energy losses due to the fact that the ligand electronic effects are transferable or additive to new organometallic complexes. Recent observations[14,19] showed that the additivity model is valid for many ligands and metal systems. With knowledge of consistent energy-loss shifts, assignment of ISEELS spectra of the complexes is simplified and the term values (See §1.6) of unknown species may be predicted empirically.

This study will illustrate how a wealth of information on the electronic structure of gas-phase organometallic compounds can be extracted from the relative energies, intensities, shapes and widths of the energy-loss bands in ISEELS spectra as well as by the dependence of these features on chemical substitutions in these complexes. Inner-shell EELS spectra have been recorded, under small momentum-transfer conditions, for the following species: $Co_2(CO)_8$, $C_5H_5Co(CO)_2$, $Co(C_5H_5)_2$ (see Chapter 3), $Fe(CO)_5$, $Fe_2(CO)_9$, $RFe(CO)_3$ ($R = C_4H_6$, C_6H_8 and C_8H_8), $C_5H_5FeC_5H_4$-R' (R'= H, C_4H_9- and CH_2=CH-) (Ch. 4), $C_6H_6Cr(CO)_3$, CH_3-$C_5H_4Mn(CO)_3$ (Ch. 5), $C_5H_5TiCl_3$, $TiCl_4$ (Ch. 6), and $Si[Si(CH_3)_3]_4$ and $(CH_3)_3SiSi(CH_3)_3$ (Ch. 7).

§1.5 Theoretical Background of Electron Energy-Loss Spectroscopy

Electron-molecule (as distinct from electron-atom) collisions[21] have several characteristics. Firstly, molecules possess rotational and vibrational degrees of freedom, which can be excited by a small amount of energy. Secondly, the electron-molecule interaction is essentially multi-centred and non-spherical owing to the presence of more than one nucleus. Thus, the interaction even at long distance is often strong and can have an orientation dependence since molecules can have permanent electric multipole moments and since molecular polarizability is anisotropic. Furthermore, molecules can be dissociated in collision with an electron. In general, the interactions between the electron and molecule can roughly be considered to be made up of three components: static, polarization and exchange portions.

The static component is the electrostatic interaction between the incident electron and the static field produced by the unperturbed target molecule at a point sufficiently away from the molecule. The field is characterized by the electric multipole moments of the molecule. If the molecule is neutral but has a permanent dipole moment, the dipole interaction is predominant. Other multipole interactions (e.g., the quadrupole interaction due to the molecular quadrupole moment) are normally weaker, but not necessarily negligible. These interactions depend on the molecular orientation relative to the direction of the incident electron. The polarization aspect of the interaction refers to the deformation of the molecular charge cloud (i.e., the induced dipole moment of the molecule) by the approach of the point charge of the incident electron. The exchange interaction describes possible exchange of the incident electron with a molecular electron. This will give rise to a non-local interaction because the exchange is controlled by the overall overlap between two-single-electron wave functions. Such an exchange takes place with an appreciable probability only when the incident and molecular electrons have comparable velocities. As soon as the incident-electron energy becomes higher, the probability of the exchange collision gets smaller and smaller. The electron exchange effect has little influence on collisions between high-impact electrons and molecules, and therefore it is often omitted.

In high-energy (>150 eV), small-angle electron-molecule collisions, electronic excitation and ionization are the dominant energy-loss processes and, the collision duration is so short that the energy and momentum transfers from the incident electron to the target molecule occur in one step and their magnitudes are very small. This means that first-order perturbation theory is appropriate to describe these processes.

Thus, the Born approximation, which is the first-order perturbation theory for collision processes, can be applied directly. The second Born and some other approximation methods have been proposed to study the deviation from the simple Born approximation.

A quantity of fundamental importance in collision theory is the differential cross-section $d\sigma/d\Omega$ (DCS), representing the collision probability of an incident electron being scattered (per unit solid angle Ω) by a molecule. The DCS depends upon the collision energy, viz., it is a function of the relative velocity of the incident electron and the target molecule, rather than the electron beam velocity. The difference, however, is not very critical unless the electrons are of very low energy or the target molecular gas is at very high temperature, or both. Obviously, it is more convenient to define a DCS per unit excitation energy (i.e., for EELS, per unit energy loss). The angular and energy dependencies of scattering are thus specified by a double-differential cross section $d^2\sigma/d\Omega dE$.

Fast electrons are inelastically scattered through interaction with either outer- or inner-shell electrons of the molecule, and these two processes predominate in different regions of the EELS spectrum. Inner-shell scattering takes place with comparatively low cross section and therefore the probability that a fast electron gives rise to more than one inner-shell excitation is generally negligible. In order to describe more precisely the inelastic scattering of electrons by a molecule, one must evaluate transitions from an initial state of wavefunction ψ_0 to a final state of wavefunction ψ_n. Using the first Born approximation the DCS for the transition is[22,23]

$$d\sigma/d\Omega = (m_0/2\pi\hbar^2)^2 \cdot (k_1/k_0) \cdot |<\psi_n|V(r) \cdot \exp(iK \cdot r)|\psi_0>|^2 \qquad (1.5.1)$$

where k_0 and k_1 are wavevectors of the fast incident electron before and after scattering, $\hbar\mathbf{K} = \hbar(\mathbf{k}_0 - \mathbf{k}_1)$ is the momentum transferred to the molecule (Fig. 1.3), $\mathbf{r}$ denotes the coordinate of the fast electron, and $V(r)$ represents the perturbing potential responsible for the collision.

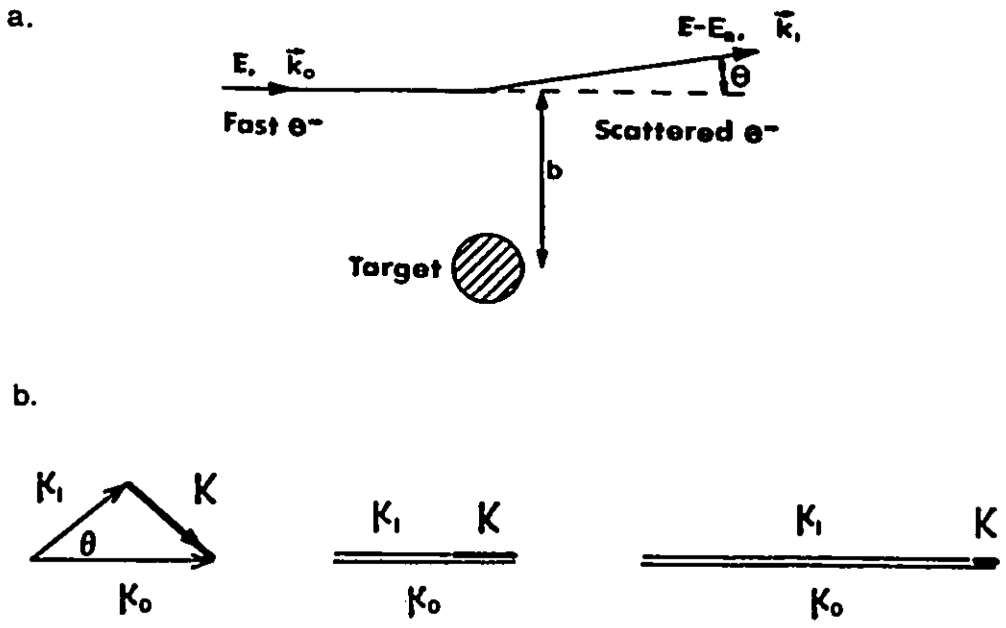

Fig. 1.3

(a) Schematic illustration of inelastic scattering of a fast electron from a molecular target: E, impact energy; E_n, energy loss; $\mathbf{k}_0$ and $\mathbf{k}_1$, wavevectors of the fast incident electron before and after scattering; $\boldsymbol{\theta}$, scattering angle; ***b***, impact parameter. (b) Transferred momentum, **K**, dependent on the scattering angle and/or the incident electron $\mathbf{k}_0$. E_n has the same magnitude for the three cases.

Under negligible momentum-transfer conditions, an energy loss spectrum is analogous to a photoabsorption spectrum. This analogy was first established by Bethe[22] in 1930. The key quantity in Bethe theory is the generalized oscillator strength (GOS), $f_n(K)$, which describes the response of an atom or molecule when a given energy and momentum are transferred from an external source (e.g., by collision of a fast electron). The GOS is defined as

$$f_n(K) = (E_n/R)\cdot(Ka_0)^{-2}\cdot |\langle\psi_n|\Sigma_j \exp(iK\cdot r_j)|\psi_0\rangle|^2 \qquad (1.5.2)$$

where E_n is the excitation energy associated with the $|0\rangle \rightarrow |n\rangle$ transition, R is the Rydberg energy, a_0 is the Bohr radius, and the summation is over all the electrons in the molecule. Bethe treated the effect of a fast electron as a weak perturbation, i.e., within the first Born approximation, and showed that there is a quantitative relationship between the DCS of electron scattering and the GOS,

$$d\sigma/d\Omega = (4R/E_n)\cdot(k_1/k_0)\cdot K^{-2}\cdot f_n(K) \qquad (1.5.3)$$

Thus, the analysis of fast collisions reduces to the study of a transition matrix element, just as the analysis of the photoeffect does. For inelastic scattering, the value of K depends on both the scattering angle θ and the energy loss E_n. The dependence of K on θ is derived by applying the conservation of momentum to the collision,[24] and is given by:

$$K^2 = k_0^2 + k_1^2 - 2k_0k_1\cos\theta \qquad (1.5.4).$$

It is necessary to distinguish small-angle from a large-angle scattering since they have entirely different effects on collision phenomena. When the incident electron is scattered by a small angle, the momentum transfer $\hbar K$ is small according to Eq. (1.5.4).

Intuitively such a collision may be characterized by a large impact parameter[24] $b \approx 1/K$. The force then exerted by the incident electron is uniform over the spatial extent of the target molecule, in the same way as implied by the dipole approximation for photoabsorption. Yet the same force is sharply peaked at time, owing to the high velocity of the incident electron, and therefore its Fourier components are widely and smoothly distributed in frequency ω, resulting in an ideal "continuum light source" of virtual photons. Each of the Fourier components excites the excited state at $E = \hbar\omega$. Consequently, electron collisions at small K are similar to irradiation with a photon flux having a wide and calculable spectrum, hence the name "pseudo-photon".[1]

To see further this connection mathematically, one may expand the exponential in Eq. (1.5.2) if $(Ka_0) < 1$, leading to an expansion[22,23] of the GOS in even powers of (Ka_0),

$$f_n(K) = f^{opt.} + (Ka_0)^2 f^{(1)} + \tfrac{1}{2}(Ka_0)^4 f^{(2)} + \ldots \qquad (1.5.5)$$

where $f^{opt.}$ is the familiar optical (dipole) oscillator strength, the quantity that is found to be proportional to intramolecular dipole transition probabilities and simply linearly-related to the cross section for absorption of radiation. $f^{opt.}$ has a non-zero value only when the optical selection rules for the excitation are obeyed, thus giving an optically-allowed electric dipole transition.

When $Ka_0 < 1$, which can be achieved by using high electron-impact energy and small scattering angle, only the first term in Eq. (1.5.5) is significant, and then the electron scattering cross section (DCS) is directly related to the optical oscillator strength. Thus, an electron energy-loss spectrum simulates effectively the photoabsorption spectrum, except for the difference in intensity associated with the kinematic factor $[(4R/E_n)(k_1/k_0)K^{-2}]$. In the limit of negligibly small momentum transfer electric-dipole-allowed selection rules will govern the transitions in the EELS spectrum. A substantial body of work of EELS in or near the dipole region is based on this thesis. With regard to the study of molecular pseudo-optical spectroscopy, the work by Brion and co-workers[1,4,9] has been most influential.

The second $f^{(1)}$ and other higher-order terms of the expansion (1.5.5) are defined in Ref. 23. They correspond to mixtures of electric multipole (i.e., electric quadrupole, octupole, etc.) transitions, all of which are optically forbidden. In inner-shell excitation experiments the momentum transfer **K** may sometimes be large enough so that these higher-order terms cannot be neglected, and therefore the ISEELS spectrum reveals some peaks because of non-electric-dipole transitions.[25,26] Consequently, those optical selection rules are substantially relaxed. The effect can be enhanced if the K value is raised by a judicious choice of the scattering angle and/or the incident impact energy. When the impact energy (E_0) of fast electrons is comparable to the excitation energy (E_n) of the target state, the electron exchange becomes possible, and then spin-forbidden transitions can be excited, such as a singlet-triplet transition.[3] This type of electron-molecule collision affords essentially the only way of causing the spin-exchange effect. Clearly, non-dipole excitation is a major difference between electron collision and photoabsorption, and the electron-impact excitation has the great advantage of being able to induce electric-dipole-forbidden transitions.

§1.6 Resonant Features in ISEELS Spectra

Characteristic resonances appearing in ISEELS spectra are attributed to the promotion of inner-shell electron to virtual MOs near the vacuum level and therefore fall at excitation energies close to the ionization potential (IP), the minimum energy required to excite an electron to the continuum states above the vacuum level. The corresponding cross sections of the molecular partial-channel electron impact ionization can be determined by Eq. (1.5.1) provided that the initial and final states are well defined. In general, the virtual MOs can lie either below the IP, resulting in the discrete features, or above the IP where they are merged into ionization continuum (See Figure 1.4). Thus, the initial orbital of the inner-shell transition is always a non-bonding,

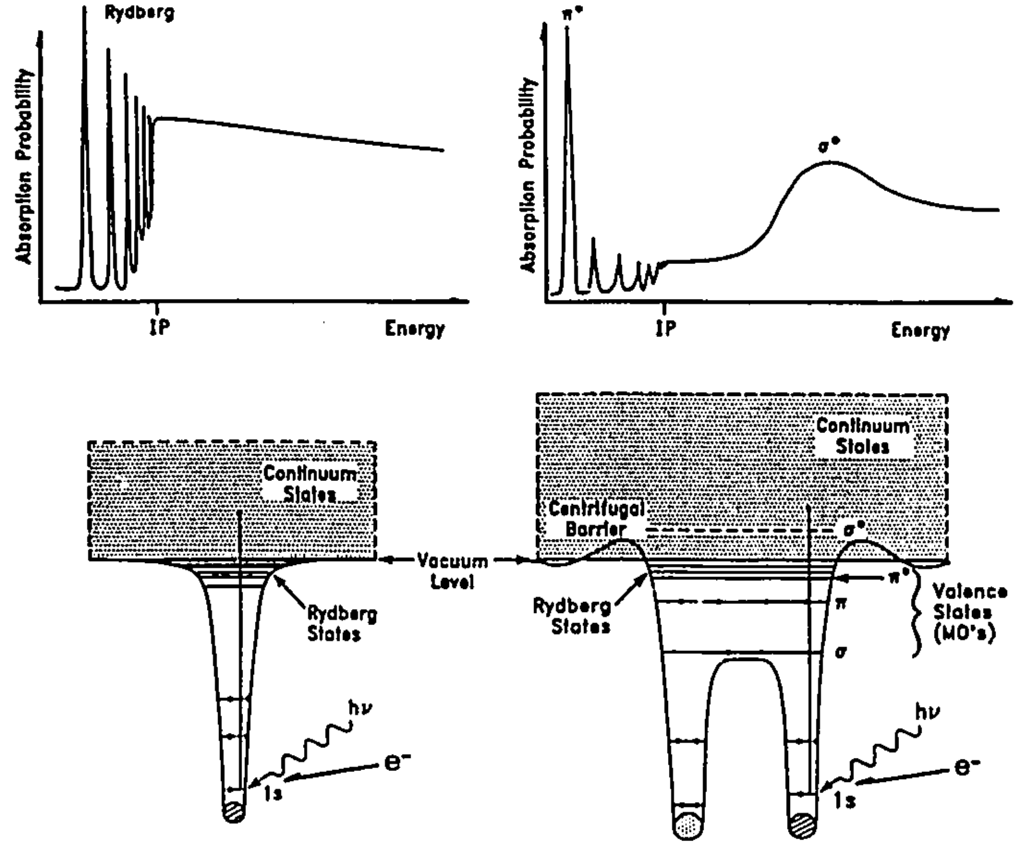

Fig. 1.4 Mechanism at work in core excitation generated by either photons or fast electrons. Inner-shell electrons are excited to final states in a hypothetic atom (left) or molecule (right); i.e., bound states (such as partially-filled valence-orbital or π^* states) and quasi-bound states in the continuum (shape resonances). The corresponding core-excitation spectra are illustrated on the upper of the figure.

localized core-shell MO, while the final orbital can, in principle, be either a bound (non-ionized) or a continuum (ionized) orbital. The bound-state transitions involve final states below the vacuum level. They correspond to inner-shell excitation into the virtual valence MOs derived from valence electron shells of the atoms, which frequently have antibonding character, as well as to the well-known Rydberg orbitals with non-bonding character, lying outside the virtual valence MOs.

Very often, the origin and nature of the resonances are associated with certain final-state molecular symmetry. The simplest symmetry classification for the low-Z molecules is in terms of σ and π orbitals. In the case of a diatomic molecule the σ MOs are symmetric relative to reflection through a plane containing the molecular axis while the π MOs are antisymmetric. For polyatomic species the MOs derived from the more-extended atomic orbital overlap can still be labelled either σ symmetric π antisymmetric with respect to a local symmetry plane. In σ bonds (or MOs), the plane containing the bond axis has no node, but has one for π bonds. The σ bond exists in a molecule without exception whereas the presence of a πbond is not always necessary, depending on the number of valence electron available for bonding. However, both σ and π symmetries involve not merely bonding but also antibonding MOs.

For ISEELS spectra, it is the unoccupied orbitals (indicated by an asterisk) that are of significance in general, since the observed spectral features correspond to electric-dipole-allowed transitions from a core orbital to typically σ^* and π^* antibonding MOs. For example, in K-shell excitations the initial 1s state is always of σ symmetry, while the final states allowed by the dipole-selection rule have to contain an atomic p-orbital component on the core-excited atom, and may be of σ and/or π symmetry. It should be noted that because the inner-shell excitation takes place on a particular atom due to the spatial localization of the core-shell initial state only the local symmetry of the MO final state on the excited atom determines whether the transition is allowed or not. Therefore, for the above example it is the overlap of the 1s and p functions near the atomic core that determines the dipole matrix elements in $f_n(K)$ of Eq. (1.5.3). One more word of emphasis concerns the symmetry or angular momentum of the final-state wavefunction. The $\ell=1$ (p-wave) nature only holds in the coordinate system of the excited atom for this case. Relative to the whole molecular coordinate system all ℓ values are allowed. Brief accounts are given in the following section of selected aspects of the characteristic resonances met in ISEELS spectra.

§1.6.1 π^* Resonances

A π^* resonance (e.g., a C 1s → π^* transition in an orbital model) is observed only for molecules having π bonding as the π^* orbitals are the antibonding counterparts of the π bonding MOs that are partially responsible for the chemical bonds in a molecule. Broadly, the lowest unoccupied MO (LUMO) for a diatomic (such as CO and N_2) or a polyatomic molecule containing at least a double bond (e.g., C_2H_4) is always a π^* orbital, with σ^* MO(s) occurring at higher energy. Therefore the lowest energy peak in the ISEELS spectra of these species always corresponds to a transition to a π^* antibonding orbital of the molecule. In the ground state the unfilled final states (e.g., $2\pi^*$ MO in CO) are normally located above the vacuum level (E_v). but in the core excited state, there is a downward shift of the outer "optical" orbitals because there is one electron less in the core orbital to screen the nuclear charge and thus there is an increased attractive Coulomb interaction between the nuclear charge and the excited electron in the outer virtual valence MOs.[27] This Coulomb effect is responsible for the π^*-resonance transition energy being less than the IP. It is in this sense that such features are sometimes referred as "discrete" shape resonances.

The π^* resonance is often the most intense feature in ISEELS spectra. Up until today, the explanation of the large intensity of core → π^* transitions is still not certain. The high oscillator strength reflects a large spatial overlap between the core and π^* orbitals, implying strongly that the latter is an inherently-localized orbital, having probably about the same size as the molecular core. In contrast to the "shape-resonance" explanation of the MS-Xα multicenter model[5] introduced briefly earlier, Pavlychev and

Vinogradov[28] propose that the unusually strong π^* resonance in the N_2 molecule is simply an intrinsically strong atomic N 1s → 2p transition in a single free nitrogen atom. Redistribution of the electron density in the N_2 molecule will simply lead to a reduction of the intensity of this resonance. Interestingly, Schwarz *et al*[29] consider the π^* feature below the IP as a Feshbach resonances.

The width of π^* resonant features is determined by both the natural linewidth associated with the lifetime of the ($1s^{-1}$, π^*) excited state and the vibrational band structure of the transition. For the π^* resonance, the lifetime of the ($1s^{-1}$, π^*) state is determined by the decay of the core hole, which undergoes predominantly autoionization, a process similar to Auger decay that involves filling the core hole with a less-tightly bound electron and simultaneous emission of a valence electron. In cases where there is negligible vibrational excitation, such as the C 1s → $2\pi^*$ transition in CO, the width of the transition observed under high energy resolution (e.g., $\Delta E = 68$ meV FWHM) reflects directly the natural linewidth. For free CO, this is 175±20 meV (FWHM),[20] which is extremely narrow and therefore this line has often been utilized directly in determining the energy resolution of an ISEELS spectrometer. In $Ni(CO)_4$, it is 232±20 meV, slightly larger than in CO.[20]

§1.6.2 σ^* Shape Resonances

In the C K-edge spectrum of CO (See Figure 1.1), two resonances are observed above the 1s IP. The broader band of higher energy is a so-called σ^* shape resonance.[5] Shape resonances are one of the intriguing phenomena in molecular core-excitation spectra. They are quasi-bound states in which an outgoing excited electron is temporarily trapped by a potential barrier, through which the electron may eventually tunnel to escape. The term "shape" resonance refers simply to the fact that the outgoing electron is momentarily bound because of the "shape" (i.e., the barrier and associated inner and outer wells) of a local potential. This idea is illustrated schematically in Figure 1.5.[30] There, an effective molecular potential experienced by the excited electron is described to have two wells: the inner well (IW) at small distances and the outer well (OW) at large separations; and one barrier, viz., the often-referred centrifugal barrier (CB), lying between the two wells.

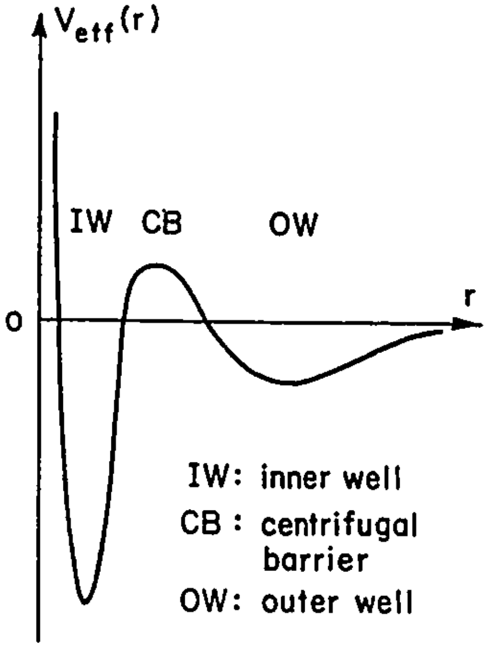

Fig. 1.5 A hypothetical double-well potential curve.[30]

This barrier arises from a competition between repulsive centrifugal potential $\ell(\ell+1)/2r^2$ and attractive Coulomb electrostatic potential V(r), and normally resides on the perimeter of the molecular charge distribution. This suggests that the OW is situated outside the molecule where the Coulomb potential ($\sim$-r^{-1}) dominates the centrifugal term in the molecular field. The final states may be approximate eigenstates of either the IW or the OW. The CB controls a finite number of bound and/or quasi-bound states in the IW, some of them may perhaps be resonant. The OW potential is asymptotically hydrogenic and it sustains an infinite number of Rydberg states, forming a so-called "Rydberg sea". For the inner-shell excitation the initial orbital is mainly confined in the IW (See Figure 1.4) and, consequently, only those virtual-valence MOs or Rydberg orbitals that have some IW amplitude will couple with the ground state. Being quasi-bound inside a CB on the periphery of the molecule, the shape resonances are localized, and coupled poorly with the external environment of the molecule. This localization usually gives rise to intense spectral features, but suppresses the nearby Rydberg and/or continuum structure.

According to this single-channel, barrier-penetration model, the CB plays a vital role in shape resonant phenomena. Since the CB shape and height depend on the angular momentum of the final electronic state, shape resonances are associated with particular ℓ components of the outgoing electronic wavefunction and these components are blocked only in certain directions, for instance, along the internuclear axis for the σ^* shape resonance. In the case study of N_2, it has been found that the Rydberg series of the σ^* partial cross section are strikingly weak. However, a broad intense band emerges from the low-energy continuum, about 1 Ry above the IP. This was attributed to the CB acting on the $\ell=3$ (f-wave) component of the σ_u^* wavefunction.[5]

Instead of applying the molecular potential scattering model discussed above, the resonance can also be described by a MO (Stieltjes) theory.[6] As discussed in detail by Sheehy *et al*[31] the MO method naturally produces final states of enhanced amplitude on the molecule lying above the vacuum level, without utilizing specifically the potential-barrier concept. For this reason σ^* shape resonances are sometimes referred simply as σ^* resonances. According to this MO theory the σ^* resonance can be viewed as a two-step one-electron process in which an inner-shell electron is first pumped into an unfilled virtual-valence MO of σ symmetry, and then decays into the continuum as a photoelectron.[32]

Although σ^* MOs largely appear in continuous regions in most cases, they can also be localized spectrally as bound states. A crucial parameter is the bond length, as is demonstrated by the simple diatomics N_2, O_2 and F_2. In the triply-bound N_2 of a very short bond length the $3\sigma_u$* MO appears about 10 eV above the threshold.[4,33] For the double-bond O_2 molecule the corresponding MO is right at the threshold,[34] whereas in the single-bond F_2 it is a bound MO,[35] about 14 eV below the IP. In fact, the energy position of the σ* resonance is rather sensitive to the internuclear separation due to the fact that σ* MOs are directed along the internuclear axis between two atoms, the excited electron trapped in the σ* MO potential scatters back and forth between the atom bearing the hole and its neighbour and therefore the resonant condition depends upon the internuclear distance, as has been discussed in detail in Ref. 31 and 36. On the contrary, the bond-length dependence of the π* resonance position is expected (and found) to be much smaller, which has been rationalized in terms of the fact that π* MOs are perpendicular to the internuclear axis.

The energy breadth of the σ* resonance is determined by the lifetime of the quasi-bound electronic final state. Since the probability for decay of the quasi-bound electron to continuum states rises gradually with energy, the σ* resonances become broader. According to the calculation of the σ* shape resonance for N_2, the lifetime of the trapped electron is shorter than that of the core hole and therefore the hole will live long enough to affect the resonant escaping electron.[37] The asymmetric line shape of the σ* resonances can be explained readily in terms of the barrier-penetration picture: Since the probability for tunnelling through the CB increases with the kinetic energy of the escaping electron, the σ* resonance shape is more peaked at lower energy side with a tailing toward to higher energy.

§1.6.3 Rydberg Structures and Valence/Rydberg Mixing

A question often-raised is "What is a Rydberg state?". Several criteria may be applied for the definition of the highly-excited Rydberg states in a molecule: (i) The energy of the term value (T) for any member (n,ℓ) of a series should obey the Rydberg formula

$$T = IP - E_n = R/(n - \delta_\ell)^2 \qquad (1.6.1)$$

where R is the Rydberg energy (13.6 eV) and δ_ℓ the quantum defect associated with the angular-momentum quantum number ℓ; (ii) Molecular Rydberg orbitals (MRO) should have principal quantum numbers (n) larger than that of the outermost occupied valence shell of the molecule under question; (iii) The main density maximum of a MRO should abide outside the molecular core and, the shape and the number of its nodal surfaces should be similar to those of its atomic counterpart, viz., the corresponding hydrogenic orbital; (iv) MROs should be large as well as diffuse,[38] their mean radii increase as n^2 and their oscillator strengths should approach a Coulomic n^{-3} behaviour with increasing n; (v) A Rydberg state should undergo a strong perturbation and blue shift upon condensation of the molecule; (vi) MROs should have non-bonding character and very little influence on molecular bonding, therefore their energy should be relatively independent of changes in bond length.

In contrast to MROs, virtual-valence (VV) MOs are relatively compact, being made up of valence-shell principal-quantum-number atomic orbitals. They result from the splittings of valence-shell AOs that occur upon formation of the bond. As a result of their compact nature, excitations between the inner-shell levels and VV MOs can have large transition moments. Since each molecule has only a small number of such MOs, it is a simple matter to determine the VV class of MOs for any molecule from the atomic shells of the atoms comprising this molecule as well as from the total number of electrons that fill the MOs.[39]

In ISEELS spectra Rydberg structures usually appear between the π^* resonances and the IP. Their intensities are very weak generally owing to the poor spatial overlap between the inner-shell orbital and the MORs. This is especially true for higher energy edges because of the reduced size of the core orbital and hence the smaller orbital overlap with MROs. In the case of CO, high-resolution studies show that Rydberg states are a cluster of sharp features appearing about 2 eV below the IP, and converging to the onset of the ionization continuum.[3] The excitations to higher n Rydberg states are commonly blurred by the increased state density near the continuum as well as by the rapid fall-off in the transition probability as n^{-3}. The weak intensity of the Rydberg peaks for CO is readily ascribed in the double-well potential picture to the fact that Rydberg MOs have most of their spatial extent and orbital density in the outer well.

In molecules with bonds to hydrogen atoms, mixing of the Rydberg MOs with hydrogen-derived virtual-valence MOs of the same symmetry usually enhances the intensity of the corresponding resonances on account of the more compact nature of the valence orbitals. Such a mixing is believed to be a fairly general phenomena in ISEELS spectra of hydrocarbons and/or other hydrogen-containing species,[40-42] and therefore many "pure Rydberg" structures assigned over years may be better described as mixed valence/Rydberg resonances.

§1.6.4 Muiltielectron Excitations

Thus far all the spectral features discussed above have been described within a one-electron-transition framework. Obviously the major reason for utilizing such a treatment is its simplicity. It is true in general that the excitation spectra are dominated by single-electron processes, yet electronic excitations are essentially a multi-electron-transition process in nature. This is especially the case for inner-shell excitations due to strong relaxation and correlation effects, as is reflected sometimes by the emergence of multiple ionization processes or double excitation in the ISEELS spectra. In the cases of ionization, an inner-shell electron is ionized and often concomitant with this, one of the valence electrons in the outer-shell MO of symmetry Γ is "spontaneously" knocked out either into an unoccupied virtual MO of the same symmetry Γ or into the ionization continua. The term "shake-up" is given to the process when the resulting excited ion state is a bound state, while the term "shake-off" is used for the process when it is a continuum state. These two types of processes appear as satellite peaks and continua respectively, lying above the main ionization line in photoelectron spectra (PES). In excitation spectra, however, they are presented as additional ionization continuum onsets at energies above the IP equal to the separations between PES satellites and the main line. Broadly, the shake-up structures are peak-like whereas the shake-off ones are step-like or just like a smooth background. Since the excited ion state must have the same symmetry as its parent ion state in order to produce the non-zero overlap integral between them, the valence electron transition must comply with monopole selection rules. Monopole shake-up transitions to Rydberg MOs are also possible, but this time the electron in a Rydberg orbital is bound to a doubly-charged core.

Another multielectron feature often observed in the near continuum is double excitation caused by electron correlation effects, in which the sudden promotion of a core-electron simultaneously induces a monopole excitation of a valence electron. Thus, the shake-up transition is a type of two-electron excitation. However, double excitations can also be generated in neutral molecules with their intensity being related to configuration interaction. In this case, the two-electron excited configuration cannot be reached directly from the ground state by means of electric-dipole absorption, unless this configuration is mixed with a single-electron excited configuration that can be reached from the ground state. Therefore, the double excitation process emerges in excitation spectra by virtue of its partial one-electron character. Examples of double-excitation in ISEELS spectra can be observed in the K-shell spectra of N_2 and CO (carbon).[4] In both cases a pronounced peak-like feature is present about 5 eV above the IP, just right below the σ^* shape resonance (See Fig. 1.1). The high-resolution spectrum of free CO reveals quite rich vibronical fine structure in this resonance.[3] Both MS-Xα and MO theories, however, fail to account for multielectron excitations due to the fact that both treatments adopt a one-electron-excitation calculation and ignore utterly the multielectron effect.

§1.7 Extended Hückel Theory

Extended Hückel molecular orbital (EHMO) theory has been used in some cases to assist the interpretation of ISEELS spectra since it has proven rather helpful in facilitating the spectral assignments.[13] As spectroscopists we are interested in employing theoretical methods to predict the results of possible experiments and to analyze our results. At the present time, computer programs are really available for many theories and the main problem we face is which theory is the best for our spectral data and how reliable is that theory.

Hückel molecular orbital (HMO) theory of π-electron systems is familiar to most chemists. The theory has been very successful in tackling many properties of organic molecules as it finds its simplest form in rationalizing and correlating experimental results for a class of related compounds. However, this method suffers many drawbacks, especially in dealing with problems regarding properties associated with σ orbitals, even though these deficiencies are partially compensated by the generation of a very simple computational scheme. Mulliken[43] and, Wolfsberg and Helmholtz[44] proposed a quite simple means of parameterization for HMO calculations which greatly facilitates their extension to σ-electron problems and the treatment of entire valence-electron structure as well. The Coulomb integrals for an orbital i ($\alpha_i = H_{ii}$) are taken as the appropriate valence-state ionization potentials and the resonance integrals ($\beta_{ij} = H_{ij}$) are expressed by an arithmetic mean formula:

$$H_{ij} = \tfrac{1}{2}kS_{ij}(H_{ii} + H_{jj}) \tag{1.7.1}$$

Based on this method, Hoffmann[45] put forward his extended Hückel MO theory (EHT). In EHMO, both σ and π electrons are treated. Like in HMO, the total electronic wave function is separated into an inner-shell nonbonding portion and a valence-shell bonding portion. None of the valence electrons are neglected, but inner-shell electrons are usually neglected; yet they are considered implicitly in so far as they provide a non-polarizable core. Instead of using hybrid orbitals, Hoffmann used pure atomic orbitals and included all interactions and all overlap integrals that can be calculated analytically. EHMO can be applied without difficulty to three-dimensional molecules and eventually any type of molecule (inorganic, saturated, unstable, etc.) with the possibility of varying the assumed geometry. Generally speaking, the simple MO methods at the Extended Hückel level of approximation are supposed to have some problems in describing the structural or dynamic properties of a large molecule containing a transition metal atom or ion, due to difficulties of generating a set of proper basis functions for the metal valence-level atomic orbitals (AOs) entering the MOs and of estimating a set of proper Coulomb integrals for the transition AOs. However, Hoffmann and co-workers[46-49] have shown that EHMO is an effective technique of exploring potential surfaces, energy differences between conformers, barriers to internal rotation and some other molecular properties.

§1.7.1 Parameters in EHMO

It is well known that appreciable discrepancies exist between the EHMO and the Hartree-Fock potential energy surfaces. One should realize that the energy scale in EHMO is entirely dependent on one's choice of Coulomb integrals as well as the choice of formula for H_{ij}, and thus it is rather empirical. Therefore, the computed values of energies (or energy differences) only have relative significance. The choice of Coulomb integrals has the effect of positioning the calculated results on the energy scale, and it dictates the magnitude of the energy difference obtained. The parameters are selected in such a way that they are reasonable in the sense that the Coulomb integrals are in accord with our chemical "intuition" and a chemically-reasonable population-analysis results.

The Coulomb integrals of the transition-metal AOs have been obtained by the self-consistent charge method of calculation, in which the parameters are assumed to depend on the molecular charge distribution. Such a dependence allows one to correct for interelectronic repulsion effects. For the Group VIIIB elements of iron, cobalt and nickel, there exist two sets of the Coulomb integrals generated by this means, both of which are extensively employed in EHMO organometallic chemistry at the present time.

In the earlier set the H_{ii}'s for Fe and Co, given by Summerville and Hoffmann,[48] were obtained from a charge iterative calculation on suitable model compounds $Fe_2(NO_2)_4I_2$ and $Co_2(NO_2)_4Cl_2$, assuming a quadratic dependence of metal H_{ii}'s on charge. Charge iterations for the later set, refined by Albright et al,[49] were performed on the organometallic complexes $C_4H_6Fe(CO)_3$ and $C_3H_5Co(CO)_3$. The Coulomb integrals for other 3d transition metals were generated in the same manner by Hoffmann and co-workers in the 1970s', thus, they are all of empirical origin. Summerville and Hoffmann's set of H_{ii}'s were selected in Alvarez's newly-released table of EHMO parameters[50] because they seem to fit better with trends along a series of the periodic table. However, both sets of the parameters were found to produce identical orbital ordering and very similar energies in the metallocene case study,[13] although Albright's set was derived directly from organometallic species. Albright's Hückel parameters of the Group VIIIB metals have been chosen in chapters 3 (Co species) and 4 (Fe species) of this thesis for consistency and continuity with the previous work,[13,18] in which the reliability of these parameters has been addressed. EHMO parameters for Mn, Cr and Ti elements, which have also been utilized in this work, are obtained from Alvarez's parameter table. They are identical in different sources.[46-49]

§1.7.2 Application of EHT to Core Excitation

There are two goals in the use of the EHMO program:

1>. To obtain the frontier MO picture for the molecules under investigation, especially the unoccupied MO part, for helping spectral interpretation. The MO diagram provides not only the MO ordering, but also atomic or fragment orbital constitution of the MOs of interest, their symmetry and spatial distribution.

2>. To simulate the recorded ISEELS spectra using the LCAO coefficients.

Calculated LCAO-MO coefficients with a theoretical computation method[51,52] can be used to simulate the observed core-excitation intensities within some approximations. As pointed out earlier, the spatially-localized core orbital has greatest overlap with compact virtual-valence orbitals, but poor overlap with Rydberg orbitals. Thus, for the C 1s spectrum of a molecule the transition probability of the C 1s → unoccupied MO transition is large if this MO (e.g., π^* or σ^*) has a substantial contribution from the C 2p AO on the core-excited carbon atom. The relative intensity of such a transition can then be approximated by the sum of the square of the C 2p AO coefficients in that MO.[52] It is noteworthy that this model is an atomic one essentially, but it does not signify that transitions to orbitals having 2p-AO contributions from the neighbouring atoms always give negligible intensities. For 2p excitation of 3d transition metals both metal 2p → 3d and 2p → 4s transitions at the central metal atom are in principle electric dipole allowed and thus might be important. Certainly, the general question of dipole allowed or forbidden character for any given transition is best treated by group theory with consideration of the full molecular symmetry. The 2p → 4s component is, however, neglected usually in the treatment[18] based upon the observation that for atomic matrix elements, $<4s|\mu|2p> \ll <3d|\mu|2p>$. Indeed, the 4s contribution to the low-lying unoccupied valence MOs are found extremely small in the EHMO results, and can be neglected relative to the 3d contributions.

The EHMO calculations have been used to generate predictions of the inner-shell spectra of some species in this study, by means of summing the square of the appropriate coefficients on the core-excited atom (e.g., 2p for 1s excitation) and assuming that the transition probabilities are proportional to such sums. As a simple example, the EHMO prediction of the C 1s excitation spectrum of free CO is the sum of Gaussian lines with relative energy position given by the virtual orbital eigenvalues, a width of 1.0 eV fwhm and intensities determined by $\Sigma c_{ij}^2(N2p)$, where $c_{ij}(N2p)$ is the LCAO-MO coefficient, the contribution of the N 2p AO to the unoccupied MO in the molecule, in which a nitrogen atom replaces the CO carbon atom to account for the created core hole within the equivalent core approximation (*vide infra*).

The EHMO programme[53] comes with four different computing schemes (0-3) chosen according to the user's needs. METHOD0 is the normal extended Hückel MO calculation, while METHOD1 involves charge iteration, in which the Coulomb integral has a linear dependence on the net atomic charge. In METHOD2, there is also charge iteration but H_{ii} has a non-linear relationship with the atomic charge. In METHOD3, H_{ii} is modified further by an additional Madelung correction term on the basis of the METHOD2, to correct for the influence of interatomic Coulomb interactions on the Coulomb as well as resonance integrals. All of the four methods (0-3) included in the EHMO package have been evaluated by computing the trial molecule of free CO in the ground and core excited states. The resulting simulated C 1s spectra are compared with experiment in Fig. 1.6. The spectral simulation from METHOD1 is left from the figure for the better illustration of other spectra as it is almost identical to that from METHOD0. As for METHOD2 and 3, the results show that the MO ordering remains unchanged but the energy levels and their corresponding features in the simulated spectra systematically shift to lower energy. Compared to the results of METHOD0, there are no significant improvements provided by METHOD2 and 3, although these two higher level EHMO schemes were expected to give better results. Since METHOD2 and 3 are rather time-consuming, and the obtained π^*-MO level is excessively low in energy relative to the experimental π^* term value, the simple METHOD0 was selected for this project.

It is of interest to note that the EHMO results show a very strong dependence on the molecular geometry. This is chiefly because the EHMO treatment includes all the σ electrons, which play the primary role in determining the geometry of molecules, and all interactions as well as all overlap integrals are calculated explicitly, which depend very much upon the atomic coordinates in a molecule. As an example, Figure 1.7 displays EHMO simulated results for the Co 2p spectrum with several different geometries[54] of $Co_2(CO)_8$, where C_s is that found in the solid state; $C_{2v}(1)$ is a symmetrized version of the same doubly-bridged structure; $C_{2v}(2)$ and $C_3(3)$ are related structures having small distortion of the $\angle$CCoCo angles from the $C_{2v}(1)$ structure; and D_{3d}, D_{4h} are two non-bridged structural conformers which are postulated to be present

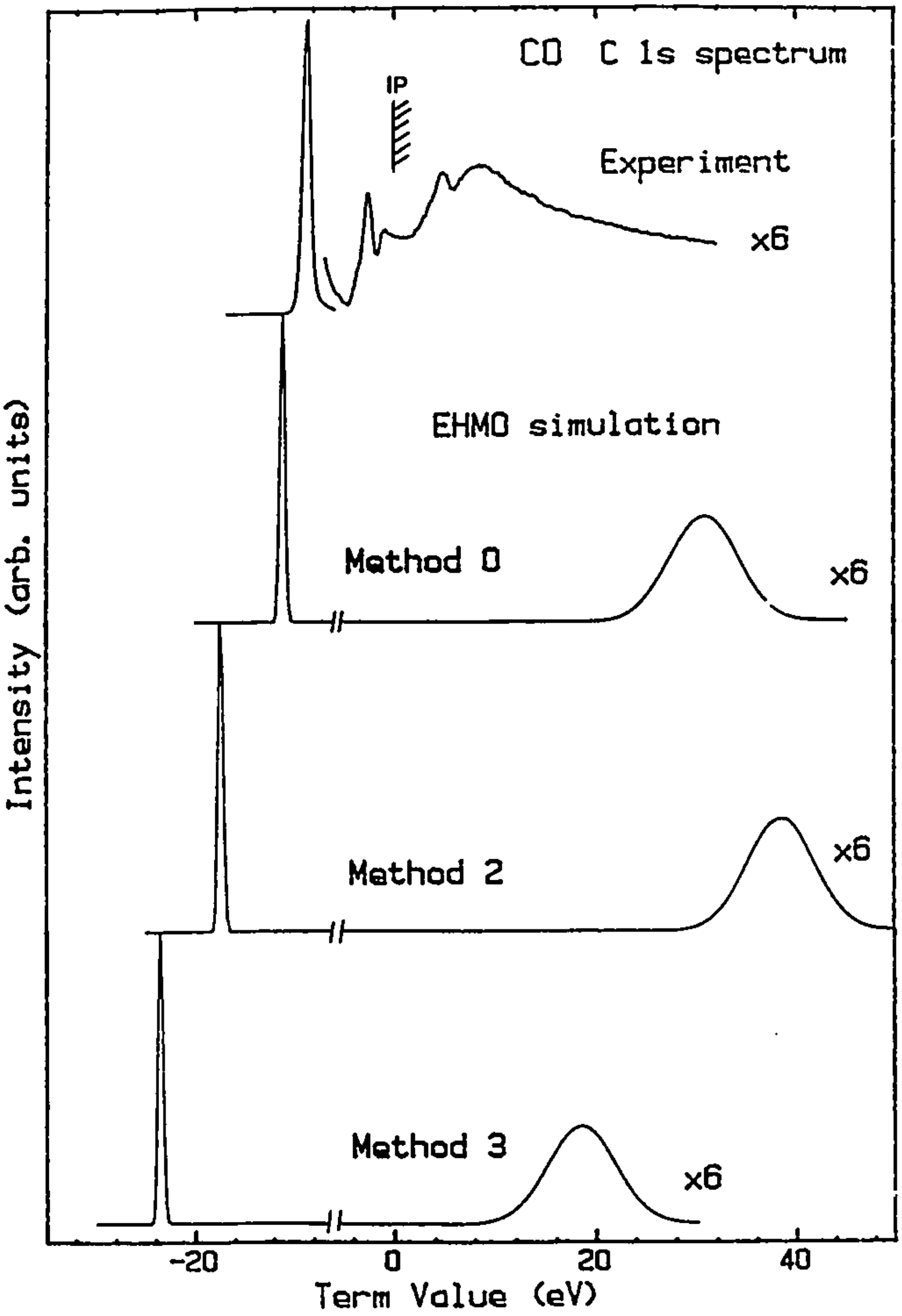

Fig. 1.6 C 1s spectra of CO predicted by EHMO methods 0, 2 and 3, along with the experimental spectrum.

in equilibrium in solution or matrix isolation. Figure 1.7 illustrates that the Co 2p spectrum should be strongly dependent upon the detailed geometric arrangement of ligands. According to the EHMO predicted spectra, the D_{4h} geometry gives the best agreement with experiment (see Chapter 3).

§1.8 Equivalent Core Model

The EHMO program has been applied to studies of metallocenes, metal carbonyls and complexes of mixed ligands. Overall, the EHMO calculations on metallocenes give better results relative to the systems of the carbonyl and mixed ligands, especially when the calculations are performed within the framework of an equivalent core model. An early discussion of the equivalent core model is contained in Prins[55] inner-shell excitation experiment of X-ray absorption in N_2. Prins observed an intense absorption peak at the energy of about 401 eV, which is 9 eV below that of the nitrogen K-shell ionization threshold. He correctly assigned this to the transition of an atomic K-shell electron to the lowest unoccupied $2p\pi^*$ orbital of the N_2 molecule. In this same paper he suggested that the outer electron moves in an effective field resembling that experienced by the valence electron of the NO molecule, since the removal of a K-shell electron from the vicinity of a N nucleus is equivalent to an increase by unity in the nuclear charge. This gives rise to a close correlation between the energies of the valence and/or Rydberg structures of inner-shell excited N_2 (and CO) and those of the valence-excited NO molecule (See Fig. 1.1). Generally speaking, the energy levels and valence-shell properties of an atom or molecule losing a non-bonding core electron (Z^*, the asterisk represents the core excitation) will be nearly the same as those of a species with one more proton but with fully occupied electronic core. The idea is now known also as the equivalent core or $Z+1$ analogy model.[4,8,9,56]

The application of the $Z+1$ model requires in general that the valence orbitals of the Z^* and $Z+1$ systems are very similar and the two systems have almost the same nuclear geometry. Thus, the ($Z+1$) analog of $Fe^*(CO)_5$ is, for instance, $Co(CO)_5$ with

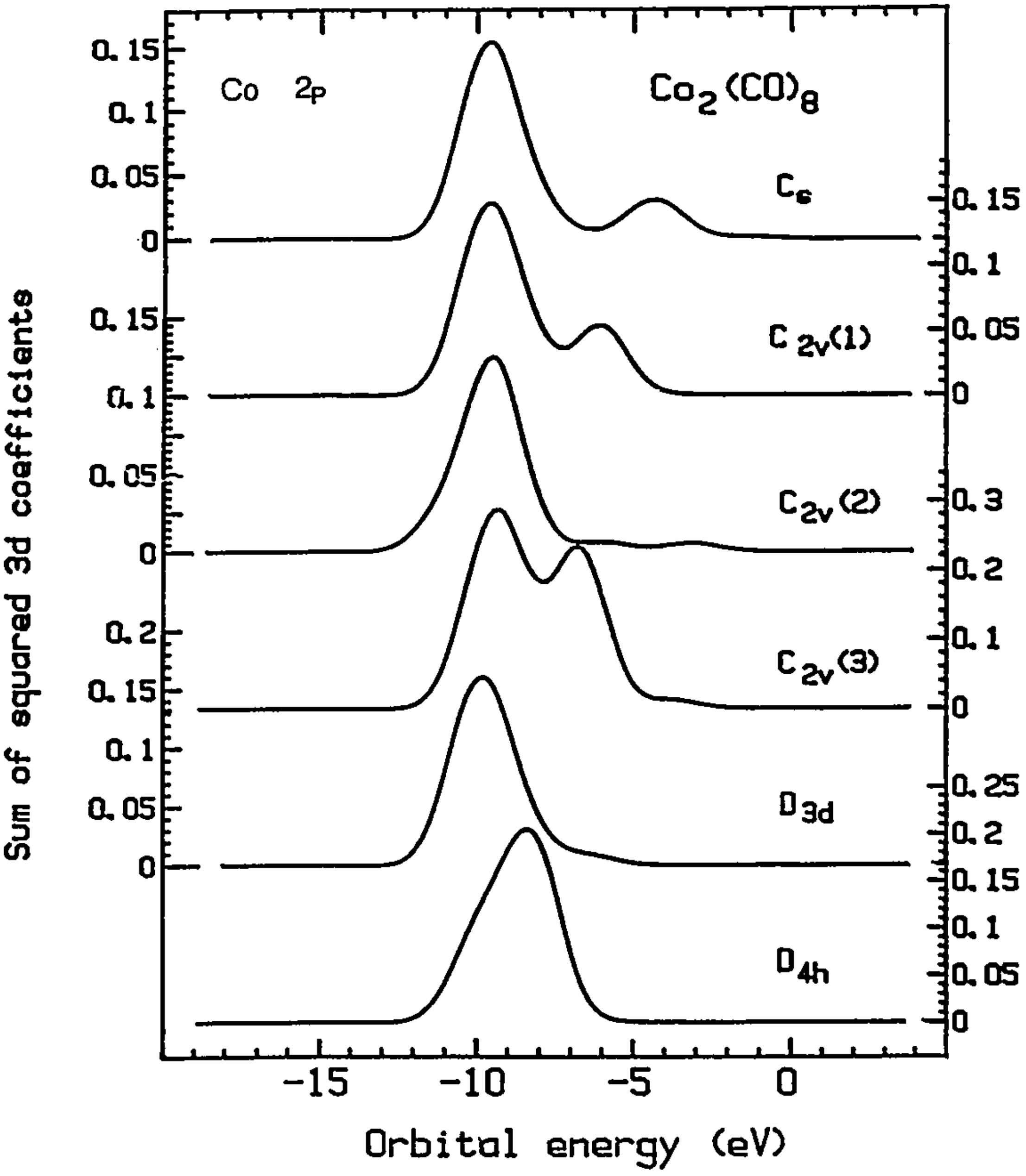

Fig. 1.7 Co 2p spectra of $Co_2(CO)_8$ predicted by EHMO with several different molecular geometries.

exactly the same geometry of $Fe(CO)_5$. However, this Z+1 model sometimes fails to predict correct term values for the lower excited states associated with virtual-valence MOs. Two points may be responsible for this failure.[57,58] First, the identical geometry is often difficult to satisfy because (1) the excited Z* molecule in many cases will have a slightly larger equilibrium internuclear distance by virtue of the population of the excited core electron on the antibonding MO level and (2) there exists an additional 'valence electron' in the Z+1 molecule. Secondly, even after the geometric correction has been taken into account, there is an exchange interaction that needs to be corrected, which arises from the effect of electron exchange interaction between the valence shell and the core (say 1s) shell that is closed in the (Z+1) analogy but has a hole in the core excited Z* molecule. The magnitude of this interaction may be estimated by the singlet-triplet splitting of the Z* molecule (e.g., in CO, $^1\Pi$-$^3\Pi$ is about 1.5 eV[3h]). Subtraction of this value from the term values of the Z+1 molecule usually gives better agreement with the experimental data of Z*.

In addition, the simple Z+1 core analogy ignores in general the fact that the two molecules being compared do not have the same number of electrons. To minimize the discrepancies, we use the molecular ion as the analogy for the excited species, e.g., using $Co(CO)_5^+$ for $Fe^*(CO)_5$ instead of $Co(CO)_5$. Thus, except for the core hole being introduced in the (Z+1) system at the desired spot the two species possess exactly the same electrons; viz., after the core excitation a closed-shell system is still closed-shell while an open-shell system remains open. Schwarz and co-workers[57,58] have first shown that the term values of core-excited states are better approximated by the virtual-orbital energies of the positive ion of the Z+1 analogous molecule, and this is even true for some cases without exchange correction. Such results lead to the equivalent ionic core virtual orbital model (EICVOM). It is this analogous ionic core model that has been applied in this work.

When carried out with *ab initio* or semi-empirical SCF calculations, EICVOM has proven useful in interpreting the core excitation phenomena of atoms and molecules.[57,58] This has been found to be true also in the present application of the semi-empirical, non-SCF EHMO calculations. With simple EHT treatments, a fairly moderate agreement between experimental and theoretical spectra is achieved for core excitation of organometallic complexes, provided that the EICVOM model is adopted. This is presumably because (1) the Z+1 model tacitly includes the core-hole relaxation effect (see Chapter 4) and (2) the interaction of the low-lying core-hole state with the excited electron is relatively small and can be either neglected or treated easily by perturbation theory (compared to the situation in valence electron excitations, where electron-electron interaction has an extremely strong influence). Thus, the theoretical study of ISEELS spectra is relatively easier and, can often be accomplished purely with the aid of simple models, without long and complicated quantum-chemical calculations.

§1.9 Objectives of the Project

The major goals of this thesis study are outlined as follows:

1). To find appropriate ways of handling low-volatility solid organometallic species for gas-phase ISEELS experiments.

2). To probe the electronic structure of some gas-phase organometallic complexes (metal carbonyls, ferrocene and its derivatives, mixed-ligand species) as well as metal-ligand bonding interactions in these complexes using ISEELS.

3). To investigate the influence of different ligands on each other via the metal atom when they are combined in the same complex, and the effect of the electronic perturbations caused by chemical modifications to a ligand.

4). To explore the sensitivity of 3d-transition-metal 2p inner-shell excitation to a variation in ligand and/or electronic environment as well as to the presence of the metal-metal σ^* antibonding valence MO in binuclear metal carbonyl species.

5). To endeavour to interpret the recorded core spectra in terms of semi-empirical theoretical calculations and/or a theoretical model of core excitation.

6). To examine the resonance associated with the Si-Si σ^* antibonding valence MO.

Chapter 2

EXPERIMENTAL

§2.1 Instrumentation

All of the ISEELS measurements reported in the present work were recorded by a home-made inner-shell electron energy-loss spectrometer. The spectrometer was built initially by Steel,[59] and its performance was improved by Newbury.[60] A schematic diagram of it is presented in Figure 2.1. Minor changes aimed at enhancing the target-gas density in the scattering region have been made for this project to better sample the low volatility organometallic species. The spectrometer is operated under the conditions of small momentum transfer to ensure that the electronic excitations are dominated by electric-dipole-allowed transitions. In general, a very small scattering angle of 1° ~ 2° and a high electron-impact energy of 2.5 keV plus the energy loss have been employed in the experiments. The overall spectral resolution was typically into a range of 0.5 ~ 0.8 eV, full width at half maximum (FWHM), as measured by the width of the zero-energy-loss peak. Descriptions of this apparatus and its operations have been presented earlier in detail[59-62] and therefore only brief accounts are given in the following of basic aspects of the spectrometer and of its general characteristics of performance.

§2.2 Energy Analyzer

One of the major parts of a typical electron-impact spectrometer is its electron energy analyzer. The type of the analyzer used is a hemispherical (180°) electrostatic analyzer, which has proven to be well suited for coupling with strongly retarding lenses of axial symmetry prior to analysis.[63] The kinetic energies of scattered electrons are measured by deflecting the electrons in the electric field of the analyzer. The inner hemisphere is set at a positive potential relative to the centre of the entrance slit, while the outer one is maintained at a negative potential. Electrons follow a curved path since they are attracted by the inner sphere potential and repelled from the outer one. Only

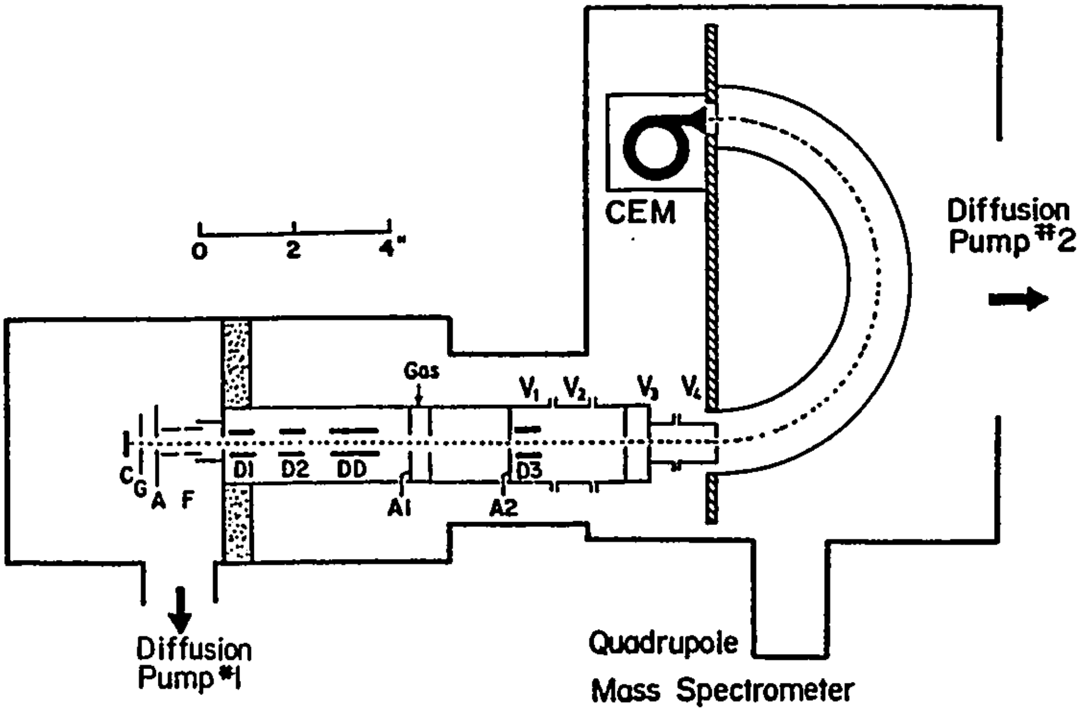

Fig. 2.1 Schematic of the ISEELS spectrometer.

those electrons within a narrow range of kinetic energy will have the correct radius of curvature to pass through the exit slit to the detector (channeltron) at the end of the analyzer. The whole analyzer is placed in a vacuum chamber pumped by a diffusion pump. A vacuum of better than 10^{-4} torr is necessary for the electron mean free path to be long enough for electrons to reach the channeltron. To observe different kinetic-energy electrons, the potentials applied on the sphere can be scanned. However, this mode of operation is not usually convenient as it leads to a changing energy resolution over the spectrum (i.e., $\Delta E/E$ is constant instead of ΔE).

An alternative procedure to avoid this is to utilize a constant-residual-energy mode. In this mode the pass energy (E_p) of the analyzer for the scattered electrons is, together with the scattering angle, kept constant, the scattered electrons are decelerated to this pass energy by the analyzer entrance lens system[59] (E_L) and the impact energy of incident electrons is varied. The consequence of this is that when measuring the yield of the electrons, a peak appears when the incident energy E_0 is equal to the sum of E_n [see Eq. (1.1.1)] and E_R, where $E_R = E_L + E_P$, the constant residual energy. Therefore each excited state is recorded at the same energy (E_R) above its own threshold excitation energy. The actual operation of this mode in our apparatus is to apply the energy loss on top of the accelerating potential (2.5 keV) by adding a negative potential equal to the sum of E_n and E_R to the cathode potential of the electron gun. The lower pass-energy affords in general higher energy resolution of the spectrum, but reduces the transmission efficiency of the analyzer. Such an efficiency often varies significantly with pass energy and high efficiency is vitally important in measuring the very low-volatility species.

§2.3 Electron Source

The electron source is most commonly a thermionic emitter. An electron gun from a Philips black-white TV served as the source for the spectrometer. It is composed of a filament, indirectly-heated oxide cathode (labelled by **C** in Figure 2.1), grid (**G**), anode (**A**) and focusing element (Einzel lens, **F**). The oxide cathode source can provide a well-collimated and reasonably monoenergetic beam [ΔE(FWHM) $\approx$ 0.3 eV, at 1100 °K temperature] with a Maxwell-Boltzmann distribution of energies as a result of its low work-function.[64] This beam can be utilized directly, without energy selection, for a spectrometer needing only moderate resolution. This is especially the case when higher beam currents (with larger FWHM) are desired for studying weak energy loss signals as well as for extensive measurements of several samples in a short period of time. A disadvantage is that the oxide cathode is readily subject to attack by some chemical gases (*e.g.*, strong oxidizers). One way to overcome this problem is to heat the gun hotter with a higher filament voltage, but this tends to reduce the useful lifetime of the gun, degrades the spatial resolution by a wider range of emission angles and degrades the energy resolution by virtue of the beam broadening. The energy broadening arises from the fact that charged particles (electrons here) in a beam repel each other, which tends to spread an otherwise collimated beam to a significant extent unless the particle density in the beam is small (Boersch effect). An alternative solution is to use a directly-heated, sharp tungsten-wire hairpin as an electron emitter, which is much less sensitive to chemical vapours but often leads to a relatively larger FWHM. The gun is enclosed in a differentially pumped chamber to further reduce the effect of poisonous and/or background gases and to minimize the stray electron background as well.

§2.4 Spectrometer Operation

Electrons are extracted from the emitting surface of the cathode and formed into a collimated beam by a grid-anode-Einzel lens multistage system. The beam is accelerated to its impact energy by a positive high voltage (2.5 keV) and then directed towards the scattering region by the quadrupole deflectors **D1**, **D2** and **D3**. To suppress a large background caused by scattering of the main beam off the inner surface of the analyzer outer sphere into the detector,[4] a double-deflector system (**DD**) is used for interception of the main-beam electrons prior to the analyzer. Accordingly, however, zero-angle scattering cannot be studied.[3b,65] Fast electrons are inelastically scattered in the collision chamber by a target gas, and only those having an average scattering angle of 2° (±1) will be able to pass through the angular-selection-plate aperture ($\mathbf{A}_2$) into the decelerating lenses $\mathbf{V}_1$ - $\mathbf{V}_4$, which retard the scattered electrons to the constant-pass energy of the analyzer. After transmitting the analyzer the electrons are collected by the detector, a channeltron continuous dynode multiplier mounted behind the aperture at the analyzer exit. Output pulses from the multiplier are amplified and processed by conventional pulse counting techniques (e.g., a preamplifier followed by an amplifier), and then fed to a Nicolet 1170 signal averager, whose channel address is advanced synchronously with the scanning voltage applied to the cathode of electron gun (See Fig. 2.2).

The spectrometer was tuned on the main beam of impact electrons,[60] the zero-energy-loss position was determined by the elastically-scattered electron signal, and the ISEELS spectrum was recorded under the same conditions except for angular deflection. Though some spectral features soon showed up after only a couple of scans, for weak structures or those of high energy edges (e.g., metal 2p edges) and/or for the better signal-to-noise ratio the spectral acquisition time lasted for hours, often, overnight. Once adequate statistical precision was obtained, the spectrum was transferred via a serial interface to an IBM-PS/2 microcomputer for data analysis, such as calibration, background subtraction, conversion to oscillator strengths, and determination of peak energies.

The overall energy resolution of the spectrometer depended largely on the running conditions of the gun, the pressure of target gases, the stability of electronics and the pass energy of the analyzer. The theoretical resolution of this specific apparatus ($\Delta E_{tot.}$) is approximated by

$$\begin{aligned}\Delta E_{tot.} &= (\Delta E_{gun}{}^2 + \Delta E_{anal.}{}^2)^{1/2} \\ &= (\Delta E_{gun}{}^2 + 0.01 E_p{}^2)^{1/2} \qquad (2.4.1)\end{aligned}$$

where ΔE_{gun} denotes the energy bandwidth (FWHM) of the electron beam produced in

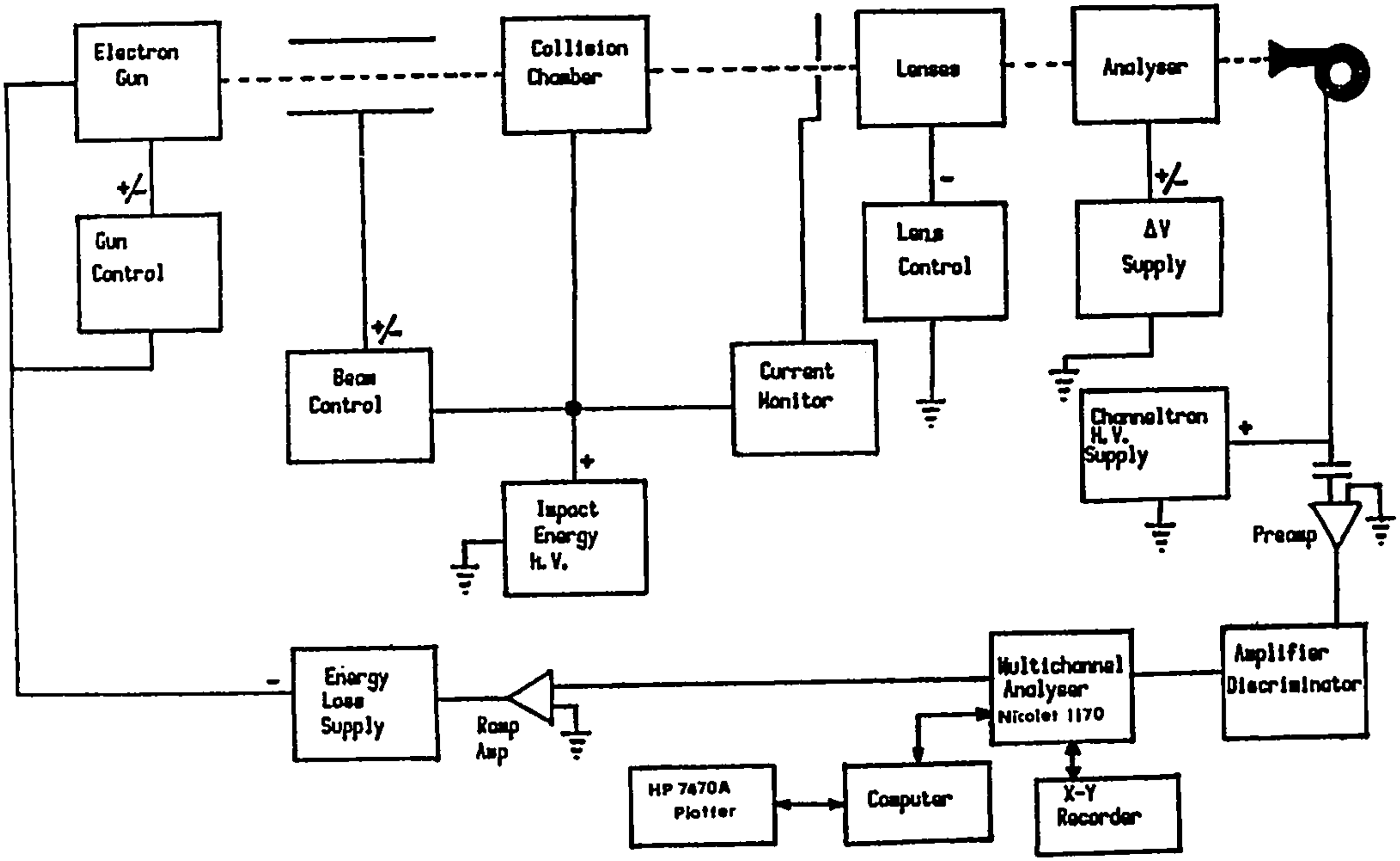

Fig. 2.2 Schematic of the electronics used with the ISEELS spectrometer.

the gun, which normally has a value of about 0.4 eV here, whereas $\Delta E_{anal.}$ represents the theoretical resolution of the analyzer.(4) Therefore, the $\Delta E_{tot.}$ will mainly depend on the analyzer resolution if the gun contribution stabilizes at 0.4 eV. In order to boost the electron transmission associated with the weak structures of low volatile organometallic species, relatively high pass energies (30 ~ 70 eV) were used, and the corresponding theoretical resolutions (FWHM) are between 0.42 and 0.76 eV, according to Eqn. (2.4.1). The experimental resolution obtained on the profile of the primary unscattered electron beam (zero-energy-loss) fell into a 0.5-0.8 eV bracket when the pass energy varied from 30 to 70 eV. This is in reasonable agreement with the theoretical values. Small differences from the predicted values may result from some small deviations of the actual operating conditions away from those ideal and/or theoretical ones. Thus, moderate alterations in resolution can be made merely by adjusting the pass energy of the analyzer and/or by decreasing the incident beam current (to limit the space charge broadening) without having to completely retune the spectrometer to new values.

§2.5 Energy Calibration

Meaningful energy-loss measurements rely essentially on obtaining a precise energy-loss scale. This scale is calibrated in general against a main line of a reference molecule whose energy is accurately known from previous studies or spectroscopic data. The energy difference between the main line of the reference and that of the sample is measured with a precision Keithley 175 autoranging digital multimeter and the unknown sample's energy scales are determined using this difference value. In practice calibration of the electron energy scale in most ISEELS experiments was performed by mixing the compound of interest with the reference molecule. Several main lines from different reference molecules were used commonly in this work and they are summarized in Table 2.1. As an example, the C 1s spectrum of $Fe(CO)_5$ was calibrated using the discrete main line of the C 1s → π^* transition in CO_2, whereas the energy-loss scale of the O 1s spectrum was determined by the calibration to the O 1s → π^* transition of CO_2.

Table 2.1 Main Lines of Reference Gases Used for ISEELS Energy Calibrations[a]

Molecule	Inner-Shell Excitation	Excitation Energy (eV)
SF_6	S $2p_{1/2}$ --> t_{2g}	184.54(5)[b]
CO	C 1s --> π^*	287.40(2)
CO_2	C 1s --> π^*	290.74(4)
N_2	N 1s --> π^*	401.10(2)
O_2	O 1s --> π^*	530.8(2)[c]
CO	O 1s --> π^*	534.21(9)
CO_2	O 1s --> π^*	535.4(2)
SF_6	F 1s --> a_{1g}	688.27(15)

a. Taken from Ref. 1c, 60 and 66.
b. The figure within brackets denotes the uncertainty.
c. The data from Ref. 67.

§2.6 Sample Handling

Most of the organometallic samples used in this project, along with a silicon compound $(CH_3)_3SiSi(CH_3)_3$, were purchased commercially from Strem Chemical Co. and utilized without further purification. $Fe(CO)_5$ and $TiCl_4$ were obtained from Aldrich Chemical Co. The latter, a highly corrosive liquid, was further purified by distillation for satisfactory spectral results. Observation of the Si-Si bond became possible by courtesy of Drs. K.M. Baines and T.K. Sham at University of Western Ontario, who generously supplied a silicon compound $Si[Si(CH_3)_3]_4$.

A double-gas-inlet-line system, which has been described by Newbury,[60] was used for gas introduction after a minor modification, in which a Whitey ball valve was added between the collision chamber and the leak valves for studying low-volatility solid complexes. For liquid samples such as $Fe(CO)_5$ and $CpCo(CO)_2$, the normal degassing procedure was followed, namely, several freeze-pump-thaw cycles were carried out to remove any dissolved impurity gases or highly volatile components before opening the leak valve. In a few cases the initial spectra were found to contain some contributions from residual volatile impurities even after the pre-treatment. These impurity signals disappeared with time through preferential evaporation. In such cases only those spectra acquired after a stable spectral shape was attained were used for further analysis. Where necessary, sample transfers were performed under an inert atmosphere. The sample purity was regularly checked *in situ* by a quadrupole MS monitor. In some cases of the solid samples the chamber was heated slightly to further increase the signal (*vide infra*). In such cases care was taken to monitor for possible decomposition of the complexes. As an example, this was readily detectible for the carbonyl complexes by the appearance of the sharp Rydberg structure of CO around 294 eV. For the low-volatility solid compounds, the spectra presented here are those of the compounds that are sufficiently stable for thermal vaporization and considered to be without the occurrence of any decomposition during the period of spectral acquisition.

Before this project, only a small number of organometallic complexes had been investigated by ISEELS. The limitation in the range of subjects is largely due to the availability of volatile samples for gas-phase studies, problems associated with sample handling and with possible chemical decomposition in the spectrometer. The concept of ISEELS is fairly simple, yet application of ISEELS to organometallic species needs a considerable commitment of talented and skilful manpower. The gas-phase ISEELS experiment is especially capricious since during the measurement the entire vacuum chamber is exposed to a hazardous vapour of organometallic complexes, which coats the electron source, optics, detector and pumping hardware (for example, the deposition of a sample on the aperture, slit and analyzer surfaces alters the electrostatics), thus leading to the degradation of the performance of the apparatus. In some cases, even a single experiment cannot be finished before losing performance of the spectrometer. Therefore diligent maintenance of the surface conditions of electron optics, analyzer and detector is essential to keep resolution and sensitivity.

However, there seems to be a couple of advantages to our spectrometer for tough organometallic measurements. First, our relatively big spectrometer provides a larger area of interior surface, this means that more chemical contamination is tolerable. Our separate, strong differential pumping system of the gun and collision chambers (See Fig. 2.1) has also proven very useful in attenuation of the contaminating rate. Secondly, the use of a relatively large hemispherical analyzer in our apparatus provides a higher rate of electron transmission of the analyzer with reasonable resolution, and hence a higher analyzer sensitivity. This means that lower vapour-pressure organometallic complexes can be studied and less sample is needed. In principle, almost any organometallic sample that can be sublimed is able to be investigated in the gas phase by ISEELS. Air and/or moisture sensitivity has not been found to be an issue since the sample transfers are carried out in an inert-gas glove box and the actual measurements are accomplished in a high vacuum chamber.

However, there exists a common problem associated with gas-phase ISEELS experiments of organometallic complexes, which is, to obtain a sufficient target vapour pressure within the scattering region of the spectrometer, as these complexes are quite involatile frequently. Provisions for operation at elevated temperature are desirable as well as necessary. Several measures had been taken in tackling this problem. (a) A small sample cell containing an organometallic complex was mounted directly on the outside of the vacuum chamber (i.e., without the control of the leak valve), which is connected by 15 cm of 0.5 mm ID teflon tubing to the collision region. (b) The sample cell and the vacuum-chamber sector surrounding the collision region were mildly heated externally by heating tapes that were wrapped around the cell and sector and powered by a variac to control the temperature, if applicable or necessary. (c) Temperature-adjustable hot water circulated in a copper tubing that was wrapped around the electron-gas collision cell located inside the vacuum chamber so as to ensure that the sample vapour did not condense (and/or deposit) in the inlet tube connecting the sample and collision cells after its departure from the externally-heated area and that the adequate sample vapour finally reached the scattering region. Caution needs to be taken in this case since the copper tubing is directly connected to the high voltage supplying the electron impact energy. (d) For extremely low volatility species, the sample cell was attached directly to the collision cell inside the vacuum chamber, just about 2 cm away from the incident electron beam, in order to reduce substantially the travelling distance of the gaseous target molecule. (e) To boost the vapour pressure in the scattering region for solid complexes of rather low volatility, the sample (cell) was further heated by a halogen quartz light bulb that was installed in the brass walls of the collision cell, and powered by variable DC to adjust the needed temperature. Cold water was circulated simultaneously to two cooling plates on each side of the collision cell in this case to protect the electron optics and related insulator materials that separates the optics and, to minimize the possible thermal chaos arising from the bulb heating as well.

All of these measures and/or combinations of them have made considerable improvement in handling organometallic samples for gas-phase ISEELS experiments. An interesting illustration of this is the B 1s excitation of $Ni(C_2B_9H_{11})_2$, whose spectrum recorded with the measures (c) and (d) is given on the top of Figure 2.3. Upon using a combination of the measures (d) and (e), the count rates improved remarkably and the spectral acquisition time significantly dropped as well[68] (See Figure 2.3, the bottom). However, the experimental experience tells us that in general if the melting point of an organometallic complex is higher than 300°C, the ISEELS measurements may face a challenge of getting adequate vapour pressure for the experiment as overheating can decompose the complex. One way to deal with this problem is simply to run a test for the sample in the spectrometer. Raising the temperature slowly, one can obtain a series of spectra. If there are no unreasonable variations occurring in the spectra with temperature and time, and there is no sample residue left, then a stable vaporization has

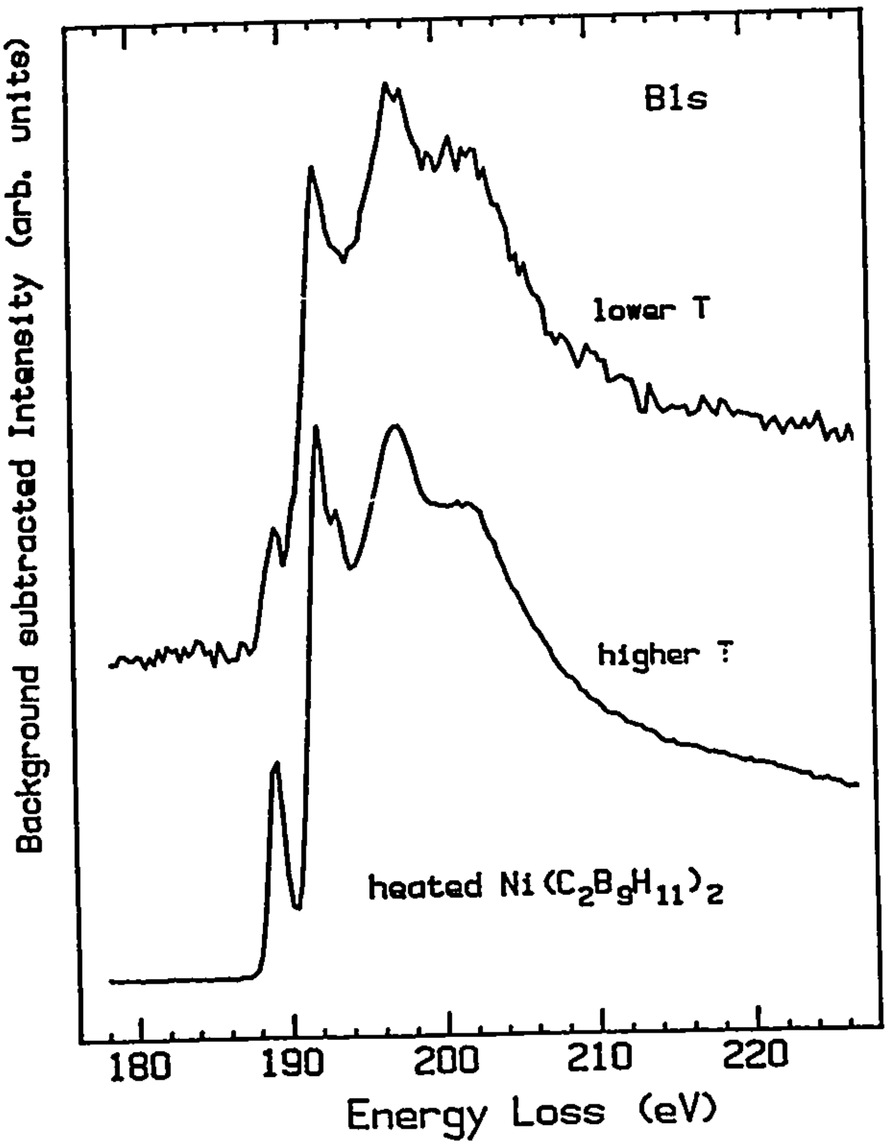

Fig. 2.3 Comparison of B 1s spectra of $Ni(C_2B_9H_{11})_2$ obtained at the "lower T" temperature (about 50-70°C) and the "higher T" temperature (about 120-150°C).

achieved. If the complex happens to decompose during the course of elevating the temperature, the breakdown fragments are normally simpler ligands that sometimes can be identified in the ISEELS spectrum, since most of the free ligands have been studied previously. Further information of sample integrity can be obtained through the on-line quadrupole MS monitor as well as comparisons between the spectra of related series of complexes.

§2.7 Oscillator Strengths

Optical oscillator strengths (OS) have traditionally been measured by photon absorption methods, but they can be derived also from inelastic-scattering differential-cross-section (DCS) measurements under certain conditions in terms of the Bethe theory discussed in §1.5. At the zero-momentum-transfer limit, the optical OS $f_n^{\mathrm{opt.}}$ is related explicitly to the scattering DCS $d\sigma/d\Omega$ by the following formula[23,69]

$$f_n^{\mathrm{opt.}} = [(16a_0^2R^2E_0)^{-1} \cdot E_n^3] \cdot d\sigma/d\Omega \qquad (2.7.1)$$

where E_n is the energy loss associated with the transition from the ground state to the excited state n, and $E_0 = E_n + 2500$, the impact energy of the incident electron. This relationship indicates that the OS and DCS differ by a kinematic factor within the square brackets of Eq. (2.7.1) at $\mathbf{K} = 0$. However, the limit $\mathbf{K} \rightarrow 0$ is never precisely realized in any inelastic electron collision, and then the kinematic factor somehow differs from the one in Eq. (2.7.1) by virtue of the non-zero momentum transfer and/or the finite acceptance angle in a real situation. In general, there is a range of angles and **K**s in a real experiment. Averaging over this range is accomplished by choosing the following factor in our conversion of the DCS into the OS;[70]

$$(f_n^{\mathrm{opt.}})_{\mathrm{rel}} = [\ln(1 + \theta_m^2/\theta_E^2)]^{-1} \cdot (d\sigma/d\Omega)_{\mathrm{rel}} \qquad (2.7.2)$$

where $\theta_m = 2°$ and $\theta_E = E_n/2E_0$. After removal of the underlying valence-continuum background, which is done by subtracting an extrapolation of a fit of $a(E - b)^c$ to the pre-edge data [where the constants a, b and c are determined from a least-squares best fit, ($c \approx 4$)], an ISEELS spectrum was converted to a relative optical spectrum through Eq. (2.7.2). Compared with literature optical data, it was found that this formula gave a quite agreeable simulation over a wide range of energy losses.[71] It should be pointed out that the proper background subtraction plays an important role here, and therefore more spectral points before the discrete transition region are preferable for a better pre-edge data fit.

The absolute optical OS was derived from normalization of the converted relative optical spectrum to a calculated atomic continuum photoionization OS, *viz.*, a one-point continuum normalization by using absolute photoabsorption data from the literature.[72] The single energy point is usually set at 25 eV above the experimental IP for molecules of low-Z elements, as shape resonances generally become less than 1% of the total intensity above a photoelectron energy of about 2 Ry (~27 eV). The good agreement of the resulting absolute OS with atomic values can be ascribed to the fact that for photoelectron energies above 25 eV the kinetic energy of the highly excited outgoing electron becomes much larger than the molecular potential. Thus, the atomic character emerging in the deep ionization continuum region is the basis of the one-point continuum normalization procedure. The total absolute optical OS for one type of atom is obtained simply being multiplied by the number of such atoms in the molecule. More detailed discussions and tests of the accuracy of the OS conversion have been given by McLaren *et al.*[71] More recent work in this regard proposed that ≈30 eV above the inner-shell ionization limit be the lower limit for such conversions.[73] The single-energy points chosen for transition metal atoms are summarized in Table 2.2, along with those for some ligand atoms appearing in the present work.[72] All of the ligand 1s and metal 2p spectra recorded for this study have been routinely converted to absolute OS scales.

Table 2.2 Calculated Atomic Continuum Ionization Oscillator Strengths[72]

Element	Energy Point	Calc. OS ($10^{-2}eV^{-1}$)	Element	Energy Point	Calc. OS ($10^{-2}eV^{-1}$)
C 1s	IP + 25	0.78	O 1s	IP + 25	0.47
	IP + 35	0.74		IP + 35	0.45
	IP + 45	0.71		IP + 45	0.44
Si 2p	IP + 30	4.33	Cl 2p	IP + 30	3.11
Ti 2p	IP + 35	1.63	Cr 2p	IP + 35	1.32
Mn 2p	IP + 29	1.35	Fe 2p	IP + 33	1.18
Co 2p	IP + 33	0.94			

Chapter 3

CORE EXCITATION OF ORGANOCOBALT COMPLEXES

§3.1 Introduction

Organometallic complexes of 3d transition metals are involved in a large number of synthetic and catalytic processes.[74] Broadly speaking, these complexes either have coordination sites available for interaction with incoming molecules or have oxidation states readily available for oxidative additions, rearrangements, reductive eliminations and other important chemical transformations. Cobalt carbonyl, cobalt cyclopentadienyl and their derivatives have been receiving increasing attention recently regarding both preparative and catalytic processes. In the latter context, these molecules offer molecular analogues of small organic molecules adsorbed on metal surfaces and thus they may give information concerning heterogeneous catalytic processes.

Gas phase inner-shell electron energy loss spectroscopy has long been used to study small molecules. Recently, it has been applied to organometallic systems, such as transition metal carbonyls[11,12,14,20] and metallocenes.[13] With precise measurements and careful interpretation, core excitation energies and intensities can be used to investigate ground state bonding and electronic structure as well as relaxation effects associated with the creation of core excited states. In this chapter we extend previous work on complexes with a single type of ligand to consider for the first time a molecule containing different types of ligands bound to the same metal atom. The goal is to determine whether the inner-shell excitation spectra of such complexes can provide information on how the electronic structure is affected by ligand-ligand interactions mediated by the central metal atom. If successful, such studies will help understand the electronic interactions between small molecules and metal atoms both in organometallic complexes and in cases of co-adsorption of organic compounds on metal surfaces.

This chapter reports the gas-phase core-excitation spectra (Co 3p, Co 2p, C 1s, and O 1s) for three organocobalt complexes $Co_2(CO)_8$, $Co(Cp)_2$ and $CpCo(CO)_2$ (Cp

= η^5-C_5H_5). The carbon 1s spectra of cyclopentadiene (Cp-H) and its Diels-Alder dimer, dicyclopentadiene [$(Cp\text{-}H)_2$] have been recorded also to provide information concerning the carbon 1s spectrum of the free cyclopentadienyl ligand. The carbon 1s spectrum of $Co(Cp)_2$ has been reported and interpreted in detail previously[13] while the C 1s and O 1s spectra of $Co_2(CO)_8$ have been presented briefly in comparison to those of other transition metal carbonyls.[14] Here, the ligand core excitation spectra are emphasized, in particular, analysis of the C 1s spectrum of $CpCo(CO)_2$ in relation to the spectra of $Co(Cp)_2$ and $Co_2(CO)_8$. The spatially-localized character of core excitation means that sums of model compound spectra[75] can be used to facilitate analysis of the inner-shell spectra of more complex species. Differences from additivity predictions may then be related to ligand-ligand interactions. The Co 2p and 3p spectra of all three cobalt species have been discussed recently.[18] An extension of the previous spectral interpretation is given. An interesting aspect of the discussion of the electronic structure of $Co_2(CO)_8$ has been the existence and correct description of the Co-Co single bond that is predicted for this compound by the 18-electron rule.[76] The unoccupied MOs of $CpCo(CO)_2$ have been studied previously by semi-empirical quantum calculations[77] and electron transmission spectroscopy.[78] The nature of inter-ligand charge transfer[79] and the distortion of the Cp ligand from 5-fold symmetry[80] are important themes in electronic structure studies of $CpCo(CO)_2$.

As in the previous work[13,18] extended Hückel calculations, carried out within the equivalent ionic core virtual orbital model,[57] are used to assist spectral assignments. The calculations for $CpCo(CO)_2$ were performed with the carbon 1s hole on each of the four symmetry inequivalent carbon atoms. The virtual orbital energies of the ground state of the cation are assumed to approximate the relative energies (term values) of core → valence excited states while the intensities of the core excitation to a given virtual orbital are assumed to be proportional to the sum of the squared coefficients of atomic orbitals on the core excited atom which are electric dipole coupled to the excited core orbital.[52] For example, $\Sigma c^2(N2p)$ in the EHMO result for $Co_2(CO)_7(NO)^+$ is used to simulate the

C 1s spectrum while Σc^2(Ni3d) in the EHMO result for $CoNi(CO)_8^+$ is used to simulate the Co 2p spectrum. This approach assumes that the overall transition matrix element is dominated by the atomic-like intra-shell terms, which is reasonable on the grounds of spatial overlap with the very compact core orbital.[81] As found in previous work[13,18] EHMO with this approach seems to reproduce the shapes and relative positions of core-excitation spectral features of organometallic complexes, giving some confidence in using the virtual MO character as a guide to spectral assignment. The geometries used for $Co(Cp)_2$ and $CpCo(CO)_2$ are those determined experimentally.[82,83] A non-bridged D_{4h} geometry was used for the $Co_2(CO)_8$ calculations since this has been proposed to be the stable form in the gas phase.[54]

§3.2 C 1s Spectrum of $Co_2(CO)_8$ and O 1s Spectra of $Co_2(CO)_8$ and $CpCo(CO)_2$

C 1s and O 1s oscillator strength spectra of CO, $Co_2(CO)_8$ and $CpCo(CO)_2$ are shown in Figs. 3.1 and 3.2. In each case the spectra are plotted on common vertical scales with the oscillator strength divided by the number of carbonyls in the molecule in order to emphasize the systematics of the intensities of carbonyl core excitation. The energies and proposed assignments of the C 1s and O 1s spectral features for all species are presented in Tables 3.1 and 3.2. As found in previous studies of metal carbonyls complexes,[11,12,14] the C 1s and O 1s spectra of $Co_2(CO)_8$ are dominated by intense π^* and σ^* resonances similar to those of free CO, indicating that C 1s and O 1s excitation is localized on a single carbonyl. This is in sharp contrast to the Cp ligand where there is a major qualitative change in its C 1s spectrum when it is bound to a metal atom[13] (*vide infra*).

While the main features are similar, close inspection reveals that there are some differences between the spectra of cobalt carbonyl and CO, particularly in the region between the π^* and σ^* resonances. These differences include: small and opposite shifts in the transition energies for the carbon and oxygen $1s \rightarrow \pi^*$ excitations; additional weak bands 2-3 eV above the main π^* resonances; suppression of Rydberg structure; and a

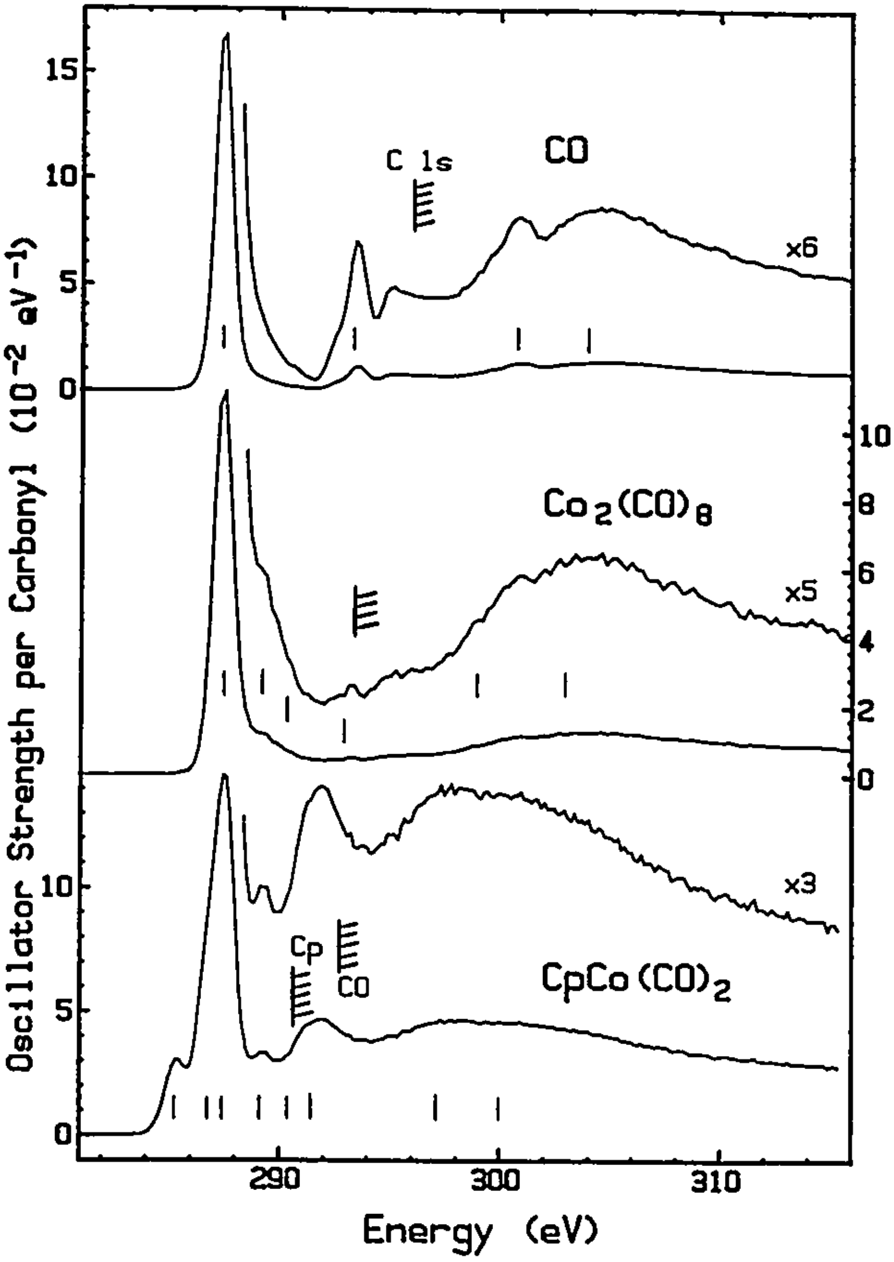

Fig. 3.1 Oscillator Strengths for C 1s excitation of CO, $Co_2(CO)_8$ and $CpCo(CO)_2$ derived from ISEELS spectra. The hatched lines indicate the location of the C 1s IPs as dtermined by XPS.[92] The tics indicate the features whose energies are tabulated in Table 3.1. This procedure has been followed in the spectra of this thesis.

Table 3.1 Energies (E, eV), Term Values (T, eV), and Proposed Assignments for Features in the C 1s Spectra of CO, $Co_2(CO)_8$, $CpCo(CO)_2$, and $Co(Cp)_2$

CO		$Co_2(CO)_8$		$CpCo(CO)_2$			$Co(Cp)_2$		Assignment (final orbital)	
E	T^{a}	E	T	E	T_{Cp}	T_{CO}	E	T	Cp	CO
				285.4	5.3		284.8	5.2	$4e_{1g}$(Co 3d)	
							285.3	4.7	$4e_{1g}$(Co 3d)	
				286.8^{c}	3.8		286.82^{b}	3.1	$\pi^*(C=C)$	
287.40	8.7	287.43^{b}	6.0	287.49^{b,c}	5.0					$\pi^*(CO)$
		289.3	4.1							π^*_{deloc}
		290.4	3.0	289.2		3.5				π^*_{deloc}
293.3	2.8			290.3		2.4				3p Ryd
		293.1	0.3				289.4	0.6	Ryd	
				290.64			289.96		IP(Cp)^{d}	
				291.4	-0.8		291.9	-1.9	$\sigma^*(C-C)$	
296.1		293.40		292.73						IP(CO)^{d}
300.8	-4.7	298.8	-5.4						double excitation	
				297.3	-6.6		297.7	-7.7	$\sigma^*(C=C)$	
304.^{e}	-8.	303.^{e}	-10.	300.^{e}		-8.				$\sigma^*(CO)$
							302.^{e}	-12.	shake-up	

a. T = IP - E.

b. Calibration relative to CO_2 (C 1s –> π^*: 290.74 eV): ΔE = -3.31(5), -3.25(7), -3.92(6) eV for $Co_2(CO)_8$, $CpCo(CO)_2$, and $Co(Cp)_2$, respectively.

c. The energies of these components of the main peak (maximum at 287.5 eV) have been dervied from a fit to Gaussian lineshapes (See Fig. 3.7). The curve fitting was employed to obtain more precise energy locations of overlapping features in many other spectra in this thesis. The curve fits were not shown in some cases in order to keep the thesis to a manageable size.

d. IPs from XPS [92]. This is the energy of the main XPS line.

e. Broad features have an uncertainty greater than the 0.1 eV intrinsic uncertainty due to calibration because of the difficulty of precise determinations of the feature locations. In general, the location of such features are uncertain to ±0.5 eV or ±1 eV if no decimal place values are provided in the tabulated energy.

reduction of f(π^*), the 1s → π^* oscillator strength. We have shown previously that the reduction of f(π^*) can be used to estimate the extent of dπ-pπ back-bonding in metal carbonyls.[14] The sensitivity of 1s → π^* intensities to this aspect of metal-ligand bonding has been documented in the DV-Xα calculations of CO and NiCO clusters by Kojima *et al.*[84] Oscillator strengths for the low energy 1s → π^* transitions derived from the experimental spectra by curve fitting to Gaussians are summarised in Table 3.3.

Compared to the inner-shell spectra of free CO, the small energy shifts in the π^* resonance, of opposite direction in the C 1s and O 1s spectra, are attributable to differential relaxation effects.[11,12,85,86] In the O 1s → π^* excited state the electron in the CO 2π^* orbital is largely localized at the O atom. The core hole is also shielded by an increased charge at the oxygen site as the occupied 1π orbital becomes polarized toward the O atom. Consequently, in a metal carbonyl the 2π^* space at the carbon end of the ligand is available for increased backdonation from the central metal atom, thus stabilizing the (O 1s^{-1}, π^*) state and lowering the transition energy. On the other hand, in the (C 1s^{-1}, π^*) excited state the 2π^* charge is mainly concentrated at the C site of the CO. Therefore, in a metal carbonyl complex the metal-to-2π^* backdonation, which already exists in the ground state, will not be enhanced by the core excitation, leading to a less-stabilized (C 1s^{-1}, π^*) state and thus to a higher-energy C 1s → 2π^* transition than in free CO. This point of view is based on the fact that the core hole localizes the excitation essentially on a single atom and its potential is "self-screened" by the electron in the π^* orbital, so that metal-to-carbonyl charge transfer only plays a relatively minor role in core excited states.[11,12,85,86]

The weak features lying 2-3 eV above the main 1s → π^* resonance in the C 1s and O 1s spectra of $Co_2(CO)_8$ are interpreted as transitions to delocalized π^* states. According to MO calculations,[87-90] the π^*(CO) orbitals in the ground state of metal carbonyls can span an appreciable energy because of interactions among π^* orbitals of adjacent CO ligands. Our EHMO results predict that there are nine virtual MOs of strong π^*(CO) character which span 1.5 eV in ground state $Co_2(CO)_8$ (Table 3.4).

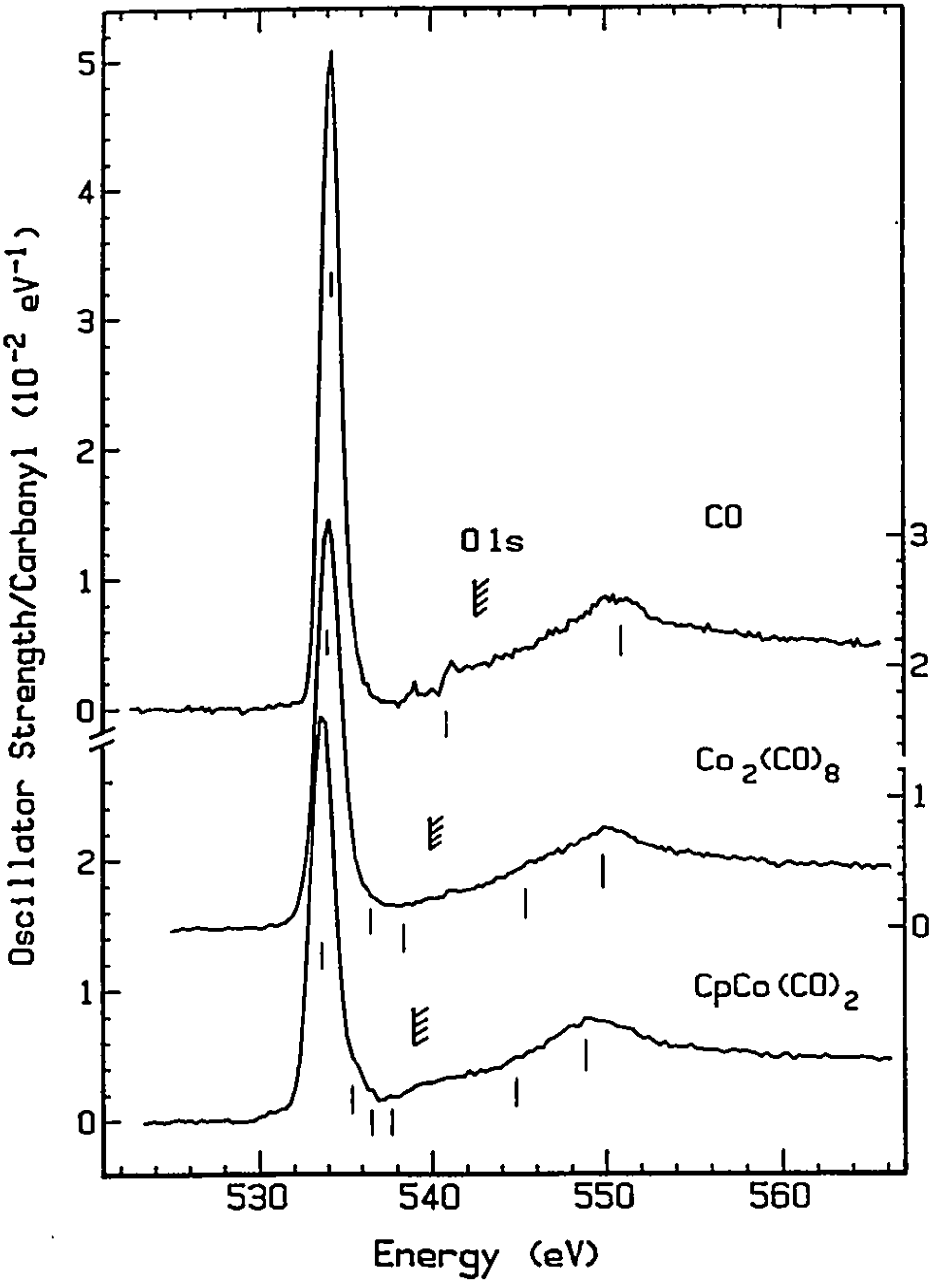

Fig. 3.2 Oscillator Strengths for O 1s excitation of CO, $Co_2(CO)_8$ and $CpCo(CO)_2$

Table 3.2 Energies (E, eV), Term Values (T, eV) and Proposed Assignments for Features in the O 1s Spectra of CO, $Co_2(CO)_8$ and $CpCo(CO)_2$.

CO		$Co_2(CO)_8$		$CpCo(CO)_2$		Assignment (final orbital)
E	T	E	T	E	T	
534.11	8.3	534.1[a]	5.7	533.7[a]	5.3	$\pi^*(C=O)$
		536.7	3.5	535.6	3.4	$\pi^*_{delocal}$
				536.4	2.6	$\pi^*_{delocal}$
541.0	1.4	538.6	1.1	537.6	1.4	Rydberg
542.4		539.78		538.97		IP[b]
		545.6	-5.8	544.7	-5.8	double excitation
550.9	-8.5	549.9	-10.2	548.9	-9.9	$\sigma^*(C\text{-}O)$

a. Calibration relative to O_2 (O 1s → π^*: 530.8 eV): $\Delta E = 3.3(1)$ and 2.9(1) eV for $Co_2(CO)_8$ and $CpCo(CO)_2$, respectively.

b. IP from XPS [92]. This is the energy of the main XPS line.

Table 3.3 Oscillator Strengths[a] for 1s → π^* Transitions Derived from Experimental Spectra

	C 1s			O 1s
Species	$4e_{1g}(Co3d_{xz,yz})$[b]	$\pi^*(Cp)$[b]	$\pi^*(CO)$[c]	$\pi^*(CO)$[c]
CO			0.170	0.076
$Co_2(CO)_8$			0.162[d]	0.061
$Co(Cp)_2$	0.045	0.140		
$CpCo(CO)_2$	0.077	0.145	0.143	0.065[d]

a. Integrated peak areas.

b. Intensity per Cp group (symmetry label refers only to $Co(Cp)_2$).

c. Intensity per CO group.

d. These values differ slightly from those reported in [18] because of improved background subtraction.

Table 3.4

Properties (E, Σc^2) of selected virtual MOs of the ground and excited states of $Co_2(CO)_8$ with D_{4h} symmetry[a] derived from extended Hückel calculations

Virtual MO		Ground state			
D_{4h}	Character	Energy (eV)	ΣCo3d	ΣC2p	ΣO2p
b_{1u}	$C2s+Co(d_{x^2-y^2}-d_{x^2-y^2})$	−4.25	0.360	0.059	0.006
b_{2g}	$C2s+Co(d_{x^2-y^2}+d_{x^2-y^2})$	−4.73	0.372	0.053	0.007
b_{2u}	$\pi(CO2p_x,2p_y)$	−7.79	0.000	0.145	0.035
b_{1g}	$\pi^*(CO2p_x,2p_y)$	−7.91	0.000	0.143	0.036
e_g	$\pi^*(2p_z)+Co(d_{xz},d_{yz})$	−8.28	0.086	0.229	0.060
		−8.28	0.086	0.012	0.003
b_{1u}	$\pi^*(2p_z)$	−8.52	0.002	0.133	0.037
e_g	$\pi^*(CO2p_x,2p_y)$	−8.69	0.002	0.103	0.030
		−8.69	0.002	0.150	0.044
e_u	$\pi^*(x,y,z)+Co(d_{xz},d_{yz})$	−8.71	0.036	0.083	0.025
		−8.71	0.036	0.155	0.047
b_{2u}	$\sigma^*(M\text{-}CO)$, $Co(d_{xz}-d_{xz})$	−9.09	0.201	0.085	0.028
e_u	$\pi^*(M\text{-}CO)$, $Co(d_{xz}+d_{xz})$	−9.11	0.081	0.091	0.031
		−9.11	0.081	0.122	0.042
b_{2g}	$\sigma^*(M\text{-}CO)$, $[C2p_{x,y}+Co(d_{xy})]$	−9.21	0.210	0.082	0.028
a_{2u}	$\pi^*(2p_z)+Co(d_{z^2}-d_{z^2})$	−9.23	0.089	0.096	0.031
b_{1g}	$\pi^*(2p_z)$	−9.33	0.008	0.116	0.042

Virtual MO #	C1s excited state				O1s excited state				Co2p excited state			
	E(eV)	ΣCo3d	ΣC2p	ΣO2p	E(eV)	ΣCo3d	ΣC2p	ΣO2p	E(eV)	ΣCo3d	ΣC2p	ΣO2p
17	−4.46	0.028	0.058	0.003	−4.29	0.287	0.038	0.004	−4.48	0.001	0.004	0.000
18	−5.44	0.728	0.089	0.008	−4.79	0.453	0.050	0.006	−7.79	0.000	0.145	0.035
19	−7.84	0.000	0.007	0.000	−7.82	0.000	0.043	0.006	−7.91	0.000	0.143	0.036
20	−8.11	0.010	0.010	0.002	−7.96	0.001	0.130	0.018	−8.06	0.319[b]	0.097	0.021
21	−8.29	0.083	0.007	0.000	−8.28	0.088	0.006	0.000	−8.43	0.076	0.091	0.024
22	−8.39	0.039	0.005	0.001	−8.33	0.068	0.096	0.013	−8.43	0.076	0.006	0.002
23	−8.63	0.009	0.002	0.000	−8.57	0.003	0.089	0.012	−8.58	0.043	0.165	0.046
24	−8.70	0.030	0.000	0.000	−8.70	0.001	0.011	0.001	−8.70	0.000	0.011	0.002
25	−8.79	0.004	0.007	0.001	−8.70	0.028	0.001	0.000	−8.70	0.000	0.301	0.090
26	−8.97	0.175	0.003	0.001	−8.75	0.039	0.097	0.014	−8.79	0.006	0.096	0.029
27	−8.98	0.040	0.024	0.004	−8.83	0.051	0.226	0.034	−8.79	0.006	0.127	0.039
28	−9.10	0.130	0.001	0.004	−9.10	0.135	0.002	0.000	−9.15	0.000	0.001	0.000
29	−9.17	0.090	0.004	0.001	−9.15	0.097	0.044	0.007	−9.39	0.033	0.229	0.082
30	−9.18	0.089	0.000	0.000	−9.16	0.031	0.056	0.009	−9.39	0.033	0.106	0.038
31	−9.30	0.041	0.002	0.000	−9.27	0.074	0.043	0.006	−9.43	0.047	0.103	0.039
32	−10.24	0.111	0.191	0.070	−9.34	0.304	0.509	0.083	−9.47	0.016	0.082	0.028
33	−10.74	0.167	0.702	0.315	−9.46	0.051	0.397	0.066	−10.16	0.108	0.189	0.085

[a] The non-bridged D_{4h} geometry taken from ref. 24 is the minimum energy configuration proposed to be the most stable gas phase conformer.

[b] Underlined values ($\sum c^2 > 0.05$) are expected to correspond to major transitions.

Upon C 1s excitation, the energy spread increases to 3 eV but all of the π^* oscillator strength is concentrated in excitations to the two lowest energy π^* MOs, those localised on the core excited carbonyl. The C 2p contribution to the LUMO changes from 0.12 in the ground state to 0.70 in the C 1s excited state (Table 3.4). The other π^* components in the EHMO calculation of C 1s (O 1s) excitation correspond to the $(1s^{-1},\pi^*_{delocal})$ states.

The C 1s and O 1s continua of $Co_2(CO)_8$ are dominated by a broad σ^*(C-O) shape resonance which occurs about 1 eV lower in energy than in free CO. This shift to lower energy, which has also been observed in the C 1s and O 1s spectra of other transition metal carbonyls,[11,12,14] is associated with a weakening and lengthening of the C-O bond upon metal complexation.[11,14,84,90] This is consistent with the conventional model of the linear M-C-O bond as one involving two interactions, σ-donation and π-back-donation. The latter weakens the C≡O bond which lengthens and approaches a double-bond in character. Increased bond lengths have been deduced from vibrational spectra as well as direct measurements of the structure. The shift in absolute energy of the C 1s → σ^*(C-O) energy is consistent with the structural change within the bond length correlation,[36] although there are complications to the application of this model to organometallics because of large differences in core hole relaxation with and without an adjacent metal atom.[11]

An interesting aspect of the C 1s spectrum of $Co_2(CO)_8$ (Fig. 3.1) is the absence of any spectral features associated with Co-Co antibonding orbitals. Since the formal single bond between the two Co atoms has a rather low bond strength, the "weak bond" concept[91] predicts that there should be a σ^*(Co-Co) orbital at low energy. DV-Xα MO calculations on $Co_2(CO)_8$ predict an a_{2u} LUMO of Co-Co character[76] which is somewhat isolated from the higher energy orbitals that are largely of π^*(C-O) character. In our EHMO calculation for the ground state the a_{2u} MO has σ^*(Co-Co) antibonding character but it is 0.1 eV less stable than the π^*(CO) LUMO (Table 3.4). Since EHMO indicates that this orbital also has moderate π^*(C-O) character, one might expect C 1s → a_{2u}

"σ^*(Co-Co)" transitions to produce a shoulder to the π^* feature, perhaps on the low energy side if the weak-bond hypothesis is adopted. However the 1s → π^* peak appears rather regular on the low energy side. Previously[11] a comparison of the core spectra of $Mn_2(CO)_{10}$ with several mono-metallic Mn carbonyls also did not reveal any evidence for a low lying C 1s → σ^*(Mn-Mn) transition which had been predicted to exist in that species.[91] It was tentatively concluded that such a transition was not observed in $Mn_2(CO)_{10}$ because of spatial overlap limitations. The EHMO results for $Co_2(CO)_8$ predict that the relatively-localised σ^*(Co-Co) character of the a_{2u} orbital is lost with C 1s excitation so that it is unlikely that a spectral feature assignable to C 1s → σ^*(Co-Co) can be identified. The corresponding O 1s → σ^*(M-M) transitions would be even less likely. On both symmetry and spatial overlap grounds, it is more likely that the metal *np* edges would contain spectral signatures of a low energy σ^*(M-M) orbital. Although the EHMO results suggest that the second virtual-valence MO retains a distinct σ^*(Co-Co) character during Co *np* core excitation, no evidence was found for low-lying Co *np* → σ^*(Co-Co) excitations[18] (*vide infra*). A comparison of high resolution core spectra (C 1s and Co 2p) of $Co_2(CO)_8$ and $HCo(CO)_4$ might be a more fruitful way of searching for evidence of core → σ^*(Co-Co) transitions.

The O 1s spectrum of CO, $Co_2(CO)_8$ and $CpCo(CO)_2$ are compared in Fig. 3.2. The main π^* and σ^* resonances are found to have very similar shapes and energies in all three species, while the Rydberg features found in free CO are weaker or absent in metal-complexed CO and the oscillator strength f(π^*) is considerably reduced. The O 1s spectra of $Co_2(CO)_8$ and $CpCo(CO)_2$ are very similar, as expected from the spatially localised character of core excitation. The maximum of the σ^*(CO) resonance is about 1 eV lower in $CpCo(CO)_2$ than in $Co_2(CO)_8$. This is likely associated with the chemical shift of -0.8 eV between the O 1s ionization potentials of $CpCo(CO)_2$ and $Co_2(CO)_8$,[92] which is associated with electron-donation from the Cp^- anion to the Co atom which, in turn, enhances back-donation into the π^*(CO) orbital, thereby transferring electron density from the CpCo fragment to the carbonyls, and decreasing the O 1s IP.[79]

§3.3 C 1s Excitation of $Co(Cp)_2$ and Models for the Free Cp Ligand

In order to understand how π-bonding to a metal atom affects the C 1s spectrum of a Cp ring, it would be useful to compare the C 1s spectrum of cobaltocene with that of an isolated Cp ring —— either as the $Cp^{\cdot}$ radical or the Cp^- anion, which are limiting electronic models for the Cp ligand bound to a metal atom.[82] Unfortunately, such a direct comparison is not yet possible since the C 1s spectrum of C_5H_5 has not yet been obtained. Nevertheless, a reasonable estimate of the C 1s spectrum of the $C_5H_5^-$ anion can be made from its well-known MO structure[93] along with the experimental spectra of closely-related species such as cyclopentadiene and those of aromatic analogues such as benzene and pyridine. The latter are perhaps more appropriate analogues than Cp-H, since they are 6-electron aromatic systems like the Cp^- anion. This isoelectronic nature should lead to similar orbitals and thus similar carbon 1s excitation, although benzene does have one more π^* orbital than Cp^-. In order to develop insight into the carbon 1s spectrum of Cp^- we first discuss the spectra of Cp-H and its Diels-Alder dimer $(Cp\text{-}H)_2$.

The carbon 1s spectra of cyclopentadiene, cyclopentene and dicyclopentadiene $[(Cp\text{-}H)_2]$ are presented in Figure 3.3. The C 1s spectrum of cyclopentene[42] has been reported earlier while this is the first presentation of the spectra of Cp-H and $(Cp\text{-}H)_2$. The energies and proposed assignments for the spectral features of Cp-H and $(Cp\text{-}H)_2$ are listed in Table 3.5. The C 1s spectra of Cp-H and $[Cp\text{-}H]_2$ both exhibit an intense low-energy peak around 285 eV which is assigned to C 1s → $\pi^*(C=C)$ transitions. Relative to the C 1s continuum this peak is more intense in Cp-H than in the dimer, consistent with the higher density of double bonds in Cp-H. π-conjugation in Cp-H shifts the C 1s → π^* transition 0.4 eV lower than that in the dimer and cyclopentene. The second peak around 287 eV in the $(Cp\text{-}H)_2$ and C_5H_8 spectra is assigned to a mixed Rydberg/valence state of predominantly $\sigma^*(C\text{-}H)$ character associated with the saturated regions in these molecules. The corresponding second feature in Cp-H has contributions from 1s → $2\pi^*$ transitions in addition to 1s → $\sigma^*(C\text{-}H)$. The two broad features in the C 1s continua of the spectra (around 291 and 297 eV respectively) are assigned to shape

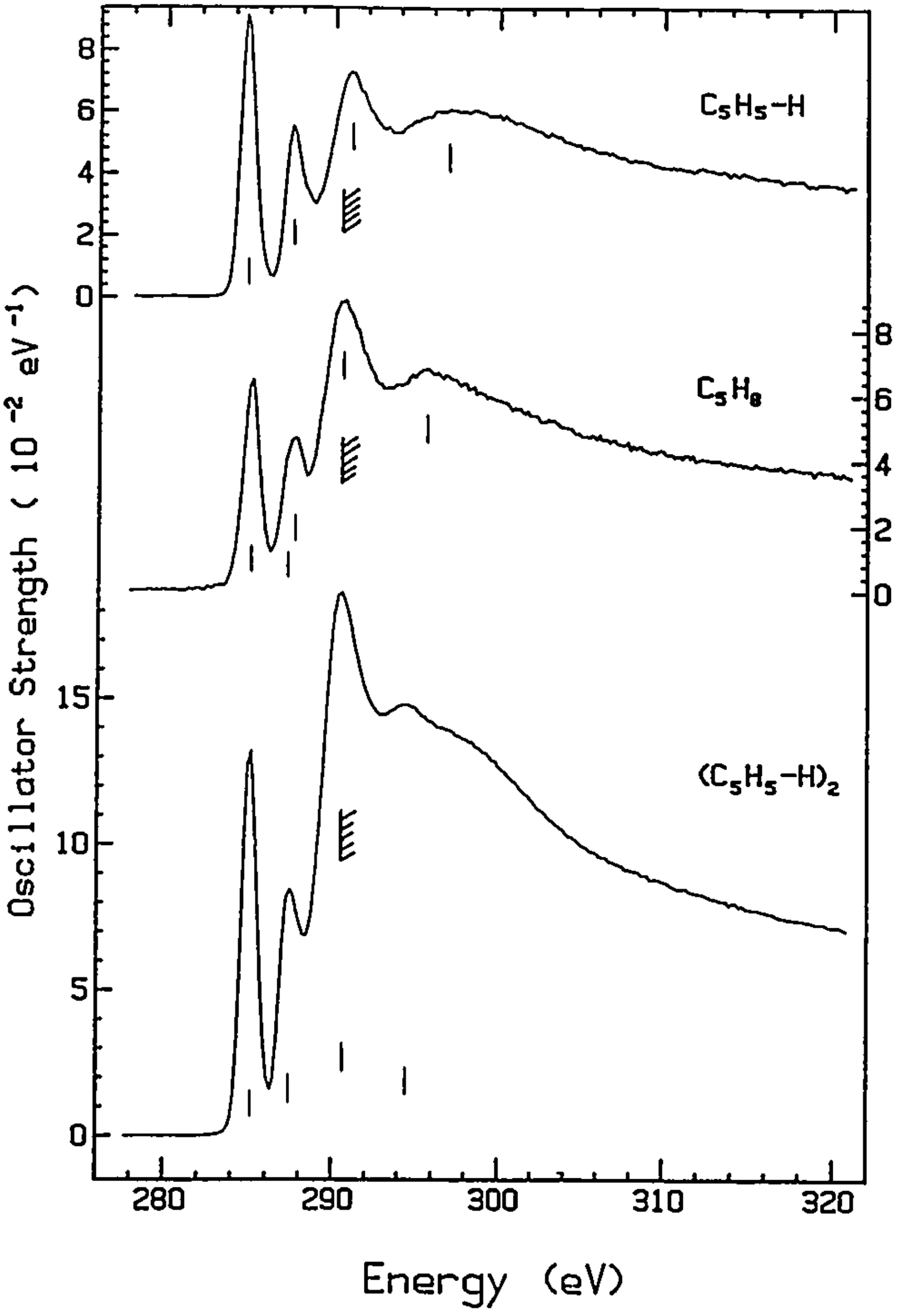

Fig. 3.3 Comparison of the C 1s oscillator strength spectra of cyclopentadiene (C_5H_6), cyclopentene (C_5H_8) and dicyclopentadiene [$(C_5H_6)_2$].

Table 3.5 Energies (E, eV), Term Values (T, eV) and Proposed Assignments for Features in the C 1s Spectra of C_5H_5-H, $(C_5H_5\text{-}H)_2$, C_5H_8 and $C_5H_5^{\cdot}$ (inferred)

Feature	Cp-H		$(Cp\text{-}H)_2$		C_5H_8		$C_5H_5^{\cdot}$	Assignment
	E	T	E	T	E	T	E(est)	(final orbital)
1(A)	284.7[a]	5.8	285.1[a]	5.3	285.0	5.3	285.0(5)	$\pi^*(C=C)$
2(B)	287.4	3.1	287.4	3.0	287.6	2.7		$\sigma^*(C\text{-}H)$
					287.2	3.1	287.0(5)	3p Rydberg
	290.5(e)		290.4		290.3		290.5(e)	IP[b]
3(C)	291.0	-0.5	290.6	-0.2	290.6	-0.3	291.0(5)	$\sigma^*(C\text{-}C)$
4(D)	297.0	-6.5	294.3	-3.9	295.6	-5.3	297(1)	$\sigma^*(C=C)$

a. Calibration relative to CO_2: $\Delta E = -6.02(7)$ and $-5.68(8)$ eV for C_5H_5-H and $(C_5H_5\text{-}H)_2$, respectively. See [42] for calibration data for C_5H_8.

b. IP from XPS [92]. (e)=estimated from IPs of similar species.

Table 3.6 Properties (E, Σc^2) of Virtual Orbitals of the Ground and Excited States of $Co(Cp)_2$ in D_{5d} Symmetry Derived from Extended Hückel Calculations

	ground state			C 1s excited			Co 2p excited		
MO	E(eV)	ΣCo3d	ΣC2p	E(eV)	ΣCo3d	ΣC2p	E(eV)	ΣCo3d	ΣC2p
$4e_{2g}$	-6.42	0.075	0.104	-6.42	0.075	0.000	-6.55	0.000	0.108
$(\pi^*-\pi^*)$		0.075	0.198	-6.48	0.043	0.001	-6.55	0.000	0.205
$3e_{2u}$	-6.55	0.000	0.108	-6.55	0.000	0.000	-6.69	0.021[a]	0.105
$(\pi^*+\pi^*)$		0.000	0.205	-7.86	0.071	0.304	-6.69	0.021	0.200
$4e_{1g}$	-9.67	0.646	0.018	-9.69	0.640	0.009	-11.17	0.207	0.018
$d_{xz,yz}$		0.646	0.099	-10.01	0.673	0.147[b]	-11.17	0.207	0.153

a. The highlighted contributions are believed to dominate the experimental spectra.

b. Note that the $4e_{1g}$ orbital is singly occupied. Thus when using these results to prepare the predicted C 1s spectrum this value was divided by two to correct for Pauli-excluded transitions.

resonances associated with the C-C bonds. The intensity of the lower energy σ^*(C-C) shape resonance is highest in $(Cp\text{-}H)_2$, consistent with this molecule containing the greatest number of carbon-carbon single bonds. The σ^* shape resonance of higher energy is associated with the shorter carbon-carbon double bond in the unconjugated species. It is part of a characteristic two-peak pattern of multiple σ^* features in the conjugated species.[94]

We have estimated the C 1s spectrum of the Cp^- free ligand from those of Cp-H and aromatic analogues. This estimate is compared to the C 1s spectra of $Co(Cp)_2$ and benzene in Figure 3.4. Since the spectra of benzene and Cp-H are dominated by the lowest energy C 1s $\rightarrow \pi^*$ transition, we expect that the low-energy π^*(C=C) region of the Cp^- spectrum should be dominated by a strong single peak (**A**). Based on the spectra of benzene and pyridine, peak **A** is expected to occur around 285.0±0.5 eV. Above the C 1s IP limit the Cp^- spectrum is expected to be characterized by two strong bands (**C** and **D**) associated with the characteristic two-peak pattern of σ^*(C-C) shape resonances observed in conjugated systems. Recently, Schwarz *et al*[95] and Medhurst *et al*[96] have argued that peak **C** in benzene is a doubly excited discrete state, perhaps overlapping with a one-electron C 1s $\rightarrow \sigma^*$(C-C) transition.[95] Band **C** in Cp^- is estimated to be located at 291.0±0.5 eV, a sharp feature with the second highest intensity. A second continuum σ^* resonance, band **D** should occur around 297±1 eV. From comparison with the pre-edge region of benzene, a weak band (**B**) is inferred around 287.0±0.5 eV, just below the C 1s threshold, which would be associated with a transition to a state of mixed 3p Rydberg, σ^*(C-H) character. Clearly, there is a strong qualitative difference between the single π^* feature expected in free $C_5H_5^-$ and the two discrete features observed in cobaltocene and other metallocene spectra.[13]

We turn now to the C 1s spectrum of a Cp ring bonded to a metal atom as in cobaltocene and $CpCo(CO)_2$. The energies and assignments for the $Co(Cp)_2$ spectral features are summarised in Table 3.1. The spectrum of $Co(Cp)_2$ has been discussed[13] extensively earlier, in comparison with those of $Fe(Cp)_2$ and $Ni(Cp)_2$. A brief summary

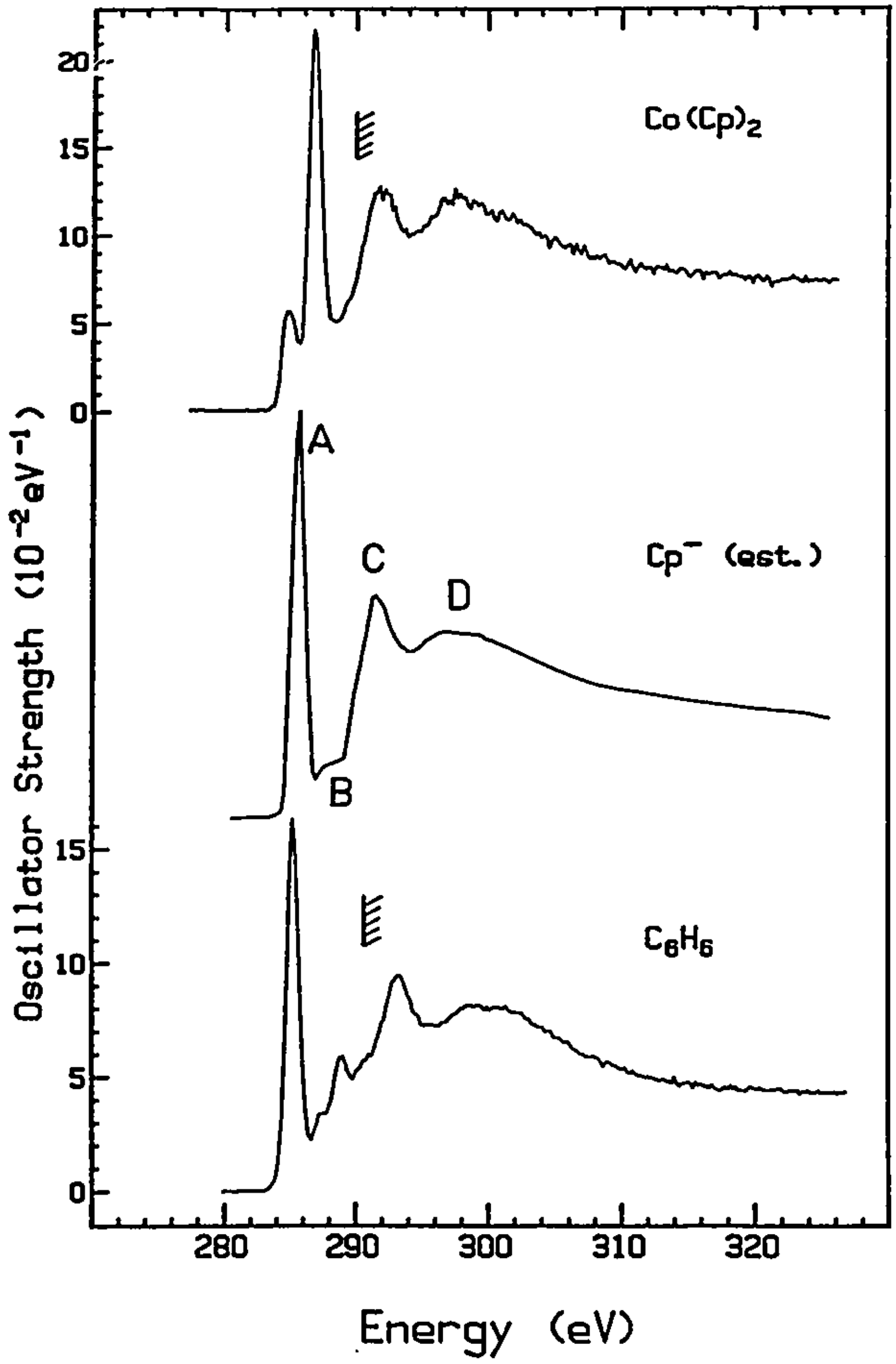

Fig. 3.4 C 1s oscillator strength spectrum of $Co(Cp)_2$ compared to that of benzene and that estimated for a free cyclopentadienyl anion (Cp^-).

of our interpretation of the cobaltocene spectrum is given here in order to assist the interpretation of the $CpCo(CO)_2$ spectrum and to point out an additional feature not detected or assigned earlier. The C 1s spectrum of cobaltocene and other metallocenes[13] exhibit two sharp resonances in the pre-edge region and two broad bands above the C 1s IP. Relative to the spectrum expected for the free Cp^- ligand, there is an additional low-lying band (Fig. 3.4). This is attributed to C 1s excitations to a $4e_{1g}$ orbital of mixed π^*(Cp) and metal d_{xz}, d_{yz} character. Curve fitting (Fig. 3.7a) clearly shows that there is a high energy shoulder on the first peak which may correspond to transitions to a second electronic state arising from the (C $1s^{-1}$, $4e_{1g}^2$) configuration. The main peak in the cobaltocene spectrum is ascribed to C 1s → $3e_{2u}(\pi^*)$ transitions, with minor contributions from C 1s → $4e_{2g}(\pi^*)$ excitations. The π^*(Cp) $3e_{2u}/4e_{2g}$ peak occurs at 286.8 eV, higher than its counterpart in the inferred, free Cp^- spectrum (≈285 eV). The increased energy is attributed to the interaction between the metal 3d and Cp $e_2''(\pi^*)$ orbitals. The two continuum bands around 292 and 298 eV are assigned to one-electron C 1s → σ^*(C-C) transitions.

§3.4 C 1s Spectrum of $CpCo(CO)_2$

A molecular orbital diagram for the ground state of $CpCo(CO)_2$, based upon EHMO calculations and consistent with previous theory,[77] is presented in Figure 3.5. The EHMO results for the ground state and various core excited states are summarised in Table 3.7. The dominant interactions of the Cp^- ligand with the $Co(CO)_2^+$ fragment occur between the filled e_1'' set of the Cp^- ring and filled or empty 'molecular' orbitals of $Co(CO)_2^+$, arising from the appropriate linear combination of Co and CO MOs. The HOMO in $CpCo(CO)_2$ is Co d_{xz} and can be regarded as a nonbonding electron pair at the metal, stabilized by back-bonding. In the ground state the LUMO and next-to-LUMO orbitals are heavily concentrated on the uncoordinated portion of the Co and have some CO character but very little contribution from π^*(Cp). Both HOMO and LUMO, originating from the $Co(CO)_2^+$ fragment, are destabilized by antibonding

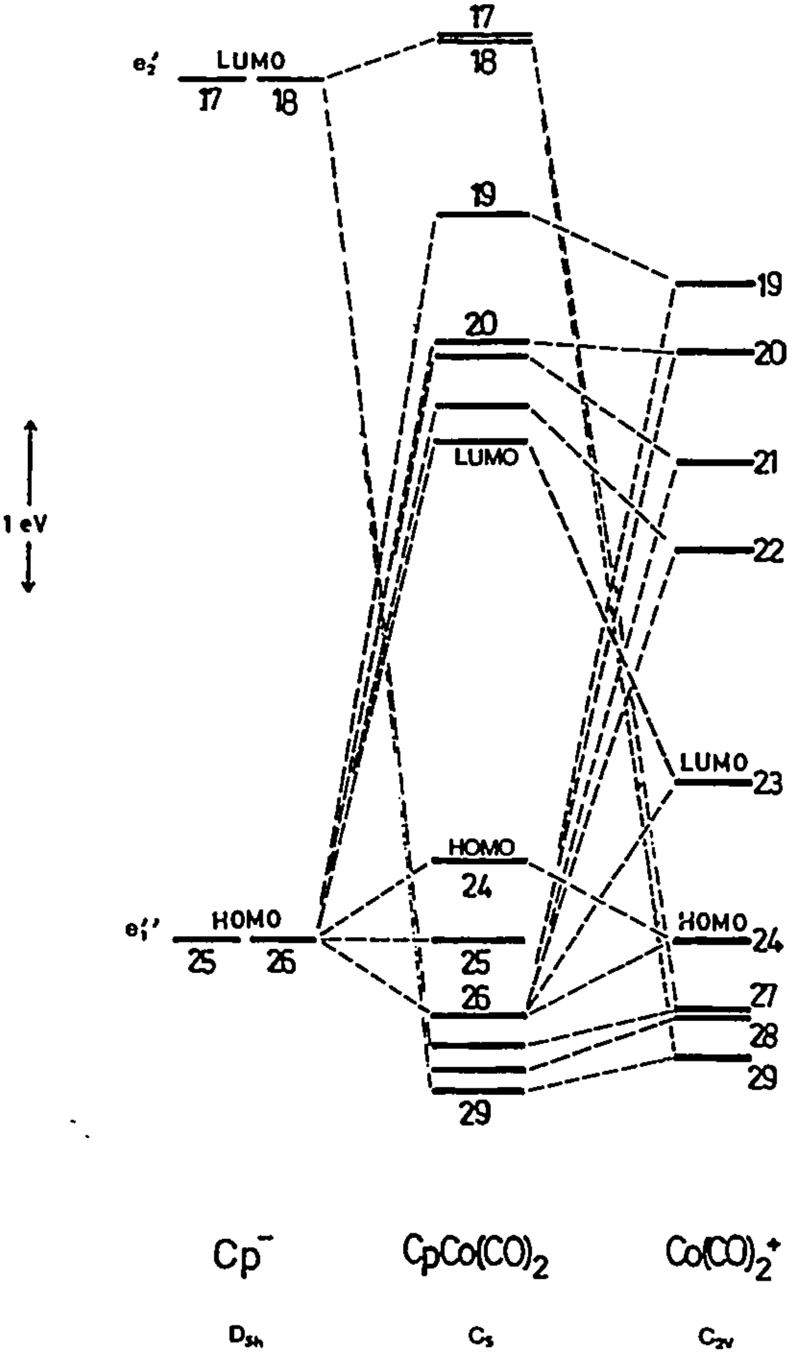

Fig. 3.5 Sketch of the frontier molecular orbitals of $CpCo(CO)_2$ in terms of the overlap of the orbitals of Cp^- and $Co(CO)_2^+$ fragments, based on EHT calculations for the ground state species (See also Table 3.7).

Table 3.7

Properties (E, Σc^2) of Virtual Orbitals of the Ground and Excited States[a] of $CpCo(CO)_2$ with C_s symmetry Derived from Extended Hückel Calculations.

Virtual MO		Ground state				
C_s	Character	*E*(eV)	Co3d	C(Cp)2p	C(CO)2p	O2p
a'	π^*(C–C)	−6.797	0.050	0.199	0.004	0.007
a'	π^*(C–C)	−6.799	0.037	0.389	0.005	0.001
a"	d_{yz},σ^*(M-CO)	−7.815	0.457	0.014	0.295	0.074
a'	σ^*(M-CO), $d_{x^2-y^2}$	−8.563	0.360	0.004	0.392	0.108
a'	π^*(C–O), d_{xy}	−8.615	0.173	0.002	0.432	0.120
a"	d_{xz},π^*(C–O)	−8.921	0.354	0.066	0.316	0.094
a"	d_{yz},σ^*(M-CO)	−9.180	0.279	0.024	0.249	0.078

Virtual MO	C1s(Cp) excited state[b]					C1s(CO) excited state				
C_s	*E*(eV)	Co	C(Cp)	C(CO)	O	*E*(eV)	Co	C(Cp)	C(CO)	O
a'	−6.47	0.046	0.000	0.004	0.001	−6.80	0.046	0.203	0.001	0.000
a'	−7.97	0.106	$\underline{0.121}$[c]	0.200	0.049	−6.81	0.041	0.394	0.000	0.000
a"	−7.62	0.415	$\underline{0.142}$	0.269	0.059	−8.28	0.532	0.016	$\underline{0.064}$	0.010
a'	−8.64	0.362	0.001	0.372	0.103	−8.78	0.269	0.023	0.003	0.001
a'	−8.67	0.174	0.005	0.335	0.093	−8.89	0.465	0.013	0.042	0.010
a"	−9.03	0.297	0.015	0.288	0.089	−10.24	0.478	0.075	$\underline{0.409}$	0.140
a"	−9.46	0.305	$\underline{0.158}$	0.278	0.092	−10.60	0.260	0.004	$\underline{0.587}$	0.226

Virtual MO	O1s excited state					Co2p excited state				
C_s	*E*(eV)	Co	C(Cp)	C(CO)	O	*E*(eV)	Co	C(Cp)	C(CO)	O
a'	−6.80	0.050	0.200	0.003	0.000	−6.92	0.010	0.382	0.011	0.002
a'	−6.80	0.038	0.389	0.003	0.000	−6.93	0.009	0.203	0.001	0.000
a"	−7.93	0.482	0.016	0.259	0.032	−8.49	0.034	0.001	0.521	0.138
a'	−8.68	0.390	0.002	0.330	$\underline{0.049}$	−9.08	$\underline{0.050}$	0.000	0.477	0.148
a'	−8.71	0.205	0.002	0.172	$\underline{0.026}$	−9.50	$\underline{0.108}$	0.012	0.421	0.144
a"	−9.08	0.362	0.069	0.578	$\underline{0.090}$	−9.76	$\underline{0.115}$	0.054	0.341	0.126
a"	−9.30	0.253	0.023	0.403	$\underline{0.064}$	−10.62	$\underline{0.296}$	0.034	0.063	0.023

[a] Excited states simulated by $Z+1$ species. In each case the square of the $2p_z$ (for C1s or O1s excitation) or Co3d (for Conp excitation) coefficients are listed.

[b] Energies and coefficients are weighted averages over values predicted with the C1s core hole on each carbon atom. The spread of energies and coefficients was quite small.

[c] Underlined values should dominate the experimental spectra.

interactions with the Cp$^-$ e_1" orbitals (See Fig. 3.5). There are five virtual MOs above the LUMO and next-to-LUMO. Three of these five MOs are predominantly Co 3d in character, one with some π^*(C≡O), the other two with some σ^*(M-CO) character; the other two upper MOs are π^*(C=C) orbitals of a' symmetry which are the Cp$^-$ e_2' set interacting weakly with filled frontier orbitals of the $Co(CO)_2$ fragment.

Two factors complicate the application of the ground state MO scheme to the interpretation of the core spectra of $CpCo(CO)_2$. First of all, the orbital character can change rather dramatically with addition of a localised core hole [See $Fe(CO)_5$ story in Ch. 4]. Secondly, the C 1s spectrum of $CpCo(CO)_2$ is the overlap of transitions from Cp carbons and from CO carbons. Transitions to the same virtual orbital in the two sets of localised transitions should be separated by *ca.* 2 eV since the C 1s (Cp) IP is 2.1 eV lower than the C 1s (CO) IP.[92] This may be taken into account in making correlations between EHMO orbital energies and experimental results either by comparisons via term values relative to each of the IPs, or by shifting the EHMO predictions for Cp excitations several eV below the EHMO predictions of CO excitations prior to comparison with the experimental spectrum.

The C 1s spectrum of $CpCo(CO)_2$ (Figs. 3.1, 3.6 and 3.7; energies, term values and proposed assignments in Table 3.1) is characterized by four strong resonances, two below the C 1s IP and two in the continuum. These are assigned by a combination of spectral comparison and the EHMO data. For the latter it is essential to use the equivalent core analogy. For example, when the core hole is placed on the Cp ligand the C_{2p}(Cp) character of the LUMO increases considerably (from 0.024 to 0.158) and the orbital adopts a distinct M-π^*(Cp) character, similar to that assigned for the C 1s → LUMO transition in the metallocenes.[13] Thus we assign the first feature at 285.4 eV to C 1s(Cp) → [$d_{xz,yz}$, π^*(Cp)] transitions, consistent with the spectrum of cobaltocene.

The second intense peak is composed of a main transition at 287.7 eV and a second peak at 286.8 eV which produces a distinct shoulder (See Fig. 3.7a). This band is attributed to the overlap of a lower energy C 1s(Cp) → π^*(Cp) component and a

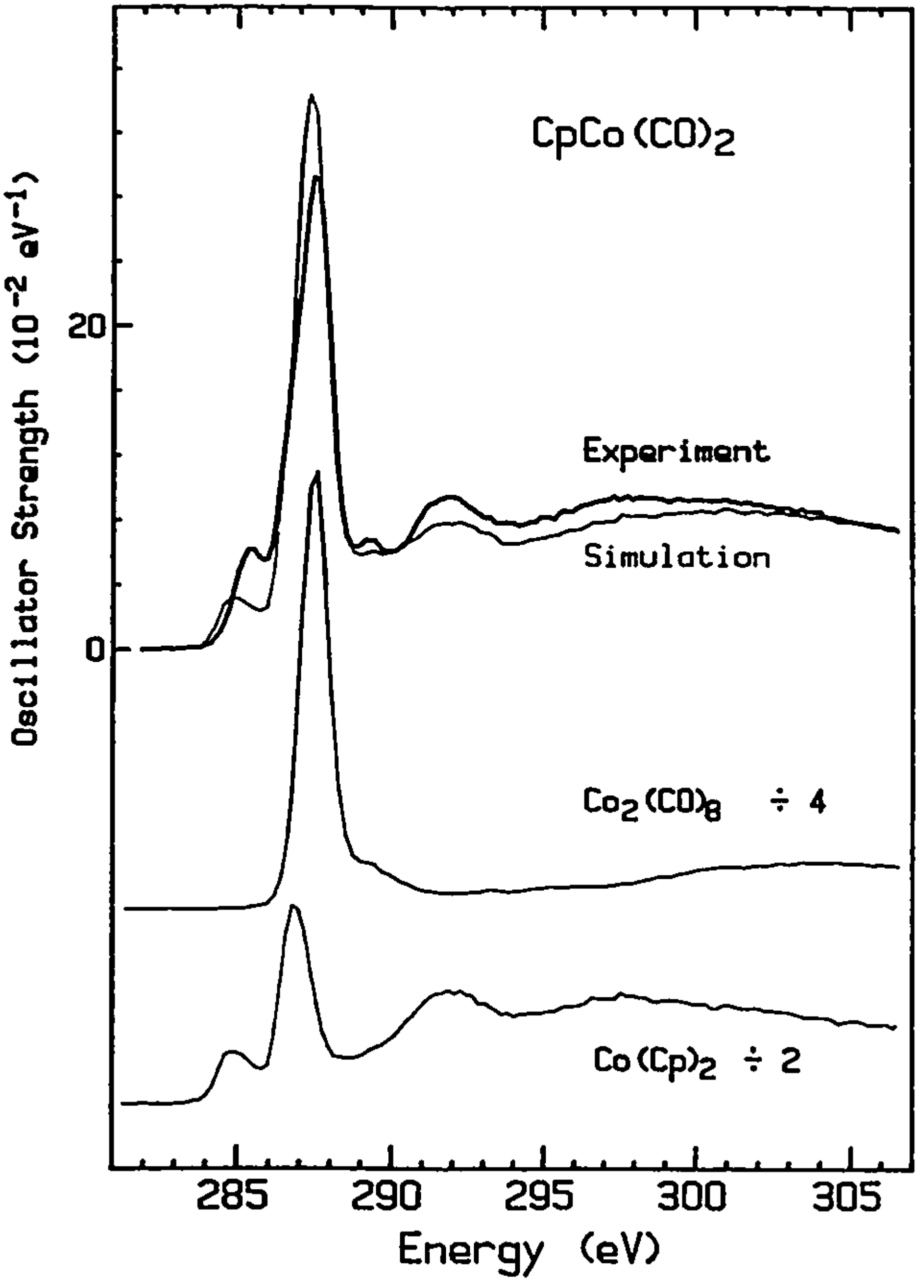

Fig. 3.6 Comparison of the C 1s oscillator strength spectrum of $CpCo(CO)_2$ with a simulation consisting of one-quarter of the $Co_2(CO)_8$ and one-half of the $Co(Cp)_2$ spectrum. The two components of the simulation spectrum are shown in the lower part of the figure on the same vertical scale.

higher energy C 1s(CO) → π^*(CO) component, based on comparison to the spectra of $Co(Cp)_2$ and $Co_2(CO)_8$. A simulation of the C 1s excitation spectrum of $CpCo(CO)_2$ has been prepared by adding 0.25 times the C 1s spectrum of $Co_2(CO)_8$ to 0.5 times that of $Co(Cp)_2$ (See Fig. 3.6). The simulated spectrum has essentially the same shape as the experimental one and reproduces all major features in the $CpCo(CO)_2$ spectrum, consistent with the general observation of spatial localisation of core excitation. Tracing the origin of the second feature in the simulation indicates that it is the overlap of C 1s → π^*(Cp) and C 1s → π^*(CO) transitions with the Cp component at lower energy. The EHMO calculations generally support this assignment except that, if the experimental separation of the CO and Cp C 1s energies (2.1 eV[92]) is employed, they suggest that the relative order of the Cp and CO π^* components should be reversed.

By analogy with cobalt carbonyl, the relatively weak feature at 289.2 eV is considered to be transitions to higher energy π^*_{delocal} orbitals of carbonyls. It could also contain some contributions from Rydberg or Co 4p excitations, as suggested in previous discussions of core excitation[12] and ETS results.[78] However the EHMO calculations predict negligible Co 4p contributions to any of the negative energy virtual orbitals. The two strong bands at 291.8 and 297 eV in the continuum are ascribed largely to C 1s → σ^*(C-C) transitions at the Cp ligand. The broad band around 297 eV will also contain the C 1s → σ^*(C=O) resonance which is produces the shoulder around 301 eV.

While the simulated and experimental C 1s spectra of $CpCo(CO)_2$ are in semi-quantitative agreement (See Fig. 3.6), there are quantitative discrepancies. One of the central goals of this study is to determine if deviations from an additivity model can provide information on ligand-ligand interaction in organometallic complexes. The most noteworthy difference is that the first resonance of Co $3d_{xz,yz}$ orbitals is more intense in the experimental than in the simulated $CpCo(CO)_2$ C 1s spectrum. The EHMO results are in qualitative accord with this observation (Tables 3.6 and 3.7). The estimated intensity of the C 1s(Cp) → LUMO transition increases from 0.075 in $Co(Cp)_2$ to 0.158 in $CpCo(CO)_2$ [N.B. as noted earlier,[13] the value for $Co(Cp)_2$ includes a 50% intensity reduction relative to that indicated by the squared LCAO coefficient to correct for 50% occupancy and thus Pauli-excluded transitions]. This is in reasonable agreement with the change in the experimental C 1s → $3d_{xz,yz}$ oscillator strength which increases from 0.045 to 0.077 between $Co(Cp)_2$ and $CpCo(CO)_2$ (Table 3.3).

There are two possible interpretations of the increased intensity. The first is that it is associated with transitions into low-lying π^*(CO) virtual orbitals. While the ground state EHMO result indicates that the LUMO of $CpCo(CO)_2$ has π^*(CO) character, the LUMO adopts a larger π^*(Cp) character when a C 1s(Cp) core hole is added (Table 3.7). The suggested C 1s(Cp) → π^*(CO) excitation would be of charge transfer character. These types of transition are generally weaker and shifted to higher energy relative to a frozen ground state orbital prediction. It is unlikely the extra intensity in the first peak is associated with a direct C 1s(CO) → π^*(CO) component on account of the 2.1 eV chemical shift. The alternate and most likely explanation is that the $d\pi^*$-$p\pi^*$ orbital has a larger C 2p character in $CpCo(CO)_2$ than $CoCp_2$. If this is the case, there would most likely be a larger carbon 2p component in the counterpart $d\pi$-$p\pi$ bonding orbital, thus implying a stronger Co-Cp bond in $CpCo(CO)_2$ than in $CoCp_2$. Comparison of the EHMO calculations for $CpCo(CO)_2$ and $Co(Cp)_2$ suggests that the increased C 2p (Cp) character in the $d\pi$-$p\pi$ and $d\pi^*$-$p\pi^*$ orbitals of $CpCo(CO)_2$ is associated with charge transfer from the Cp ligand onto the Co atom and the CO ligands, as found in other theoretical work.[79] Supporting evidence for the charge transfer is found in the C 1s oscillator strength spectrum of $CpCo(CO)_2$ since the C 1s → π^*(CO) oscillator strength decreases [relative to the per-CO value deduced from $Co_2(CO)_8$, see Table 3.3], as expected from increased occupancy of the π^* orbital with increased backbonding, an effect that has been deduced previously from the decrease in the carbonyl stretching frequency from 2025 cm^{-1} in $Co_2(CO)_8$ to 1988 cm^{-1} in $CpCo(CO)_2$ [97]. Such a reduction in the π^* oscillator strength is the explanation for the deviation at the π^* peak (285 eV) between the simulated and experimental C 1s spectra of $CpCo(CO)_2$ (Figure 3.6). Overall this brief analysis suggests that detailed analysis of experimental core

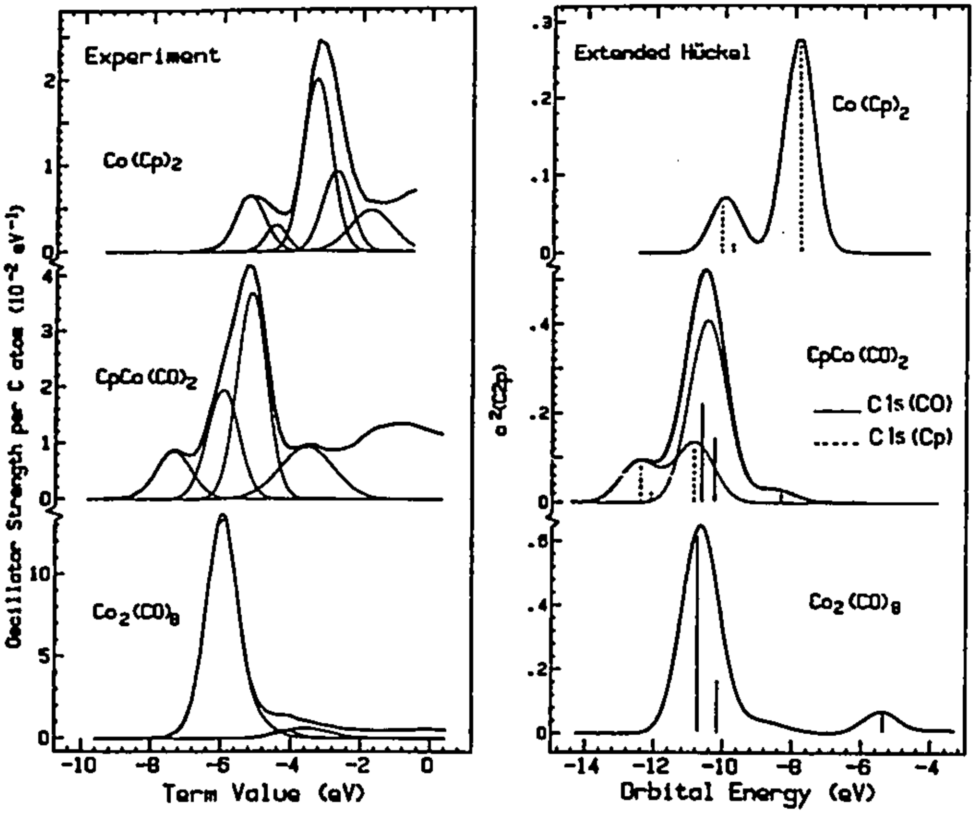

Fig. 3.7 (a; left) Expansions of the discrete portion of the C 1s spectra of $Co_2(CO)_8$, $CpCo(CO)_2$ and $Co(Cp)_2$ on a term value scale with resolution into individual components through fitting to Gaussian line shapes. Only the most significant components are plotted. (b; right) Predictions of the C 1s spectra of $Co_2(CO)_8$, $CpCo(CO)_2$ and $Co(Cp)_2$ based on extended Hückel calculations (Tables 3.4, 3.6 and 3.7). Gaussians of 1.2 eV fwhm at the indicated orbital energy positions with areas given by $\Sigma c^2(C2p)$ were added to generate the simulated spectra. The Cp and CO components of the simulated C 1s spectrum of $CpCo(CO)_2$ are shifted 3.0 eV and the orbital energy scale refers to that for CO excitation. The measured chemical shift is only 2.1 eV.[92]

excitation spectra of mixed ligand organometallic compounds can give insight into ligand-ligand interactions.

The EHMO results (Tables 3.4, 3.6, 3.7) have been used to simulate the discrete portions of the C 1s spectra of all three organocobalt species. Corresponding results for the Co 2p spectra have been presented earlier.[18] A sum of Gaussian peaks of 1.2 eV fwhm located at the EHMO eigenvalues with areas equal to the sum of the squares of the 2p AO coefficients are plotted in Fig. 3.7b in comparison with the experimental spectra plotted on term value scales (See Figure 3.7a). The C 1s(CO) and C 1s(Cp) components of the C 1s spectrum of $CpCo(CO)_2$ were generated independently (with separate treatment of each of the 3 chemically distinct Cp carbons), and summed after a shift of 3.0 eV. This shift, which is somewhat larger than the 2.1 eV chemical shift in the C 1s IPs,[92] was chosen to optimise agreement with experiment. In general the IP is considered an adjustable parameter in matching semi-empirical calculations to experimental findings. Given the crudeness of both the EHMO calculations and the use of squared 2p coefficients to estimate spectral intensities, the trends in the simulation spectra, in terms of spectral shapes and relative intensities throughout the 3 molecules, are in remarkable agreement with those observed experimentally (compare Figs. 3.7a and 3.7b, which are on similar scales). This gives some confidence in the validity of EHMO for interpreting core spectra, although difficulties in its use for interpreting metal 2p spectra have been noted.[18]

§3.5 Co 2p and Co 3p Spectra

The Co 2p and Co 3p excitation spectra of $Co_2(CO)_8$, $CpCo(CO)_2$ and $Co(Cp)_2$ are presented in Figures 3.8 and 3.9, respectively. A smooth background extrapolated from the underlying continua at lower energy has been subtracted from each spectrum [indicated in Figure 3.9 for the Co 3p spectrum of $Co_2(CO)_8$] and the Co 2p spectra have been converted to absolute oscillator strengths. No attempt was made to generate absolute Co 3p optical oscillator strengths because of uncertainties in the continuum excitation spectra of mixed ligand organometallic compounds can give insight into ligand-ligand interactions.

The EHMO results (Tables 3.4, 3.6, 3.7) have been used to simulate the discrete portions of the C 1s spectra of all three organocobalt species. Corresponding results for the Co 2p spectra have been presented earlier.[18] A sum of Gaussian peaks of 1.2 eV fwhm located at the EHMO eigenvalues with areas equal to the sum of the squares of the 2p AO coefficients are plotted in Fig. 3.7b in comparison with the experimental spectra plotted on term value scales (See Figure 3.7a). The C 1s(CO) and C 1s(Cp) components of the C 1s spectrum of $CpCo(CO)_2$ were generated independently (with separate treatment of each of the 3 chemically distinct Cp carbons), and summed after a shift of 3.0 eV. This shift, which is somewhat larger than the 2.1 eV chemical shift in the C 1s IPs,[92] was chosen to optimise agreement with experiment. In general the IP is considered an adjustable parameter in matching semi-empirical calculations to experimental findings. Given the crudeness of both the EHMO calculations and the use of squared 2p coefficients to estimate spectral intensities, the trends in the simulation spectra, in terms of spectral shapes and relative intensities throughout the 3 molecules, are in remarkable agreement with those observed experimentally (compare Figs. 3.7a and 3.7b, which are on similar scales). This gives some confidence in the validity of EHMO for interpreting core spectra, although difficulties in its use for interpreting metal 2p spectra have been noted.[18]

§3.5 Co 2p and Co 3p Spectra

The Co 2p and Co 3p excitation spectra of $Co_2(CO)_8$, $CpCo(CO)_2$ and $Co(Cp)_2$ are presented in Figures 3.8 and 3.9, respectively. A smooth background extrapolated from the underlying continua at lower energy has been subtracted from each spectrum [indicated in Figure 3.9 for the Co 3p spectrum of $Co_2(CO)_8$] and the Co 2p spectra have been converted to absolute oscillator strengths. No attempt was made to generate absolute Co 3p optical oscillator strengths because of uncertainties in the continuum

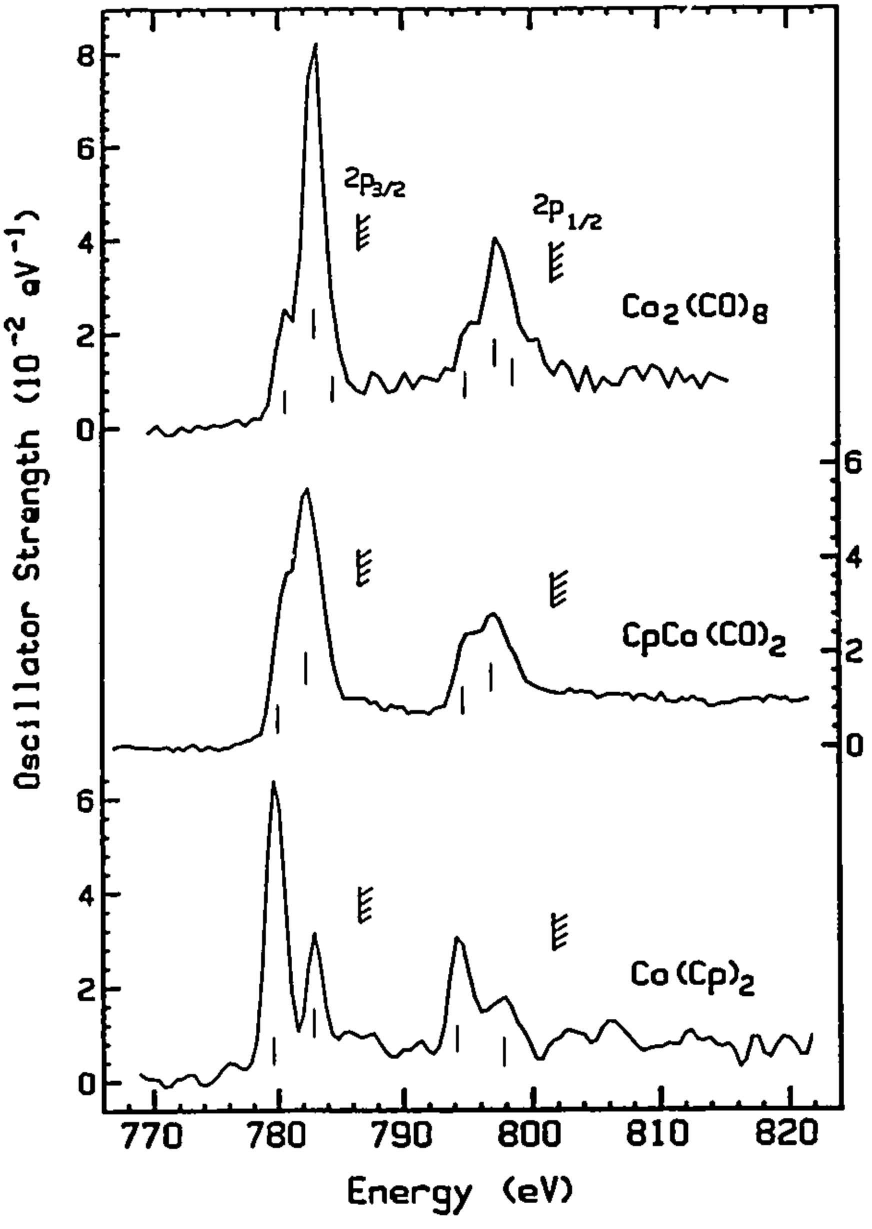

Fig. 3.8 Co 2p oscillator strength spectra derived from ISEEL spectra of $Co_2(CO)_8$, $CpCo(CO)_2$, and $Co(Cp)_2$.

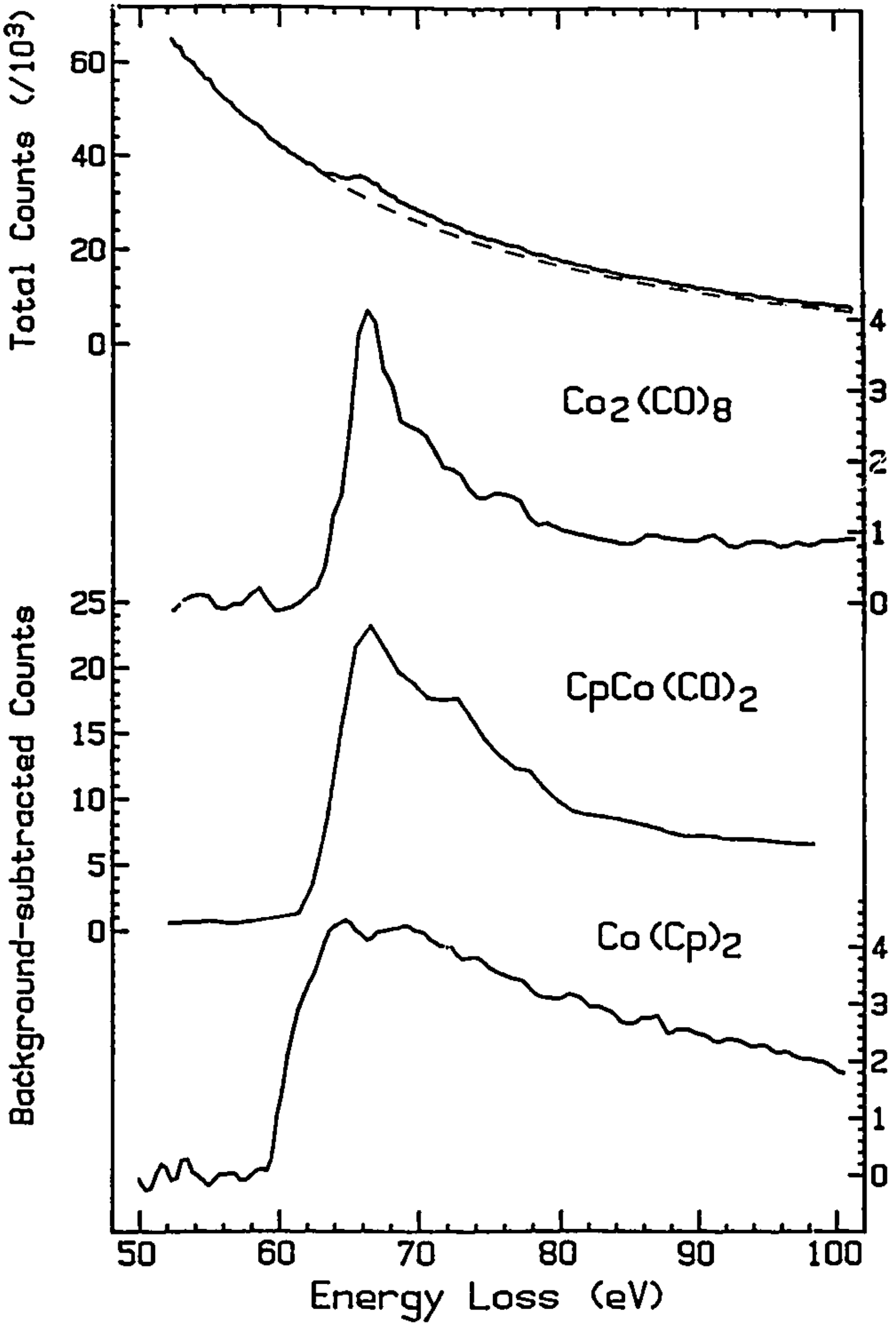

Fig. 3.9 ISEEL spectra of $Co_2(CO)_8$, $CpCo(CO)_2$, and $Co(Cp)_2$ in the region of Co 3p excitation. A large background has been subtracted from each spectrum. The raw data and subtracted background are indicated at the top for $Co_2(CO)_8$.

shape associated with the difficult background subtraction. This is especially challenging for the Co 3p signal which is remarkably weak and superimposed on a large valence-shell continuum (see top portion of Fig. 3.9). The energies, term values and proposed assignments of the observed features are presented in Table 3.8.

The Co 2p spectra of $Co_2(CO)_8$ and $Co(Cp)_2$ are quite different from each other while the spectrum of $CpCo(CO)_2$ has an intermediate shape. The metal 2p spectra of Mn[18] and Fe[18] (see also Chapters 4 and 5) carbonyl and metallocene complexes are strikingly similar to cobalt species with similar ligands. A simplified interpretation of the observed trends in terms of relative energies of $d\pi^*$ and $d\sigma^*$ virtual orbitals has been given recently.[18] A more detailed interpretation of the cobalt 2p spectra, based on the EHMO results, is given here.

Excitations to MOs of large metal 3d character are expected to dominate M *np* core excitation spectra. The EHMO results suggest that MOs constructed mainly from ligand π^* orbitals, which lie energetically above the 3d-dominated MOs, are involved also in the 2p excitations. Since the Co 2p IPs do not change very much among these three compounds (<0.5 eV[92]), the large changes in the Co 2p spectra must chiefly be associated with the Co 3d energy levels as well as those of π^*-related MOs. The basic pattern is a shift from domination of the M-Cp spectrum by lower energy (Co $2p^{-1}$,3d) states to domination by higher energy (Co $2p^{-1}$,3d) states in M-CO. The unoccupied M 3d atomic orbital character contributes mainly to a doubly degenerate e-type ($4e_{1g}$) orbital in $Co(Cp)_2$ and likely to two closely spaced counterparts in the other two species which are of lower symmetry. Thus focusing solely on a ligand-field type of picture of the Co 3d orbitals does not appear adequate to fully explain the relatively large spread between the two main bands observed in each Co $2p_{3/2}$ (and Co $2p_{1/2}$) spectrum. Instead, the two-band aspect of each spectrum may consist of a lower energy metal 2p → metal 3d band and a higher energy metal 2p → ligand 2p 'charge transfer' band. Multiplet effects (exchange splittings), which are very important in the metal 2p spectra of open shell species,[98] are unlikely to be involved in $Co_2(CO)_8$ and $CpCo(CO)_2$ since they have

Table 3.8

Energies, term values and proposed assignments for features in the Co3p and Co2p spectra of $Co_2(CO)_8$, $CpCo(CO)_2$ and $Co(Cp)_2$

Co3p

$Co_2(CO)_8$		$CpCo(CO)_2$		$Co(Cp)_2$		Assignment (final orbital)
E(eV)	*T*(eV)	*E*(eV)	*T*(eV)	*E*(eV)	*T*(eV)	
65(1)	1.5	-		61.4 (sh)	5.1	3d
66.4(2)[a]	0.1	66.2	0.3	64.5	2.0	Ligand 2p charge transfer
66.5		66.5		66.5		IP (estimated)[b]
70(1)	−3.5	73	−6.5	69	−2.5	

Co2p

$Co_2(CO)_8$				$CpCo(CO)_2$				$Co(Cp)_2$				Assignment
$Co2p_{3/2}$		$Co2p_{1/2}$		$Co2p_{3/2}$		$Co2p_{1/2}$		$Co2p_{3/2}$		$Co2p_{1/2}$		
E(eV)	*T*(eV)	*E*(eV)	*T*(eV)	*E*(eV)	*T*(eV)	*E*(eV)	*T*(eV)	*E*(eV)	*T*(eV)	*E*(eV)	*T*(eV)	
780.6	5.6	795.1	5.4	780.2	6.0	794.9	6.0	779.7	5.1	794.3	5.1	3d
782.8	3.4	797.5	4.2	782.4	3.8	797.0	3.9	782.9	2.4	797.0	2.4	Ligand 2p charge transfer
784.7	1.5	798.5	3.0	786.0	0.3			785.4	1.1			Rydberg/ continuum
786.34		801.5		786.25		800.9		784.8		799.4		IP

[a] Co3p calibration (relative to main C1s→π^* feature in the same molecule): $Co_2(CO)_8$, 224.8(5) eV; $CpCo(CO)_2$, 224.5(5) eV; $Co(Cp)_2$, 226.2(3) eV.

[b] $Co3p_{3/2}$ IP estimate is that of $Co(CH_3COCHCOCH_3)_2$ (66.4 eV) [92]. The spin-orbit splitting is around 1.5 eV.

[c] Co2p calibration relative to O1s→π^* (535.40 eV) of CO_2: $\Delta E = 247.5(2)$ eV for $Co_2(CO)_8$, 244.3 eV for $Co(Cp)_2$; relative to O1s→π^*(CO) of same species, $CpCo(CO)_2$, $\Delta E = 248.6(2)$ eV.

[d] Co2p IPs from XPS [92].

closed-shell ground states and only singly degenerate virtual orbitals.

The invocation of charge-transfer contributions is suggested by the EHMO analysis which predicts (on energetic grounds at least) that the lower-energy features in the 2p spectra arise largely from M 2p → M 3d transitions, whereas the higher-energy ones are almost completely due to M 2p → π^*(Cp/CO) charge-transfer type transitions. In the case of $Co(Cp)_2$, the lower-energy feature is assigned to Co 2p → LUMO $4e_{1g}$ (Co $d_{xz,yz}$) transitions, while the higher-energy peak is attributed to promotions from Co 2p to the $3e_{2u}$ (and perhaps $4e_{2g}$) MOs which are the π^*(C=C) MOs of the Cp ring (Table 3.6). Experimentally, the two peaks are well resolved. One expects the virtual-valence MOs accessed in Co 2p excitation to have strong metal 3d character and only small ligand 2p character. The weakness of the higher energy band in the cobalt 2p spectrum of $Co(Cp)_2$ reflects the fact that the Co 2p core hole does not have substantial overlap with MOs localised on the Cp ligands.

The Co 2p spectrum of the carbonyl $Co_2(CO)_8$ differs dramatically from that of cobaltocene. The intensities of the two peaks are reversed and the lower-energy peak shrinks into a shoulder on the more intense higher-energy peak, with an intensity ratio of approximately 1:3. The two peaks are not fully separated in $Co_2(CO)_8$, suggesting that there is a wide distribution of Co 3d density associated with strong interactions between Co and CO of both $d\pi$-$p\pi$ and $d\sigma$-$p\sigma$ character. The EHMO calculations for Co 2p excitation of $Co_2(CO)_8$ (Table 3.4) suggest that the low-energy shoulder is associated with Co 2p excitations to a group of frontier MOs (# 29-33). The lowest energy b_{1g} MO of this group (the LUMO) is basically CO $2p_z$ but it has a remarkably enhanced Co $3d_{xy}$ character on Co 2p excitation —— the Co 2p coefficient rises from .008 in the ground state to 0.108 in the Co 2p excited state. The high-energy Co 2p band may be related to another group of virtual MOs (# 20-23). This includes a b_{1g} MO (# 20) which is almost a pure $\pi^*(2p_x, 2p_y)$ MO of the CO ligand in the ground state but becomes a Co-$3d_{x2-y2}$-dominated orbital upon cobalt 2p excitation. The ratio of the squared cobalt 3d coefficients of these two b_{1g} MOs (0.108:0.319) is close to 1:3, in good agreement with the experimental intensity ratio. Compared to $Co(Cp)_2$ there is a greater change in the Co 3d coefficients between the ground and Co core-excited states of $Co_2(CO)_8$. This is consistent with stronger interaction between Co and CO in $Co_2(CO)_8$ than between Co and Cp in $Co(Cp)_2$. The energies of the two b_{1g} MOs with large Co 3d character in $Co_2(CO)_8$ are much closer to each other than their counterparts in cobaltocene (Table 3.6). In addition, there are several CO localised MOs (# 24-27) filling the gap (ca. 2.1 eV) between the two b_{1g} MO levels (Table 3.4). Both factors help explain why the two major peaks are less well resolved in the Co 2p spectrum of $Co_2(CO)_8$ than in that of $Co(Cp)_2$.

The EHMO results for $CpCo(CO)_2$ (See Table 3.7) also help to explain its Co 2p spectrum. In this mixed ligand species, the two cobalt 2p features are even less well resolved, perhaps reflecting more complicated bonding between Co and the two types of ligands. The $CpCo(CO)_2$ and $Co_2(CO)_8$ spectra look similar —— the energies of the two major features are almost identical (Table 3.8). This suggests that the two carbonyls play more important roles than the Cp ring in determining the Co 3d content of the frontier unoccupied MOs of $CpCo(CO)_2$, consistent with stronger M-CO than M-Cp interactions. Co 2p excitations to the d_{yz}/d_{xz} components of the LUMO and next-to-LUMO, which are M-Cp antibonding in character, enhance the first peak compared to its counterpart in $Co_2(CO)_8$.

Based on these EHMO results, a logical interpretation of the Co 2p spectrum of $CpCo(CO)_2$ would be to assign the first feature to Co 2p excitations into the three lowest-energy virtual MOs, which are two a" MOs followed by an a' MO (Table 3.7). All three contain substantial Co 3d components, especially the a" LUMO. Thus the first feature in the Co 2p spectrum is chiefly a Co 2p → 3d excitation. The second peak can be attributed to Co 2p excitations to the four remaining upper unoccupied MOs which have smaller Co 3d character. In this second group, two are mainly associated with the carbonyl ligands, and the rest are largely localised on the Cp ring. Co core excitations to the two highest energy, Cp-based virtual MOs may contribute on the high-energy side of the second spectral feature.

The Co 3p spectra (Fig. 3.9) are much less detailed than the Co 2p spectra partly because of the small spin-orbit splitting which leads to complicated spectral overlap, and partly because of the large natural linewidth associated with the rapid Coster-Kronig decay of metal 3p states. Even so the trends observed in the metal 2p spectra are also discernable in the 3p spectra. $Co_2(CO)_8$ shows a low energy shoulder on the main part of the Co 3p → 3d resonance, whereas the Co 3p spectrum of $Co(Cp)_2$ is strongest at lowest energy. It is possible that the second peak in the $Co(Cp)_2$ spectrum is stronger than the first feature only because of overlap with a strong, lower energy Co $3p_{1/2} \rightarrow$ Co 3d component. There does not appear to be any evidence for a Co *np* → σ^*(Co-Co) transition in either the 2p or 3p spectra of $Co_2(CO)_8$. Comparison of the Co 2p spectrum of $Co_2(CO)_8$ with the Fe 2p spectrum of $Fe(CO)_5$ (see Chapter 4) does not reveal any evidence for an additional σ^*(Co-Co) feature in the former.

§3.6 Summary

The C 1s, O 1s, Co 2p and 3p core excitation spectra of $Co_2(CO)_8$, $Co(Cp)_2$ and $CpCo(CO)_2$ have been recorded by ISEELS and analysed with the aid of EHMO calculations as well as spectral comparisons. Simple spectral additivity gives a reasonable first order description, but it is inadequate to quantitatively reproduce the carbon 1s spectrum of $CpCo(CO)_2$. The differences between the additivity-simulation and experiment have been discussed in terms of ligand-ligand interactions. The core excited states associated with carbonyls are found to be much more independent of their local environment than those associated with the π-bonded Cp ligand. The Co *np* spectra are found to be extremely sensitive to the nature of the ligand.

Chapter 4

CORE EXCITATION OF ORGANOIRON COMPOUNDS

§4.1 Introduction

Organometallic complexes have been receiving considerable attention in both theoretical and experimental chemistry since the discovery of ferrocene. This is chiefly due to the many applications of these compounds in areas such as synthesis, homogeneous catalysis, cluster and solid state chemistry, chemical vapor deposition of metallic thin films etc.. Molecular spectroscopies have played a pivotal role in organometallic chemistry by addressing problems associated with electronic structure, bonding schemes, molecular formation and the chemistry of the complexes. Inner-shell excitation induced by either inelastic electron scattering (ISEELS)[99] or X-ray absorption (NEXAFS)[100] has been extended recently to gas phase organometallic complexes.[11-14,20,101] Because of the spatially localised character of core excitation, spectra recorded at several different core edges can be used to map out the unoccupied molecular orbitals as they contribute to the various inner-shell electronic excited states of a molecule.

This chapter is a systematic extension of core-excitation studies to organoiron complexes. The spectra of several series of related organoiron complexes have been recorded to investigate the sensitivity of core excitation spectroscopy to the electronic structure, particularly with regard to metal-ligand bonding and ligand-ligand interactions. The spectra of $Fe(CO)_5$ and $Fe_2(CO)_9$, were compared in order to study the sensitivity of core spectra to the weak metal-metal bond predicted by the 18-electron rule.[76] Three iron tricarbonyl complexes with butadiene (C_4H_6), 1,3-cyclohexadiene (c-C_6H_8) and cyclooctatetraene (c-C_8H_8) ligands were utilized to explore ligand-ligand interaction in mixed ligand complexes. Ferrocene ($FeCp_2$, $Cp=\eta^5$-C_5H_5) and two monosubstituted ferrocenes with a vinyl (CpFeCp-$CHCH_2$) or a butyl (CpFeCp-C_4H_9) substituent on one of the Cp rings were employed to test the sensitivity of core excitation spectra to more remote perturbations of the electronic structure. ISEELS spectra at the

C 1s, O 1s, Fe 2p and Fe 3p edges of the gas-phase complexes have been recorded using scattering conditions dominated by electric dipole transitions. All spectra, except those at the Fe 3p edge, have been converted to optical oscillator strengths in order to study trends in the transition probabilities through the molecular series. Both C 1s and O 1s spectra of $Fe(CO)_5$ have been presented briefly[14] while the C 1s spectrum of ferrocene[13] has been discussed in considerable detail previously. All other spectra are being reported for the first time, to my knowledge.

§4.2 **EHMO Calculations**

EHMO treatment has been used to help assign the spectra of the two carbonyl complexes. Calculations and qualitative descriptions of the MO structure of the *ground states* of $Fe(CO)_5$ [102], $Fe_2(CO)_9$ [76], $FeCp_2$ [82] and C_4H_6-$Fe(CO)_3$ [103] have been presented already in the literature. These articles give valuable insight into the general characteristics of bonding mechanisms and, in some cases, information about the low lying unoccupied MOs. Extended Hückel calculations have been employed in this work to obtain a more complete picture of the unoccupied MOs as sampled by inner-shell excitation. In some cases there are large changes in the virtual orbital character between the ground and core excited states because of relaxation of the valence electron distribution in the presence of a localised core hole. EHMO calculations, carried out in the equivalent ionic core virtual orbital model,[57] have been found to account for the relaxation induced by the core hole and to give a satisfactory simulation of the core excitation spectra of many organometallics.[13,18] EHMO calculations of the C 1s and Fe 2p spectra of $Fe(CO)_5$ and $Fe_2(CO)_9$ are reported in this chapter. EHMO results for C 1s excitation of ferrocene have been reported earlier.[13] The molecular geometries used in the calculation were taken from the literature {$Fe(CO)_5$ [104], $Fe_2(CO)_9$ [105]}. An idealised D_{3h} molecular geometry was adopted for both complexes for simplicity as well as convenience. This seems appropriate since the gas phase structure of $Fe_2(CO)_9$ is not precisely known. EHMO investigations[18] of the metal 2p spectra of Co complexes have indicated a rather strong sensitivity to geometry (See Fig. 1.7).

The EHMO results were used to generate spectral simulations, as described in Chapter 3. As an example, the EHMO simulation of carbon 1s excitation at the axial carbonyl of $Fe(CO)_5$ is the sum of Gaussian lines with relative positions given by the virtual orbital energies, a width of 1.0 eV FWHM and intensities given by $\Sigma c^2(N2p)$, where c(N2p) is the LCAO coefficient, the contribution of the N 2p AO to the virtual MO in the molecule where a nitrogen atom replaces one of the axial carbonyl carbon atoms to account for the core hole within the equivalent core approximation. A similar calculation and spectral simulation was carried out for C 1s excitation of an equatorial carbonyl. The EHMO simulation of the complete C 1s spectrum of $Fe(CO)_5$ is a 2:3 weighted sum of these two component spectra. The energy scale of this simulation should approximate the experimental term values. In fact EHMO energies are typically too low by about 4 eV. More suggestive comparisons have been made by aligning the most prominent feature of the EHMO simulation with that of the main feature in the experimental spectrum.

§4.3 C 1s Spectra

§4.3.1 Iron Carbonyl Complexes

The C 1s spectra of $Fe(CO)_5$ and $Fe_2(CO)_9$ are compared to that of free CO in Fig. 4.1. Energies, term values and proposed assignments of the spectral features are listed in Table 4.1. The spectra of the two iron carbonyl species are quite similar. Each is dominated by a very intense, low energy peak corresponding to C 1s → $\pi^*(C=O)$ excitation localised on a single carbonyl ligand. Several weak features are apparent between 289 and 292 eV, just above the main $\pi^*(CO)$ resonance. These are assigned to C 1s → $\pi^*_{delocal}$ transitions, which may be thought of as a type of charge transfer since the majority of the density of these orbitals is on carbonyl ligands other than that containing the C 1s hole.

The distinction between π^*_{local} and $\pi^*_{delocal}$ is well illustrated by a comparison

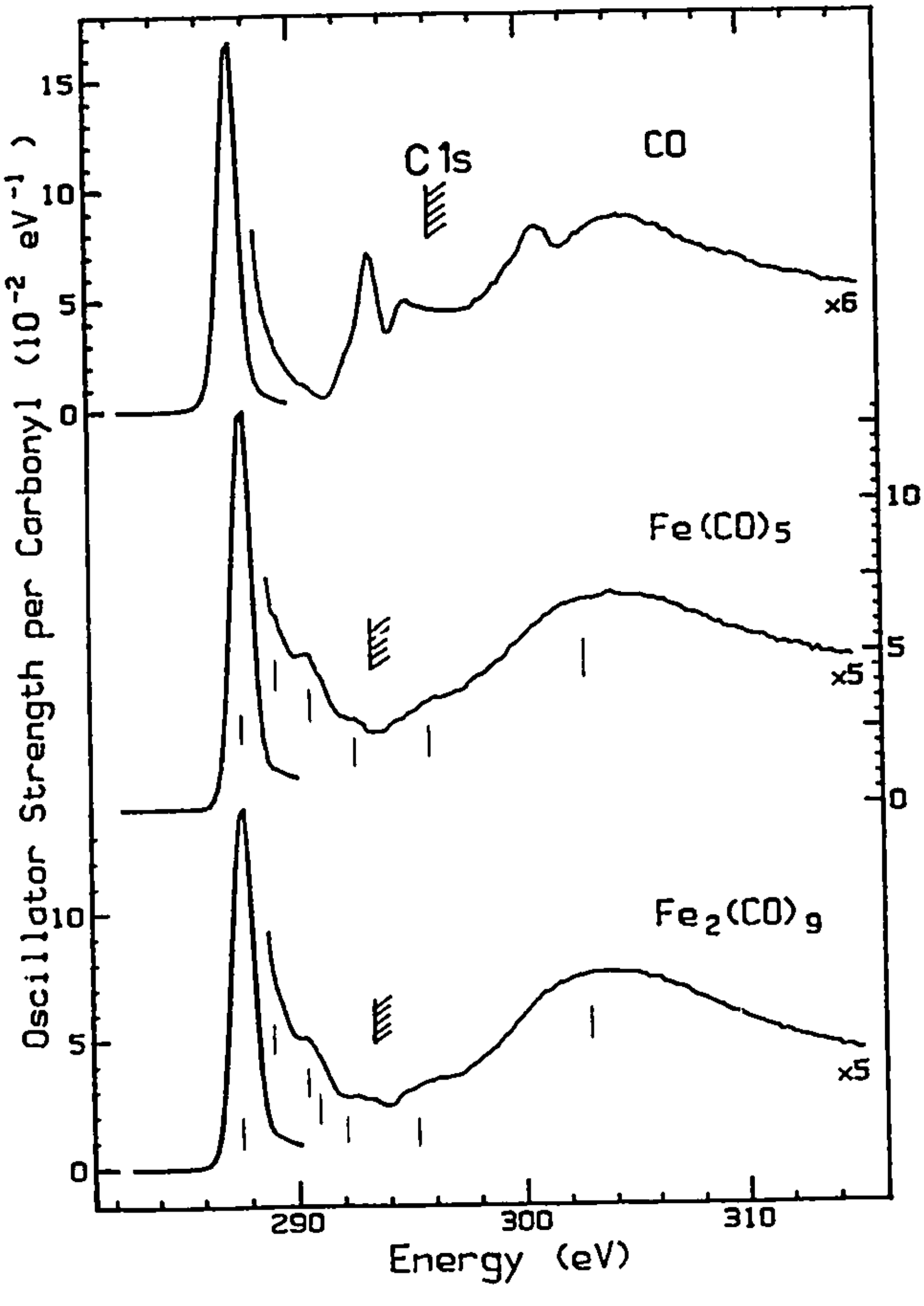

Fig. 4.1 Oscillator strengths for C 1s excitation of CO, $Fe(CO)_5$ and $Fe_2(CO)_9$ derived from ISEELS spectra. The hatched lines indicate the edges.

Table 4.1 Energies (E, eV), Term Values (T, eV) and Proposed Assignments for Features in the C 1s Spectra of CO, $Fe(CO)_5$ and $Fe_2(CO)_9$.

CO		$Fe(CO)_5$		$Fe_2(CO)_9$		Assignment (final orbital)
E	T[a]	E	T	E	T	
287.40	8.7	287.80[b]	5.7	287.66[b]	5.7	$\pi^*(C=O)$
		288.9	4.6	289.0	4.4	$\pi^*_{delocal}$
		290.5	3.0	290.6	2.8	$\pi^*_{delocal}$
		291.0	2.5	291.2	2.2	$\pi^*_{delocal}$
293.3	2.8	292.6	0.9	292.3	1.1	Rydberg
296.1		293.5		293.4		IP[c]
300.8	-4.7	296.2	-2.7	295.3	-1.9	2e (1s → π^*; 3d → π^*)
304.0	-7.9	303.2	-9.7	303.1	-9.7	$\sigma^*(C=O)$

a. T = IP - E

b. Calibration relative to CO_2 (C 1s → π^*: 290.74 eV): $\Delta E = -2.94(3), -3.08\ (2)$ eV for $Fe(CO)_5$ and $Fe_2(CO)_9$, respectively.

c. IPs from XPS[92]. The metal carbonyls have large shake up. This is the energy of the main XPS line.

of the EHMO results for ground state and C 1s excited $Fe(CO)_5$ (Figure 4.2). In the ground state the 10 π^*(CO) orbitals may be divided into axial and equatorial sets, in each case delocalised over several carbonyl ligands. If the C 1s spectrum reflected the π^* orbitals of the ground state, the C 1s → π^* region of the spectrum would consist of six rather intense transitions distributed over 2 eV (upper part of the lower panel of Figure 4.2). The resulting spectrum would exhibit obvious shoulders at our experimental resolution (0.6 eV) and clearly separated peaks at state-of-the-art resolution (45 meV). However, the C 1s core hole modifies the virtual orbitals substantially. The lowest energy virtual orbital becomes strongly localised on the C 1s excited carbonyl and is stabilised by more than 1 eV relative to the ground state. At the same time the higher energy π^* orbitals are either unchanged or are 'anti-localised' on the carbonyl ligands without the carbon 1s core hole. The energies of the 'anti-localised' MOs are unchanged or only slightly stabilised relative to the ground state. Thus, when the effect of the core hole is taken into account, EHMO predicts the carbon 1s spectrum of $Fe(CO)_5$ to be composed of three components, a doubly degenerate π^*_{local}(ax) and two orthogonal π^*_{local}(eq) resonances, separated by 0.2 eV. At higher energy, EHMO predicts weak features corresponding to small N 2p contributions to the 'anti-localised' or unmodified π^* orbitals. It is the latter that are denoted C 1s → $\pi^*_{delocal}$ transitions.

As shown in Fig.4.3, the spectral simulations derived from EHMO calculations agree well with the experimental C 1s spectra of $Fe(CO)_5$ and $Fe_2(CO)_9$. The simulated spectra are the weighted sum of two components: $[2(C_{axial}) + 3(C_{equatorial})]$ in $Fe(CO)_5$ and $[3(C_{bridging}) + 6(C_{terminal})]$ in $Fe_2(CO)_9$. These components each consist of several lines as indicated in Fig.4.3. EHMO simulates the discrete portion of both experimental C 1s spectra reasonably well, reproducing both the extraordinary concentration of the oscillator strength in the lowest energy π^*_{local} feature as well as the weakness and some aspects of the energy distribution of the C 1s → $\pi^*_{delocal}$ transitions. However, the EHMO calculations suggest that there should be additional bands at 291.5 and 293 eV in $Fe_2(CO)_9$ which are not evident in the experimental spectrum. These features could

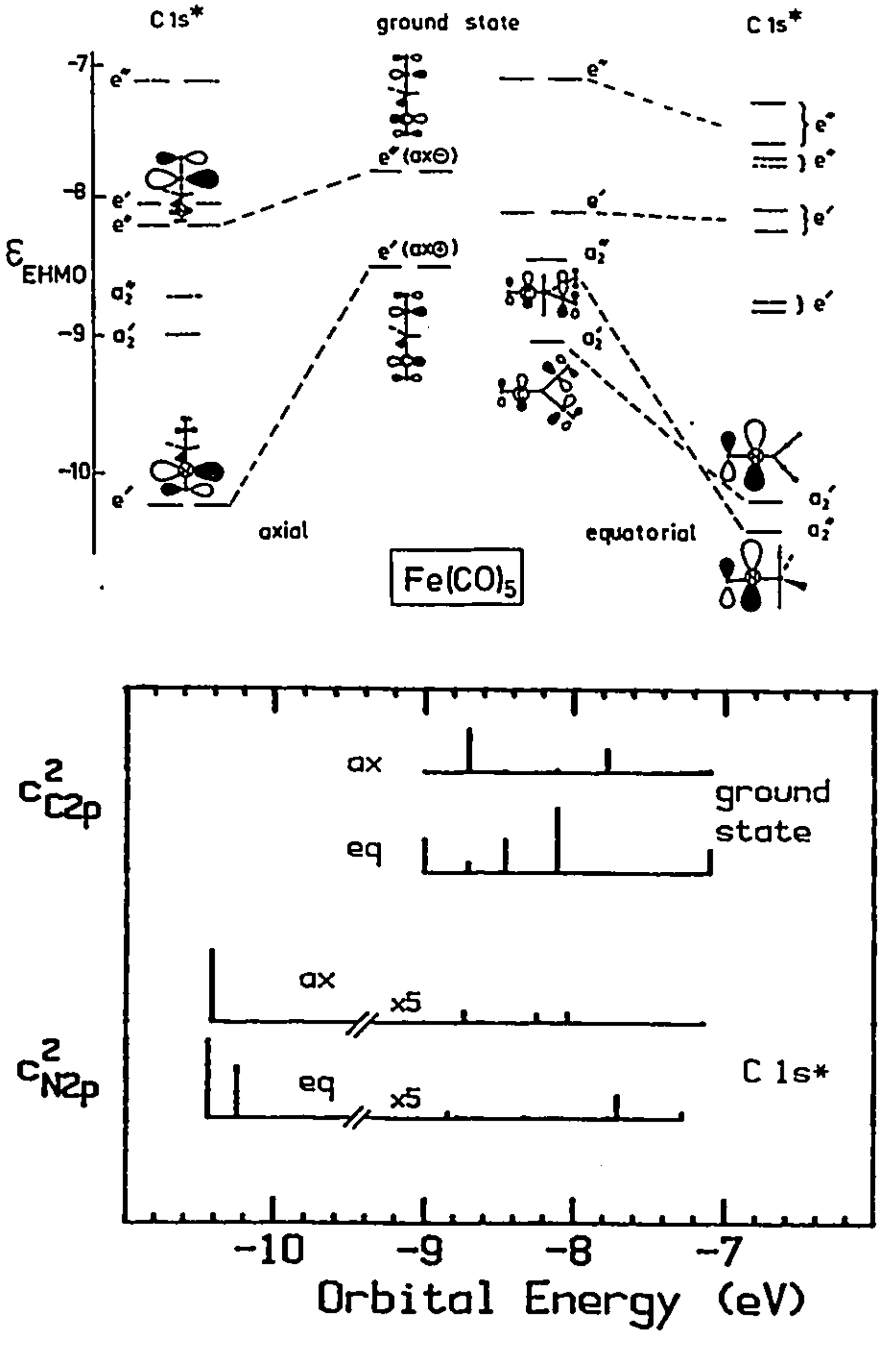

Fig. 4.2 EHMO results for the π^* orbitals of $Fe(CO)_5$ in both the ground state and in the presence of C 1s core holes. The upper portion sketches the orbital energies and selected orbital shapes. The lower portion presents the spectra on an EHMO orbital energy scale with intensities given by the square of the C 2p (ground state) or N 2p (C 1s excitation) LCAO coefficients in the π^* orbitals. Note the carbon atom considered for the spectra derived from the ground state calculation is the same as that which is replaced by the (Z+1), N atom in the C 1s excited state calculation.

be present but not observed as distinct features in the experimental spectra on account of overlap with Rydberg transitions that the minimal basis set EHMO treatment cannot predict.

The oscillator strengths for the $\pi^*(C=O)$ features [and $\pi^*(C=C)$ in the other complexes] have been derived by gaussian curve analysis and are summarised in Table 4.2. The main π^* resonance of the carbonyl complex is less intense than that of the $\pi^*(CO)$ resonance of CO. However the sum of the oscillator strengths of the $\pi^*(CO)_{local}$ and $\pi^*(CO)_{delocal}$ resonances is in rather good agreement with the π^* oscillator strength for free CO. This provides some support for our $\pi^*(CO)_{delocal}$ assignment since this observation is consistent with a simple redistribution of C 2p contributions to the π^* orbitals.

Relative to free CO, Rydberg structures and double excitations are much less prominent in the metal carbonyls. Their intensities seem to be substantially diminished, either because of extensive mixing with virtual valence orbitals (of which there is a higher density) or because large-R Rydberg orbitals are excluded from the C 1s core region by virtue of the large size of the molecule.

One motivation of the EHMO study was to investigate the possible occurrence and energy position of a postulated C 1s → σ^*(Fe-Fe) transition in $Fe_2(CO)_9$. EHMO predicts a MO of unambiguous σ^*(Fe-Fe) character at $\epsilon = -7.9$ eV for excitation at the bridging carbonyl and $\epsilon = -8.7$ eV for excitation at the terminal carbonyl. Energetically C 1s excitation to these orbitals would lie at 289 or 290 eV, but EHMO predicts zero intensity since there is no N 2p contribution to these orbitals, i.e. there should not be any signal arising from C 1s → σ^*(Fe-Fe) transitions. This agrees with experiment and our previous studies of $Mn_2(CO)_{10}$ [11] and $Co_2(CO)_8$ (see Chapter 3) where evidence for C 1s → σ^*(M-M) features was sought but also not found. Basically, if there is a well localised σ^*(M-M) virtual orbital it is not likely to be significant in the C 1s spectrum because of poor spatial overlap with the C 1s core orbital.

The $\sigma^*(C=O)$ shape resonances in the C 1s continuum of the metal carbonyls

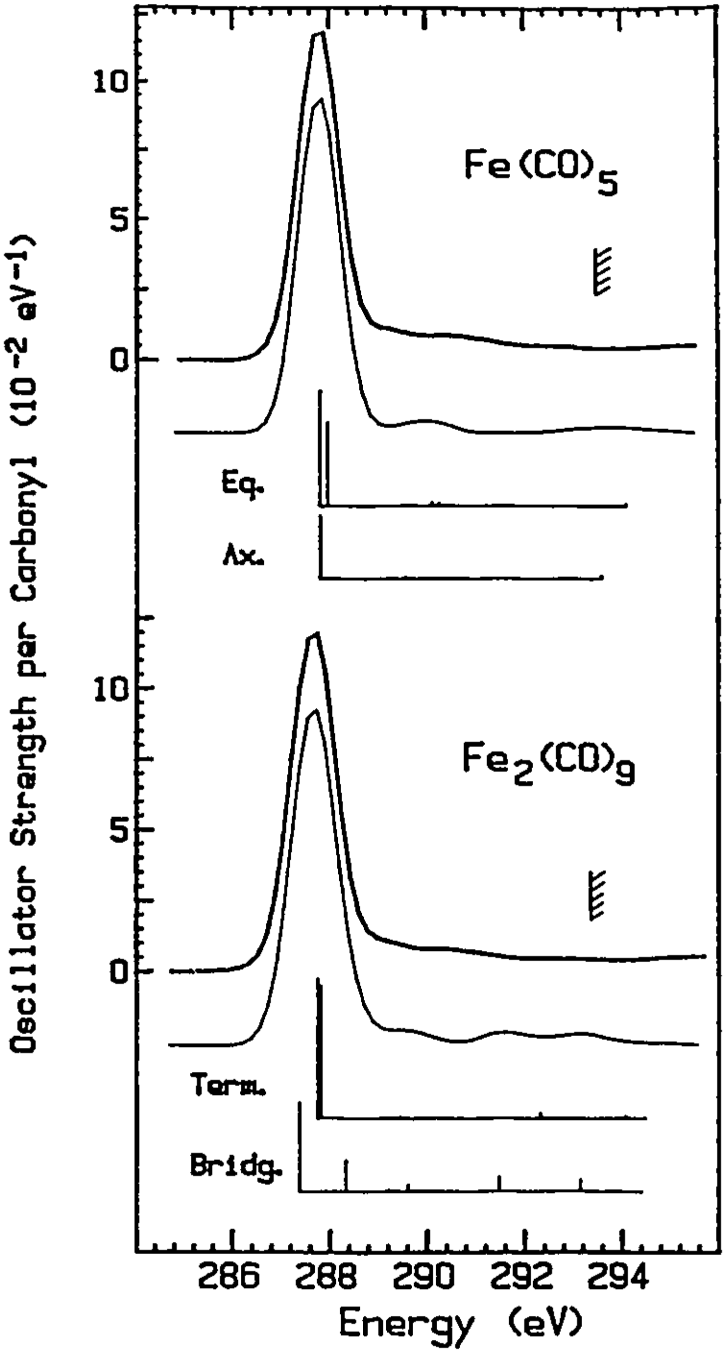

Fig. 4.3 Simulated spectra (light line) derived from EHMO calculations are compared to experimental spectra (dark line) of $Fe(CO)_5$ and $Fe_2(CO)_9$. The simulations are the weighted sum of components associated with C 1s excitation at the two different types of C atoms in each species. The absolute energy scale of the weighted sum was set by aligning the main peak in the simulation to the main C 1s → π^* peak in the experimental spectrum. The intensity of the EHMO-simulated spectrum was established by matching the main π^* peak area to the experimental value. The vertical lines under the simulated spectra indicate the positions and relative intensities of the lines of the component spectra.

Table 4.2 Integrated Intensities (f, x10^{-2}) of 1s → π* Transitions in Organoiron Complexes

	C 1s				O 1s		
	$\pi^*(CO)^a$				$\pi^*(C=O)^a$		
Species	π^*_{local}	$\Sigma\pi^*_{delocal}$	$\Sigma\pi^*_{(C=O)}$	$\pi^*_{(C=C)}{}^a$	π^*_{local}	$\pi^*_{delocal}$	$\Sigma\pi^*$
CO	18.0	-	18.0	-	7.51	-	7.51
$Fe(CO)_5$	14.9	2.8	17.7	-	7.20	0.58	7.78
$Fe_2(CO)_9$	16.0	2.3	18.3	-	6.25	1.70	7.95
C_4H_6				12.4			
$C_4H_6Fe(CO)_3$	13.6	2.6	16.2	12.2^b	6.41	0.49	6.90
C_6H_8				13.9			
$C_6H_8Fe(CO)_3$	(17.3)^c	(3.1)^c	(20.4)^c	12.2	5.83	0.89	6.72
C_8H_8				31.2^d			
$C_8H_8Fe(CO)_3$	(19.7)^c	(4.3)^c	(24.0)^c	17.9	5.93	1.02	6.95

a. The oscillator strengths for π*(C=O) are given per carbonyl for ease of comparison. The values for π*(C=C) are not normalised per C=C bond.

b. This is the area of all structure below the main π*(C=O) line.

c. These f-values are believed to be too high because of contributions from underlying C 1s → π*(C=C) transitions.

d. This value includes π*(C=C) signal which most likely underlies the π*(C=O) feature in the $C_8H_8Fe(CO)_3$ complex.

are red shifted by about 1 eV relative to free CO, as found in other 3d transition-metal carbonyls.[11,12] This is consistent with the increase in C-O bond-length and hence the weakening of the CO bond, as predicted by the dπ-pπ back-donation model for bonding of CO to metals.[106] The σ^* shape resonance is considerably broader than that in free CO. This could be related to the existence of numerous closely-spaced final states in this region. Alternatively the σ^* resonances of metal carbonyls could decay into the direct C 1s ionisation continuum more rapidly than in free CO. The photoelectron at the metal carbonyl σ^* peak has several eV greater kinetic energy than in CO since the C 1s IP of the metal carbonyls is about 2 eV below that of free CO.[92] This should result in an increase of 2 eV in the resonance width according to a published correlation between photoelectron energy and resonance width.[107] This is in reasonable agreement with the observed increase in resonance width.

§4.3.2 Iron Tricarbonyl Complexes with Unsaturated Hydrocarbon Ligands

The C 1s spectra of three organoiron complexes [RFe(CO)$_3$, R = butadiene, cyclohexadiene and cyclooctatetraene] are presented in Figure 4.4. The energies, term values and tentative assignments for the spectral features are listed in Table 4.3. The spectra of these three complexes are similar, since the main features involve excitations to virtual orbitals associated with the Fe(CO)$_3$ fragment which is common to all three species. The sharp, intense peaks at 287.7 eV are attributed to the main carbon 1s → $\pi^*(C=O)_{local}$ transition. These occur at essentially the same energy as in the pure iron carbonyl complexes. The weak feature observed around 289.7 eV in each species is attributed to C 1s → $\pi^*_{delocal}$ transitions. In the continuum there are two major σ^* shape resonances for each complex. The first resonance at 292 eV is assigned to carbon 1s excitations to a σ^* MO associated mainly with the C-C single bonds of the polyenes. The second broad band, lying between 298 and 304 eV, likely contains contributions from both $\sigma^*(C=C)$ and $\sigma^*(C=O)$ resonances, which are expected around 299 and 303 eV, respectively.

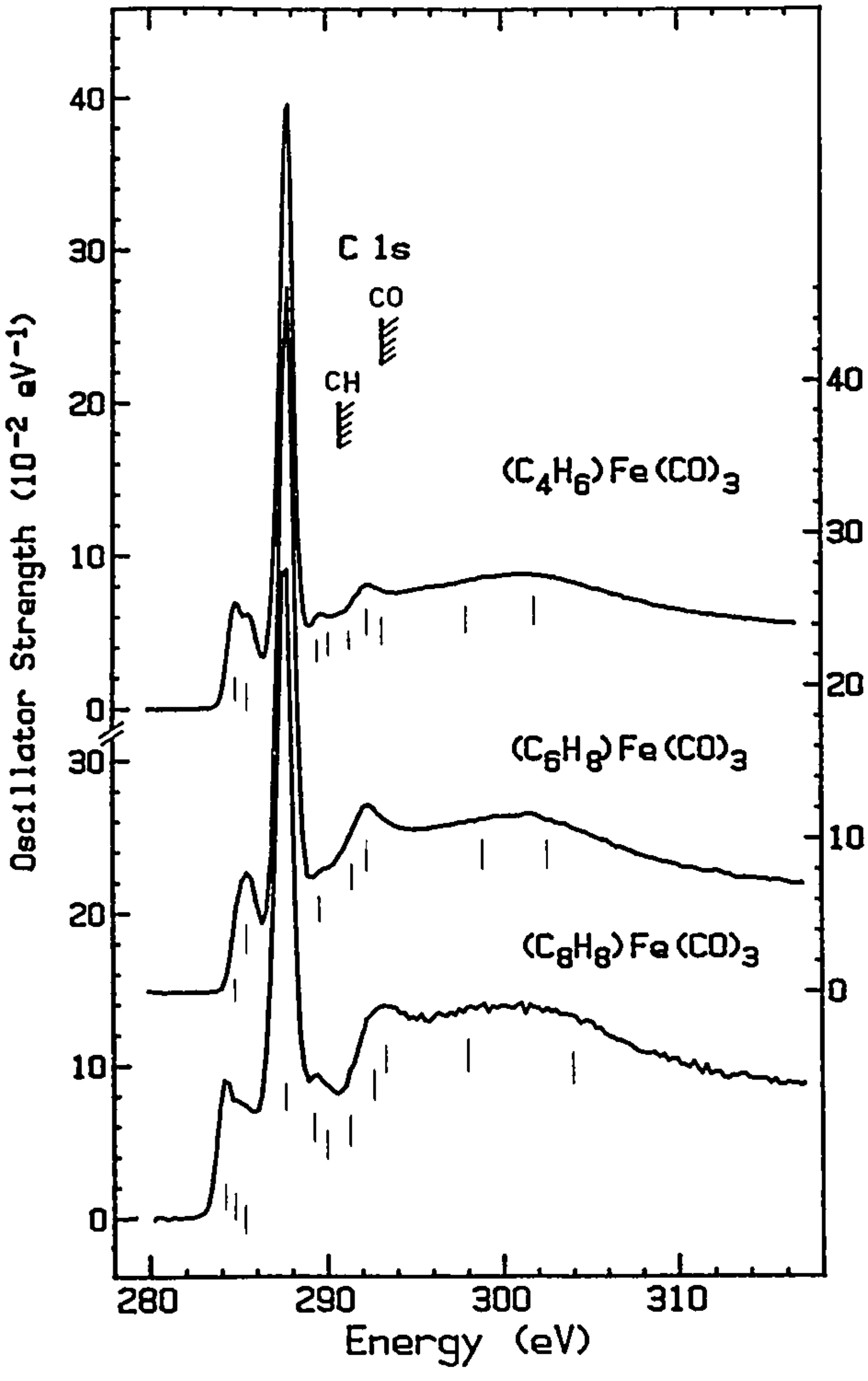

Fig. 4.4 Oscillator strengths for C 1s excitation of $(C_4H_6)Fe(CO)_3$, (c-C_6H_8)$Fe(CO)_3$ and (c-C_8H_8)$Fe(CO)_3$ derived from ISEELS spectra.

Table 4.3 Energies (E, eV), Term Values (T, eV) and Proposed Assignments for Features in the C 1s Spectra of $C_4H_6Fe(CO)_3$, c-$C_6H_8Fe(CO)_3$ and c-$C_8H_8Fe(CO)_3$

$C_4H_6Fe(CO)_3$			c-$C_6H_8Fe(CO)_3$			c-$C_8H_8Fe(CO)_3$			Assignment (final orbital)	
	T			T			T			
E	CH	CO	E	CH	CO	E	CH	CO	CH	CO
						284.2	6.2		π^*(C=C) (non-Fe)	
284.9	5.9		285.1	5.4		284.8	5.6		π^*(C=C)	
285.5	5.3		285.6	4.9		285.5	4.9		Fe 3d	
287.77^a		5.43	287.74^a		5.26	287.67^a		5.13		π^*(C=O)
289.7		3.0	289.8		3.2	289.4		3.4		$\pi^*_{delocal}$
290.2	0.6					290.1	0.3		σ^*(C-H) /Ryd	
290.8^b			290.5^c			290.4^c				IP^b(C-H)
291.6		1.6	291.5		1.5	291.4		1.4		Rydberg
292.4	-1.6		292.3	-1.8		292.4	-2.0		σ^*(C-C)	
293.2^b			293.0^c			292.8^c				IP(C=O)
						293.3	-2.9		σ^*(C-C)	
298	-7.2		299	-8.5		298	-7.6		σ^*(C=C)	
302		-8.8	303		-10	304		-11.2		σ^*(C=O)

---

a Calibration relative to CO_2: ΔE = -2.97(4), -3.00(3), -3.07(3) eV for $C_4H_6Fe(CO)_3$, c-$C_6H_8Fe(CO)_3$ and c-$C_8H_8Fe(CO)_3$, respectively.

b IPs from XPS.[92]

c IPs estimated from those of related species ($C_7H_8Fe(CO)_3$).[92]

According to literature MO schemes[103] the LUMO of $RFe(CO)_3$ is concentrated mainly on the diene portion of the complex, while the next-to-LUMO is concentrated at the Fe metal. Consequently, the lowest-energy features in the C 1s spectra of each complex [e.g. that at 284.9 eV in $C_4H_6Fe(CO)_3$] are assigned to C 1s → $\pi^*(C=C)$ transitions. For the c-C_6H_8 complex this feature only appears as a weak shoulder on the low-energy side of the first peak, and is not as well-resolved as in the spectra of the C_4H_6 and c-C_8H_8 derivatives. Above the feature associated with the LUMO, there is another feature peaked at 285.5 eV. This is assigned to C 1s excitations to the next-to-LUMO, a MO that is based largely on the Fe atom. The C 1s spectrum of $CpCo(CO)_2$ (Chapter 3) greatly resembles that of c-$C_6H_8Fe(CO)_3$ in this low-energy region. It seems that ligands having a 5- or 6-member ring structure, such as $C_5H_5^-$ and c-C_6H_8, mix effectively with the metal 3d orbitals of the $M(CO)_n$ fragment resulting in spectra which exhibit unresolved, broad band-like peaks formed by the overlap of several transitions.

The η^4-bonding between the metal and the unsaturated hydrocarbon ligands (R) is through electron donation from a diene to the $Fe(CO)_3$ fragment, which is a good acceptor by virtue of its three CO ligands. Thus, as in $CpCo(CO)_2$, a net charge transfer from the dienes to the carbonyls is expected in all three of these complexes. Can we see spectral modifications reflecting this charge transfer, similar to those which have been identified in the C 1s spectrum of $CpCo(CO)_2$? The effects of ligand-ligand interactions in mixed ligand complexes should be best identified by comparison of the experimental spectrum with that of a weighted sum of the carbon 1s spectra of FeR_2 and $Fe(CO)_5$. However, although the spectra of the free hydrocarbon ligands are available, the FeR_2 complexes which would be required to characterise the Fe-R bonding interaction are not known. Instead we have prepared simulations which are the sum of the C 1s spectrum of the free diene ligand [14,61,42] with 0.6 times that of $Fe(CO)_5$. Figure 4.5 compares the discrete region of the experimental carbon 1s spectra with these experimentally derived spectral simulations. Such simulations should give insight into the modifications of the virtual orbitals of the R group caused by metal-ligand interaction. It should also provide

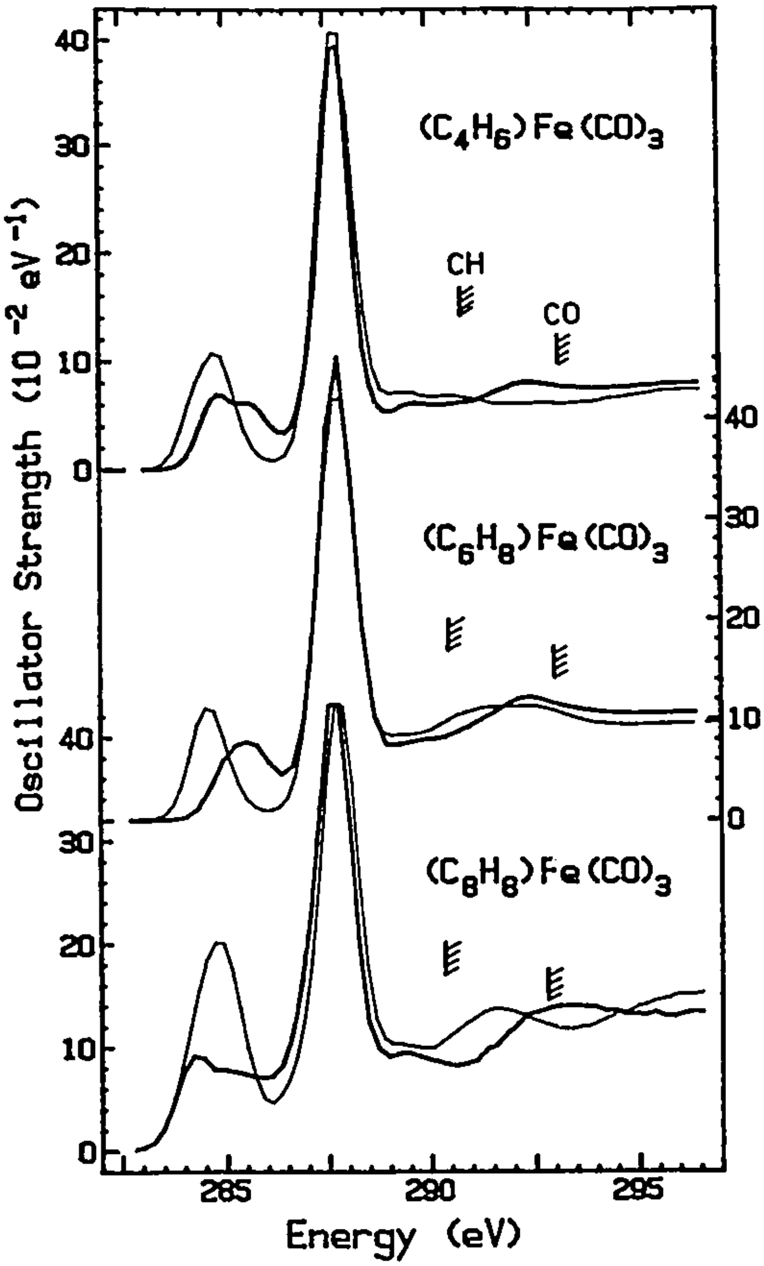

Fig. 4.5 Comparison of the experimental C 1s spectra (dark line) of $RFe(CO)_3$ (R = butadiene, 1,3-cyclohexene and cyclooctatetraene) and simulations generated by summing the C 1s spectrum of R with 0.6 times that of $Fe(CO)_5$ (light line).

some information concerning the effects of ligand-ligand interaction on the carbonyl orbitals.

The simulation of the $C_4H_6Fe(CO)_3$ complex supports assignment of the lowest energy peak to the C 1s → π^* transition on the diene ligand but it does not predict the 286 eV feature which we have attributed to excitations to Fe-3d-dominated MOs. This is understandable since a simulation consisting of the spectrum of free ligand R and $Fe(CO)_5$ can not be expected to predict spectral features associated with Fe-R antibonding levels. Thus, the comparison predicts that the carbon 1s spectrum of the hypothetical species $Fe(C_4H_6)_2$ should contain a 286 eV feature associated with R-Fe bonding. This feature would be analogous to the C 1s → $4e_{1g}$ ($3d_{xz,yz}$) transition in the metallocenes[13] and thus we label such transitions "$4e_{1g}$" to emphasize the analogy with ferrocene. In all three species the diene-metal interaction causes a marked suppression of the C 1s → π^* intensity on the diene and introduction of one or two additional levels at slightly higher energy, apparently of mixed π^*(C=C) and Fe-3d character. The discrepancy between simulation and experiment is greatest for the c-C_8H_8 complex, implying a stronger interaction between the c-C_8H_8 and $Fe(CO)_3$ fragments than in the other two species. According to the simulation, the spectrum of c-$C_8H_8Fe(CO)_3$ should be much more intense in the diene π^* region than observed. Cyclooctatetraene (COT) has 3 low-energy π^* resonances at 284.8, 287.3 and 289.3 eV.[42] Since the η^4-diene bonding involves only two of the four C=C bonds in COT, the π^* orbitals associated with those two bonds should mix more extensively with the Fe 3d orbitals than those associated with the two C=C bonds which are remote from the iron. There is negligible delocalization in COT due to the non-planar structure. Thus it is conceivable that part of the π^* density is rather similar to that in free COT, giving rise to the low energy π^*(C=C) structure at 284.2 eV which is much less intense but otherwise similar to the lowest π^* feature in COT (284.8 eV). The π^*(C=C) MOs at the η^4-bond are modified extensively through mixing with Fe 3d. The latter would then give rise to the features at 284.8 and 285.5 eV, which are similar to those observed in the spectra of the other Fe-diene complexes.

The C 1s → $\pi^*(C=O)_{local}$ transition is much more intense than the C 1s → $\pi^*(C=C)$ transition. Why? $\pi^*(C=C)$ resonances are intrinsically weaker than those $\pi^*(C=O)$ resonances.[71] This difference is further magnified because Fe 3d orbitals mix better with $\pi^*(C=C)$ than with $\pi^*(C=O)$ MOs owing to more appropriate spatial and energy matches between Fe 3d and the diene π^* orbitals. Strong backdonation of metal 3d density into the empty π^* orbital of the polyene can be thought of as "blocking" the promotion of the carbon 1s electron into this π^* orbital, thus diminishing the transition probability. Less pictorially, but more correctly, the reduced intensity is associated with changes in the orbital mixing which result in a smaller C 2p contribution to the dπ-pπ orbital. This point is well illustrated by Fig. 4.5 —— in each species the experimental feature associated with $\pi^*(C=C)$ is much weaker than predicted by the simulation.

We expect the $RFe(CO)_3$ spectra to be influenced by charge transfer between the donating diene and the accepting carbonyls. From analogy to $CpCo(CO)_2$, notable effects should include a weaker $\pi^*(CO)$ resonance and a stronger "$4e_{1g}$" peak, than in the FeR_2 and $Fe(CO)_5$ complex. Although we cannot compare to FeR_2, a comparison of the $\pi^*(CO)$ intensity of $Fe(CO)_5$ with that of the $RFe(CO)_3$ complexes should be sensitive to the ligand-ligand interaction. The integrated $\pi^*(CO)$ oscillator strength (per carbonyl) for all species are summarised in Table 4.2. While the precision of the peak integration is not high because of its sensitivity to details of background subtraction, the results do seem to support the expected charge transfer in $C_4H_6Fe(CO)_3$. The evidence is contradictory in the other two $RFe(CO)_3$ complexes. In these other species $f(\pi^*_{CO})$ is greater than in free CO, presumably because of contributions from underlying C 1s → $\pi^*(C=C)$ transitions on the C_6H_8 and C_8H_8 ligands.

§4.3.3 Substituted Ferrocenes

The carbon 1s spectra of $FeCp_2$ and the two ring-substituted ferrocenes are presented in Figure 4.6. Energies, term values and proposed assignments are given in

Table 4.4. This comparison shows directly that substituents on the Cp ring have little influence on the basic electronic structure of ferrocene, since the spectra of all three species exhibit the four major spectral features of ferrocene. There is an additional low-energy feature in the spectrum of CpFeCp-C_2H_3 which is associated with C 1s → π^* transitions at the vinyl substituent. The C 1s excitations at the butyl substituent do not appear to give rise to distinct features but changes in the relative intensities of the four ferrocene features are consistent with broad underlying bands at the positions expected from the carbon 1s spectrum of butane.[41] The sharp peak at 285.6 eV is assigned to C 1s → $4e_{1g}(3d_{xz,yz})$ in ferrocene[11] and to a "$4e_{1g}$-like" orbital in the other two species. The main line at 287 eV is attributed to C 1s → π^*(Cp) transitions. Just below the ionization potential there are weak structures between 288 and 289 eV which are attributed to C 1s → σ^*(C-H)[41] and Rydberg transitions. These features are clearer in the spectra of the two ferrocene derivatives, perhaps because these two complexes contain more C-H bonds.

As discussed previously,[108] the strong interaction of adjacent C-C bonds in aromatic ring structures produces a large splitting in the energies of σ^*(C-C) orbitals. This leads to two prominent continuum resonances in ferrocene. The strong band at 292 eV in the continuum is assigned to ligand σ_1^*(C=C) shape resonances while the intense, broad band between 297 and 298 eV is labelled the σ_2^*(C=C) shape resonance. Both are associated with the Cp ring. For the two ring-substituted ferrocenes the continuum resonances are more intense than the 286 eV "$4e_{1g}$-like" excitation, whereas the opposite is the case for ferrocene. Since the intensities of the "$4e_{1g}$-like" and π^*(Cp) transitions are rather constant in all three complexes, this implies that the change in the relative intensity of discrete and continuum features is associated with more intense continuum features, consistent with additional contributions from σ^* resonances associated with the substituent C-C bonds.

The feature at 284.5 eV, a low energy shoulder to the first peak in the carbon 1s spectrum of CpFeCp-C_2H_3, is assigned to excitations to the π^* level of the vinyl

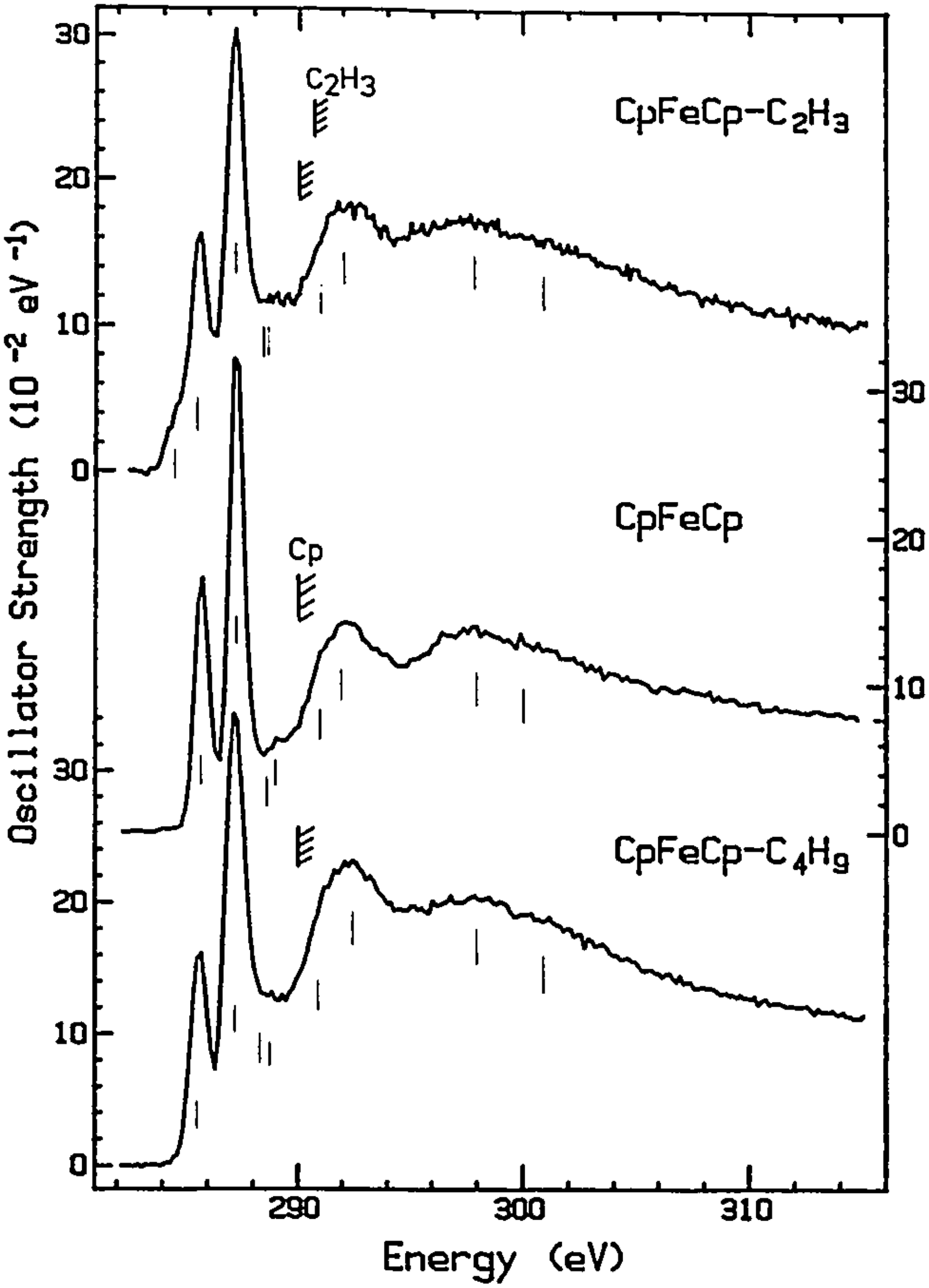

Fig. 4.6 Oscillator strengths for C 1s excitation of CpFeCp-C_2H_3 (Cp: C_5H_5), $FeCp_2$ and CpFeCp-C_4H_9 derived from ISEELS spectra.

Table 4.4 Energies (E, eV), Term Values (T, eV) and Proposed Assignments for Features in the C 1s Spectra of CpFeCp-CH=CH$_2$, CpFeCp-H and CpFeCp-C$_4$H$_9$.

CpFeCpC$_2$H$_3$			FeCp$_2$		CpFeCpC$_4$H$_9$		Assignment (final orbital)	
E	T_{Cp}	T_R	E	T	E	T	Cp	R
284.4		6.4						π*(CH=CH$_2$)
285.6	4.5		285.7	4.3	285.6	4.4	"4e$_{1g}$-like"(Fe 3d)	
287.14^a	2.91		287.21^a	2.82	287.18^a	2.82	π*(Cp)	
288.4	1.7		288.7	1.3	288.4	1.6	σ*(CH)	σ*(CH)
288.7	1.4		289.1	0.9	288.8	1.2	Rydberg	
290.0^c			290.03^b		290.0^c		IP(Cp)	
290.8^c								IP(C$_2$H$_4$)
291.4	-1.4		291.1	-1.1	291.2	-1.2	double excitation	
292.3	-2.3		292.2	-2.2	292.4	-2.4	σ_1*(C=C)	σ*(C-C)
298	-8		298	-8	298	-8	σ_2*(C=C)	σ*(C=C)
301	-11		300	-10	301	-11.2	shake-up	

---

a Calibration relative to CO$_2$: $\Delta E = -3.60(4), -3.53(2), -3.56(3)$ eV for CpFeCp-CH=CH$_2$, FeCp$_2$ and CpFeCp-C$_4$H$_9$, respectively.

b IPs from XPS.[92]

c IPs assumed to be the same as ferrocene and ethene.

substituent. Spectral simulation supports this assignment. In Fig. 4.7 the experimental spectra of both derivatives are compared to simulations created from the sum of the C 1s spectrum of the ring substituent (ethene[71] and butane[41]) and that of $Fe(Cp)_2$. The simulation suggests that the lowest-energy $\pi^*(C=C)$ feature of $CpFeCp$-C_2H_3 should be more intense than observed. This indicates there is significant interaction between the vinyl $\pi^*(C=C)$, the $\pi^*(Cp)$ and the Fe 3d orbitals such that the contribution of carbon 2p orbitals of the vinyl substituent to the "$\pi^*(C=C)$" is considerably less than in free ethylene. Overall the simulated spectrum of $CpFeCp$-C_2H_3, although it does predict all major spectral features, has significant disagreement regarding relative intensities. This is expected, since the vinyl substituent interacts with the Fe 3d orbitals through the Cp ring ligand, an effect which this type of simulation can not be expected to reproduce. The simulated and experimental spectra of $CpFeCp$-C_4H_9 are in much better agreement. This may be interpreted in terms of a poor energy as well as spatial match and thus less mixing between the Fe 3d orbitals and the virtual orbitals of the alkyl group relative to that with the $\pi^*(C=C)$ orbitals. This observation is consistent with that of Waite and Popadopoulis[109] who note that a vinyl has a much larger effect than a methyl substituent on the polarizability and valence charge transfer excitations of substituted ferrocenes.

§4.4 O 1s Spectra

The O 1s spectra of all five oxygen-containing complexes, two iron carbonyl and three mixed ligand, are presented in Fig. 4.8, along with that of CO. The energies, term values and proposed assignments of the O 1s spectral features are given in Table 4.5. The O 1s spectra of all carbonyl complexes have very similar shapes and energies. Like the O 1s spectrum of CO, they are dominated by the intense O 1s $\rightarrow$ $\pi^*(C=O)$ transition which occurs at 533.8 eV, 0.3 eV lower than in CO, and the strong, broad $\sigma^*(C=O)$ shape resonance around 550 eV, again red-shifted relative to free CO. As discussed for the corresponding C 1s $\rightarrow$ $\sigma^*(CO)$ feature (*vide supra*), the red shift of the $\sigma^*(C=O)$ shape resonance is believed to be associated with weakening of the C=O

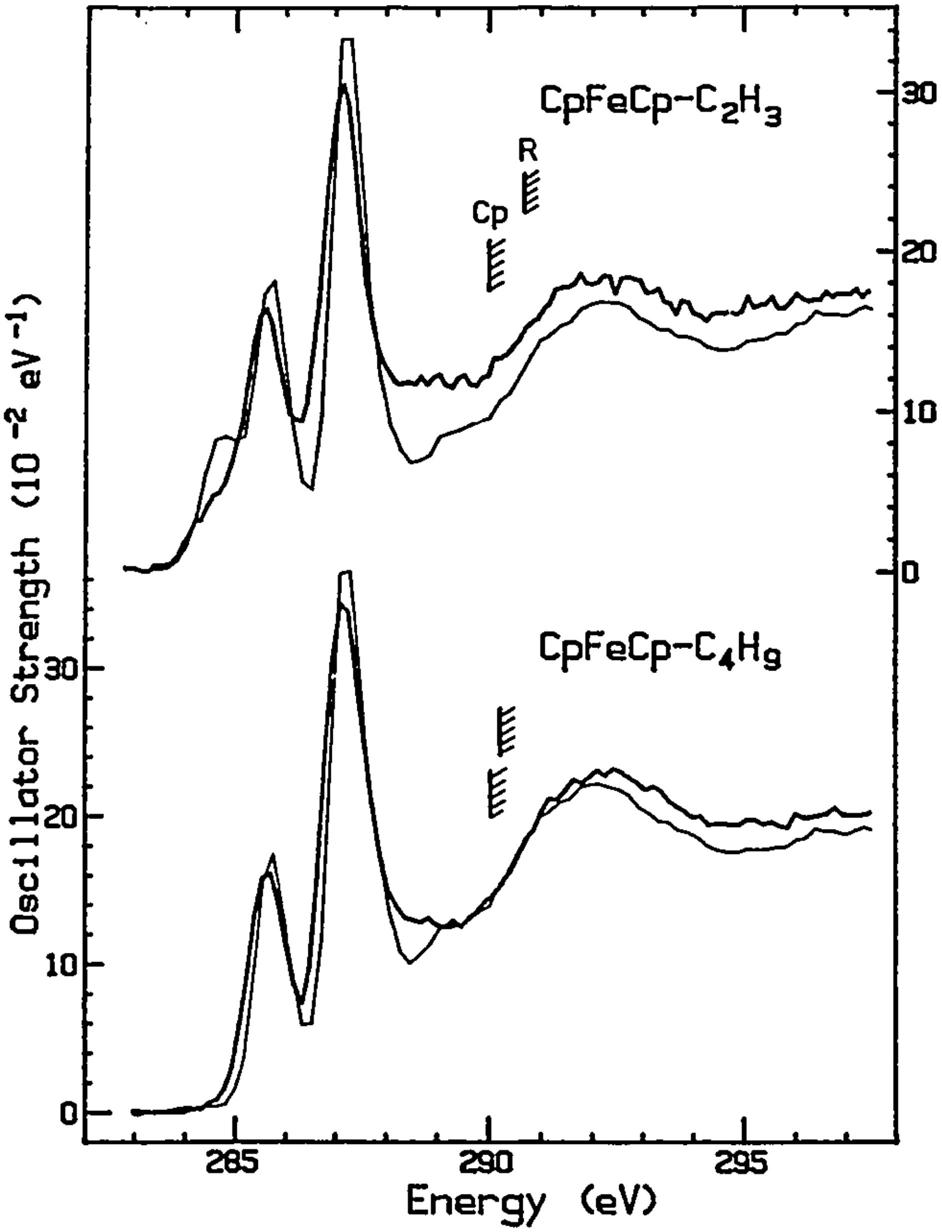

Fig. 4.7 Comparison of the experimental C 1s spectra of CpFeCp-R (R = C_2H_3 and C_4H_9) (dark line) and simulations which are the sum of the C 1s spectra of R-H (ethene and butane) and $Fe(Cp)_2$ (light line).

bond by virtue of backdonation from the iron atom. The backdonation also reduces the oscillator strength of the O 1s → π^*(C=O) transition[14] by almost 20% (note the vertical scales in Figure 4.8). The interpretation of the energy shift of the π^*(C=O) excitation has been discussed in detail previously.[11] In addition to the intense O 1s → π^*(C=O) and σ^*(C=O) resonances, weak O 1s → $\pi^*_{delocal}$ transitions can be detected around 536 eV, particularly in $Fe_2(CO)_9$ and c-$C_8H_8Fe(CO)_3$. Rydberg transitions seem to contribute around 538 eV, although they are much weaker than in the spectrum of free CO, as expected in bulky molecules by virtue of greater valence-Rydberg mixing associated with the increased density of valence MOs. Because all the oxygen atoms are at the periphery of these molecules one might expect the Rydberg contributions to be less "quenched" than at the C 1s edge. This factor is counter-balanced by the reduced size of the O 1s core orbital. The outcome seems to be a small absolute intensity but less change in Rydberg intensity from free CO at the O 1s than at the C 1s edge. Overall, all O 1s spectra look strikingly similar, not only in energy but also in relative intensity, signifying that they have essentially the same origin. This is consistent with localisation of the core excitation and very little modification of the virtual orbitals of the $Fe(CO)_3$ fragment with other changes in the molecule.

§4.5 Fe 2p Spectra

The Fe 2p spectra of all eight species are compared in Fig. 4.9. The energies, term values and proposed assignments for the spectral features are listed in Tables 4.6 and 4.7. As noted in Chapter 3 the shape of metal 2p spectra correlates closely with the type of ligands in a complex. Among these species, the Fe 2p spectra of $Fe(CO)_5$ and $Fe_2(CO)_9$ are very similar, but quite distinct from those of ferrocene and substituted ferrocenes which, in turn, are distinct from the Fe 2p spectra of the $RFe(CO)_3$ species, whose spectra are in certain ways intermediate between the spectra of the carbonyls and metallocenes. The Fe 2p spectra of $Fe(CO)_5$ and $Fe_2(CO)_9$ each exhibit a "small-big" pattern of spectral features, at both the L_3 and L_2 edges. The close similarity of the

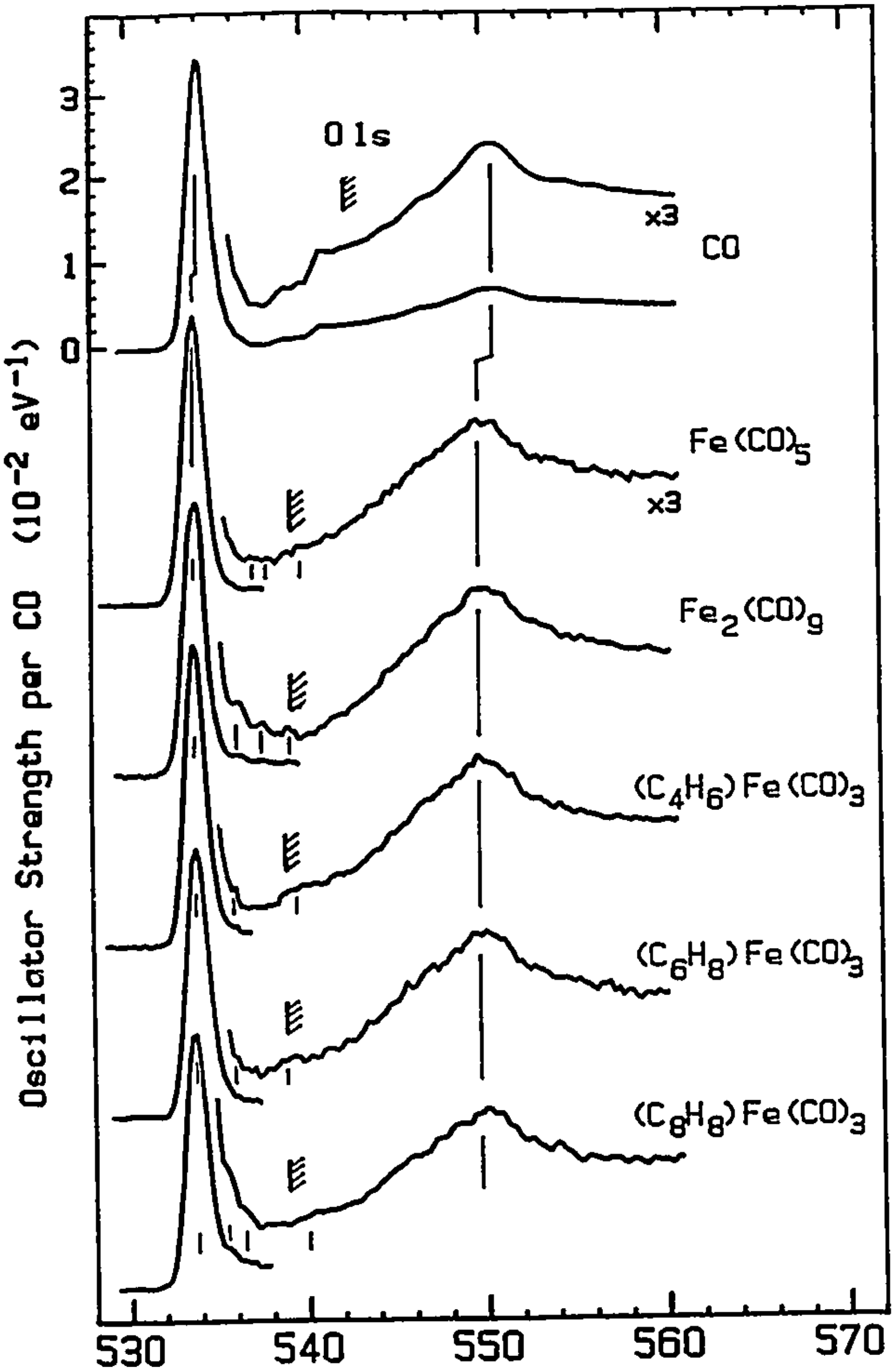

Fig. 4.8 O 1s oscillator strength spectra of CO and the five CO-containing organoiron species derived from ISEELS spectra.

Table 4.5 Energies (E, eV), Term Values (T, eV) and Proposed Assignments for Features in the O 1s Spectra of CO, $Fe(CO)_5$, $Fe_2(CO)_9$, $C_4H_6Fe(CO)_3$, c-$C_6H_8Fe(CO)_3$ and c-$C_8H_8Fe(CO)_3$.

CO		$Fe(CO)_5$		$Fe_2(CO)_9$		$C_4H_6Fe(CO)_3$		$C_6H_8Fe(CO)_3$		$C_8H_8Fe(CO)_3$		Assignment
E	T	E	T	E	T	E	T	E	T	E	T	(final orbital)
534.1	8.3	533.8[a]	5.7	533.9[a]	5.8	533.9[a]	5.1	533.9[a]	5.2	533.7[a]	5.4	$\pi^*(C{=}O)$
		536.0	3.5	535.7	4.0					535.3	3.8	$\pi^*_{delocal}$
		537.2	2.3	537.0	2.7	536.0	3.0	535.9	3.2	536.3	2.8	$\pi^*_{delocal}$
										536.9	2.2	$\pi^*_{delocal}$
541.0	1.4	538.1	1.4	537.9	1.8	538.0	1.0	537.8	1.3	537.6	1.5	Rydberg
542.4[b]		539.5[b]		539.7[b]		539.0[b]		539.0[c]		539.0[c]		IP
		546.4	-6.9	547.1	-7.4	546.4	-7.4	545.6	-6.6	545.0	-6	double excitation
550.9	-8.5	549.7	-10	549.5	-9.8	549.7	-11	550	-11	550	-11	$\sigma^*(C{=}O)$

[a] Calibration relative to CO_2 (O 1s → π*: 535.4 eV): ΔE = -1.60(6) and -1.50(8) eV for $Fe(CO)_5$ and $Fe_2(CO)_9$, respectively. Calibration relative to O_2 (530.8 eV): ΔE = 3.07(7), 3.10(7) and 2.90(8) eV for $C_4H_6Fe(CO)_3$, $C_6H_8Fe(CO)_3$ and $C_8H_8Fe(CO)_3$ respectively.

[b] IPs from XPS.[92]

[c] Estimated from the O 1s IP of $C_4H_6Fe(CO)_3$.

shape of the L_3 and L_2 edge features is characteristic of the metal 2p spectra of all near-covalent complexes.[18] This is in distinct contrast to the spectra of ionic complexes and the predictions of crystal field calculations, where there are major differences between the L_3 and L_2 components.

The apparently strong "ligand-sensitivity" of metal 2p spectra has been noted previously[18] and a simple MO-based explanation has been proposed (see Chapter 3). It suggests that transition-metal 2p excitation is closely related to the type of metal-ligand bonding, and that this is a more important factor than the d-electron count or molecular symmetry, which are traditionally used to explain the electronic structure and spectra of organometallic complexes. In contrast to this qualitative MO model, de Groot *et al*[81,110] have emphasized atomic multiplet effects and the importance of crystal field strength as determinants of metal 2p spectral shapes. Since the crystal field strength (as expressed by the 10Dq parameter of octahedral fields for example) is closely related to the charge or dipole character of the ligands, the MO and crystal field models are not necessarily mutually incompatible. The challenge is to devise ways of using comparisons between theoretical calculation and experimental spectra recorded at modest resolution to distinguish the relative importance of multiplet, crystal field and MO concepts in determining the metal 2p spectra of covalent complexes. As a step towards this goal, we have compared the experimental 2p spectra of $Fe(CO)_5$ and $Fe_2(CO)_9$ with EHMO calculations and the best estimate from the literature reports of the atomic multiplet calculations.[110]

The iron 2p spectra of $Fe(CO)_5$ and $Fe_2(CO)_9$ spectra are re-presented on an expanded scale in Fig. 4.10, in comparison to the spectrum of Fe^{2+} (d^6) in an O_h field with 10Dq = 1.2 eV, calculated by the atomic multiplet theory,[110] and to simulations derived from EHMO calculations of these carbonyl complexes. The atomic-multiplet-based prediction spectrum has been smoothed slightly from the literature presentation to account for the experimental resolution. The EHMO-based simulated Fe 2p spectra were generated as for the C 1s simulated spectra except that c^2(Co3d) determined the

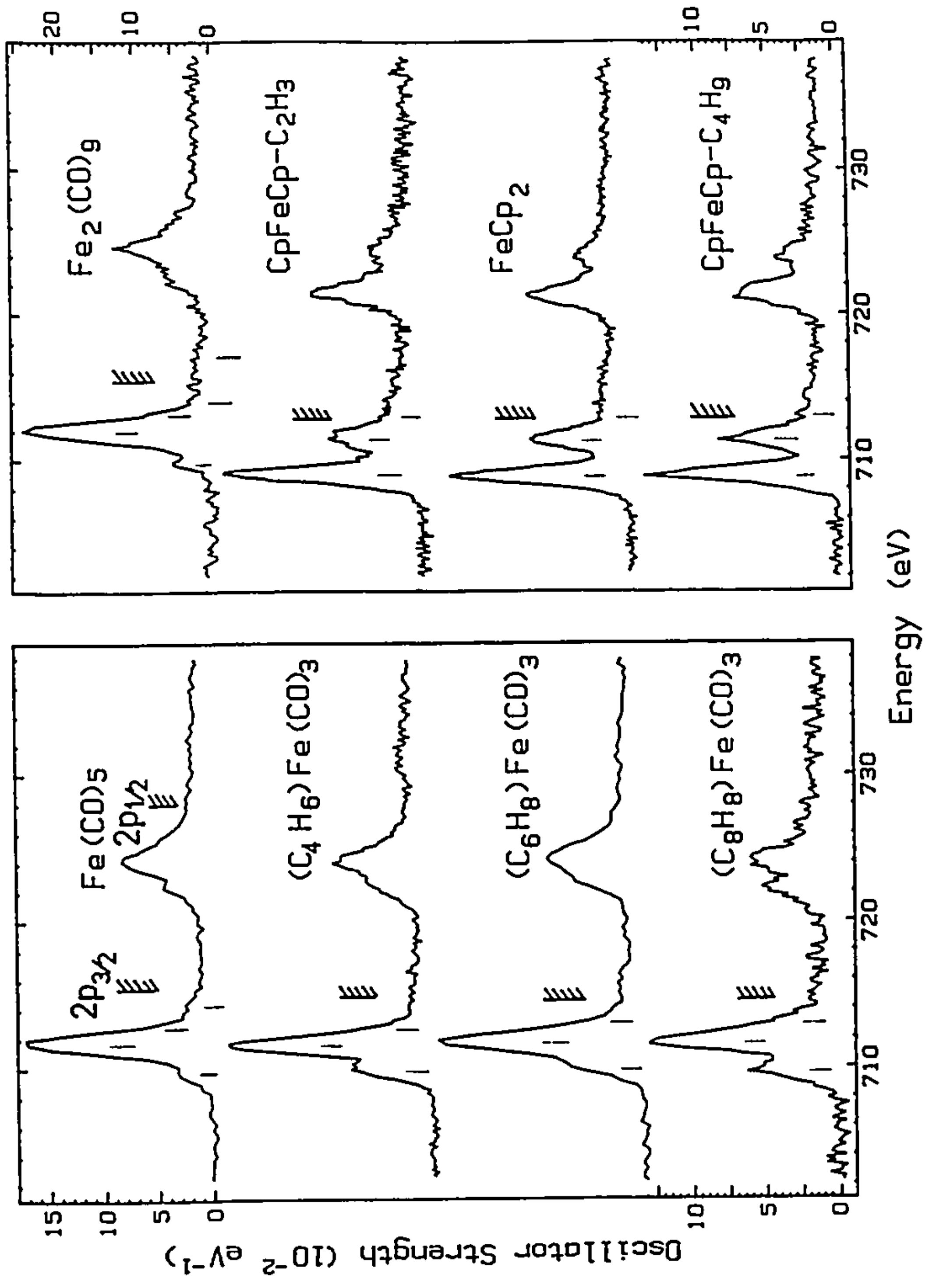

Fig. 4.9 Fe 2p oscillator strength spectra of the eight organoiron complexes, derived from ISEELS spectra. The hatched lines indicate the location of the Fe L_3 ($2p_{3/2}$) ionization potentials as measured by XPS[72] or estimated from similar species.

Table 4.6 Energies (E, eV), Term Values (T, eV) and Proposed Assignments for Featunres in the Fe 2p Spectra of $Fe(CO)_5$, $Fe_2(CO)_9$, $C_4H_6Fe(CO)_3$, c-$C_6H_8Fe(CO)_3$, c-$C_8H_8Fe(CO)_3$

$Fe(CO)_5$		$Fe_2(CO)_9$		$C_4H_6Fe(CO)_3$		$C_6H_8Fe(CO)_3$		$C_8H_8Fe(CO)_3$		Assignment final orbital
E	T	E	T	E	T	E	T	E	T	
L_3:										
709.9	5.8	709.9	5.6	709.9	4.9	710.0	4.5	709.8	4.8	Fe3d
711.8[a]	3.9	712.1[a]	3.4	711.7[a]	3.1	711.6[a]	2.9	711.6[a]	3.0	$\pi^*(CO)$
712.9	2.8	713.2	2.3	712.8	2.0	713.2	1.3	713.2	1.4	$\pi^*(CO)$
714.5	1.2	714.1	1.4							Ryd
715.7[b]		715.5[c]		714.8[b]		714.46[b]		714.6[d]		$2p_{3/2}$ IP
		717	-1.5							double excitation
L_2:										
722.5	5.6	722.5	5.5	722.7	4.7	722.5	4.5	722.3	4.7	Fe 3d
724.2	3.9	724.6	3.4	724.2	3.2	724.3	2.7	724.2	2.9	$\pi^*(CO)$
725.4	2.7	726.0	2.0	725.2	2.2	725.8	1.2	725.3	1.8	$\pi^*(CO)$
728.1		728.0		727.4		727.0		727.1		$2p_{1/2}$IP[e]
728.6	-0.5	728.5	-0.5							double excitation

a Calibration relative to CO_2 (O 1s → π^*: 535.4 eV): ΔE = 176.4(3), 176.7(2) and 176.3(2) eV for $Fe(CO)_5$, $Fe_2(CO)_9$ and $C_8H_8Fe(CO)_3$. Calibration relative to SF_6 (F 1s → a_{1g}: 688.27 eV): ΔE = 23.33(2) eV for $C_4H_6Fe(CO)_3$; to the O 1s → $\pi^*(CO)$ of the same species ΔE = 177.9(3) eV for c-$C_6H_8Fe(CO)_3$.

b IP from XPS[92].

c IP assumed the same as $Fe(CO)_5$.

d IP estimated from values for the other $RFe(CO)_3$ species.

e Derived from the L_3 IP by addition of the separation of the main L_3 and L_2 excitation peaks.

intensity (peak area). The peak widths in the $Fe(CO)_5$ EHMO-based simulation were 0.7 eV except for the peak at 716 eV for which a 4 eV fwhm linewidth was assumed. The peak widths in the $Fe_2(CO)_9$ EHMO-based simulation were 1.0 eV except for the 716 eV peak where a linewidth of 2.0 eV was used. The atomic multiplet theory clearly provides a superior representation of the spectrum even though the symmetry and ionic charge are not correct.

According to the EHMO results almost all of the low lying virtual orbitals of the iron carbonyls have a dominant π^*(CO) character with varying admixtures of Fe 3d. It is the latter which is associated with the Fe 2p spectra. A low intensity band is observed between 709 and 710 eV in the spectra of both species. However, the EHMO calculation does not predict any feature in this region for $Fe(CO)_5$ and provides only a poor match for $Fe_2(CO)_9$. In contrast the atomic multiplet calculation reproduces almost all of the structure in the experimental spectra, both in position and relative intensity. The most intense peak at 712 eV in each species is assigned to Fe 2p excitation to the Fe 3d component of the main density of π^*(CO) MOs. The EHMO results indicate the intense 712-eV peak arises mostly from excitations to a small number of π^*(CO) type MOs [2 in $Fe(CO)_5$ and one in $Fe_2(CO)_9$]. There is rather serious disagreement in the lowest energy region for $Fe_2(CO)_9$. EHMO suggests that there should be quite strong excitations to a number of molecular orbitals, the lowest energy of which is of σ^*(Fe-Fe) character. However, while the $Fe_2(CO)_9$ spectrum does have intensity in this region, so does $Fe(CO)_5$ which the EHMO simulation does not predict.

Metal carbonyls have a strong preference for the 18-e^- configuration to achieve coordinative saturation. CO ligands also favour the formation of M-M bonds[76] and metal clusters, owing to their small size and the fact that their bonds to metals are covalent rather than ionic which leaves the metal atom in an environment perhaps similar to that of the bulk metal. Cotton[105] interprets $Fe_2(CO)_9$ as having a single Fe-Fe bond. This is consistent with the short Fe-Fe distance of 2.523 Å. From the weak bond concept[91] and MO considerations a low-lying σ^*(Fe-Fe) MO of large Fe 3d character is expected in

$Fe_2(CO)_9$. Transitions to such an orbital should appear as low-lying features in the Fe 2p (as well as Fe 3p) spectra. However the experimental Fe 2p spectra do not support these concepts. It seems that either the Fe 2p → σ^*(Fe-Fe) transition is too weak to be detected or the σ^*(Fe-Fe) character is distributed over such a large number of MOs that there is very little difference from the spectrum of mononuclear metal complexes.

The crystal field/atomic multiplet approach to the 2p x-ray absorption of 3d transition-metal compounds[110] predicts that such spectra should have very complicated multiplet-line structure, typically consisting of many hundreds of lines for 3d elements such as Fe which are in the middle of the period and have a large d-count. A series of X-ray absorption metal 2p spectra of ionic complexes in the solid state at systematically increased resolution have been reported more recently.[110,111] With each improvement in resolution additional spectral detail is revealed, supporting the belief that metal 2p spectra are very complex. If this atomic-like model is relevant to covalent organoiron complexes, explaining the detailed origin of metal 2p spectra will seemingly be beyond the capabilities of EHMO. De Groot *et al*[110] and Chen *et al*[111] have presented examples of the very complex, many-line spectra that appear characteristic of the metal 2p core excitation. The multiplet-crystal field theory of de Groot *et al*[110] seems to be very successful in predicting the spectra of ionic 3d complexes as well as complexes with ligands such as cyanide which generate large crystal fields. The degree of relevance of this approach to the spectroscopy of more covalent, weak crystal field transition-metal compounds remains to be determined. Certainly, inclusion of MO considerations, i.e. full ligand field theory, has been found to be important in obtaining a proper and clear understanding of the electronic structure and chemical properties of 3d transition metal complexes. It is possible however that the short range, spatially localised character of inner-shell excitation could mean that the 3d density in the region of the compact 2p core orbital is adequately described by a theory which only considers the net effective charge that the ligands present to the small-R region of the Fe 3d orbitals. In that case, crystal field theory could be adequate.

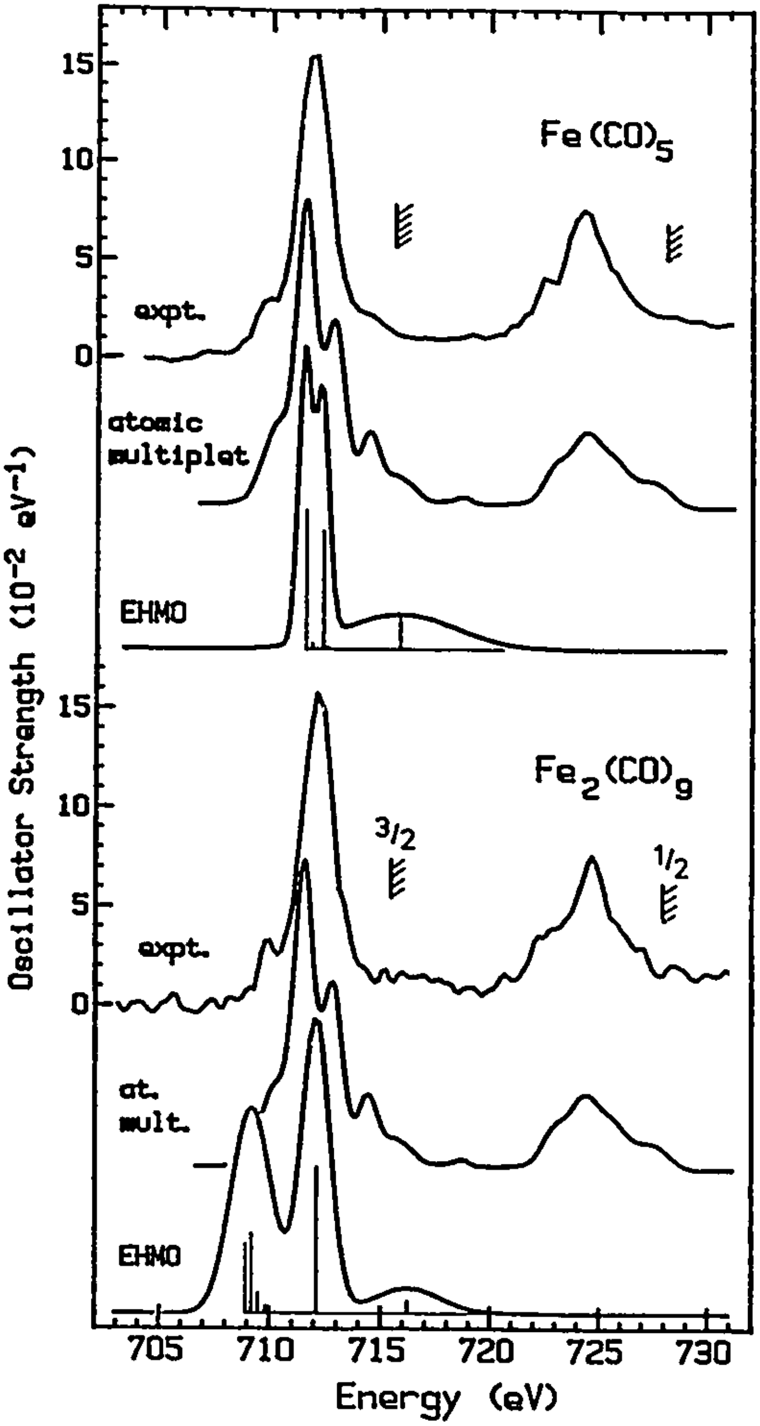

Fig. 4.10 Comparison of the experimental Fe 2p spectra of $Fe(CO)_5$ and $Fe_2(CO)_9$ with EHMO spectral simulations of these species and the atomic multiplet calculation for Fe^{2+} (d^6) in an O_h field with 10Dq = 1.2[110]. In the EHMO simulation the relative intensities are established from Σc^2(Co 3d) and the individual linewidths are 0.7 eV (4 eV for the 715 eV peak) for $Fe(CO)_5$ and 1.0 (2 eV for the 715 eV peak) for $Fe_2(CO)_9$. The main line of the EHMO calculation is aligned with the main peak of the experimental spectrum. The digitized atomic multiplet spectrum[110] has been smoothed in order to better match our experimental resolution and shifted by 1.6 eV to align the main L_3 peak. For both predicted spectra the intensity scale was calibrated from the area of the experimental spectrum between 707 and 716 eV.

The Fe 2p spectra of the three $RFe(CO)_3$ species are similar to each other and more similar to the iron carbonyls than to the ferrocenes, as found at the C 1s edge. Parallel to the carbonyls, we assign the most intense peak to Fe 2p excitations to the Fe 3d component of the π^*(CO) MOs. Weak shoulders are found around 713 eV, similar to those seen in the carbonyls. The greatest difference from the Fe 2p spectra of the carbonyls is the greater intensity and higher energy of the first band around 710 eV in the spectrum. This band also varies considerably among the three R-$Fe(CO)_3$ species. It is best resolved in $C_8H_8Fe(CO)_3$ and least well resolved in $C_6H_8Fe(CO)_3$. Clearly the first feature is more strongly associated with the π-bonded R-group than the $Fe(CO)_3$ fragment. The Fe 2p spectra of the ferrocenes have their strongest transition at 709 eV, very close to the energy of the first peak in the Fe 2p spectra of the $RFe(CO)_3$ species. The η^4 bond of dienes is similar to the η^5 bond of a Cp. Thus one might expect that the additional intensity in the 710 eV peak observed in the $RFe(CO)_3$ complexes relative to the pure iron carbonyls has an origin similar to that for the main peak in the iron 2p spectra of the ferrocenes, namely Fe 2p excitations to a molecular orbital of mainly Fe 3d character but with admixture of $\pi(C=C)$. In addition, the three $RFe(CO)_3$ complexes dispay small variations in the shape of the 710-eV peak which are rather similar to the variations in the shapes of the lowest energy peak in the carbon 1s spectra of the same species. This suggests that the $\pi^*(C=C)$ and "$4e_{1g}$"-like orbitals, which are believed to be relevant in the C 1s spectrum are also the final orbitals in the lowest energy Fe 2p excitations. However, it is the Fe 3d component of these orbitals rather than the C 2p component which determines the relative intensity. Higher resolution ISEELS or X-ray absorption spectra would be very useful to further investigate the parallels between the C 1s and Fe 2p spectra.

The dramatic change between the Fe 2p spectra of the ferrocenes and the iron carbonyl complexes well illustrates the strong dependence of the Fe 2p spectra on ligand type. Again, the spectra of the three ferrocene complexes are quite similar, indicating that alkyl or vinyl substitution has very little influence on Fe 2p excitation of ferrocene.

Table 4.7 Energies (E, eV), Term Values (T, eV) and Proposed Assignments for Features in the Fe 2p Spectra of $\mathrm{CpFeCp\text{-}CH{=}CH_2}$, $\mathrm{FeCp_2}$ and $\mathrm{CpFeCp\text{-}C_4H_9}$.

$\mathrm{CpFeCpC_2H_3}$		$\mathrm{FeCp_2}$		$\mathrm{CpFeCpC_4H_9}$		Assignment
E	T	E	T	E	T	(final orbital)
L_3						
709.1[a]	3.9	708.9[a,b]	4.1	708.9[a]	4.1	"$4e_{1g}$-like" (Fe 3d)
711.7	1.3	711.5	1.5	711.3	1.7	"$3e_{2u}$-like" (Cp π^*)
713.0[c]		713.05[d]		713.0[c]		$2p_{3/2}$IP
L_2						
721.4	3.9	721.2	4.2	721.2	3.9	"$4e_{1g}$-like" (Fe 3d)
724.2	1.1	723.9	1.5	723.8	1.5	"$3e_{2u}$-like" (Cp π^*)
725.3		725.4		725.3		$2p_{1/2}$IP[e]

a Calibration relative to $\mathrm{CO_2}$ (O 1s → π^*: 535.4 eV): ΔE = 173.7(3), 173.5(4) and 173.5(2) eV for $\mathrm{CpFeCp\text{-}CH{=}CH_2}$, $\mathrm{FeCp_2}$ and $\mathrm{CpFeCp\text{-}C_4H_9}$, respectively.

b Note these values are values are 0.6 eV higher than those reported previously[18] owing to an accurate recalibration.

c IPs estimated from that of $\mathrm{Fe(Cp)_2}$.[92]

d IP from XPS.[92]

e Derived from the L_3 IP by addition of the separation of the main L_3 and L_2 excitation peaks.

This could be a consequence of the large distance between the Cp-substituents and the Fe 3d orbitals directly involved in the Fe 2p excitation. The most intense peak at 709 eV is attributed to Fe 2p → "$4e_{1g}$-like" transitions, since simple MO concepts and EHMO calculations[13,18] indicate these orbitals have a large Fe 3d contribution. The less intense peak around 711 eV is ascribed to Fe 2p → "$3e_{2u}$-like" excitations. The $3e_{2u}$ MO is localized largely on the Cp rings of the molecule. Thus, this excitation has metal-to-ligand charge-transfer character.[18] While the reduced symmetry of the substituted ferrocenes should split the degeneracy of both the "$4e_{1g}$-like" and "$3e_{2u}$-like" MOs, there is no clear indication of this effect. A pseudo-degenerate character of these virtual MOs is suggested by valence excitation spectroscopy of ring-substituted ferrocenes.[74] The latter work showed that substituted ferrocenes have similar electronic structures to that of $Fe(Cp)_2$ and that substituents cause very small energy shifts but no changes in orbital ordering.

§4.6 Fe 3p Spectra

The Fe 3p spectra of the eight complexes are presented in Figure 4.11 on a common energy scale. A smooth background extrapolated from the underlying valence-shell continuum has been subtracted. No attempt was made to convert these spectra to oscillator strength scales or to derive a detailed assignment. Broadly, the Fe 3p spectra are characterized by two features. The peak at 60 eV occurs below the 3p IP which is expected around 66 eV.[112] This peak likely arises from Fe 3p excitations to the Fe 3d component of the lower energy MOs responsible for the Fe 2p structure. It is possible the individual transitions making up this feature have non-symmetric Fano lineshapes. Evidence for this has been presented in studies of the momentum transfer dependence of the Ni 3p edge of solid nickel,[113] and the calculations of van der Laan[114] predict significant interaction between the 3p excited states and the underlying 3d continuum, the phenomenon responsible for Fano lineshapes. A broad band around 68 eV is also a common feature of all eight spectra. Both of these spectral features are likely

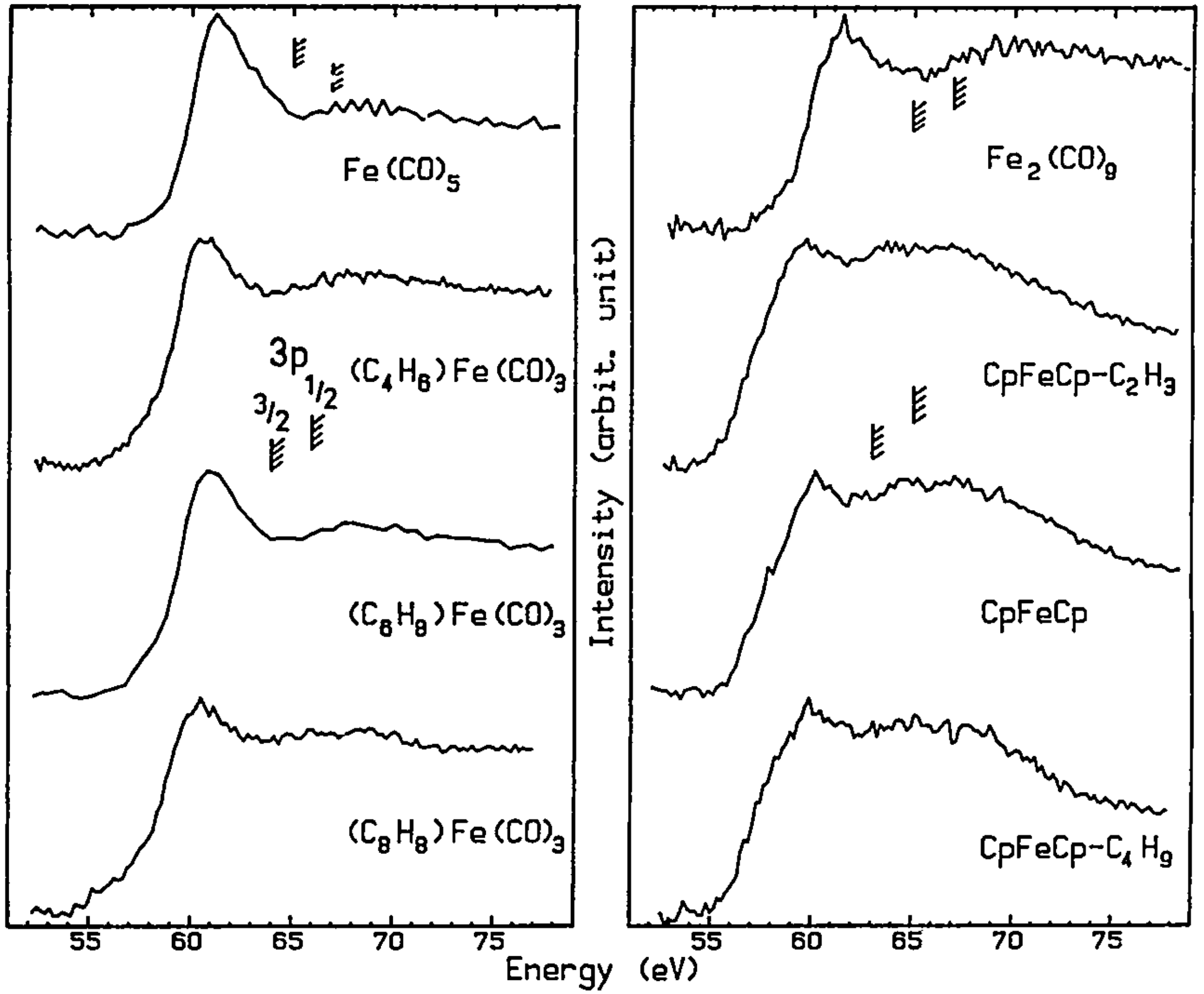

Fig. 4.11 Fe 3p energy-loss spectra of the eight organoiron complexes. A smooth curve extrapolated from the valence continuum background has been subtracted from each spectrum. The S:B at the Fe 3p edge was typically 1:10. The hatched lines indicate the $3p_{3/2}$ and $3p_{1/2}$ IPs estimated from the atomic 3p IP[112] and the chemical shifts of the $2p_{3/2}$ IPs.

comprised of a number of unresolved Fe $3p_{3/2}$ and $3p_{1/2}$ components.

As noted in the chapter 3, the shapes of the Fe 3p spectra appear to track those of the 2p spectra, with the same systematic relationship to types of ligand. In particular the 60 eV peak of the iron carbonyl complexes has an abrupt edge with a low energy shoulder, while the ferrocene complexes give rise to a more rounded peak with distinct evidence of a shoulder which could be the relatively intense low lying Fe $3p_{3/2} \rightarrow$ "$4e_{1g}$-like" peak. The shift by about 2 eV to lower energy in the Fe 3p → 3d structure in $Fe(Cp)_2$ and derivatives relative to that in the carbonyl complexes is associated with a lower Fe 3p ionisation energy, based on the 2 eV chemical shift between the Fe $2p_{3/2}$ IP of ferrocene and $Fe(CO)_5$.[92]

Very recently van der Laan[114] has predicted the metal 3p absorption spectra of 3d transition metal compounds using the atomic multiplet and crystal field description developed by de Groot *et al*[110] These calculations predict that there should be a multiple line structure but that the visibility of the individual lines is very much dependent on the experimental resolution and natural linewidth as well as the interplay of the exchange, spin-orbit and crystal field interactions for a given complex. This is well illustrated by the high resolution metal 3p spectra of the transition metal atoms[115] which shows clearly resolved multiplet structure. The crystal field calculations show that it is the overlap of the two spin-orbit components, combined with resolution limitations, which causes the M_{23} spectrum to have only one strong line, whereas the L_{23} spectrum has at least two strong lines. Interestingly, the van der Laan[114] calculations do predict a higher energy peak in the region of the broad 67 eV continuum feature. However, it is most prominent in calculations carried out with large crystal field whereas experimentally the 67 eV peak is strongest in the ferrocene complexes which should have a weaker crystal field than the carbonyl complexes.

As with the Fe 2p spectrum, comparison of the Fe 3p spectra of $Fe(CO)_5$ and $Fe_2(CO)_9$ could potentially provide evidence for excitations to σ^*(Fe-Fe) orbitals. This comparison suggests that there is an additional intensity around 58 eV in the $Fe_2(CO)_9$

spectrum relative to that of $Fe(CO)_5$. This could be evidence for Fe $3p_{3/2} \rightarrow \sigma^*$(Fe-Fe) transitions in $Fe_2(CO)_9$. However this difference is rather sensitive to details of the background subtraction and there are similar low energy shoulders in some of the other complexes containing only a single Fe atom. More convincing evidence for a M *np* → σ^*(M-M) feature has recently been observed in the Co 2p and 3p spectra of complexes containing 3 Co atoms {R-C-[$Co(CO)_3]_3$}.[116]

§4.7 Summary

The C 1s, O 1s, Fe 2p and Fe 3p spectra of eight organoiron complexes have been recorded under dipole conditions. They have been converted to oscillator strengths and assigned tentatively on the basis of spectral comparisons and simulation, EHMO calculations, and comparison with previous studies of related organometallic species as well as the free ligand molecules. Each edge in the series shows a certain pattern and reveals complementary, spatially localised, symmetry-selected information about the unoccupied electronic structure of these complexes. The carbon 1s spectra are the most sensitive to minor substituent effects, as expected since the substituents in all cases contain carbon and many of these carbon atoms are directly involved in the ligand-metal bonding. All of the O 1s spectra are quite similar, indicative of a strong chromophoric character to the $Fe(CO)_3$ fragment. The Fe 2p spectra are quite sensitive to the type of ligand but insensitive to chemical substitution at remote locations on the ligands. The Fe 3p spectra are the least informative. As in previous studies of other metal-metal binuclear complexes {$Mn_2(CO)_{10}$ [11] and $Co_2(CO)_8$}, compelling evidence for inner-shell excitations to a σ^*(Fe-Fe) MO in $Fe_2(CO)_9$ was not found. Investigations of other complexes with greater number of metal-metal bonds[116] and/or compounds with multiple metal-metal bonds are expected to be more fruitful in this regard.

Chapter 5

CORE EXCITATION OF THE MIXED LIGAND COMPLEXES $C_6H_6Cr(CO)_3$ AND CH_3-$C_5H_4Mn(CO)_3$

§5.1 Introduction

$C_6H_6Cr(CO)_3$ and $C_5H_5Mn(CO)_3$ are the well-known half-sandwich complexes (referred often as the "piano stool" compounds) which belong also to the series of compounds based upon the $M(CO)_3$ group, $C_7H_7V(CO)_3$ through to $C_3H_5Co(CO)_3$. Both of the complexes have been the subject of many theoretical and electron-spectroscopic studies,[49,78a,117-120] and have stimulated interest in investigating the chemistry of other closely-related molecules, such as species in which one or more of the hydrogen atoms on the ring are substituted by other groups. The simplest case of the ring methylation in the $M(CO)_3$-family is CH_3-$C_5H_4Mn(CO)_3$, whose occupied core and valence-shell levels have been studied extensively by photoelectron spectroscopy,[121-123] but to date experimental studies of the unoccupied valence MOs have not been reported to our best knowledge. This ring-methylated compound was chosen for further investigations of ligand-ligand interaction in mixed-ligand complexes, in part because the molecule is an iso-carbon system of $C_6H_6Cr(CO)_3$, which may be of interest in making a direct oscillator strength comparison of the C 1s excitation between these two complexes, and in part because of its high volatility, superb stability and ease of handling. In this chapter the C 1s, O 1s, metal 2p and 3p ISEELS spectra of these two compounds are reported.

§5.2 General MO Schemes of $C_6H_6Cr(CO)_3$ and CH_3-$C_5H_4Mn(CO)_3$

Benzene chromium tricarbonyl (henceforth referred to as BCT) forms yellow crystals of m.p. 165°C which are stable in air. It is one of the simplest transition metal complexes possessing simultaneously metal-carbonyl bonds and metal-organic ligand bonds, and has been studied considerably, especially by IR and Raman spectroscopy.[124] Both X-ray and neutron diffraction experiments[125] indicate that the molecule adopts a staggered conformation of C_{3v} symmetry in the solid state with the C-C bonds in the ring slightly alternate in length. The ring is planar but the hydrogen atoms are bent out of the plane towards the central Cr metal by 1.6°. In this way the carbon 2p orbitals point more towards the metal, leading to better overlap. Although there are studies of the bonding[119] and core ionization[126] for this molecule in general, relatively few papers have explored the unoccupied virtual-valence MOs. Very recently, Modelli *et al*[78a] have probed the unoccupied MO levels of BCT and its ring-methylated derivative by using electron transmission spectroscopy (ETS) and MS-Xα calculations. However, these explorations are restricted to MO levels relevant to the discrete energy region of the core-shell excitation. In this chapter we have utilized ISEELS to complement the work of Modelli *et al* and to investigate the full spectrum of unfilled MOs of BCT.

A qualitative ground-state orbital diagram of the occupied and unoccupied MOs of BCT is presented in Fig. 5.1(a), based on EHMO calculations and orbital-interaction concepts taken from Ref. 49. Figure 5.1(b) is an interaction diagram[127] for the common grouping $M(CO)_3$ with orbital occupancy for $Cr(CO)_3$. Fig. 5.1 (a) indicates that there is a major interaction between the $Cr(CO)_3$ 1e and benzene e_{2u} as well as between the $Cr(CO)_3$ 2e and benzene e_{1g} fragment orbitals. In the ground state the LUMO is formed mainly by double-degenerate orbitals (2e) of the $Cr(CO)_3$ group. However, the LUMO character is changed when an arene C 1s electron is excited. EHMO data show that when there is a core hole on the arene ring one of the doubly-degenerated MOs which are associated with the e_{2u} π^* orbitals of benzene moves downwards and becomes the new LUMO of the excited state, and simultaneously the $Cr(CO)_3$-localized MOs (2e) receive a remarkable contribution from the ring carbons. This orbital-ordering swapping arising from core excitation has been seen also in $CpCo(CO)_2$ (see Chapter 3) and is seemingly a common occurrence. Above these two sets of double degenerate e MOs are four orbitals of a symmetry, the first of which is constructed chiefly by three carbonyl π^* orbitals. At even higher energy there is a MO derived from the arene b_{2g} π^* orbital. All these virtual-valence MOs fall into a 3.8-eV range and will be responsible for the

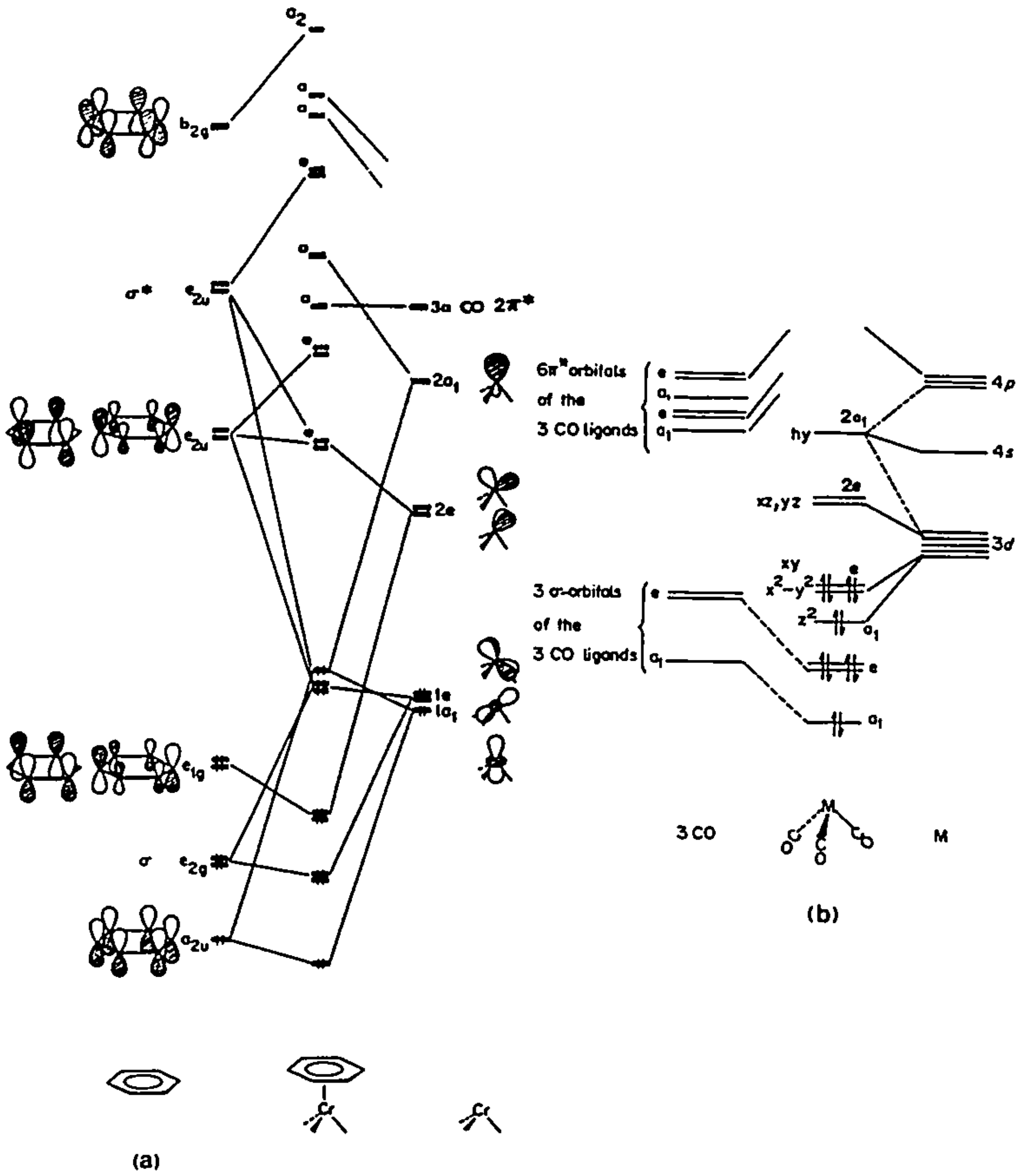

Fig. 5.1 (a) EHMO energy-level diagram showing the fragment interactions of $Cr(CO)_3$ with cyclopentadienyl unit. It was developed on the basis of Ref. 49. (b) Correlation diagram for the $M(CO)_3$ unit, and the orbital occupancy shown here is for $Cr(CO)_3$.

ISEELS features appearing in the discrete region. According to EHMO, other upper unfilled MOs are at least 8.5-eV higher in energy than the "b_{2g}-π^*" MO. They may be associated with the σ^* shape resonances in the continuum.

Methylcyclopentadienyl manganese tricarbonyl (henceforward abbreviated to MMT) is an air-stable species. Unlike solid $CpMn(CO)_3$, MMT is a yellow liquid. At first glance MMT should be like $CpMn(CO)_3$, i.e., one might expect the methylation of the Cp ring to be a minor alteration of electronic structure in spite of some resulting differences in physical properties. This seems to be the case according to the previous study of the ferrocene derivatives (see Chapter 4). It is known that CH_3 is an electron-donating group and its attachment to the Cp ligand should increase the electron charge in the ring, and hence increase the ring's net "basicity".[128] However, PES measurements of the methylated derivatives indicate that CH_3 electron-donation is a minor effect.[121,122] ETS studies of BCT and its methyl substituent also show that methylation has a rather limited effect on the electronic structure of BCT,[78a] indicating that the methylation is merely a localized perturbation and there is no appreciable orbital overlap between the methyl group and Cr metal [or more precisely, the $Cr(CO)_3$ fragment]. Therefore, one can simply use the MO picture of $CpMn(CO)_3$ directly to describe the MMT behaviour.

A simplified frontier orbital diagram for $CpMn(CO)_3$ in the ground state, along with the orbital correlation between its fragments, is given in Fig. 5.2(a). The MO structure of Cp is similar to that of C_6H_6, but the Cp ligand is a more effective donor to the metal due to its more appropriate orbital energy match with $M(CO)_3$, and hence, there is better orbital mixing [See Fig. 5.2(b)]. Notice that the symmetry of $CpMn(CO)_3$ is only C_s (as is that of MMT). However, the "apparent" symmetry is higher. This is because the symmetries of Cp and $Mn(CO)_3$ are D_{5h} and C_{3v}, respectively. The e sets of Cp find good overlap matches with the e sets on $Mn(CO)_3$. The two LUMOs are primarily metal 2e, which is composed of Mn 3d (d_{xz} and d_{yz}) antibonding to the CO donor orbitals as well as antibonding to the e_1'' set on Cp which will be split slightly on account of ring distortion in Cp-Me.[122] However, this ordering changes when a core

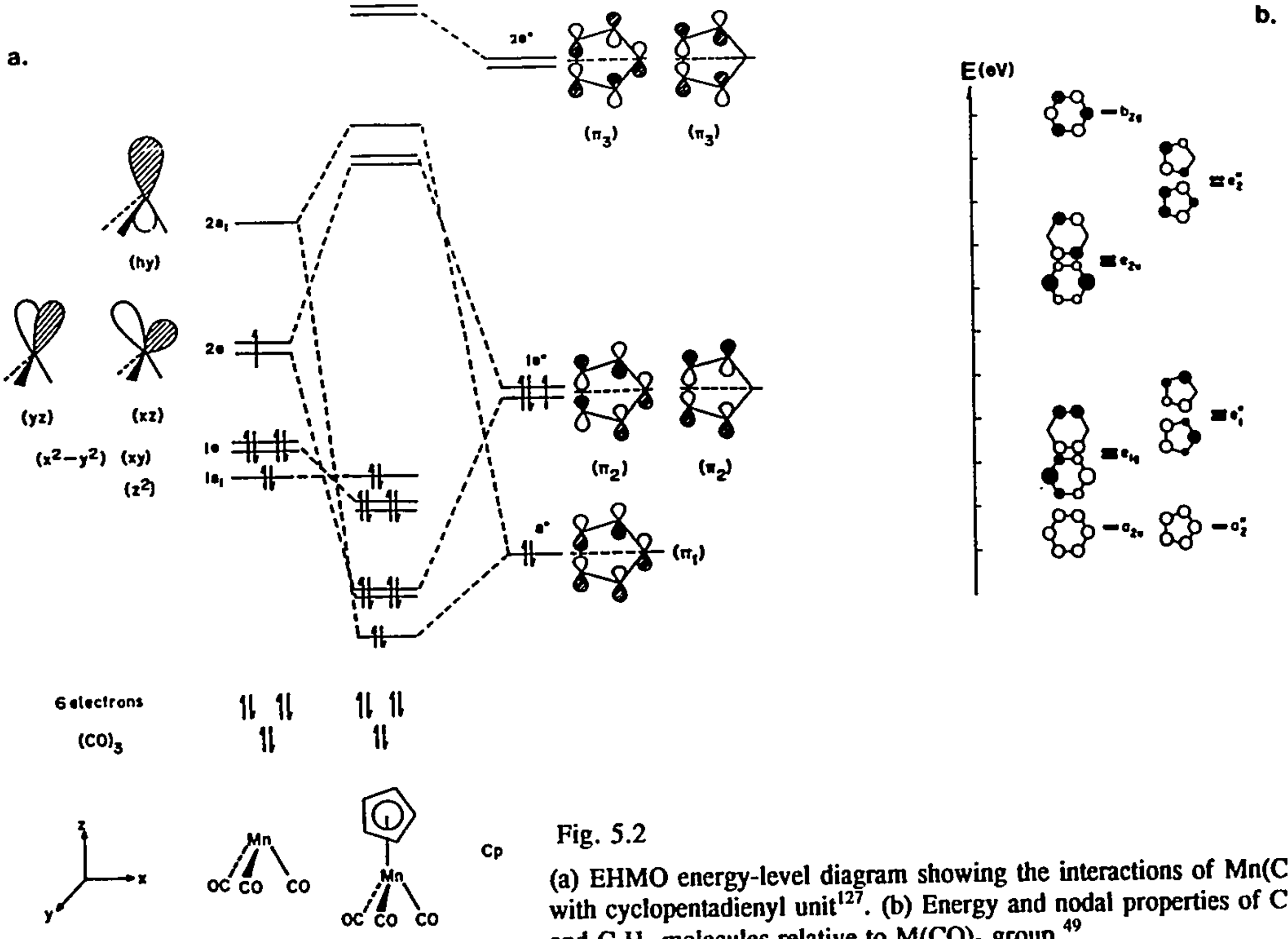

Fig. 5.2

(a) EHMO energy-level diagram showing the interactions of $Mn(CO)_3$ with cyclopentadienyl unit[127]. (b) Energy and nodal properties of C_6H_6 and C_5H_5 molecules relative to $M(CO)_3$ group.[49]

electron of the carbon atom on the Cp ring is excited, as has been discussed in the $CpCo(CO)_2$ case of the chapter 3. In the C 1s(Cp) excited state, the empty e_2'' set of Cp moves down and mixes with a Mn 3d orbital to form an orbital of Mn-π^*(Cp) antibonding character, thereby giving a substantial C 2p (Cp) contribution to the LUMO of the excited state. The whole MO depiction of $CpMn(CO)_3$ is quite similar to that of $CpCo(CO)_2$. With the above MO pictures in mind we can begin to analyze the ISEELS spectra recorded for these two complexes.

§5.3 C 1s Spectra

The C 1s spectra of BCT and MMT, together with their respective curve fits for the discrete region, are presented in Figure 5.3. The corresponding energies, term values and proposed assignments for the features in these spectra are listed in Table 5.1. In both cases, the energy, intensity and width of features below the ionization threshold are determined by Gaussian curve fitting. According to Fig. 5.1 (5.2), the first strong peak at 285.8 (286.1) eV in the BCT (MMT) spectrum may be associated with several final orbitals. For BCT, this may include two e sets of MOs immediately above the HOMO. EHMO theory shows that in the C 1s (Bz) excited state four unoccupied MOs of the two sets get well mixed with each other, in particular two MOs (e) originating from the arene e_{2u} set are split by the C 1s core hole and even separated by the LUMO e set of the ground state. This point seems to be supported by the MS-Xα transition-state calculations on BCT,[78] which showed also that the LUMO is unambiguously dominated by the arene ring. Transition of the C 1s electron to these four MOs would form an intense resonance. Similarly, in the case of MMT the first peak may involve C 1s (Cp) excitation to all five unoccupied MOs at the top of Figure 5.2(a): three unfilled $Mn(CO)_3$-based orbitals derived mainly from the two Mn-3d (d_{xz}, d_{yz}) and Mn-4s orbitals; and two empty Cp-based orbitals from the 2e" set which will also be split as the core hole is created. In short, the first intense feature in each spectrum is related to C 1s excitations to the MOs arising primarily from the empty ring and metal 3d (d_{xz},

d_{yz}) orbitals. Essentially they have nothing to do with the CO ligand.

This proposed assignment should not be surprising. According to our knowledge of core excitation of $Cr(CO)_6$ [20] and $Mn_2(CO)_{10}$ [11], we know well that the metal carbonyls do not give any spectral feature in this energy region. In terms of a localized core-hole description, any features appearing below 287.4 eV (CO) in the spectra of mixed-ligand species must be associated with the other half molecule, i.e., M-R (R = organic ligand) moiety. In this case, M-R is CrC_6H_6 or MnCp-Me, whose "parent" molecule (MR_2) with homogeneous ligands gives rise to low-energy features according to the ISEELS studies on some metallocenes (see Chapters 3 & 4). Following the MO diagrams in Fig. 5.5(A), one sees that the first of those low-energy features would be associated with a couple of empty MOs dominated by M-3d orbitals, especially that labelled e_{1g}*. Based on this argument, one may infer that the first peak in the $RM(CO)_3$ spectra comes from MR_2. Thus, we assign this peak loosely to "e_{1g}*-like" MOs (M-R) for both BCT and MMT.

In light of other work on the transition-metal carbonyls (Ch 3 & Ch 4), the most intense feature, the peak at 287.5 (287.7) eV in the BCT (MMT) spectrum is assigned to C 1s core excitation to the π^* orbital of CO, as has been supported by EHMO results (See Fig. 5.1). EHMO theory suggests also that three upper empty MOs of a symmetry may be involved in this excitation. The Gaussian fitting in this region of BCT (Fig. 5.3) indicates that there is an additional shoulder, around 288.4 eV, on the higher-energy side of the main line. This may be attributed to core excitation to a MO derived from the upper unfilled b_{2g} π^* of benzene, perhaps plus some CO $\pi^*_{deloc.}$ transitions since the delocalized π^* orbitals lie also in this region. However, for MMT there is a shoulder (286.9 eV) below the main line. It is considered to be a C 1s → π^*(Cp-Me) transition, one of the two 2e" orbitals of Cp-Me ligand (See Fig. 5.2), which remains above the three Mn-3d predominated MOs during the inner-shell excitation. Interestingly, the curve fitting suggests that there is a very weak feature below the first "e_{1g}*-like" peak for both complexes. The excited-state LUMO π^*(R), which is split out from the double-

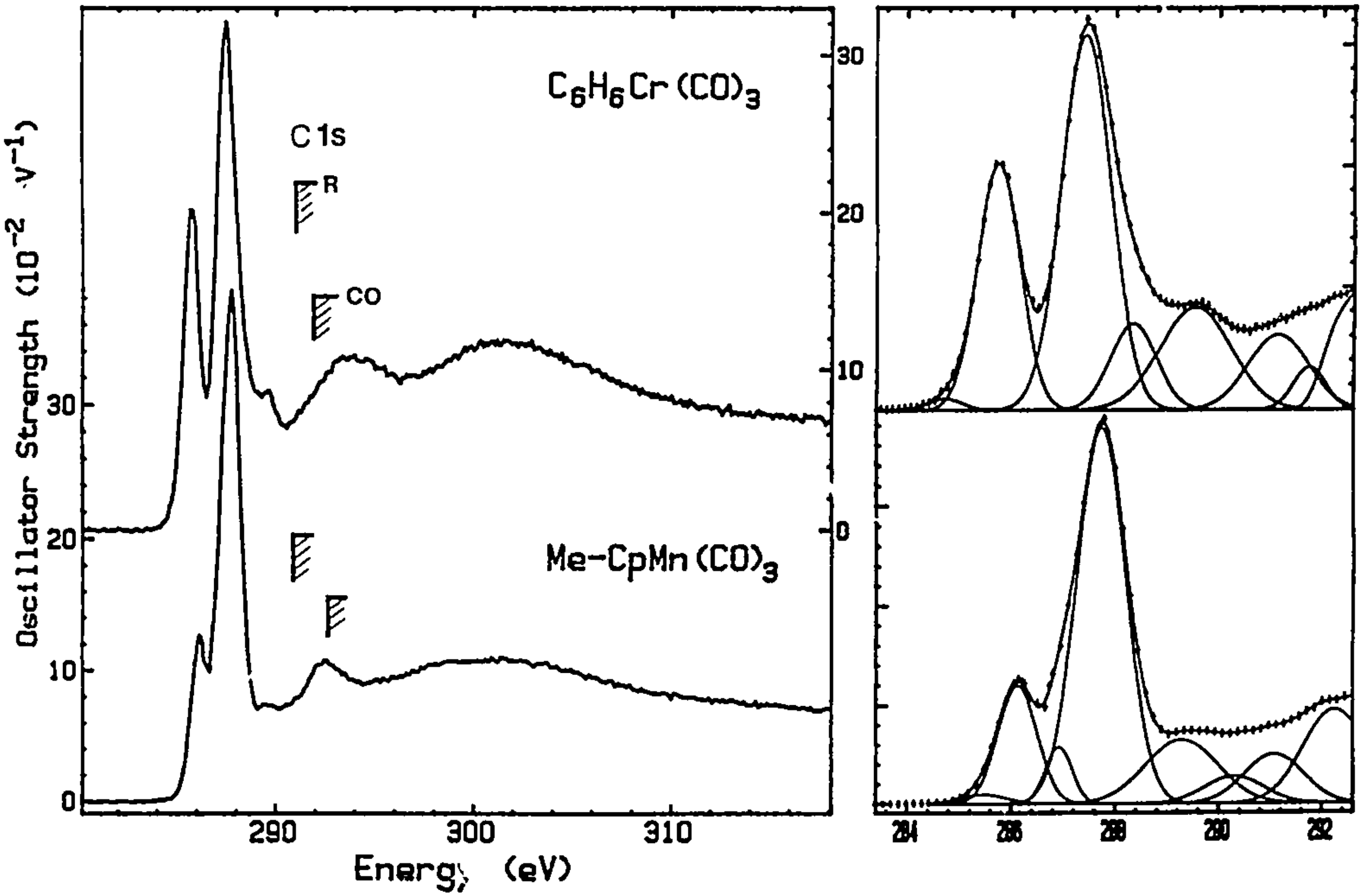

Fig. 5.3 Derived oscillator strength for C 1s excitation of $C_6H_6Cr(CO)_3$ and CH_3-$C_5H_4Mn(CO)_3$ (left), and Gaussian curve fits for the discrete C 1s excitations (right). The hatched lines indicate the location of the C 1s ionization potential determined by XPS.[92]

Table 5.1 Energies (E, eV), Term Values (T, eV) and Proposed Assignments for Features in the C 1s Spectra of $C_6H_6Cr(CO)_3$ and CH_3-$CpMn(CO)_3$.

$C_6H_6Cr(CO)_3$			$Cp'Mn(CO)_3$			Assignment
E	T		E	T		(final orbital)
	C_6H_6	CO		Cp'	CO	
284.7	6.2					$\pi^*(Bz)^c$
			285.5	5.4		$\pi^*(Cp')^c$
			286.1	4.7		e_{1g}^*-like MO (Mn 3d domin.)
285.8	5.2					e_{1g}^*-like MO (Cr 3d domin.)
			286.9	3.9		$\pi^*(Cp')$
287.50[a]		4.4	287.74[a]		4.8	$\pi^*(CO)$
288.4	2.6					b_{2g} $\pi^*(Bz)$ + some $\pi^*_{delo}(CO)$
289.6		2.4	289.3		3.2	$\pi^*_{deloc.}(CO)$
			290.3	0.5		Ryd.(Cp')
290.98			290.85			IP[b] (Bz, Cp')
291.2		0.8	291.1		1.4	Ryd.(CO)
291.8		0.1				Ryd.(CO)
			292.3	-1.5		$\sigma^*(Cp)$
291.91			292.54			IP[b] (CO)
293.8	-2.8					$\sigma^*(Bz)$
			298.6	-7.8		$\sigma^*(Cp')$
301.7		-9.8	301.5		-9.0	$\sigma^*(CO)$

a. Calibration relative to CO_2 (C 1s → π^*, 290.74 eV): $\Delta E = -3.24(5)$ eV and -3.00(8) for $C_6H_6(CO)_3$ and $Cp'Mn(CO)_3$, respectively.

b. IP from Ref. 92.

c. Bz denotes benzene and Cp' denotes C_5H_4-CH_3.

degenerate e set (e_{2u} or 2e"), is believed to be responsible for this little bump. If this assignment is correct, however, it means that core hole has produced an approximate 1.5-eV splitting for the 2e"-set orbitals of Cp-Me. Such a big splitting is somehow extraordinary, even backed by the theoretical calculations (e.g., EHMO shows that this splitting is about 1.0 eV for the benzene e_{2u}-set orbitals of BCT).

The relatively strong band centred at 289.6 eV (289.3 eV in the case of MMT) is attributable to the C 1s → $\pi^*_{deloc.}$(CO) transitions. The weak feature around 291 eV identified by the Gaussian fitting is likely Rydberg structure of the CO ligand. The first σ^* shape resonance in the MMT spectrum is at 292.3 eV, about 1.5 eV lower than its counterpart in the BCT spectrum. The spectrum of MMT exhibits another σ^* shape resonance around 298.6 eV, which is invisible or absent for BCT. Both species display a strong σ^* resonance band located around 301.5 eV, which may be a mixture of the σ^*(CO) and σ_2^*(C-C) shape resonances.

Overall, the two spectra are similar to one another in some sense: two sharp peaks below the ionization limit and two strong σ^* shape resonances above the edge. From the viewpoint of quantum chemistry, this is a rather natural result since the two complexes have almost equivalent electronic structures, thus yielding highly comparable spectral origins. Differences in intensity as well as line shape between these two spectra are evident too. Most noticeable is of course the intensity variation of the first peak in the discrete area: that in the BCT spectrum is almost as twice intense as its counterpart in the MMT spectrum. This may be associated with the chemical properties of Mn and Cp. According to Crabtree,[129] the $Cr(CO)_3$ entity acts as a π acid, so that the electron density on the benzene is reduced on complexation by virtue of electron delocalization to the carbonyls mediated by the Cr metal. Thus the benzene becomes a slightly electron deficient ($\delta+$) ligand, which should be more accessible for the excited core electron to populate the unoccupied MOs associated with the benzene e_{2u}^* set, and therefore the corresponding oscillator strength should be enhanced. In the case of MMT, however, such an electron (or charge) fluidity is somewhat inhibited due to the fact that Mn and

Cp-Me can form a relatively stable ionic-like moiety, $Mn^{\delta+}$-$Cp^{\delta-}$-Me (this is a unique exception, since only Mn can give an ionic-type metallocene). Notice that the "$Cp^{\delta-}$" ligand is a high electron-density spot as it has one less carbon to delocalize the charge compared to benzene. Consequently, there will be less empty valence C 2p character in the unfilled MOs resulting predominantly from the $Mn^{\delta+}$-$Cp^{\delta-}$-Me fragment, thereby giving rise to a peak of relatively weaker intensity. On the other hand, less negative charge flowing into the carbonyls via the metal-to-CO backbonding in $RM(CO)_3$ should lead to a more intense C 1s → $2\pi^*$(CO) transition. This is indeed the case. Close inspection of the two C 1s spectra shows that the most intense peak in the MMT spectrum is definitely higher than that for BCT. Accurate integration of the areas under these two CO-π^* peaks by means of the curve fitting (Fig. 5.3) further indicates that the π^*(CO) oscillator strength in MMT (.445 eV^{-1}) is larger than in BCT (.365 eV^{-1}).

Compared to BCT, the two sharp peaks below the IP threshold are much less resolved in MMT, reflecting better orbital mixing as well as stronger bonding between the Cp ligand and metal centre. This is consistent with the theoretical predictions on these C_nH_n organic ligands[49] (see also Figures 5.2 and 5.1). Both BCT and MMT have exactly the same number of carbon atoms and almost the same amount of hydrocarbon bonds as well, while their C 1s spectra have been normalized at about the same single-energy point (25 eV above the related IP). Although the spectral line shape above IP may look different from each other, the two spectra of BCT and MMT are expected to have approximately the same intensity in that area. This prediction seems basically correct, though the BCT spectrum displays slightly stronger σ^*-resonances than MMT. The broad-band shape of the first σ^* feature of BCT implies that it has more unfilled MO levels than MMT in this region which form the broad band. In general, the σ^* shape resonances in organometallic spectra are associated primarily with the ligands since the central metal atom has negligible influence in the continuum, although the metal may cause some energy shift of the σ^* resonances by virtue of the metal-ligand bonding, as is demonstrated by the following experimental simulation based on spectral additivity.[14,18]

§5.4 Simulated C 1s Spectra

A simulation of the C 1s spectrum was generated for BCT by adding the C 1s spectrum of benzene and half that of $Cr(CO)_6$ reported by Cooper et al[20] (the digitized spectrum of $Cr(CO)_6$ has been smoothed slightly in order to match the energy resolution of our ISEELS spectrometer). It is compared to experiment in Figure 5.4. The two components forming the simulation are also plotted on the top of the same figure to help indicate the origins of the features in the simulated spectrum. Through Figure 5.4, one can see immediately that the BCT continuum is essentially the sum of the two continua. However, the discrepancy in the discrete region between the experiment and the simulation is manifest, while the cause of this could be manifold. The large energy shift of the first peak may be due to the use of the C 1s spectrum of benzene rather than $Cr(C_6H_6)_2$, which is unavailable thus far. The same situation has also been encountered in the simulations for the $RFe(CO)_3$ species (see Chapter 4). The intensity inconsistency between the first two leading peaks seemingly supports the concept of charge redistribution within the molecule ($C_6H_6 \rightarrow Cr \rightarrow CO$), which will enhance the intensity of transitions on the C_6H_6 fragment but suppress those on the carbonyls. It appears as if the first peak in the experimental spectrum has "stolen" part of its intensity from the second peak upon comparison with the simulation. A feature around 291 eV in the simulated spectra apparently has an unusually strong intensity. It originates mainly from a feature in $Cr(CO)_6$, which was assigned to C 1s $\rightarrow \pi^*_{deloc.}$(CO) transitions.[20] The 291-eV feature might involve some underlying Rydberg transitions, which are usually very weak in the ISEELS spectra of large molecules, since it falls in that energy bracket compared to the BCT spectrum.

As mentioned above, owing to the lack of the $Cr(C_6H_6)_2$ spectrum we can not make a good example to illustrate the essence of the additivity principle. The fact is that we have made a great effort to attain this spectrum. According to the literature, it has

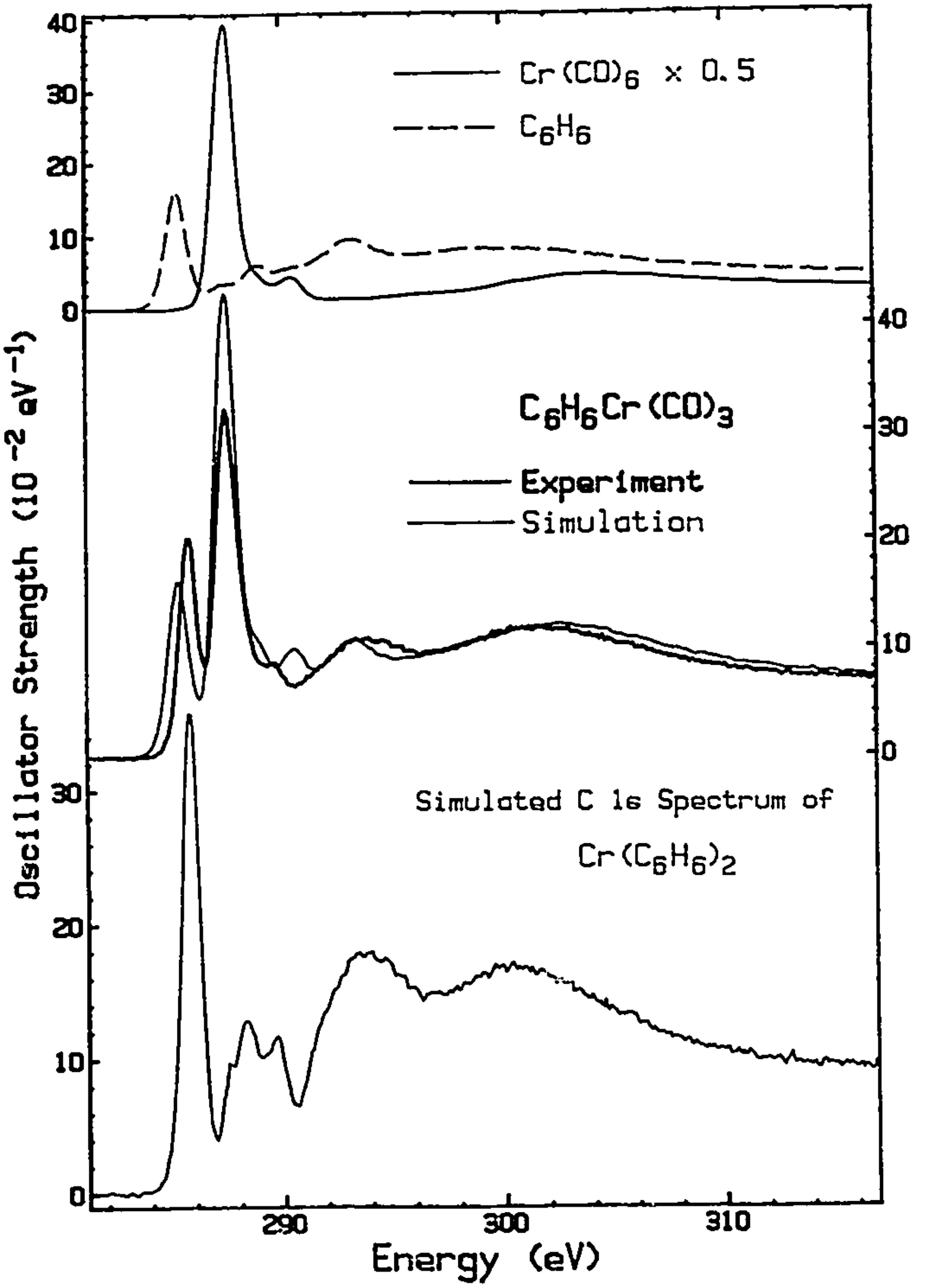

Fig. 5.4 Comparison between the experimental C 1s spectrum of $C_6H_6Cr(CO)_3$ (dark line) and simulation (light line) generated by the sum of the two components showed on the top panel, along with the simulated spectrum for $Cr(C_6H_6)_2$ (bottom).

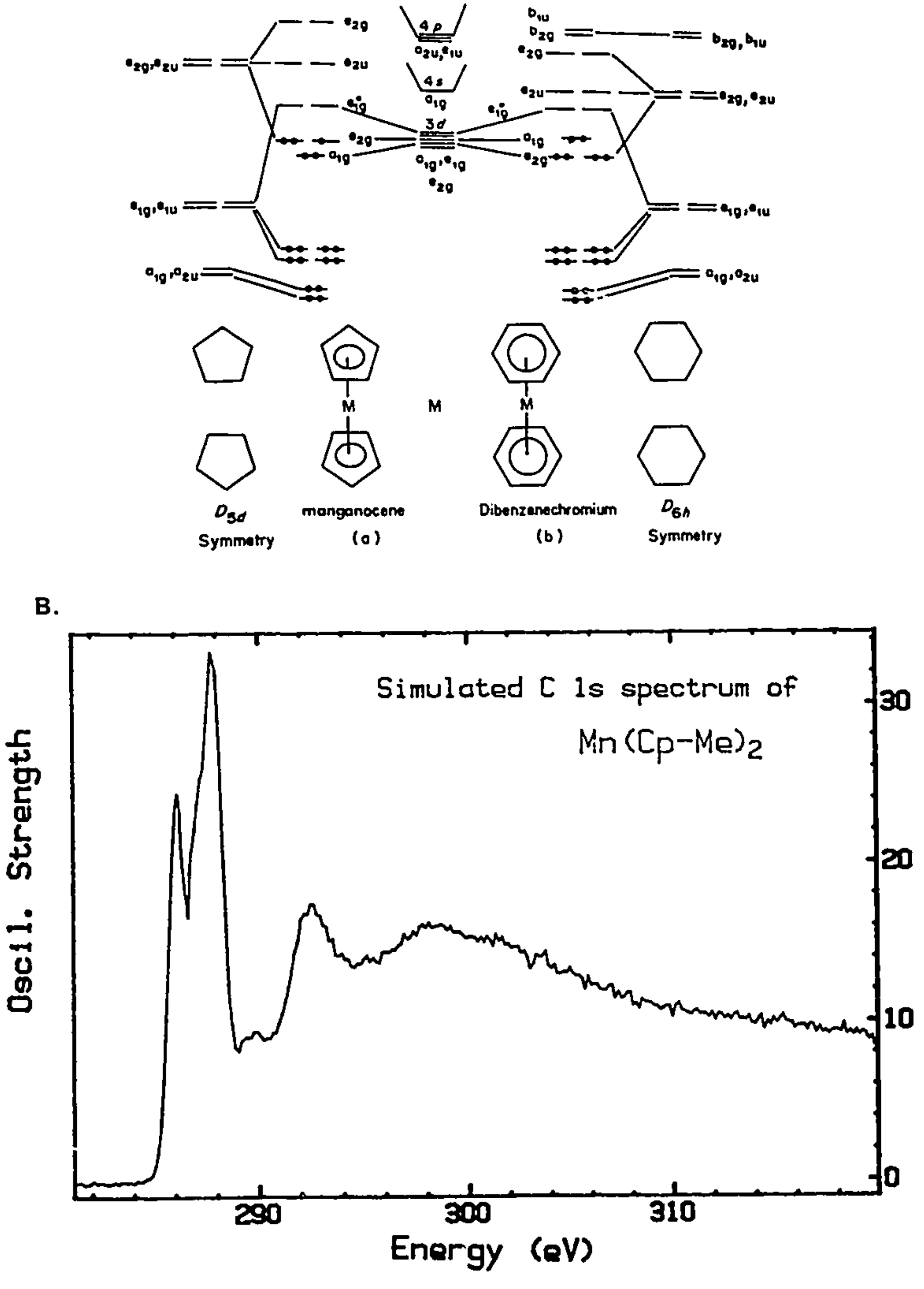

Fig. 5.5 (A) Schematic diagram of the frontier MOs for $Mn(C_5H_5)_2$ and $Cr(C_6H_6)_2$, modified on the basis of Ref. 135. (B) Simulated C 1s spectrum of $Mn(C_5H_4\text{-}CH_3)_2$.

been investigated in gas phase by PES[130] and ETS,[131] so one expects that ISEELS has the potential to measure its spectrum even though $Cr(C_6H_6)_2$ has a m.p. of 284°C. However, life is not always so obliging. The recorded spectrum varied with the temperature to which the sample was heated, which made it impossible to believe that the recorded spectra are correct.

In the absence of a reliable $Cr(C_6H_6)_2$ spectrum, we have tentatively simulated a C 1s spectrum of $Cr(C_6H_6)_2$ based upon our best knowledge of it and other related molecules. The simulation, which is presented on the bottom of Fig. 5.4, was generated by subtracting a third of the $Cr(CO)_6$ spectrum from that of BCT [not a half of the spectrum because the C 1s $\rightarrow$ π^*(CO) peak is too intense]. To compensate the intensity loss in the continuum owing to the subtraction, the simulated spectrum has been renormalized to 12-carbon atoms. Similarly, a simulation has been made for $Mn(Cp\text{-}Me)_2$ (See Figure 5.5B), whose ISEELS spectrum remains unknown at the present time. It was obtained by subtracting three tenths of the spectrum of $Mn_2(CO)_{10}$ from that MMT and then normalizing back to the intensity expected for 12 carbon atoms. The simulated $Mn(Cp\text{-}Me)_2$ spectrum seems fairly reasonable in terms of the metallocene studies.[13] However, both predictions are left unassigned here and are left for further study. The astute reader may assign these two simulated spectra himself by following the MO diagrams furnished in Fig. 5.5A. As an exercise he will have found that there will be no difficulty to label those spectral features below the ionization edge(s). But are they the correct spectra? Let's wait and see.

§5.5 Metal 2p Spectra

Oscillator-strength spectra of both BCT and MMT 2p excitations are depicted in the left-hand side of Fig. 5.6. For ease of assigning the spectral features and probing a possible trend of 3d-transition-metal core excitation in the mixed-ligand complexes, the related Fe and Co species are also presented in the right-hand-side panel of Figure 5.6. All spectra are plotted on a common energy scale of 38 eV, and their $2p_{3/2}$ IPs are

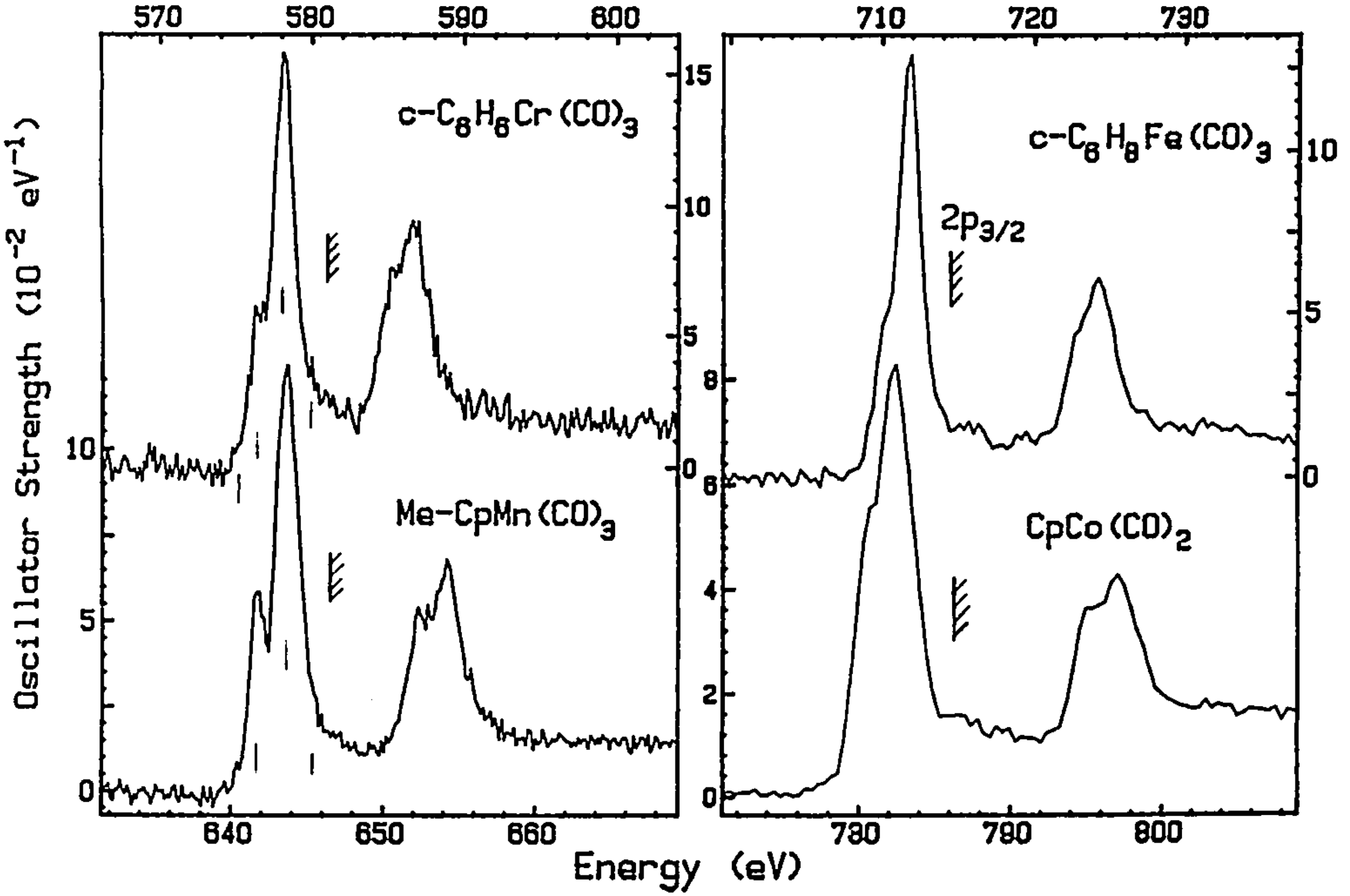

Fig. 5.6 Derived oscillator strength for the metal-2p spectra of $C_6H_6Cr(CO)_3$ and CH_3-$C_5H_4Mn(CO)_3$ (left), along with the other two spectra of related species (right) for comparison.

aligned for parallel comparison. The proposed assignments for BCT and MMT spectra are given in Table 5.2. Broadly, the two new spectra repeat the same pattern of two lines at each edge[18] regardless of the type of the central metal atom and the unsaturated hydrocarbon ligand. From the standpoint of the electric dipole selection rule, the metal 2p electron will be excited into final orbitals possessing either s- or d-character on the metal atom. But excitations to 3d-like final states will have much stronger intensity, presumably because the continuum 3d wave function is compact (compared to the 4s function) enough to fit mostly within the centrifugal barrier, thus leading to large overlap with the 2p core wave function and a large oscillator strength near the edge[132] (white line). This point appears to be supported by our EHMO and Modelli *et al*[78a] MS-Xα calculations, which indicate that despite being distributed over a wide range of the unoccupied MOs the main metal 3d orbital density is localized in the lower unfilled MO levels, especially in the vicinity of the LUMO, namely, they are in the deep inside of the potential well relative to the 4s and Rydberg series. Thus, all the features in the metal 2p spectra are more or less associated with the metal 3d orbitals mixed in the linearly-combined MOs, or perhaps even with those MOs which may contain a little metal contribution but have also some ligand character symmetry matched to the metal 3d orbitals.

On the basis of this argument, Figures 5.1 and 5.2 seemingly suggest that the two lines before each edge result primarily from the M(CO)$_3$ unit which brings in the M-3d AO components, and it is this common unit that makes all those 2p spectra of the mixed ligands look so similar. This appears correct since the spectra in Fig. 5.6 show a relative independence on the variation of the hydrocarbon ligand R. Therefore, we assign the first line of lower energy and intensity, with term value 4.5 eV, to the 2p transitions to the MOs derived from the 2e-set orbitals of the M(CO)$_3$ moiety which are constructed mainly by the metal 3d$_{xz}$, 3d$_{yz}$ atomic orbitals, viz., it is basically a "pure" metal 3d line. An analogous assignment can be made for the metallocene 2p spectra, where metal 2p $\rightarrow$ 4e$_{1g}$* excitation is accountable for the first as well as strongest peak[13]

Table 5.2 Energies (E, eV), Term Values (T, eV) and Proposed Assignments for Features in the Metal 2p Spectra of $C_6H_6Cr(CO)_3$ and Cp'Mn$(CO)_3$.

$C_6H_6Cr(CO)_3$		Cp'Mn$(CO)_3$		Assignment
E	T	E	T	(final orbital)
L_3				
575.8	5.3			$\pi^*(C_6H_6)$?
576.6	4.5	641.9	4.5	M 3d
578.2[a]	2.9	643.7[a]	2.7	σ^*(M-C)
580.0	1.1	645.4	0.9	Ryd
581.08		646.4		$2p_{3/2}$ IP[b]
L_2				
584.7	5.0			$\pi^*(C_6H_6)$?
585.5	4.2	652.6	4.3	M 3d
586.8	2.9	654.2	2.7	σ^*(M-C)
587.7	2.0	655.8	1.1	Ryd
589.7		656.9		$2p_{1/2}$ IP[c]

a. Calibration relative to O_2 (O 1s → π^*, 530.8 eV): $\Delta E = +47.4(2)$ eV for $C_6H_6CrCO)_3$; and to CO of the same species (O 1s → π^*: 533.8 eV) for Cp'Mn$(CO)_3$.

b. IP from Ref. 92.

c. Derived from the $2p_{3/2}$ IP by adding the separation between the main L_2 and L_3 peaks.

(see also Fig. 5.5A and Chapter 4).

The most intriguing aspect is the assignment of the second main line of term value about 2.8 eV in Fig. 5.6 or even in the other 2p spectra of metal carbonyls. The large intensity of this peak reflects that, in this term-value bracket, there exists either a few final states of a substantial d-orbital contribution or an overlap of many final states having reasonable d-like character. However, it has been found also that without the CO-ligand involvement the intensity of this peak diminished dramatically (see the metallocene cases), indicating definitely that the peak has a direct connection with the $M(CO)_3$ fragment. As a case study, we return now to the EHMO calculations on BCT. The results of the Cr 2p excited state suggest that five successive upper-level unoccupied MOs below the top a_2 MO of the benzene b_{2g} π^* orbital in Fig. 5.1 would contribute to the peak transition intensity. Among these five MOs, two arise from the benzene e_{2u} σ^* orbitals, while the other three of a symmetry come from the $Cr(CO)_3$ group. In particular, each of the three $Cr(CO)_3$-based MOs contains a much larger d-count and is expected to make a major contribution to the transition intensity relative to those two MOs of e symmetry. This means that most of the intensity of this line would disappear if the $Cr(CO)_3$ moiety is replaced by CrC_6H_6, and the resulting Cr 2p spectrum of $Cr(C_6H_6)_2$ would be similar to that of metallocenes. An analysis of the orbital symmetry indicates further that all five MOs possess a σ^*(Cr-C) antibonding character. In terms of the polarized property of the Cr-C bond due to the unequal electronegativity for the Cr and C atoms, it seems quite rational for the 2p → σ^*(M-C) transitions to occur below the IP threshold. An analogous occurrence has also been observed in the C 1s spectra of the methyl halides.[133] Thus, the second main line has tentatively been assigned to transitions involving promotions of the Cr 2p electron to the σ^*-antibonding MOs describing the Cr-C bond (which is in accord with the previous dσ^* description[18]), whereas its large intensity is attributed to a superimposition of several unresolved lines under the peak. Similar assignments can be made for the spectra of MMT and other $RM(CO)_3$ complexes.

It is worth pointing out that the M-C bond has quasi-double bond character by virtue of the twofold bonding mechanism: ligand-to-metal bonding and metal-to-ligand backbonding as well. This character may affect the determination of the MO angular-momentum and/or application of the dipole selection rule to the MOs of interest. An unoccupied MO of π symmetry in organic molecules always produces a sharp intense peak below the threshold in core excitation. This serves as an indicator for determining the origin of an intense feature. The high density of the M-C bonds between the metal and ligands in $RM(CO)_3$ species may also play a role in enhancing the peak intensity. This point is illustrated by the comparison to $CpCo(CO)_2$ Co 2p spectrum, in which the second main line has an unusually low intensity compared to its counterpart in the other spectra. One M-CO bond less may be the very cause of this. As for the line shape, the two lines in the MMT spectrum appear better resolved than those for BCT. This is opposite to the situation in the C 1s spectra of Figure 5.3. It is of interest to note that the intensity ratio between the L_3 and L_2 edges is roughly 2-to-1, the statistical value. In many other 2p spectra of metal compounds, however, the metal 2p → 3d transitions have a non-statistical intensity ratio.[110] Perhaps this is somehow connected with the more covalent character of these organometallic complexes, in contrast to the ionic metal compounds which have formed the major targets of other researchers. Along the fourth-period of the Periodic Table, the L-edge spin-orbit splitting, the separation between the two maxima in each spectrum, increases gradually, exhibiting values of 8.6, 10.5, 12.5 and 14.6 eV ascending from Cr to Co.

§5.6 O 1s and Metal 3p Spectra

The O 1s spectra of BCT and MMT are compared in Figure 5.7. They are practically identical, as with the O 1s spectra of all other carbonyl complexes, not only in shape but in energy also, and show no sensitivity at all to the variation of the transition metal. This reflects the localized nature of carbonyl O 1s excitation at the perimeter of the complex which only involves unfilled MOs of the CO ligand. On the other hand, this is consistent with the point that in the C 1s spectra of the mixed-ligand complexes the features appearing below the 287.4-eV (CO) must be related to the other half complex of RM, otherwise the O 1s excitation would sense their existence. Parallel to previous studies of O 1s excitation of metal carbonyl complexes, assignments for the features in these two O 1s spectra are straightforward: two strong peaks separated by the ionization limit are assigned to the O 1s → π^*(CO) excitation (533.8 eV) and the σ^* shape resonance (ca. 550 eV); two weak features are attributable to the O 1s → $\pi^*_{deloc.}$ transitions (535.9 eV) and Rydberg structure (538 eV), respectively (See Table 5.3). The chemical shift and intensity reduction relative to free CO are interpreted as before (see Chapter 3). The monotony of all these O-1s spectra of the carbonyls may indicate that, besides its highly-localized nature, the O 1s core-hole potential is rather effectively screened by the excited 1s electron remaining in the vicinity of the core hole.

The metal-3p spectra of the two complexes are plotted in Figure 5.8. No specific assignments are made for them, nor are the oscillator strengths determined. All M-edge features are superimposed on a rapidly-falling valence-electron background, which has been removed from the spectra presented. The M_{23} edges of Cr and Mn are pretty sharp here and quite resemble other core edges. Like the O 1s spectra, the M_{23} spectra are characterized by "two" strong features, one on each side of the estimated ionization thresholds[18,112] (the hatched lines in Fig. 5.8). The peak below the IP is assumed to be the metal 3p → 3d transitions, and its large intensity may be attributable to a higher density of 3d orbitals in the final states compared with the Fe and Co complexes that have more d electrons. The broad band-like feature above the IP may be associated, at least partially, with final states which are largely composed of ligand AO contributions. M_1 edges, which are usually weak and rarely observed in ISEELS, are clearly seen here (at approximately 79 and 85 eV for Cr and Mn, respectively) although they are weak relative to the more intense M_{23}-edge continuum. These features are presumably due to the metal 3s → 4p transitions.

In Figure 5.9, the Mn 2p and 3p spectra of MMT are compared to those of

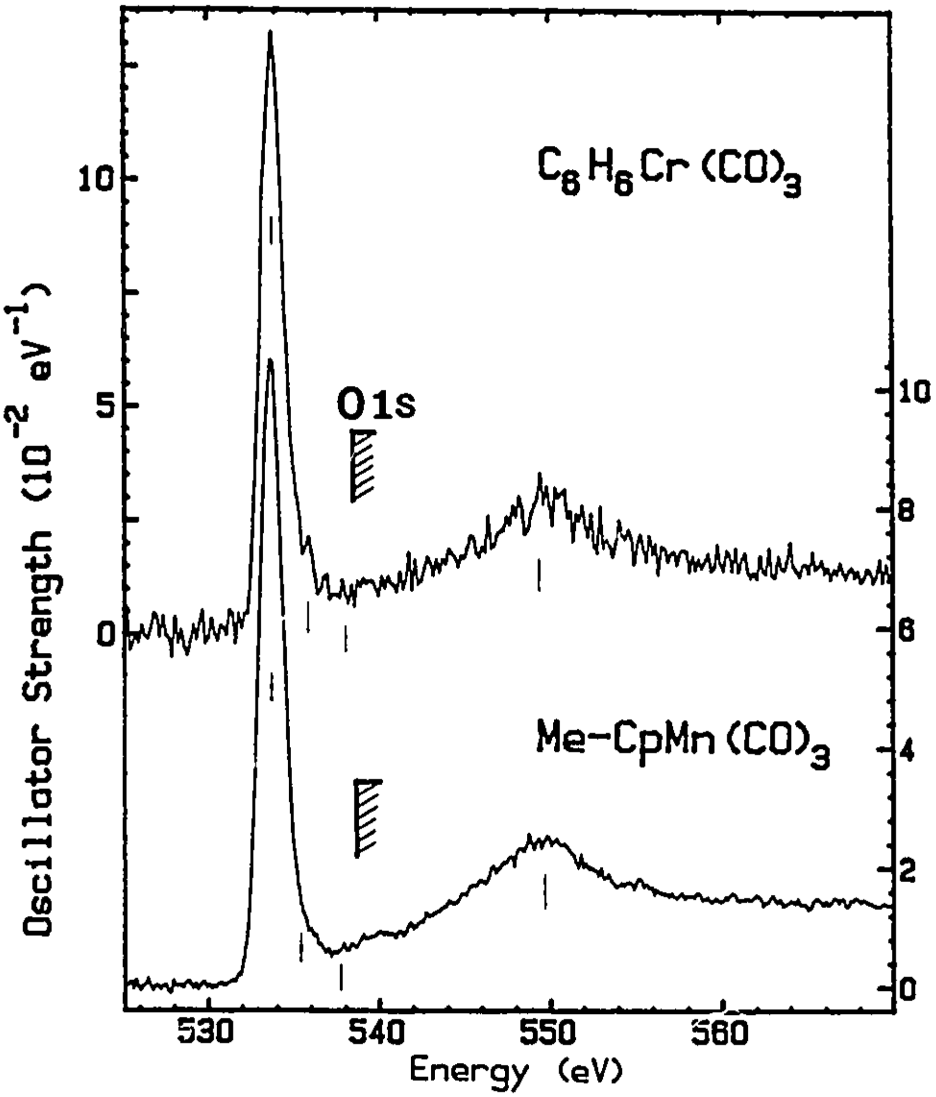

Fig. 5 7 Derived oscillator strength for the O 1s spectra of $C_6H_6Cr(CO)_3$ and CH_3-$C_5H_4Mn(CO)_3$.

Table 5.3 Energies (E, eV), Term Values (T, eV) and Proposed Assignments for Features in the O 1s Spectra of $C_6H_6Cr(CO)_3$ and Cp'Mn$(CO)_3$.

$C_6H_6Cr(CO)_3$		Cp'Mn$(CO)_3$		Assignment
E	T	E	T	(final orbital)
533.8[a]	4.6	533.8[a]	4.9	$\pi^*(C=O)$
535.9	2.5	535.8	2.9	$\pi^*_{\text{delocalized}}$
537.9	0.5	538.0	0.7	Ryd
538.39		538.65		IP[b]
549.5	-11.1	549.8	-11.2	$\sigma^*(C=O)$

a. Calibration relative to O_2 (O 1s → π^*, 530.8 eV): $\Delta E = +3.0(2)$ and $+3.0(2)$ eV for both species.

b. IP from Ref. 92.

$Mn_2(CO)_{10}$, respectively. Close inspection of both Mn 2p and 3p spectra shows that there is no visible indication to signal the presence of a Mn-Mn σ^* antibonding level.[76] Compared to the C-C bond energy in ethane (92 $kcalmol^{-1}$), the Mn-Mn bond strength in $Mn_2(CO)_{10}$ is remarkably small (*ca.* 16 $kcalmol^{-1}$),[134] and thus it is a typical weak bond. In terms of the weak-bond model,[91] this means that a small energy separation between the Mn-Mn σ and σ^* MOs is expected and a spectral feature associated with the Mn-Mn σ^* MO level should appear in the low-energy region below the lowest Rydberg excitation (see Chapter 7). The absence of such a feature in the Mn *np* spectra signifies that the Mn-Mn σ^* MO describing the single Mn-Mn antibonding bond may possess very little d-orbital character or it may be a rather deffuse orbital which lacks sufficient spatial overlap with the metal *np* orbitals.

Figure 5.9 shows that the L and M edges have very different shapes: the M-edge line seems more like a broad band, while the L-edge is peak-like. Coulomb interaction between the core hole and atomic electrons which screen the hole may be strong enough to modify the shape of an ionization edge. In the case of the M edge this modification will be larger since there is a greater spatial overlap of the excited electron and the hole. In addition, since the 3p core level has a much smaller binding energy than the 2p level, it is energetically and spatially closer to the valence shell, and thus is more likely to be affected by the chemical environment formed by the ligands. Finally, the shorter life-time of the 3p core hole may partially account for the M-edge broadening because of a higher probability of Coster-Kronig as well as super Coster-Kronig de-excitation transitions.[11,135,136]

Unlike $Mn(CO)_5Br$ [11], the 3p spectrum of MMT is different from that of the dinuclear $Mn_2(CO)_{10}$. This is especially evident in the 3p continuum region. It is apparent that the large hydrocarbon ligand Cp-Me is accountable for this deviation. Compared to van der Laan's[114] prediction of the Mn d^5 ion (see the inset in Fig. 5.9), the two Mn 3p spectra in Fig. 5.9 have a reasonable match to the simulated spectrum with a crystal field (CF) of 10 Dq between 2 and 3 eV, with the MMT spectrum closer

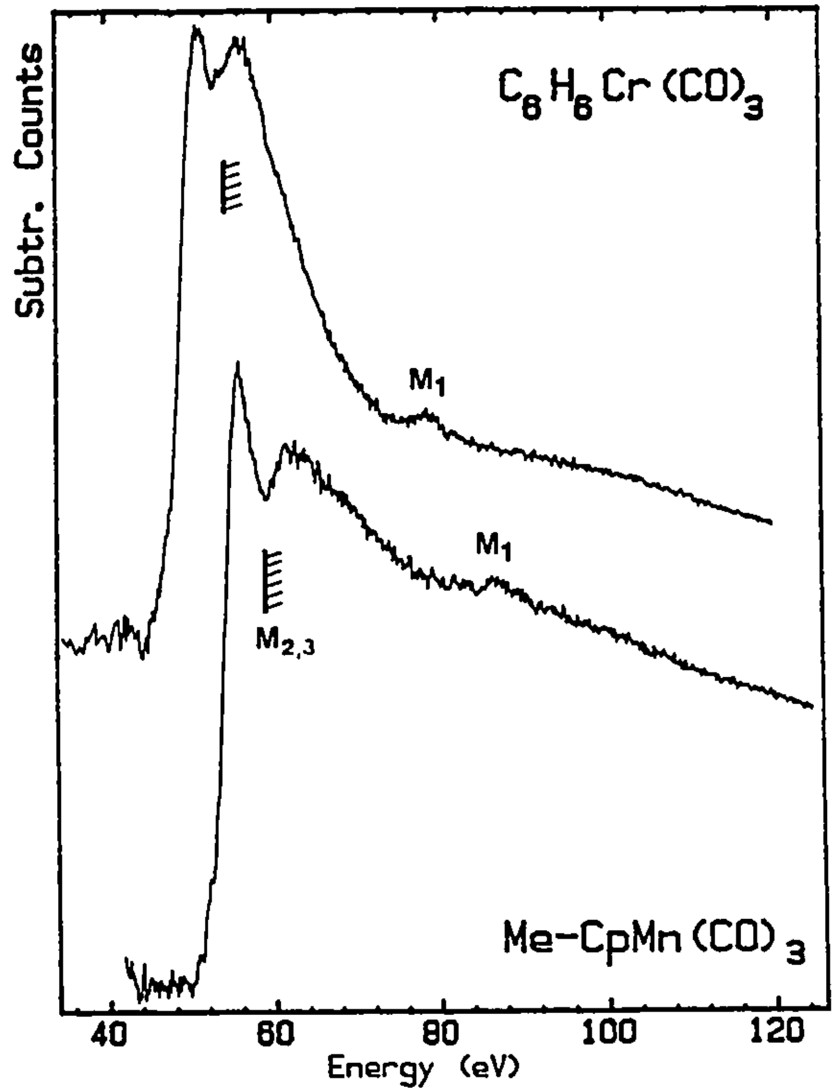

Fig. 5.8 The metal-3p spectra of $C_6H_6Cr(CO)_3$ and CH_3-$C_5H_4Mn(CO)_3$, whose backgrounds have been subtracted. The hatched lines indicate the estimated edges by assuming identical 3p → 3d and 2p → 3d term values.

to the upper limit of the prediction. If the correlation is correct, the ligands in MMT seemingly form a stronger crystal field, suggesting that Cp-Me (or Cp) has a higher position in the spectrochemical series than CO does. This point appears to be supported further by the Mn 2p spectra (Fig. 5.9). Compared to the theoretical studies[110] of the Mn^{2+} $3d^5$ ion, the spectrum of the dinuclear species could correlate with the calculation for about 1-eV crystal field, while the MMT spectrum corresponds to the calculation with a 1.8-eV field, or higher. Based on this result, the metallocenes should fall in a high CF bracket, and the sequence of the crystal field, which is generated by the ligands under investigation, placed in order of increasing strength would be CO $<$ CO+Cp $<$ Cp. Perhaps this sequence only applies to the complexes containing the Mn atom since $Mn(Cp)_2$ is strongly ionic in nature.[129] Through this discussion, one can see that the crystal field plays an important role in shaping metal 2p/3p spectra. From the viewpoint of ligand field theory, the splitting of both the L_2 and L_3 lines into two components separated by 1.5~2.0 eV may be considered as a rather direct measure of the crystal-field splitting.

§5.7 Summary

We have recorded the gas-phase ISEELS spectra of two organometallic species with different types of ligands; $C_6H_6Cr(CO)_3$ and CH_3-$C_5H_4Mn(CO)_3$. The spectra have been interpreted largely by comparison with previous studies of related organometallic species as well as by analogy with those of the free ligand molecules. EHMO calculations and spectral simulations are found to be very helpful in elucidating the spectral features. In general, the two complexes display fairly similar core spectra at each edge, not merely in overall shape but in intensity also. This has been ascribed to the fact that there are essentially the same origins for the spectral features of these two complexes despite involvement of different ligands and different central metal atoms. Some noteworthy differences of the C 1s spectrum between the two species could be explained in terms of the different metal-ligand (R) bonding character and intra-molecular electron fluidity induced by ligand-ligand interaction. The most pronounced peak in the metal 2p spectra is proposed to be associated with the 2p → σ*(M-C) transitions. Comparison between the Mn *np* spectra of MMT and $Mn_2(CO)_{10}$ shows that the features of the metal 2p spectra are largely related to the $M(CO)_3$ group. There is no clear evidence for Mn *np* → σ*(Mn-Mn) transitions.

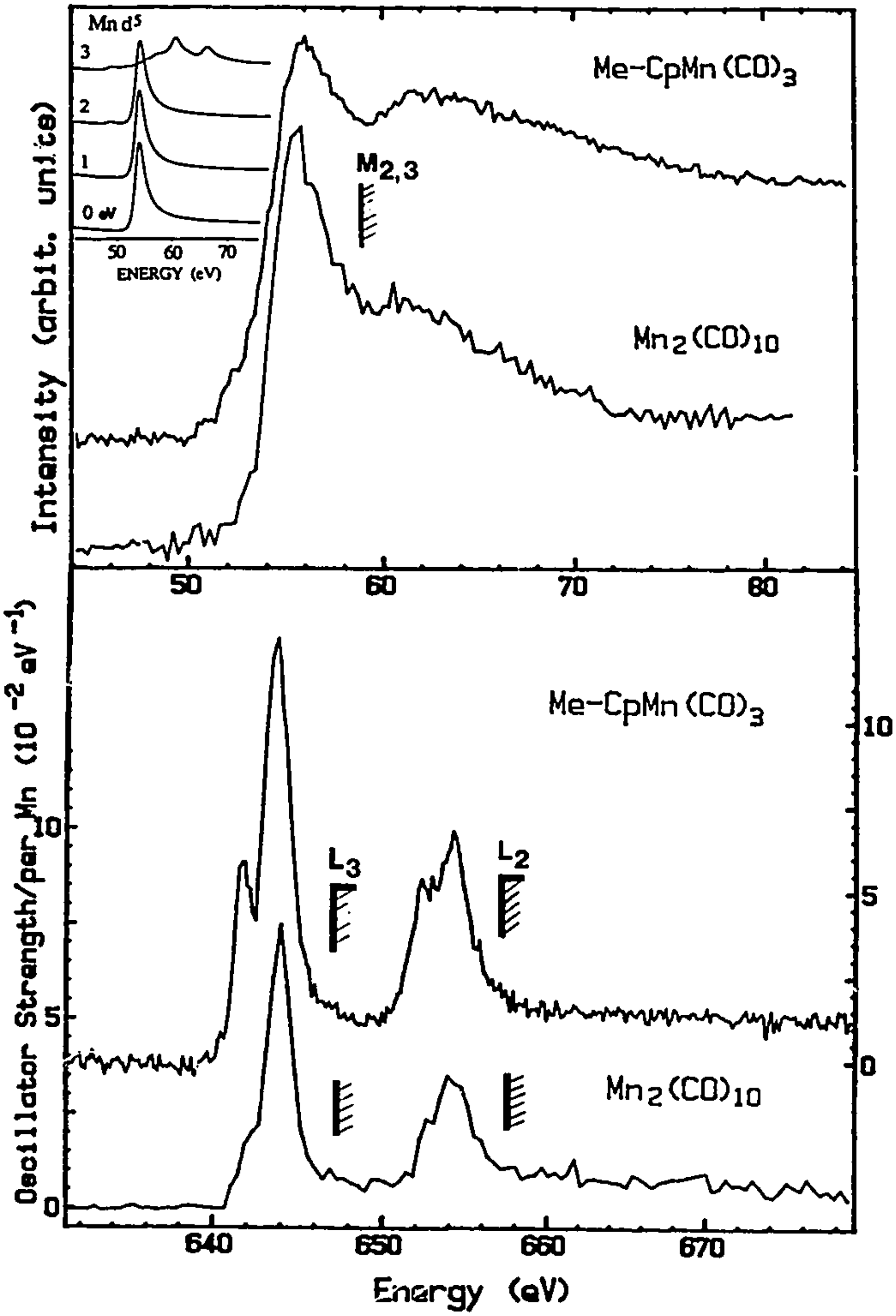

Fig. 5.9 The Mn 3p (top) and 2p (bottom) spectra of CH_3-$C_5H_4Mn(CO)_3$ are compared to those of $Mn_2(CO)_{10}$, respectively. The inset shows the Mn 3p spectra predicted by the atomic multiplet theory with the different crystal fields (0-3 eV).

Chapter 6

CORE EXCITATION OF $CpTiCl_3$ AND $TiCl_4$

§6.1 Introduction

Titanium compounds have been used in organic chemistry for many years. Initial interest in organotitanium compounds may date back to the early 1950s, following a report on ferrocene in 1951.[138] Related cyclopentadienyl complexes of titanium[139] were isolated and characterized as potentially useful agents in organic synthesis. One of these complexes is $CpTiCl_3$ which contains a single anionic π-bonded ligand Cp. This has turned out to be a starting material for the preparation of countless other mono-cyclopentadienyl derivatives of titanium, including mixed species containing σ-bonded hydrocarbon groups. Spectroscopic and thermochemical data have tended to support the view that the Ti-C bond may be fairly strong. The Cp ligand, referred often as a so-called "stabilizing" group, is now envisaged as occupying certain key coordination sites, which might otherwise be available for taking part in reactions towards decomposition, instead of stabilizing a M-C σ-bond elsewhere in the complex.[140]

In previous chapters ISEELS has demonstrated that site-selective core excitation is a rather sensitive probe of the molecular unoccupied electron structure associated with metal-ligand bonding and ligand-ligand interaction via the metal centre. Therefore, it may be helpful in providing insight into the special function of the Cp group in these related titanium complexes. This chapter reports the C 1s, Cl 2p and Ti 2p ISEELS spectra recorded for $CpTiCl_3$, and attempts to better understand its properties from the MO standpoint. To facilitate spectral assignments, the Cl 2p, Ti 2p and 3p spectra of $TiCl_4$ have also been recorded. $TiCl_4$ is a closely-related species of $CpTiCl_3$ and a major component of the Ziegler-Nata catalyst system. In addition, since both compounds have significant ionic character, they should afford a better opportunity than more covalent complexes to test the atomic multiplet theory of de Groot *et al*[110], which has not yet given a very satisfactory spectral match to 3d-transition-metal 2p spectra of organometallic complexes with more covalent bonding nature (see Chapters 3 and 4). Here the Ti 2p spectra of $CpTiCl_3$ and Ti_4 are compared to the 2p X-ray absorption spectra of $3d^0$ transition metal compounds predicted by the multiplet model within an O_h crystal field.

§6.2 EHMO Pictures of $CpTiCl_3$ and $TiCl_4$

$CpTiCl_3$ is a useful reagent for introducing the 'TiCp' moiety into a variety of complex molecules. With a m.p. around 200 °C, thermochemical data[141] indicate that the complex has a dissociation energy of 74 kcal/mol for the Ti-Cp bond. $CpTiCl_3$ is a much weaker Lewis acid than $TiCl_4$. Its molecular crystal structure, determined by Ganis and Allegra,[142] displays the molecule to be a half-sandwich with essentially equal Ti-C bond lengths and a "piano stool" configuration. Based on the crystal structural data, EHMO calculations were carried out for this molecule to provide a general MO picture of it and thus facilitate the spectral interpretation of its core excitation.

The EHMO level diagram of $CpTiCl_3$ is presented on the left-hand side of Fig. 6.1, together with the orbital correlations of its fragments. The correct symmetry of this complex is merely C_s. However, the computed MO energies (Figure 6.1) suggests that the apparent symmetry is rather close to O_h. This can be rationalized readily within the EHMO fragment-analysis model.[143] Consider a hypothetic species ML_6 of an octahedral structure (6.a), where L is a simple σ donor ligand (such as Cl^-) and has one valence orbital with two electrons pointing towards the metal centre. The σ-bonding skeleton

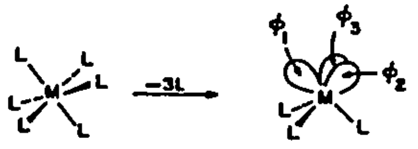

6.a 6.b

6.c

can be constructed from six equivalent sp^3d^2 hybrid metal orbitals and the σ-ligand orbitals. The valence orbitals of a pyramidal ML_3 fragment (C_{3v}) can be obtained from an octahedron by removal of three facial L ligands, leaving three low lying acceptor orbitals directed towards the vacated ligand sites (**6.b**). If the original species has a $3d^0$ metal centre (e.g., Ti^{4+}), then **6.b** will have three unfilled valence orbitals that closely correlate to the $2t_{2g}$ set of the octahedron.[144] On the other hand, if the three L ligands are removed from $CpML_3$ (such as $CpTiCl_3$), leading to the CpM fragment **6.c**, the resulting three hybrid orbitals will point towards the empty ligand sites. This is exactly the same pattern seen in the above generation of the ML_3 fragment from ML_6. In other words, the CpM group is expected to be very similar to ML_3. This means that the Cp^- ligand with six electrons is topologically equivalent to three facial ligands of the σ donor (Cl^- in our case). If the two fragments of CpM and ML_3 are put together to form the $CpML_3$ complex, no one will be too surprised at the result that $CpTiCl_3$ has a pseudo-octahedral symmetry based on the above discussion. Thus, we may consider O_h as an effective molecular symmetry for $CpTiCl_3$ and label the LUMO and LUMO+1 MOs as a combined '$2t_{2g}$' MO which is split slightly (by about 0.22 eV) in both the ground and excited states. Therefore, the labels of O_h symmetry are used loosely in Fig. 6.1 for the $CpTiCl_3$ MOs. Following the orbital correlation diagram, one should have no difficulty to locate the orbital origins. Clearly, there is a strong orbital interaction between the Cp e_1'' set and the $TiCl_3$ 1e set, which are derived mainly from the Ti 3d orbitals (d_{xz}, d_{yz}). Thus, core excitation to the LUMO+1, and the LUMO, should be informative with regard to the Ti-Cp bonding. The role of those MOs in the ISEELS spectra will be discussed further in detail in the following sections.

For $TiCl_4$, the central Ti-3d ion is situated in the tetrahedral (T_d) crystal field of the Cl^- ligands, and the crystal-field splitting of its five 3d orbitals is the reverse of its splitting in an octahedral field, as can be seen clearly in Figure 6.1. Although it has been studied here to compare with the results of $CpTiCl_3$ and to explore the nature of the Ti-Cp bond, $TiCl_4$ has long been a spectroscopist's and theorist's target in its own right[110,144-150] owing to its high symmetry, volatility and simplicity. The energy-level

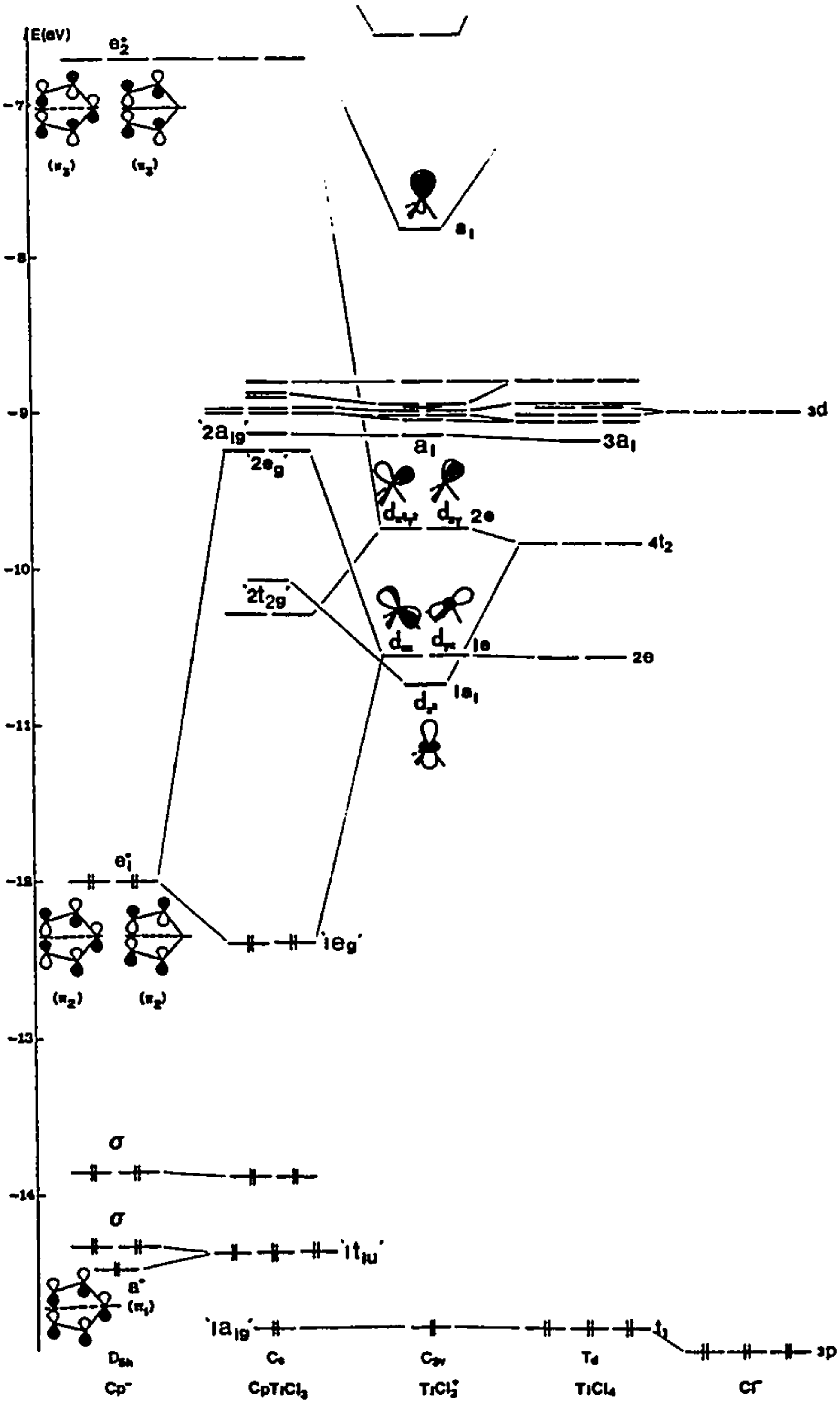

Fig. 6.1 Energy-level diagram showing the interactions of $TiCl_3^+$ with Cl^- and Cp^- anions (derived from EHMO ground-state calculations).

diagram of this molecule, presented in the right side of Figure 6.1, was obtained from EHMO calculations using the structural parameters determined by electron diffraction.[151] The ground state of $TiCl_4$ is expressed by

$$(1a_1)^2(1t_2)^6(1e)^4(2t_2)^6(2a_1)^2(3t_2)^6(1t_1)^6:\ {}^1A_1.$$

The lower-energy unoccupied levels, LUMO (2e) and LUMO+1 ($4t_2$), are basically metal-3d orbitals. The energy difference between these two levels is just the 10Dq "crystal field" splitting in a tetrahedral field. The 10Dq of the ground state predicted by EHMO is only 0.74 eV, but it is reduced to about 0.51 eV in the Ti 2p excited state. This is rather smaller than the experimental value (~0.95 eV) determined by UV absorption spectroscopy[145] and, Fenske and Radtke's result from semiempirical calculations[144] (~1.0 eV). Compared to $TiCl_4$, the HOMO's of the Cp^- ligand, viz., the double-degenerate π set (e_1''), provide a much better energy match with the vacant 1e set of $TiCl_3^+$. That is, the Cp^- ligand apparently bonds more strongly to the $TiCl_3^+$ cation than does a fourth Cl^- anion.

However, Fig. 6.1 suggests that direct substitution of a Cp^- ring for one of the chloride ligands in $TiCl_4$ does not affect the unoccupied electronic structure very much, except that the $4t_2$ set of a tetrahedron is slightly split in the pseudo O_h crystal field ("$2t_{2g}$"). This means that the two molecules may reveal similar ISEELS spectra in the common Cl 2p and Ti 2p edges. If this is the case, it may be relatively simple to extend the spectral discussion of one compound to the other. The occupied MOs of both molecules have been investigated by photoelectron spectroscopy.[147,152] There are three major bands in the $CpTiCl_3$ photoelectron spectrum which are associated with MOs derived largely from the chlorine orbitals but with some Ti-orbital participation. These are shifted by ~1 eV to lower energy relative to the corresponding bands of $TiCl_4$. Such a red shift has been attributed to the π-donor nature of the Cp ring pointing towards the central Ti atom, which induces a reduction of the bonding strength of the Cl lone pairs.

This is explicit evidence that the Cp-ring influences the Ti-Cl bonding through shifts in the occupied MO levels. In the unoccupied MO domain, there has not been any similar study thus far dealing with the same system. Although simple two-feature UV absorption spectra[153] have been reported for a related system of CH_3TiCl_3 and $TiCl_4$, chemical bonding information was not extracted from the spectral data. In the following sections the ISEELS spectra of $CpTiCl_3$ and $TiCl_4$ are used to probe their unoccupied electronic structures.

§6.3 C 1s Spectrum of $CpTiCl_3$

The C 1s spectrum of $CpTiCl_3$ is given at the top of Fig. 6.2. Energies, term values and proposed assignments are summarized in Table 6.1, together with those of ferrocene for comparison. The positions of spectral features are determined by Gaussian curve fitting (see the middle panel of Figure 6.2). The EHMO computations on this molecule produce not only the energy-level diagram but also a simulated C 1s spectrum that is compared to the experiment in the bottom panel of Fig. 6.2. The calculation of C 1s excitation was performed with the equivalent core model,[57] whereas the spectral simulation was carried out using the virtual MO levels for the relative energy positions of Gaussian lines with a width of 0.7-eV FWHM in the discrete sector, and again using ΣC^2(N2p) for the line intensities. More meaningful comparison between the simulation and experiment has been achieved by aligning the sharpest features in the two respective spectra.

Broadly, the experimental C 1s spectrum is characterized by four very intense features: two sharp ones below the ionization potential (IP) and two broad ones above the IP. The curve fit suggests that there are two features under the first peak and three underlying the second valley. The first peak has been attributed to C 1s excitations to two final-orbital levels dominated by Ti-3d character: '$2t_{2g}$' (284.6 eV) and '$2e_g$' (285.5 eV), with the higher intensity going to the latter. The '$2t_{2g}$' level can further be split into "two" levels (one of which is a quasi-doubly-degenerate level, see Figure 6.1), because the real symmetry of this molecule is much lower than O_h. However, the C 1s spectrum, recorded with an average energy resolution of about 0.6 eV, shows no sign of the splitting anyway. The EHMO data obtained from both the ground and excited states indicate that the splitting is about 0.21~0.23 eV. A high-resolution spectrometer would be required to observe this small gap.

The energy difference between the two components ('$2t_{2g}$' and '$2e_g$') of the first energy-loss peak is approximately 0.9 (±0.1) eV according to various curve fits. This corresponds to the 10Dq crystal-field splitting in the $CpTiCl_3$ quasi-octahedral field. The value determined by ISEELS is higher than predicted by EHMO (0.77 eV in the C 1s excited state), but very close to that measured for $TiCl_4$ (0.95 eV) by UV absorption experiment[145] or to the literature-value of $TiCl_4$(0.93 eV[144]), implying that there exists a very similar ligand field surrounding the Ti metal centre in both cases in spite of the fact that the two molecules have apparently different symmetries. This is rather consistent with the EHMO results depicted in Figure 6.1, in which the 10Dq values are 0.82 and 0.74 eV (in the ground state) for $CpTiCl_3$ and $TiCl_4$, respectively. The intensity imbalance between these two features, as suggested by the curve fit, is attributable to the C 2p character rooted in the '$2e_g$' MOs, which arises apparently from the interaction of $TiCl_3$ 1e orbitals with the Cp-ring e_1'' MOs. Such 2p valence-orbital character of the '$2e_g$' MOs would give rise to better overlap with the C 1s core orbital than the '$2t_g$' MOs, thus producing an enhanced resonance. In addition, symmetry analyses of the EHMO wave functions indicates that the $2e_g$ MOs are of π^* character, while the '$2t_{2g}$' are of σ^* character. For this reason, many workers[146,147,154] often refer to the 2e MOs of $TiCl_4$ as a π^*(Ti-Cl) and the t_2 MOs as σ^*(t,Ti-Cl).

The most prominent feature, peaked at 287.1 eV, is assigned to transitions from the C 1s to two quasi-degenerate unoccupied MOs of π^* symmetry, which originate from the e_2''-set LUMOs of the Cp ligand. Its large oscillator strength is ascribed to a good spatial overlap between the carbon 1s and the highly-localized e_2'' orbitals. In the ground state the π^* e_2'' MOs are energetically well-separated from other orbitals (see

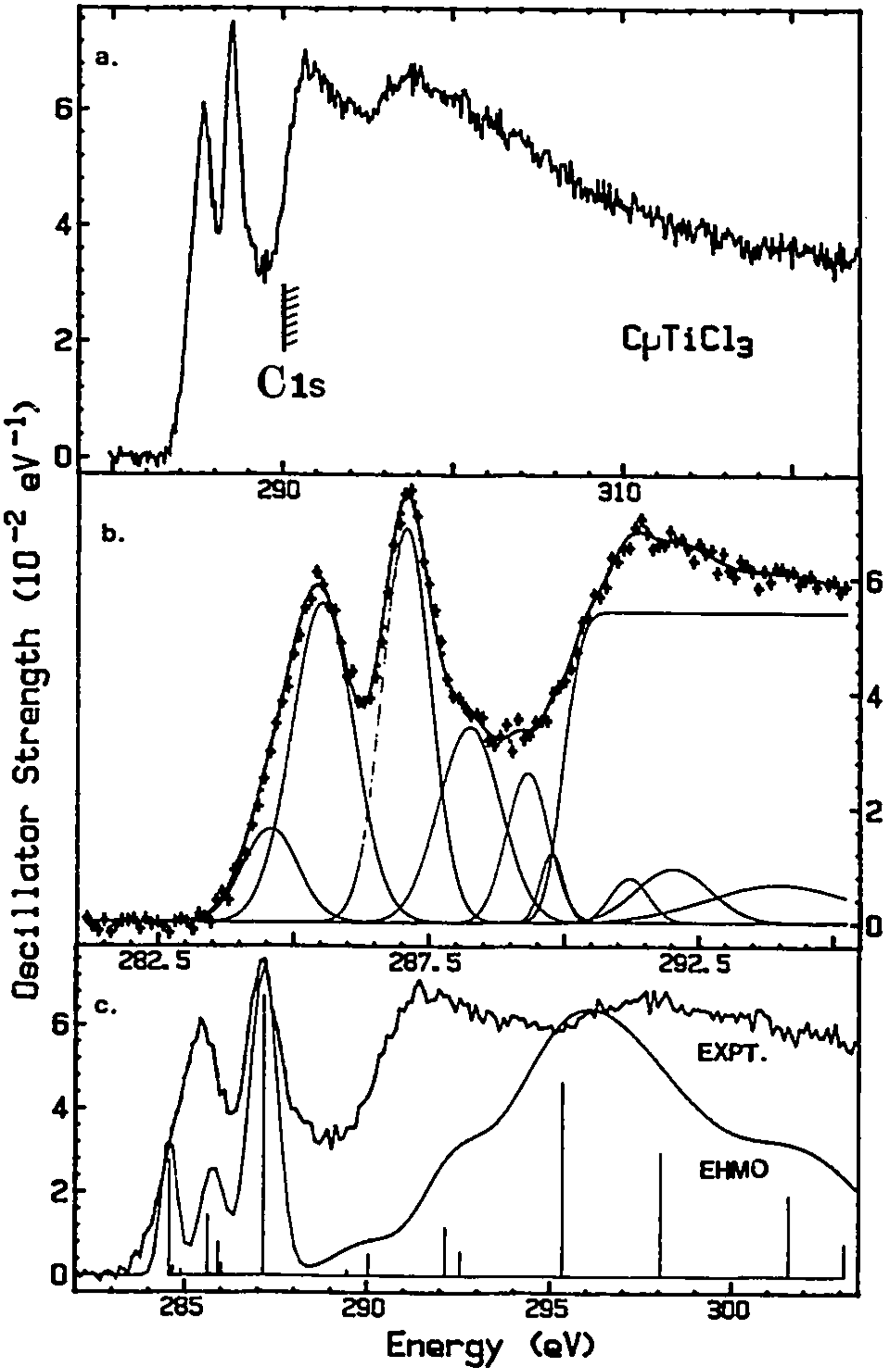

Fig. 6.2 (a) The C 1s spectrum of $CpTiCl_3$. (b) Gaussian curve fit, and (c) the EHMO spectral simulation.

Figure 6.1) and have little interaction with $TiCl_3$ orbitals. A dominant π*(Cp) character is supported by the EHMO simulation (Fig. 6.2). In the low energy zone, the simulated spectrum predicts relatively correct energy positions for the three major peaks, but a less-satisfying intensity match. For instance, the intensity ratio of the first two 'Ti-3d' features in the EHMO spectrum is the reverse of that provided by the curve fitting.

The intensity lying between 288 eV and the estimated ionization limit (290 eV) is assigned to a mixture of C 1s → σ*(C-H) transitions[41] and C 1s → Rydberg transitions. In many cases, such transitions are usually considered as a whole and termed "virtual-valence/Rydberg conjugates"[155] due to the fact that the final orbitals associated with these transitions are spatially very close and often mixed with each other. The first C 1s → σ_1*(C=C) excitation occurs in the continuum at ~291 eV, about one electron volt lower than its counterpart in ferrocene (See Table 6.1). However, a corresponding energy shift is not observed for the next σ_2*(C=C) shape resonance around 298 eV. The net effect is that in $CpTiCl_3$ there is a larger energy splitting among its σ*(C=C) orbitals, suggesting a stronger interaction between the adjacent C-C bonds of $CpTiCl_3$ relative to ferrocene,[108] consistent with the experimental findings obtained from IR studies.[156] The possible cause of this might be associated with the difference between the partially-charged $Cp^{\delta-}$ ligand in the more ionicly bonded $CpTiCl_3$ molecule and the relatively neutral Cp ring in the more covalently bonded $Fe(Cp)_2$ complex. The extra electron (or charge) density (δ-) transferred from Ti to Cp may preferably 'populate' one of the $e_1''(\pi)$ bonding orbitals of Cp, which is only half filled in free Cp. This would increase the C-C bond strength and lead to a stronger C-C bond interaction. Thus it appears that ISEELS data support the view of Ti-Cp having strong ionic character.

A weak band appearing in the deeper continuum (~301 eV) may be related to shake-up transitions. A similar feature was also observed in the C 1s spectra of other metallocenes.[13] Overall, the carbon 1s spectrum of $CpTiCl_3$ resembles those of other metallocenes, especially in the feature positions and the continuum shape. This is well illustrated in Figure 6.3, in which three experimental spectra are compared to each

Table 6.1 Energies (E, eV), Term Values (T, eV) and Proposed Assignments for Features in the C 1s Spectra of $CpTiCl_3$ and $Fe(Cp)_2$.

$CpTiCl_3$		$Fe(Cp)_2$		Assignment (final orbital)	
E	T	E	T	Ti	Fe
284.6[d]	5.4			'$2t_{2g}$*' (Ti 3d)	
285.5[d]	4.5	285.7	4.3	'$2e_g$*' (Ti 3d)	$4e_{1g}$* (Fe 3d)
287.16[a]	2.84	287.21[a]	2.82	π* (Cp e_2"*)	π* (Cp $3e_{2u}$*)
288.3	1.7	288.7	1.3	σ* (CH)	
289.3	0.7	289.1	0.9	Rydberg	
289.8	0.2			Rydberg	
290.0[c]		290.03[b]		IP	
		291.1	-1.1	double excitation	
291.2	-1.2	292.2	-2.2	σ_1* (C=C)	
297.7	-7.7	297.7	-7.7	σ_2* (C=C)	
301(sh)	-11	301(sh)	-11	shake-up	

a. Calibration relative to CO_2 (C 1s → π*: 290.74 eV): $\Delta E = -3.58(6)$ and -3.53(2) eV for $CpTiCl_3$ and $Fe(Cp)_2$, respectively.

b. IP from XPS.[92]

c. Estimated from the C 1s IPs of other metallocenes.

d. From the curve fit.

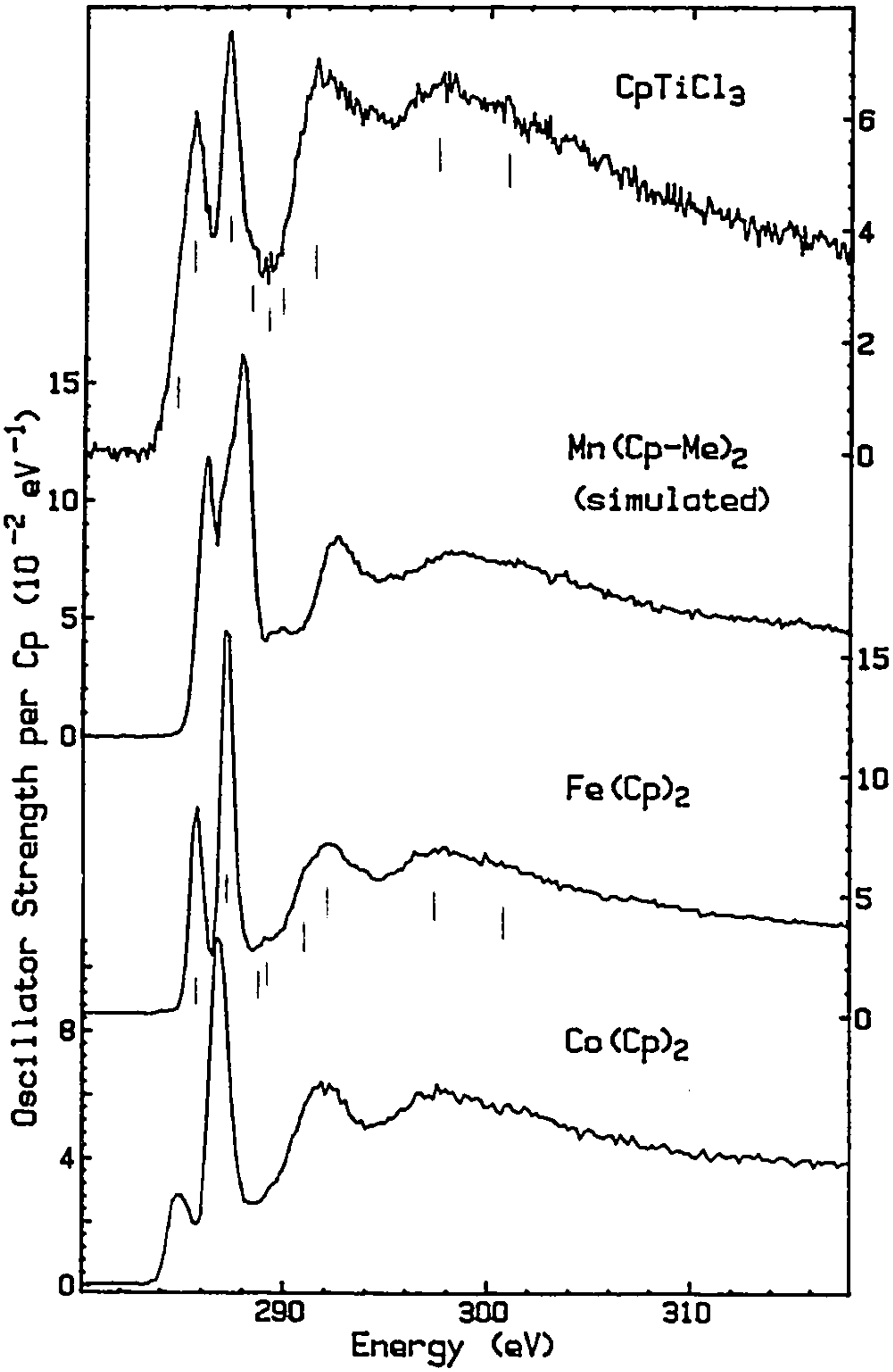

Fig. 6.3 The C 1s spectra of Cp-containing species.

other. The resemblance reflects the fact that these complexes share a similar virtual electronic structure and that the chlorine atoms have very little influence on carbon 1s excitation in $CpTiCl_3$ due to poor orbital overlap. The C 1s spectrum of $Mn(Cp\text{-}Me)_2$, simulated in Chapter 5, has also been plotted in the same figure for comparison. The resulting outcome is amazingly compatible with the other three spectra and demonstrates very impressively the degree of success and reliability of spectral additivity as applied to core excitation spectra.

However, there are systematic trends in the intensities and energies of the two major peaks below the threshold. The most notable variation of intensity is in the first peak which has C 1s → metal 3d character. It has the largest oscillator strength (peak area) for $CpTiCl_3$ but the smallest for cobaltocene. This may be rationalized in terms of the increasing population of the lower unoccupied MOs, those dominated by the metal 3d orbitals, owing to the gradual increase of the 3d-count in the metal atom from Ti to Co. The narrower line shape of the first peak in both ferrocene and cobaltocene relative to that of $CpTiCl_3$ is apparently due to missing C 1s → '$2t_{2g}$*'(3d) transitions because the '$2t_{2g}$*' orbitals are filled in these two species. The particularly low intensity of the first peak in the cobaltocene spectrum has been ascribed to the impeding function of the cobalt's additional 3d electron that has populated the $4e_{1g}$* level and reduced the empty character.[13]

§6.4 Cl 2p Spectra

The full-range ISEELS Cl 2p excitation spectra of both $CpTiCl_3$ and $TiCl_4$ are presented in Fig. 6.4b, while an expansion of the weak pre-edge structure is given in Fig. 6.4a. The quality of the $CpTiCl_3$ spectrum is poor due to the lack of a sufficient vapour pressure from the solid complex. However, a very precise spectrum has been recorded for $TiCl_4$. The Cl 2p spectra of the two species are very similar, as suggested by the ground-state EHMO studies (See Fig. 6.1), indicating that the two compounds have a rather comparable electronic structure as accessed by Cl 2p excitation, in spite of the fact that these two molecules belong to different point groups. It appears that the differences between the Cp ligand and the fourth Cl atom are of minor importance for Cl 2p inner-shell excitation. This seems rather understandable from the MO correlation diagram (Fig. 6.1), since both species possess a common band-like unoccupied structure derived chiefly from Cl empty 3d orbitals and, below it, two Ti-based levels (LUMO and LUMO+1) correlated between the two molecules via the orbitals of a common $TiCl_3^+$ unit. The five 3d orbitals of the fourth Cl anion merely insert into this group of Cl-3d-based MOs and do not make much difference. Thus, while the discussion below is focused on the $TiCl_4$ Cl 2p spectrum, it is also considered qualitatively applicable to $CpTiCl_3$ (except for reversal of ordering of the e/t_2 orbitals).

The energies, term values and proposed assignments of the two Cl 2p spectra are listed in Table 6.2. For $TiCl_4$, the first feature, that at 198.5 eV, is assigned to Cl 2p → σ^*(Ti-Cl) MOs ($4t_2$) transitions. Below this peak, there appears to be a weak shoulder around 197.8 eV, which is considered to be the Cl 2p → 2e π^*(Ti-Cl) resonance. The observed energy difference (~0.7 eV) between these two features is related to the 10Dq in $TiCl_4$, relatively lower than the 0.95-eV literature value from UV absorption measurement.[145] The lower value may be a consequence of core-hole relaxation although the reliability of the ISEELS value is somewhat questionable owing to the difficulty in locating the shoulder. A band-like feature centred at 200.4 eV may be associated with two kinds of transitions: one due to excitation of the Cl $2p_{3/2}$ → Cl 4s Rydberg orbital; and the other from the Cl $2p_{1/2}$ → $4t_2$ σ^*(Ti-Cl) transitions, although it is relatively high in energy to be the spin-orbit partner of the first peak according to the Cl 2p spin-orbit splitting observed in $TiCl_4$ (1.1 eV[150]). Nevertheless, the intensity ratio is apparently correct for a spin-orbit assignment, according to the intensity pattern observed in the ISEELS spectrum of Cl_2.[26] The sharpest peak in the Cl 2p spectrum that located at 202.4 eV, is assigned to Cl $2p_{3/2}$ → $3a_1$ transitions, a MO derived mainly from Cl 3d orbitals, and Cl $2p_{1/2}$ → Cl 4s transitions, a spin-orbit partner of the 200.4-eV feature. The large intensity is believed to be associated with the strong Cl $2p_{3/2}$ → $3a_1$(Cl 3d)

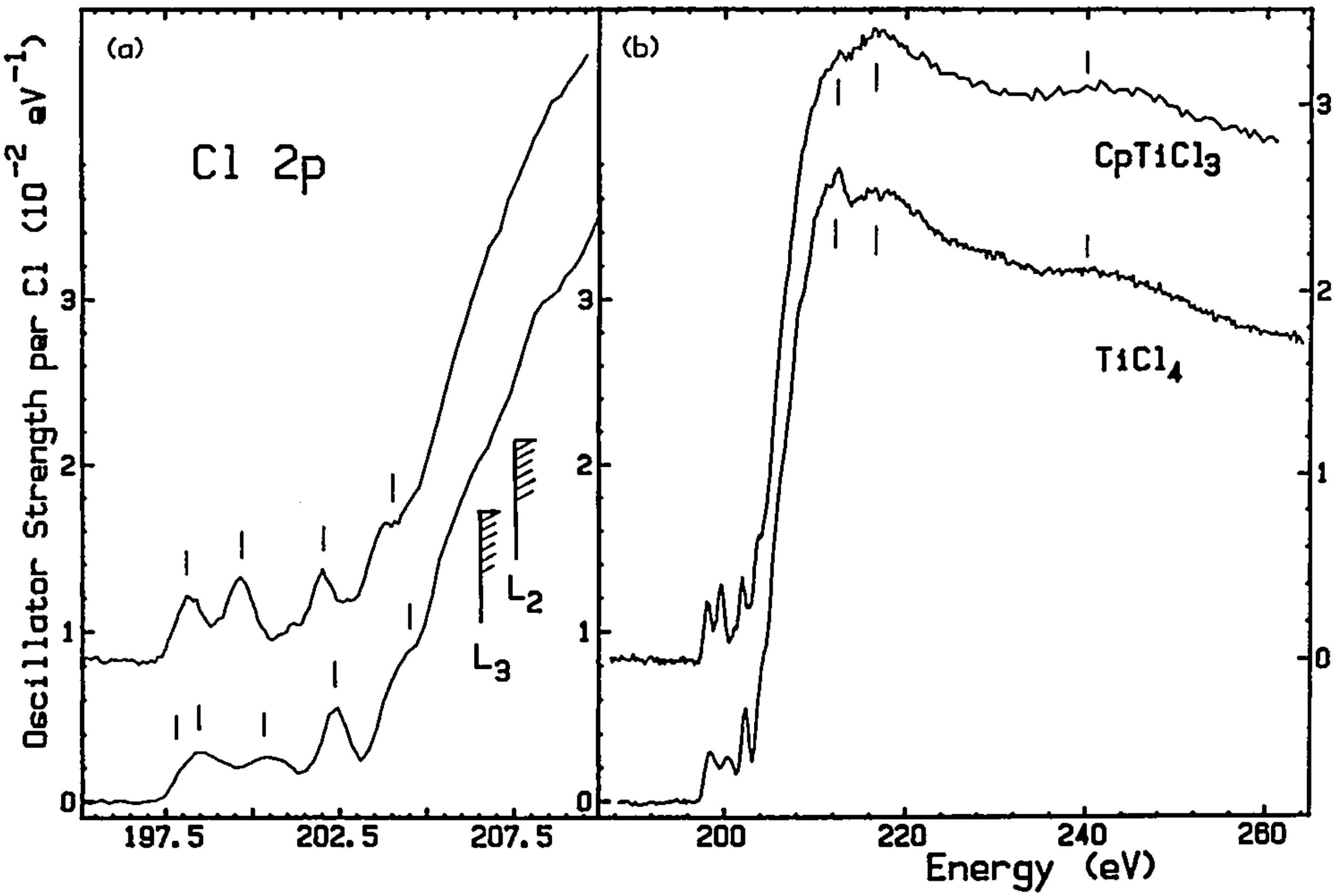

Fig. 6.4 (a) Close-up spectra of pre-IP range. (b) Full-range Cl 2p spectra of $CpTiCl_3$ and $TiCl_4$.

Table 6.2 Energies (E, eV), Term Values (T, eV) and Proposed Assignments for Features in the Cl 2p Spectra of $CpTiCl_3$ and $TiCl_4$.

$CpTiCl_3$			$TiCl_4$			Assignment (final orbital)	
E	T(L_3)	T(L_2)	E	T(L_3)	T(L_2)	$2p_{3/2}$ ($CpTiCl_3$ / $TiCl_4$)	$2p_{1/2}$
(197.7)	(8.9)		197.8	8.8		('$2t_{2g}$*') / 2e* π*(Ti-Cl)	
198.2	8.4		198.5	8.1		'$2e_g$*' / $4t_2$* σ*(Ti-Cl)	
199.9	7.0	(8.1)	200.4	6.2	7.3	4s (Cl)	$4t_2$* σ*(Ti-Cl)
202.3^a	4.3	5.4	202.4^a	4.2	5.3	'$2a_{1g}$*' / $3a_1$* (Cl 3d)	4s (Cl)
204.2		3.5	204.5		3.2		'$2a_{1g}$*' / $3a_1$*
206.6^c			206.6^b			$2p_{3/2}$ IP	
207.7^c			207.7^b				$2p_{1/2}$ IP
212.8	-5.6^d		212.5	-5.3^d		ϵd (Cl)	
217.	-9.8^d		217.	-9.8^d		σ*(Ti-Cl) shape resonance	
240	-33^d		240	-33^d		shake off or EXAFS	

a. Calibration relative to CO_2 (C 1s → π*:290.74 eV): $\Delta E = -88.42(8)$ and -88.38(8) eV for $CpTiCl_3$ and $TiCl_4$, respectively.

b. IPs from Ref. 150.

c. IPs assumed to be the same as $TiCl_4$.

d. Term value with respect to the mean Cl $2p_{3/2,\,1/2}$ IP (207.2 eV).

resonance, as the 3d channel is usually much stronger than the 4s due to larger spatial overlap. The corresponding Cl $2p_{1/2} \rightarrow 3a_1$ (Cl 3d) transition is likely the 204.5-eV feature, although it is superimposed on other underlying Rydberg structures and not well separated from the continuum onset. No spectral structure is attributed to Cl 2p → Cl 4p excitation. This is a dipole-forbidden transition in the atomic case but it has been observed occasionally in Cl 2p spectra,[26,157] because the molecular environment and intramolecular interaction in a polyatomic system relax the formal atomic selection rules.

There are three broad bands above the Cl 2p IP. The first of these bands, that peaked at 212.5 eV, has been observed as a cliff in the Cl 2p continua of some other species.[3a,26,65,157,158] This peak-like maximum above the edge may be assigned to the delayed onset of the Cl 2p → Cl ϵd continua[154,155] because the centrifugal barrier blocks the 2p → ϵd ionization channel at threshold.[159] This phenomenon is atomic essentially, and is characteristic of the 2p spectra of the late-period third-row elements.[158] The second continuum band, that around 217 eV, is tentatively attributed to a σ*(Ti-Cl) shape resonance of a term value about 10 eV. Other σ* shape resonances, such as the σ_2*(C=C) shape resonance in the case of $CpTiCl_3$, may also make some contribution to this band since such a continuum feature at a similar relative energy has already been noticed in the C 1s spectrum of $CpTiCl_3$ (*vide supra*). Finally, a quite broad band structure occurs around 240 eV. It is considered as a shake-off feature associated with multi-electron excitation. Structure of this sort will be met again in the Ti 2p spectra of these two compounds in the following section. Alternatively, this feature may be an EXAFS structure, as the Ti atom is a good backscatterer. In conclusion, the two Cl 2p spectra have a similar overall shape not only in energy but in intensity also, and the substitution of one Cl ligand with a Cp ring alters the spectrum very little, indicating that there is negligible spatial overlap between the Cl 2p and the Cp related orbitals. Therefore, although only the $TiCl_4$ spectrum has been analyzed in detail, its major results are regarded as transferable to the $CpTiCl_3$ spectrum, despite the fact that the latter has a lower molecular symmetry. It is of particular interest to note at this point that in many cases the Cl 2p spectra of various Cl-containing species are seemingly quite similar to each other, showing little of sensitivity to the change in molecular geometry and that these species may possess a fairly common electronic environment for Cl 2p excitation.

§6.5 Ti 2p Spectra

The 3d-metal 2p spectra in previous chapters have illustrated some fascinating structural changes at the edge with variation of ligands. Evidently, these spectra are good probes of the unoccupied electronic structures since the metal 2p excited states have narrow natural linewidths. Therefore, electric dipole excitations of the 2p electron in the 3d transition-metal complexes can furnish information concerning unoccupied states derived from the metal 3d orbitals. Here, the Ti 2p spectra of these two species are used to probe Ti 3d character of the unoccupied states. The molecular symmetry of $CpTiCl_3$ and $TiCl_4$ remain unchanged during Ti 2p excitation as the Ti metal occupies the centre of the molecule. Thus, the relative energy levels of the Ti-2p excited state will be analogous to those of the ground state in Figure 6.1 except that there may be a slight change in energy associated with core hole relaxation.

The wide-range Ti 2p ISEELS spectra of the two compounds are presented on the left-hand side of Fig. 6.5. Broadly, there are two sharp, intense peaks near the 2p thresholds. The one of lower energy is the transition from the Ti $2p_{3/2}$ level (L_3 edge) which is separated from the $2p_{1/2}$ (L_2 edge) transition by the spin-orbit splitting. The splittings observed here are 5.5 and 5.6 eV for $CpTiCl_3$ and $TiCl_4$, respectively. These are essentially the same value as for rutile (5.5eV),[110a,160,161] in which each Ti atom is surrounded by an octahedral arrangement of six oxygen atoms, and for $FeTiO_3$ (5.4 eV).[110a] However, they are ca. 0.5 eV smaller than the 6.1-eV spin-orbit splitting found in the XPS spectrum[150] of $TiCl_4$. A similar reduction has been seen also in the Cl 2p spin-orbit splitting between the ion state and core excited state. This may be associated

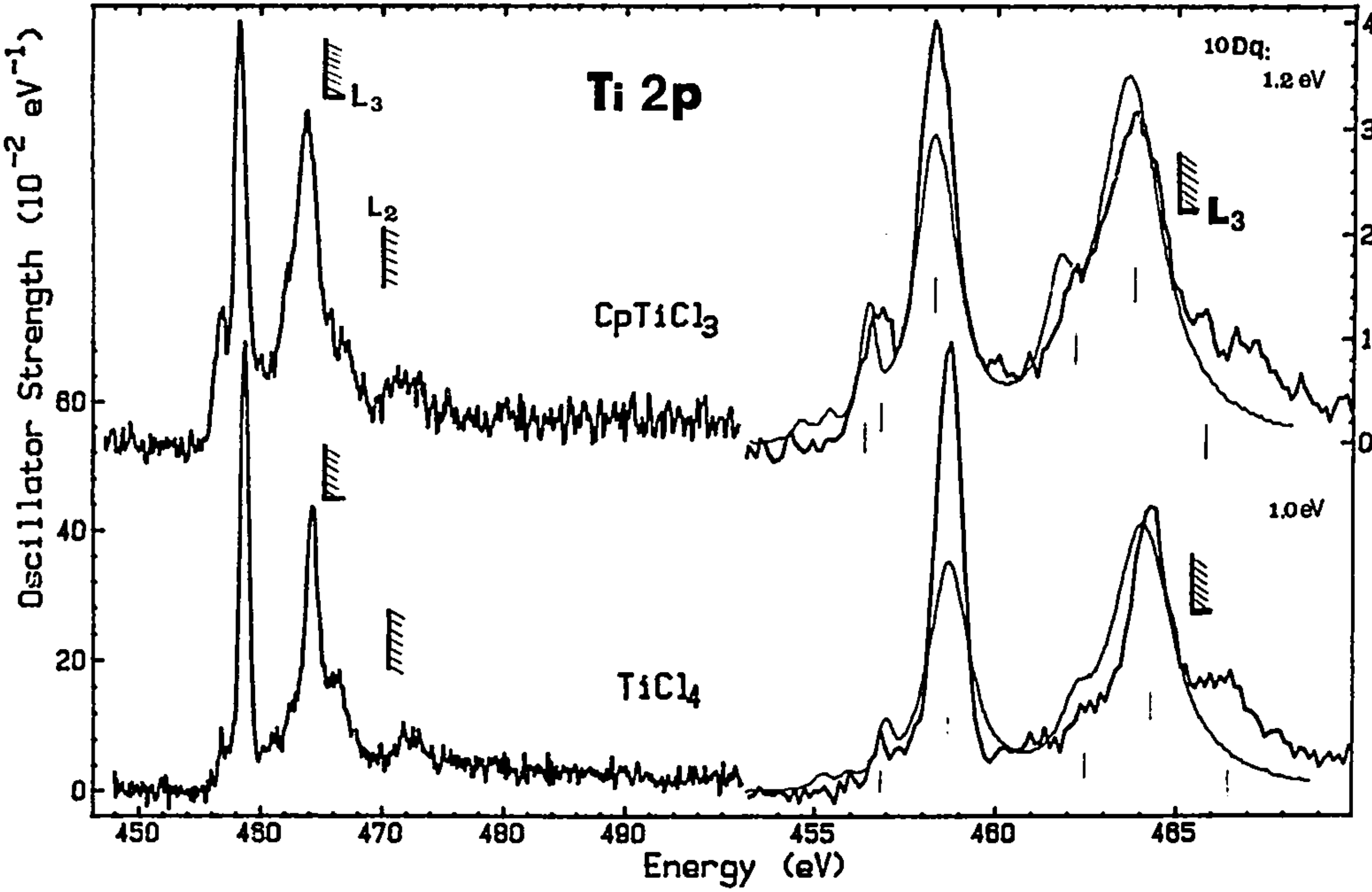

Fig. 6.5 (left) Full-range Ti 2p spectra of $CpTiCl_3$ and $TiCl_4$. (right) Comparison with the spectra predicted by the atomic multiplet theory.[110a]

with the exchange and multiplet effects of 2p core excitation, which modify the energies of the core excited states.[110a] These sharp threshold peaks are known as white lines as they were first found in X-ray absorption spectra, where the high absorption peak at the ionization limit resulted in almost no blackening on a photographic plate. Compared to the $L_{2,3}$ white lines[160] observed in metallic Ti and TiO_2, the L_3/L_2 intensity ratio in $CpTiCl_3$ and $TiCl_4$ is much closer to, though still different from, the statistical degeneracy value (2:1). A close-up of the discrete region reveals additional fine structure (see the right side of Figure 6.5). Specifically, in addition to the spin-orbit splitting, both L_3 and L_2 white lines are themselves split into at least two components. From the magnitude of the separation, this additional splitting is attributed to the ligand field effect.

The energies, term values and possible assignments for all features appearing in the Ti 2p spectra are summarized in Table 6.3. The relatively weak feature, observed at 456.9 eV (456.8 eV) in the $CpTiCl_3$ ($TiCl_4$) spectrum, is assigned to Ti 2p $\rightarrow$ '$2t_{2g}$*' (2e* for $TiCl_4$) transitions. These MOs come dominantly from the Ti 3d orbitals. For $CpTiCl_3$, an extra shoulder, around 456.5 eV, can be discerned just below this feature. It has been attributed to the other component of the Ti 2p $\rightarrow$ '$2t_{2g}$*'(Ti 3d) transitions whose triple degeneracy has been lifted slightly by virtue of the real lower molecular symmetry. The splitting of the '$2t_{2g}$' is found to be 0.4 eV, almost twice that predicted by EHMO (0.21 eV) in both the Ti 2p excited and ground states (See Fig. 6.1). The most intense line, that peaking at 458.3 eV (458.7 eV, for $TiCl_4$), is ascribed to Ti 2p $\rightarrow$ '$2e_g$*' ($4t_2$* for $TiCl_4$) transitions, about 1.4 eV (1.7 eV) above the '$2t_{2g}$*' (2e*) state. This 1.4-eV (1.7-eV in $TiCl_4$) 10 Dq splitting of the ligand field is much lower than observed in both TiO_2 (2.5 eV)[110a,160,161] and $FeTiO_3$ (2.2 eV),[110a] but it is somewhat larger than found in the C 1s spectrum (0.9 eV) and predicted by EHMO for the Ti excited state (1.0 eV).

Currently, there are two major theoretical models dealing with the electronic structures of transition metal complexes: the crystal field theory treating a perturbed

Table 6.3 Energies (E, eV), Term Values (T, eV) and Proposed Assignments for Features in the Ti 2p Spectra of $CpTiCl_3$ and $TiCl_4$.

$CpTiCl_3$			$TiCl_4$			Assignment (final orbital)	
E	$T(L_3)$	$T(L_2)$	E	$T(L_3)$	$T(L_2)$	$CpTiCl_3$	$TiCl_4$
456.5	8.5					'$2t_{2g}$*' (Ti 3d)	
456.9	8.1		456.8	8.6		'$2t_{2g}$*' (Ti 3d)	2e* (Ti 3d)
458.3[a]	6.7		458.7[a]	6.7		'$2e_g$*' (Ti 3d)	$4t_2$* (Ti 3d)
462.2		8.8	462.6		8.9	'$2t_{2g}$*' (Ti 3d)	2e* (Ti 3d)
463.8		7.2	464.3		7.2	'$2e_g$*' (Ti 3d)	$4t_2$* (Ti 3d)
465.0[c]			465.4[b]			Ti $2p_{3/2}$ IP	
465.8	-0.8		466.5	-1.1		'e_g'(Cl) → '$2e_g$*'	1e(Cl) → 2e* shake-up
471.0[d]			471.5[b]			Ti $2p_{1/2}$ IP	
471.3		-0.3	471.8		-0.3	'e_g'(Cl) → '$2e_g$*'	1e(Cl) → 2e* shake-up

a. Calibration relative to the C 1s → π^*(Cp) of the same species (287.16 eV): ΔE = 171.1(3) eV for $CpTiCl_3$; to N_2 (N 1s → π^*: 401.10 eV): ΔE = 57.6(1) eV for $TiCL_4$.

b. IPs from Ref. 150.

c. Estimated from IPs of TiX_4 (X = F, Cl, Br and I).

d. Obtained from the L_3 by adding the separation of the two main L_3 and L_2 peaks.

metal atom; and the ligand field (molecular orbital) theory capable in principle of describing charge transfer and covalent effects between metal and ligands. Seeing the EHMO calculations are unable to give a fully satisfactory explanation for our metal 2p spectra (see Chapter 4, especially, Fig. 4.10), the atomic multiplet model[110] has also been explored. However, there is still some distance between theory and reality. The problem is seemingly associated with the starting point of the model, which leads to final results that are more suitable for species of strong ionic character instead of more covalent organometallic complexes. For this reason as well as for simplicity (relatively less multiplet-splitting complication in the d^0 species), both $CpTiCl_3$ and $TiCl_4$ were selected as 'trial' molecules of considerable ionic character, to re-examine the atomic multiplet effect in 3d-metal 2p spectra. De Groot *et al*[110a] have calculated 2p inner-shell spectra for Ti^{4+} ($3d^0$) compounds of O_h symmetry using the atomic description. In order to implicitly include the electrostatic-field effect of the ligands, they introduced a variable crystal-field parameter 10Dq in their calculations with the intent of fitting and/or using the experiment to define the appropriate 10Dq value. It has been found that their simulated spectra of 1.0 and 1.2 eV 10Dq fit the Ti 2p experimental spectra best. These have been plotted in Fig. 6.5 (light line) in comparison with the experimental spectra. For comparison to experiment the simulations have been shifted about 6.7 eV and adjusted in intensity for the best match.

Figure 6.5 (right side) shows a rather good agreement between the calculation and experiment, especially for $CpTiCl_3$. This justifies that the central Ti atom is in an effective O_h coordination environment in both compounds, implying that the Cl and Cp ligands generate a comparable ligand field. The two calculated spectra suggest the 10Dq are 1.0 and 1.2 eV, but the actual values displayed in the simulations are 1.6 and 1.9 eV respectively. In other words, the energy splitting in the Ti 2p spectrum is not simply equal to the 10Dq directly. The cause of this is that the distance between the two main peaks at the L_3 (or L_2) edge is given as a function of the crystal field (10Dq). Naturally, the energy splitting in the core-excitation spectra is not equal to 10Dq in general.[110]

Nevertheless, the predicted 10Dq values are very close to the experimental splittings of the two L_3 components (See Fig. 6.5). Interestingly, it appears that the 10Dq varies with the edge and has a higher value at the metal edge, reflecting that it is presumably related to multiplet details. In the specific case here, we consider this is because the created cole hole in the Ti metal has modified the final states of the Ti 3d orbitals by virtue of interaction between the hole and excited 2p electron in the final orbitals, both of which are very much localized in the central Ti metal.

Through the comparison in Fig. 6.5, one sees that the atomic multiplet model including the crystal field does work well for the two Ti compounds here, not just in terms of believable predictions of the different splittings, but also the right line shapes for both the L_2 and L_3 edges. However, there are also some features in the continuum region of the 2p spectra which are missing in the calculated spectra. They can not be accounted for by the atomic treatment because of a missing term(s) in Hamiltonian operator of the atomic multiplet theory. It is of interest to note that the strong features shown in our Ti 2p spectra do not appear in the Ti 2p spectra of other related species (e.g. $FeTiO_3$ and TiF_3) recorded by high-resolution photoabsorption spectroscopy.[110,111] Although considerable effort has been focused on a one-electron model, it is conceded in general that correlation effects are important in core excitation of the transition-metal species. The feature of 466 eV (466.5 eV), above the $2p_{3/2}$ ionization threshold, is considered to be a monopole shake-up excitation from the ligand-based valence MOs to the unoccupied MOs of the Ti 3d orbitals, i.e., a process of ligand-to-metal charge-transfer character. According to the similar appearances of the line shape, the feature has a common origin in the two spectra.

For $CpTiCl_3$, there exist two kinds of possible charge-transfer transitions being able to meet the monopole selection rule: They are 'e_g'(Cl) $\rightarrow$ '$2e_g$*'(Ti 3d) and '$1t_{2g}$'(Cl) $\rightarrow$ '$2t_{2g}$*'(Ti 3d) shake-up excitations. In the Ti excited state, the 'e_g'-set MOs have a calculated orbital energy of -15.1 eV, which are just below the '$1a_{1g}$' MO in Figure 6.1, and are constructed almost solely by Cl 3p orbitals. This gives a 5.5-eV energy difference between the two 'e_g' sets and a reasonable close match to the 7.5-eV separation between the shake-up and the main $L_2 \rightarrow$ Ti-3d line. Next to the 'e_g' level, the '$1t_{2g}$'-set MOs of 15.3-eV orbital energy derive mainly from the Cl orbitals but with a sizable Ti-metal participation, and produce only a 4.7-eV energy separation between the two 't_{2g}' sets. Therefore, without ruling out the possibility of the 't_{2g}'(Cl) → 't_{2g}*'(Ti) transition, we assign preferably the shake-up feature to the 'e_g'(Cl) → 'e_g*'(Ti) transitions. This is seemingly supported by Larsson's[162] studies on the octahedral species TiC_6^{8-} and TiF_6^{2-}. In the case of $TiCl_4$, we face a similar situation encountered in $CpTiCl_3$, i.e., one must make a choice between the 1e(Cl) → 2e*(Ti) and $3t_{2g}$(Cl) → $4t_{2g}$*(Ti) transitions. In terms of the EHMO energy levels of the Ti excited state, the gap between the two e sets is ca. 4.6 eV, slightly lower than that of the two t sets (4.8 eV). Obviously, it is quite tempting to attribute the shake-up feature of the 7.8-eV separation in $TiCl_4$ mainly to the $t_2 \rightarrow t_2$* transitions. Upon comparison to the $CpTiCl_3$ case, however, we maintain our assignment of the e → e* transition for the shake-up excitation observed in the $TiCl_4$ spectrum, but consider that it may also involve the t-type multiplet transitions. A similar assignment has been given by Wallbank *et al*[150] for shake-up features in the XPS spectra of TiX_4. Interestingly, Tossell[163] considered these continuum features to be associated with the ligand-to-4s/4p(Ti) transitions based on his MS-Xα calculations on TiO_2.

Having discussed the energies of the line, we turn now to the line shape of the features in the two Ti 2p spectra. There are two points deserving to be singled out for recognition here. The first is associated with the oscillator strength of the two spectra, At the L_3 edge, the main line (458 eV) in the $CpTiCl_3$ spectrum has a smaller intensity than its counterpart in $TiCl_4$. This is understandable as the final states in the two species are related to doubly ('$2e_g$*') and triply ($4t_g$*) degenerate orbitals, respectively, with a degeneracy ratio of 2-to-3. This is fairly similar to the relative heights of the two 458-eV peaks (40:68) in Figure 6.5. If one considers the low-energy region as a whole in the respective spectra, viz., including both features below the threshold, there should be an approximately equal oscillator strength for this region since in both cases the signal derives from five Ti-3d orbitals. This proves to be the case. Integration of the 455-460 eV region shows that the oscillator strength observed for $CpTiCl_3$ (0.73 eV^{-1}) is very close indeed to that found in $TiCl_4$ (0.77 eV^{-1}), indicating that the transition probability of $TiCl_4$ is re-distributed for $CpTiCl_3$ in this energy region. Secondiy, the peak at the L_2 edge looks broader than its spin-orbit mate at the L_3 edge. This is particularly manifest in the $CpTiCl_3$ spectrum. Several factors may cause the broadening, among which lifetime effects probably come into play since in principle the more highly excited the state, the shorter lifetime (comparison over a large energy range), and thus a relatively wider natural line width. Yet, the lifetime effect is expected to be negligible here as the spin-orbit splitting in Ti-containing compounds is relatively small (*ca.* 5.5 eV). In general, L_2 features are always broader because of the reduced core-hole lifetime associated with the L_2L_3M super-Coster-Kronig (CK) Auger decay processes. It is because of this Auger effect that the Ti L_2 line predicted by de Groot *et al*[110a] becomes wider than the L_3 line. However, the occurrence of such a decay process appears right on its limit, since the 5.5-eV spin-orbit splitting does not seem to provide enough energy to eject a valence-shell electron from the two Ti compounds, whose lowest ionization energy is 9.8 eV.[147,152] As pointed out by de Groot *et al*[110] themselves that the energy difference between the $2p_{1/2}$ and $2p_{3/2}$ core hole must be larger than the binding energy of the d electron, otherwise the CK decay channel will be closed. According to the graphic table of atomic-level widths of the elements,[136] Ti is almost the first element to begin to have the CK decay process for $2p_{1/2}$ core excitation. From the nice agreement of the L_2-edge major features between the simulated and experimental spectra (Figure 6.5), it appears that the L_2-edge broadening is indeed associated with the CK Auger decay. Other mechanisms of the intrinsic broadening in 2p core excitation have been discussed by de Groot *et al*[110] in some detail.

be an approximately equal oscillator strength for this region since in both cases the signal derives from five Ti-3d orbitals. This proves to be the case. Integration of the 455-460 eV region shows that the oscillator strength observed for $CpTiCl_3$ (0.73 eV^{-1}) is very close indeed to that found in $TiCl_4$ (0.77 eV^{-1}), indicating that the transition probability of $TiCl_4$ is re-distributed for $CpTiCl_3$ in this energy region. Secondly, the peak at the L_2 edge looks broader than its spin-orbit mate at the L_3 edge. This is particularly manifest in the $CpTiCl_3$ spectrum. Several factors may cause the broadening, among which lifetime effects probably come into play since in principle the more highly excited the state, the shorter lifetime (comparison over a large energy range), and thus a relatively wider natural line width. Yet, the lifetime effect is expected to be negligible here as the spin-orbit splitting in Ti-containing compounds is relatively small (*ca.* 5.5 eV). In general, L_2 features are always broader because of the reduced core-hole lifetime associated with the L_2L_3M super-Coster-Kronig (CK) Auger decay processes. It is because of this Auger effect that the Ti L_2 line predicted by de Groot *et al*[110a] becomes wider than the L_3 line. However, the occurrence of such a decay process appears right on its limit, since the 5.5-eV spin-orbit splitting does not seem to provide enough energy to eject a valence-shell electron from the two Ti compounds, whose lowest ionization energy is 9.8 eV.[147,152] As pointed out by de Groot *et al*[110] themselves that the energy difference between the $2p_{1/2}$ and $2p_{3/2}$ core hole must be larger than the binding energy of the d electron, otherwise the CK decay channel will be closed. According to the graphic table of atomic-level widths of the elements,[136] Ti is almost the first element to begin to have the CK decay process for $2p_{1/2}$ core excitation. From the nice agreement of the L_2-edge major features between the simulated and experimental spectra (Figure 6.5), it appears that the L_2-edge broadening is indeed associated with the CK Auger decay. Other mechanisms of the intrinsic broadening in 2p core excitation have been discussed by de Groot *et al*[110] in some detail.

§6.6 Ti 3p Spectrum

The Ti 3p inner-shell excitation spectrum of $TiCl_4$ is presented in Figure 6.6 (left side), along with the Cr 3p spectrum of $C_6H_6Cr(CO)_3$ and the Mn 3p spectrum of CH_3-$C_5H_4Mn(CO)_3$. These three molecular metal 3p spectra have also been compared to the corresponding atomic spectra of the same edges[164] in Fig. 6.6 (right side). Apparently, the molecular spectrum looks simpler than its pure atomic counterpart, but much more complicated than predicted by van der Laan's[114] atomic multiplet model, which suggests that the Ti 3p spectrum of $3d^0$ species will be characterized by a single sharp line. In part the reduced details of molecular spectra may be associated with the lower experimental resolution (0.6 eV) than in the atomic spectra (~0.2 eV). No detailed discussion of assignments is given here, but the spectral silhouette can be drawn readily from Figure 6.6. The maxima, at the Ti 3p ionization threshold[150] 44.6 eV, are attributed to $3p^63d^0 \rightarrow 3p^53d^1$ transitions. The strong band around 48 eV may result from the delayed maxima of the Ti 3p continua, due to the centrifugal barrier to the $3p \rightarrow \epsilon d$ ionization channel, or may arise from σ^* shape resonances, or a combination of both. Like the 3p spectra of the Cr and Mn complexes, the Ti 3p spectrum of $TiCl_4$ reveals also a weak M_1-edge feature at *ca.* 62 eV, superimposed on the $M_{2,3}$ edge continua.

All the metal 3p spectra of the compounds exhibit a pronounced asymmetry which may arise from interference between $3p \rightarrow 3d$ resonances and background (3d) absorption. This effect seemingly suggests that the 3d states are not completely localized in the compounds. Comparisons between the molecular and atomic spectra do not reveal a close correspondence. This is in agreement with the partly itinerant character of the d electron in the molecule. It has been expected that $3p \rightarrow d$ resonances will be modified unequally in the presence of a different molecular environment, as can be seen readily in the metal 3p spectra on going from metal-carbonyl complexes to mixed-ligand species to metallocenes (see Chapters 3 and 4).

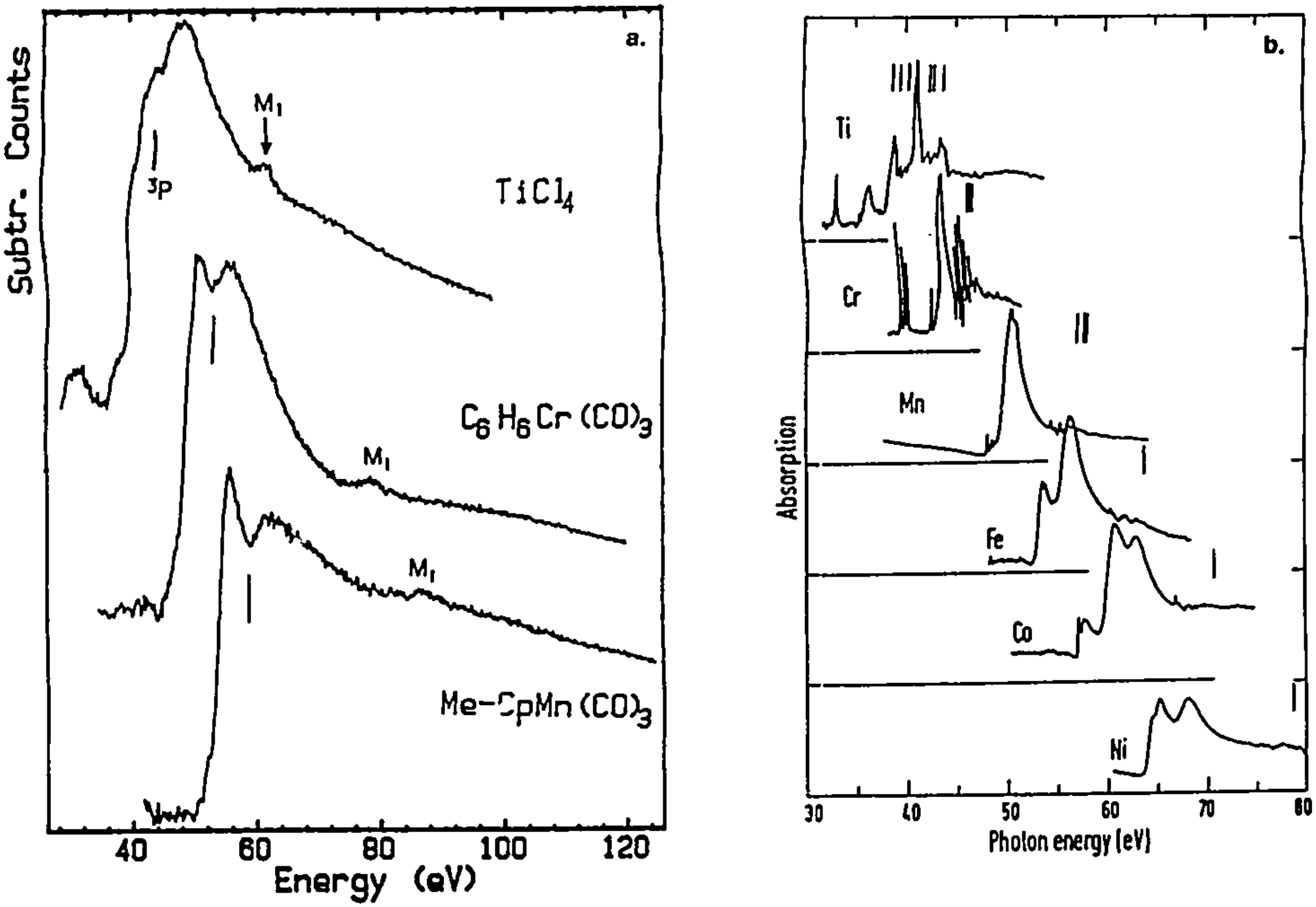

Fig. 6.6 (a) The Ti 3p spectrum of $TiCl_4$, compared to the 3p spectra of the Cr and Mn complexes. (b) photoabsorption spectra[164] of atomic 3d transition metals. The vertical bars mark the 3p IPs.

§6.7 Summary

The inner-shell spectra of $CpTiCl_3$ and $TiCl_4$ have been interpreted with the aid of EHMO calculations. The splittings related to 10Dq values differ at different edges. The one from C 1s excitation of $CpTiCl_3$ seems closer to the value determined by other experiments. However, it should be pointed out that the splittings observed in the core excitation spectra do not directly give 10Dq values due to multiplet details as well as relaxation effects associated with the created core hole. Therefore, the 10Dq data obtained here only have relative significance. Strong multi-electron excitation has been observed in Ti 2p spectra. According to the Cl and Ti 2p spectra, it appears that the difference between the Ti-Cp and Ti-Cl bonds does not affect core excitation very much, although the EHMO results suggest that there is stronger bonding between the Ti metal and Cp ligand than between Ti and Cl. This may reflect that the Ti-Cp and Ti-Cl bonds have a comparable bonding strength as well as similar nature. The Ti 2p spectra of the two compounds have been compared to two atomic-multiplet spectra simulated for the $3d^0 \rightarrow 2p^5 3d^1$ excitation of Ti^{4+} by the atomic multiplet theory. The results show that in the pre-edge region there is good agreement between theory and experiment, implying the presence of strong ionic character in these two covalent Ti compounds.

Chapter 7

CORE EXCITATION OF GAS-PHASE ORGANOSILICON COMPOUNDS $(CH_3)_3Si$-$Si(CH_3)_3$ AND $Si[Si(CH_3)_3]_4$: WHERE IS THE Si-Si σ^* RESONANCE?

§7.1 Introduction

The molecular and electronic structure of organopolysilanes has long been an intriguing topic due to their wide practical application in the semiconductor industry. The great attention paid to these compounds stems in part from the fact that they show unusual properties, implying remarkable electron delocalization.[165] Furthermore, polymethylsilanes have become important as precursors for silicon carbides, which may be of industrial significance, especially in the form of high-strength fibres.[166] Knowledge of the electronic structure is undoubtedly valuable to the better understanding of the intrinsic properties of these molecules. However, spectral information on compounds containing a silicon-silicon bond is relatively sparse and unsatisfactory. Until recently the chemistry and physics of Si-Si bonded species was primarily that of the disilanes, of which a very large number are known, such as hexamethyldisilane (HDS): $(CH_3)_3Si$-$Si(CH_3)_3$. More recently, however, research emphasis has shifted toward compounds with larger numbers of silicon atoms, such as tetrakis-(trimethylsilyl)silane (TTS) $Si[Si(CH_3)_3]_4$, or even toward Si-related polymers.[167] The molecular structures of both molecules have been determined by gas-phase electron diffraction. HDS exists in a staggered conformation like that of ethane,[168] whereas TTS is distorted from the tetrahedral structure by a twisting of each trimethylsilyl group by about 11°.[169]

A notable property of the alkylpolysilanes is that their electronic absorption occurs at low energy relative to alkanes, which do not absorb above 160 nm in general. This was somehow surprising when first discovered,[170] since these molecules have no π, d or lone-pair electrons whatsoever; in fact they were the first substances bearing only bonding σ-electrons to demonstrate such a long-wavelength absorption. Photoelectron spectroscopy (PES) indicates that the HOMOs in polysilanes (Si_nH_{2n+2}) are essentially Si-Si σ-orbitals.[170,171] The first ionization potential decreases with increasing chain length, consistent with bond-bond interaction and splitting of the energies of the Si-Si σ MOs. Electronic transition energies for the linear permethylsilianes are well correlated with the ionization potentials, with $IP/h\nu \approx 1.4$ (e.g., for HDS: IP = 8.46, $h\nu = 6.41$ eV[172]). This suggests that the unoccupied antibonding (σ^*) MOs are also split by bond-bond interaction, although the splitting seems to be only about 40% of that for the Si-Si bonding MOs.

As already noted above, it may appear somewhat preposterous at first glance that saturated systems like alkylpolysilanes could have their lowest electronic excitation in the near ultraviolet region. However, such low-lying excitations have been elucidated already in some saturated species on the basis of the 'weak-bond model'.[91] In terms of this model, a weak σ bond in a saturated species results in a small σ-σ^* splitting that in turn can give rise to low-energy $\sigma \rightarrow \sigma^*$ excitations. Such a weak-bond situation is especially favourable when atoms in the second and higher rows of the Periodic Table are involved. It is therefore of particular interest at this point to compare the Si-Si bond energy in a polysilane with the C-C bond energy in the corresponding alkane. The thermochemical strength of the Si-Si bond appear somehow controversial for years. The more reliable estimates[173] of this elusive quantity place it between 63 and 79 kcal/mol. This is just slightly weaker than the C-C bond in alkanes (*ca.* 81.3 kcal/mol). For instance, in the molecular pair of disilane and ethane, the bond energies for the central bonds are 74 and 88 kcal/mol, respectively, whereas for the isostructural pair elemental silicon and diamond, the bond energies are 54 and 85 kcal/mol.[174] According to these data, it appears that the Si-Si bond falls in the weak-bond category, those with 50-80 kcal/mol bond energy. Thus, there is thermochemical support, within the weak-bond model, that one or more low-lying σ^* MOs may occur in the polysilanes and that $\sigma \rightarrow \sigma^*$ excitations will fall below the lowest Rydberg excitation.[91] This line of thinking has motivated the present study of core excitation of HDS and TTS and a search for Si 2p spectral features associated with the weak Si-Si σ^* bond.

On the other hand, it has been believed in general that the lowest-energy transition in the longer alkanes is actually a promotion to valence rather than Rydberg state,[175] namely, a $\sigma \rightarrow \sigma^*$ valence promotion. In a similar manner, as the number of silicon atoms increases in organopolysilanes, the lowest-energy promotion in valence excitation may change its character from Rydberg to valence. This means that in core excitation the lowest-energy transition will also terminate at the virtual-valence MO(s) of σ^* symmetry. According to various theoretical calculations of the polysilanes, the HOMO σ consists of only Si 3s and 3p AOs, while the LUMO σ^* is comprised largely of either Si 3s, 3p,[176-178] 3d[179], or 4s, 4p AOs.[180] Since the 3d, 4s and 4p AOs are Rydberg orbitals in the polysilanes, whereas the transition in valence excitation has shown clearly valence instead of Rydberg character,[181] emphasis is placed principally on 3s and 3p AOs forming the σ^* MO(s). In order to explore the energy position and orbital compositions of the Si-Si σ^* virtual-valence level in the organopolysilanes, HDS has been selected as a trial target for gas-phase ISEELS investigations.

Judging from the above argument and the case study[91] of $(CH_3)_3CO\text{-}OC(CH_3)_3$, one may expect the Si 2p spectrum of HDS to exhibit a low-lying excitation feature terminating at a Si-Si σ^* MO, and even more, such an excitation should be the first spectral feature, separated from higher-energy Rydberg structures. For core excitation originating at Si 2p AOs, transitions will occur to virtual-valence orbitals possessing 3s character in their AO makeup (3d orbitals are energetically located above the ionization threshold and thus not of concern here). Thus, if the Si-Si σ^* MO contains substantial 3s character, the Si 2p spectrum of an organopolysilane should indicate directly the presence of the Si-Si σ^* resonance. However, such a resonance is expected to be weak in intensity if only one Si-Si bond is present in the molecule, as 2p → 3s excitations are weak relative to 2p → 3d exci-tations. In order to enhance the weak intensity of the Si-Si resonance, TTS, which contains four Si-Si bonds, was chosen for study. The results presented below have proven that this strategy works well.

The present thesis work was initiated in part by the quest for a metal-metal σ^* resonant feature in the ISEELS spectrum of the dinuclear organometallic complexes. Yet no such resonance has been found in any spectrum of the dinuclear complexes thus far, even in the metal 2p spectra, presumably because of the intrinsically weak nature of the single M-M σ^* resonance, which might be overshadowed or even masked completely by other adjacent resonances of strong intensity. The failure to observe a M-M σ^* feature shifted the attention to compounds of the main group elements of mildly metallic character. The position of silicon in the upper centre of the Periodic Table classifies it as the gentlest of metals. It has few of the metallic features of the heavier elements of group IVA, with empty 3d AOs and little tendency to form stable divalent derivatives. Successful observation of the Si-Si σ^* resonance of the organosilicon compounds should give some clues to the characteristics of features postulated in the context of the weak bond model to be associated with the M-M σ^* MO level in the dinuclear metal species. It has been assumed that this would appear as a weak feature at lowest energy, since the M-M bond is normally a weak bond owing to the long bond distance and poor orbital overlap.

High-resolution ISEELS spectra of tetramethylsilane[182] (TMS), $Si(CH_3)_4$, have been cited here as a reference to facilitate identification of the Si-Si σ^* resonance as well as to assist the assignments of the ISEELS spectra of HDS and TTS. It has been well known that the Si $2p_{3/2}$—$2p_{1/2}$ spin-orbit splitting is 0.61 eV, as determined by XPS for a variety of silicon-containing compounds.[183] It follows that in high-resolution work on TMS both Si $2p_{3/2}$ and $2p_{1/2}$ excited states should be taken into account when the Si 2p spectrum is analyzed. In the present work, however, the spin-orbit splitting is not considered since the energy resolution of the spectrometer employed is approximately of the same magnitude as the spin-orbit splitting and detailed fine structures were not observed in the recorded Si 2p spectra of HDS and TTS. In addition, the major objective of this work is to search for the Si-Si σ^* resonance, and therefore the interpretation of the spectra becomes relatively simple and can be focused primarily on the main lines and the broad picture or trend.

§7.2 Si 2p Spectra

ISEELS spectra in the silicon 2p edge region of HDS, TTS, and TMS[183] are presented in Figure 7.1. The energies of the spectral features, term values relative to the Si $2p_{3/2}$ edge value, and possible assignments are given in Table 7.1. The most notable feature of these three spectra is the first peak of large intensity in the low-energy region of the TTS spectrum, which also appears as a distinct shoulder in the HDS spectrum but is completely missing for TMS. The previous work on TMS[182] has already determined that the pre-edge features are dominated by Rydberg structures with the lowest-energy shoulder at 103.6 eV, being assigned to the Si 2p → a_1*(4s), t_1*(4p) transitions. MS-Xα calculations[184] show that there are no low-lying antibonding orbitals in TMS, and the lowest empty MO is just the lowest Rydberg orbital.[185] It is clear that the LUMO in both TTS and HDS is a strongly antibonding, valence-type orbital rather than a Rydberg orbital. Therefore, the first feature in the discrete region, peaked at 102.5 eV with a 4-eV term value, is assigned to Si 2p → Si-Si σ^* transitions for both TTS and HDS. This is consistent with the weak bond model, owing to the relatively weak Si-Si bonds. The width of the peak is also in accord with a dissociative character to the (Si $2p^{-1}$, Si-Si σ^*) state.

The unambiguous observation of this low-lying feature in HDS indicates that the Si-Si σ^* MO possesses a sizable Si 3s character. Involvement of Si 3s AOs in the Si-Si σ^* MO is in accord with a virtual-valence nature of this level (*vide supra*). This result is supported by several calculations on the polysilanes[177,186] and ESR studies on some stable anion radicals of cyclic methylated silanes which have revealed evidence for a uniformly-distributed lowest unoccupied level with 3s-orbital character.[165] The large oscillator strength of the Si-Si σ^* resonance in the Si 2p spectrum of TTS is attributed to the presence of a large number of Si-Si bonds in this compound, which results in a large number of near-degenerate Si-Si σ^* orbitals and a high Si 3s density in the valence

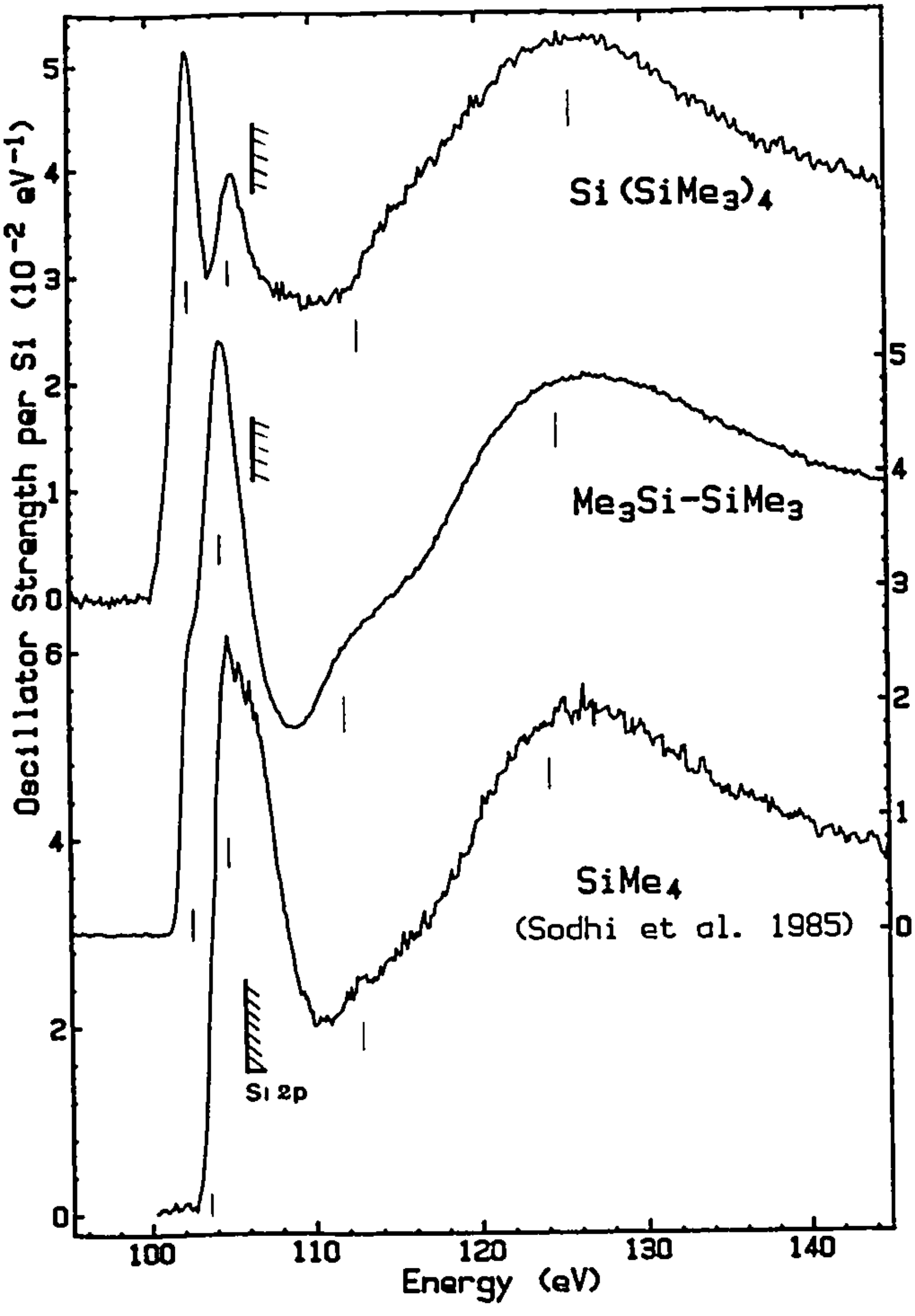

Fig. 7.1 Si 2p electron energy loss spectra of $Si[Si(CH_3)_3]_4$, $(CH_3)_3Si\text{-}Si(CH_3)_3$ (this work) and $Si(CH_3)_4$ (digitized from ref. 182).

Table 7.1 Energies (E, eV), Term Values (T, eV) and Proposed Assignments for Features in the Si 2p Spectra of $Si[Si(CH_3)_3]_4$, $(CH_3)_3Si\text{-}Si(CH_3)_3$ and $Si(CH_3)_4$ [Ref. 182].

$Si[Si(CH_3)_3]_4$		$(CH_3)_3Si\text{-}Si(CH_3)_3$		$Si(CH_3)_4$		Assignment
E	T	E	T	E	T	(final orb.)
102.54^a	4.0	102.6	3.9			σ*(Si-Si)
				103.60	2.34	a_1*(4s), t_2*(4p)
105.2	1.3	104.46^a	2.0	104.73	1.21	3d, 4d, 5s, 5p (Rydberg)
106.5^b		106.5^b		105.94^c		$2p_{3/2}$ IP
(113)	(-6.5)	112	-5.5	(113)	(-7.)	2e ? or σ* shape resonance?
125	-18.5	125	-18.5	124.1	-18.2	Si 2p → εd ? σ* shape resonance?

a. Calibration relative to CO_2 (C 1s → π*; 290.74 eV); ΔE = -188.20(6) and -186.28(8) eV for $Si[Si(CH_3)_3]_4$ and $(CH_3)_3Si\text{-}Si(CH_3)_3$, respectively.

b. Estimated from the data of $H_3Si\text{-}SiH_3$ [Ref. 92]

c. IP from Ref. 183.

Si-Si σ^* antibonding MOs, forming a Si 3s-AO-like band that has effective orbital overlap with the Si 2p core orbitals. It is of interest to note here that ISEELS is in effect being used to map the AO contribution of virtual-valence MOs.[52]

On the other hand, if one considers just one single Si-Si bond, as in both $(CH_3)_3Si\text{-}Si(CH_3)_3$ and $(CH_3)_3Si\text{-}Si[Si(CH_3)_3]_3$, one would expect the $Si(CH_3)_3$ group to have an inductive electron-withdrawing effect relative to CH_3 according to the large intensity of the first feature displayed in the TTS spectrum (Fig. 7.1). This effect would lead to electron delocalization while the Si 2p electron is promoted to the Si-Si σ^* MO, which in turn would help stabilize the (Si $2p^{-1}$, σ^*) excited state. This seems consistent with the concept that an underlying electron-delocalization is responsible for various unusual properties exhibited by organopolysilanes.[165]

The second sharp peak appearing at 105.2 eV in the TTS spectrum has a term value of 1.3 eV, and apparently can be correlated with the main line at 104.73 eV in the TMS spectrum. The latter feature has been assigned by Sodhi *et al*[182] to a cluster of Rydberg transitions. Parallel to this, the 105.2-eV peak in TTS is ascribed to transitions from Si 2p to a convolution of Si 3d, 4d, 5s and 5p Rydberg orbitals. In HDS, the counterpart of this must be the second strong peak at 104.5 eV, whose 2-eV term value is somewhat larger than those in TTS and TMS. The greater term value as well as greater intensity of the second peak in HDS relative to the second peak in TTS may reflect that Rydberg orbitals in HDS are mixing with the Si-Si σ^* antibonding valence MO. The small energy separation between the first and second features in the HDS Si 2p spectrum also supports this point of view. Interestingly, the oscillator strength of the second peak gradually decreases on going from TMS (0.06 eV^{-1}) to TTS (0.04 eV^{-1}), indicating that the Rydberg structures undergo a strong perturbation and suppression when going from mononuclear TMS to polynuclear TTS. This is in accord with general results from condensed-phase studies, where Rydberg orbitals normally collapse into a weak broad band structure upon chemisorption or solidification.

Beyond the Si 2p ionization limit, the HDS spectrum shows a relatively strong, broad band-like feature around 112 eV, which is also present in the TTS spectrum (~113 eV) although with much weaker intensity. Sodhi *et al*[182] did not observe this feature in their high-resolution ISEELS spectrum of TMS. However, it does appear in the TMS photoabsorption spectrum reported by Bozek *et al*,[187] who speculated that the feature is a shape resonance in the κe symmetry channel.[188] Evidently, there are some difficulties in accurately determining the nature of this feature. This can be perceived by the irregular shape of this feature in the three compounds (See Fig. 7.1). In addition to the shape-resonance assignment, which might be associated with the Si-C σ^* MOs, double excitations (2e) may be another possibility of accounting for this spectral feature.

The most intense feature in the continuum region of all three Si 2p spectra is centred at 125 eV, approximately 18 eV above the ionization threshold. The oscillator strength (per Si atom) of this band is basically constant at 0.05 eV^{-1} and the peak position does not vary markedly in any of the three spectra. Such consistent positions, intensities and shapes indicate that the band has a bond-length independent character. It is unlikely that it results from scattering of the ejected Si 2p electron from the surrounding atoms in the molecule (EXELFS). For TMS, this continuum feature has been attributed to a d-like $\sigma^*(7t_2^*)$ shape resonance.[182] The peak energy has also been related to the bond-length correlation model.[36] More recently, Bozek *et al*[188] proposed it to be an atomic-like delayed onset of Si 2p → ϵd transitions based on the similarities of the cross sections between different silicon molecules and even atomic silicon. However, such a large delayed onset (*ca.* 18 eV) arising from the centrifugal barrier to the κt_2 channel is apparently rather exceptional. The exact nature of this strong continuum resonance is still not certain and needs further exploration, especially from theory. Although it may be considered to be an admixture of the two types of resonances mentioned above, more likely it may be the shape resonance associated with the Si-C σ^* MOs based on the shape of this feature in the HDS and TTS spectra, where it is slightly broadened relative to TMS. This is reasonably consistent with the greater number of Si-C bonds existing in the polysilane species. The bond-length independence implies formation of a rather narrow Si-C σ^* band, which is consistent with the existence of a similar Si-C bond in each compound.

§7.3 C 1s Spectra

Figure 7.2 compares the C 1s spectra of the two polysilane molecules with that of TMS.[182] The energies, term values and spectral interpretations are listed in Table 7.2. The overall shapes of the three spectra show considerable similarity: a sharp pre-edge jump; most intensity being concentrated near the ionization threshold; and a weakly-featured continuum, rather consistent with the C 1s spectra of methane.[189] This is understandable since the C 1s spectrum originates in each species from the CH_3 group. One may expect the spectra to be composed mainly of Rydberg transitions. All three spectra are dominated by a very sharp intense peak at 287.3 eV with an average term value of 2.4 eV. As previously suggested for TMS,[182] this peak is assigned to C 1s → 4p transitions (which are labelled t_2^* for the T_d species TMS and TTS). The constant energy position and similar intensities indicate that C 1s excitations are quite insensitive to the replacement of CH_3 with $Si(CH_3)_3$ and are principally localized on a single CH_3 group.

Below this major peak, the C 1s spectrum of TMS has a weak shoulder around 286.4 eV, which seems to be missing in the polysilane spectra. This feature has been assigned to the C 1s → Rydberg 4s (a_1^*) dipole-allowed transition based upon analysis under local C_{3v} symmetry.[182] It is noteworthy that both the HDS and TTS C 1s spectra do not exhibit an obvious sign of this feature except for a very weak shoulder at the foot of the first intense peak (See Figure 7.2 and Table 7.2). If the separation from the main peak was 0.9 eV as in the TMS spectrum, the feature should be resolvable by the current spectrometer. Its absence in the polysilane spectra reflects its dominant Rydberg character and is consistent with a gradual loss of its identity upon aggregation of the $Si(CH_3)_3$ units. It is of interest to note also that the Si-Si σ^* feature, which is so prominent in the Si 2p spectra of HDS and TTS, is completely absent in both C 1s

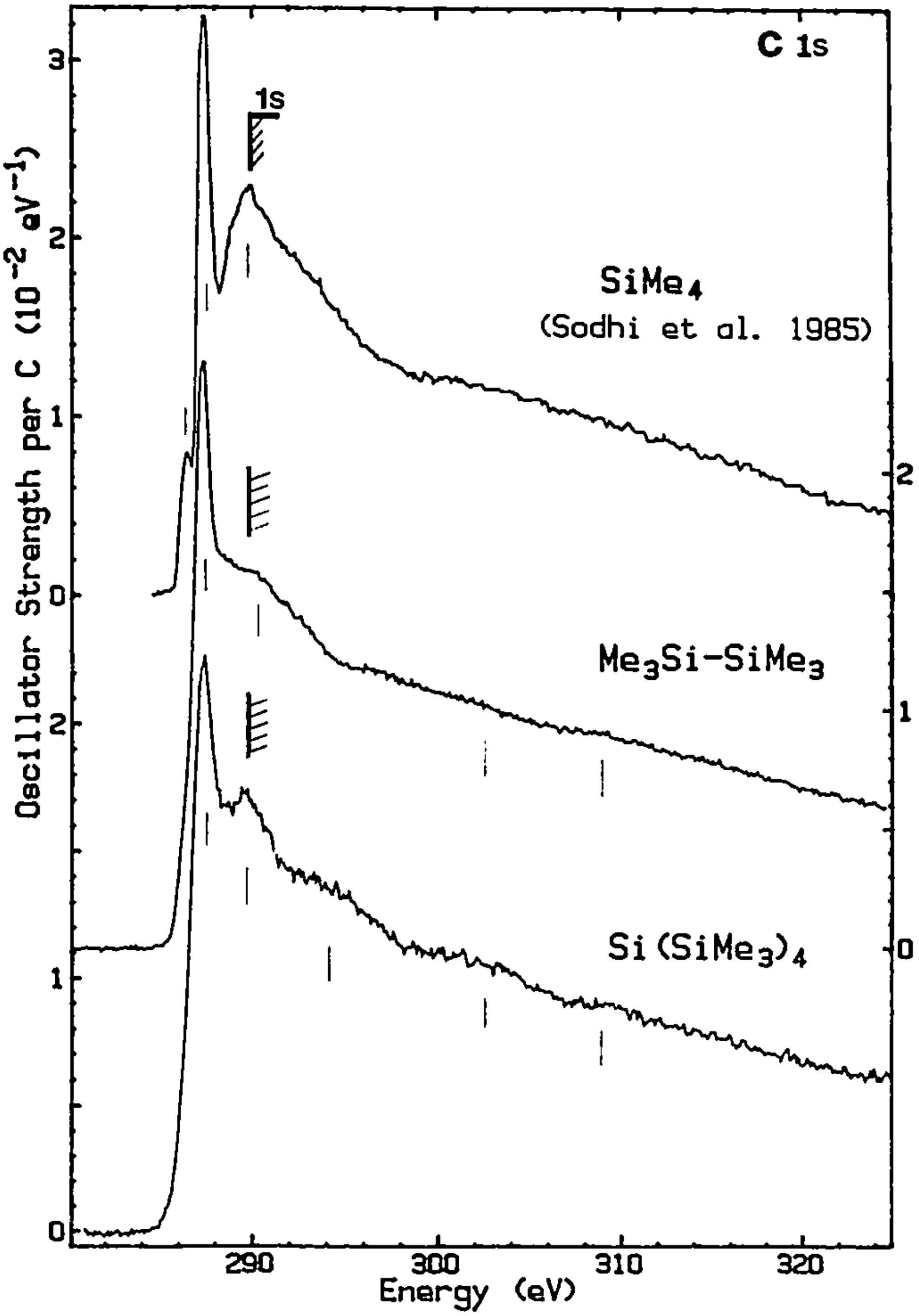

Fig. 7.2 C 1s electron energy loss spectra of $Si[Si(CH_3)_3]_4$, $(CH_3)_3Si\text{-}Si(CH_3)_3$ (this work) and $Si(CH_3)_4$ (digitized from ref. 182).

Table 7.2 Energies (E, eV), Term Values (T, eV) and Proposed Assignments for Features in the C 1s Spectra of $Si[Si(CH_3)_3]_4$, $(CH_3)_3Si\text{-}Si(CH_3)_3$ and $Si(CH_3)_4$ [Ref. 182].

$Si[Si(CH_3)_3]_4$		$(CH_3)_3SiSi(CH_3)_3$		$Si(CH_3)_4$		Assignment
E	T	E	T	E	T	(final orbital)
286	(3.7)	286	(3.7)	286.39	3.4	$6a_1$* (4s)
287.37[a]	2.3	287.31[a]	2.4	287.31	2.5	4p (t_2*)
289.5	0.2			289.6	0.2	Rydberg?
289.7[b]		289.7[b]		289.78[c]		IP
(290)		290.	-0.3	(290)		σ*(Si-C) ?
294.	-4.3					2e ? or σ*(Si-C) ?
303	-13			303	-13	σ* shape resonance? or EXAFS ?
309	-19	309	-19			shake-off? or EXAFS?

a. Calibration relative to CO_2 (C 1s → π*; 290.74 eV): ΔE = -3.37(3) and -3.43(5) eV for $Si[Si(CH_3)_3]_4$ and $(CH_3)_3Si\text{-}Si(CH_3)_3$, respectively.

b. IP estimated from TMS and $[(CH_3)_3Si]_2O$ [Ref. 92].

c. XPS value from Ref. 92.

spectra. This signifies strongly that the Si-Si σ^* MO is essentially localized on the Si-atoms and that there is negligible C 1s → Si-Si σ^* charge transfer. This is a nice demonstration of the application of ISEELS to mapping the spatial distribution of virtual-valence MOs.

The large band-like feature near the carbon 1s ionization limit is attributed to unresolved C 1s → Rydberg excitations converging on the C 1s IP. This feature is relatively weaker in HDS than in TMS and TTS, both of which have a T_d-symmetry molecular geometry and thus are "cage" compounds which may have a larger potential barrier effect. A low-intensity broad band around 303 eV in the continuum is considered to be a shape resonance. Alternatively, it may be the first Si-C EXAFS peak according to its shape and intensity. Again, this feature is weaker in HDS than in TMS and TTS. It is surprising that this resonance has such a weak intensity compared to the situation in the Si 2p spectra, presumably because either the involved σ^* MOs, like the Si-Si σ^* MO, have their large intensities mainly around the Si atoms in the molecule or there does not exist an effective potential barrier to delay the outgoing C 1s electron, since it originates at the periphery of the molecule.

§7.4 Si 2s Spectra

Compared to the Si 2p-edge signals, the energy-loss signal associated with the Si 2s edge is normally much weaker due to the fact that the scattering cross sections are intrinsically small at this edge. This can be seen clearly in the full range spectrum of HDS depicted on the top of Figure 7.3. Although challenging to measure, the Si 2s spectrum is valuable since it investigates the Si 3p character of empty orbitals and thus gives a more complete picture of the electronic structure at Si atom which could be useful for confirming an assignment of the Si 2p spectrum.[182,187] The Si 2s spectrum has been recorded for both HDS and TTS. The full-range (Si 2p, Si 2s and C 1s) spectrum of HDS is shown at the top of Figure 7.3, whereas a comparison of the background subtracted Si 2s spectra of TTS, HDS and TMS[182] is presented at the bottom of Figure

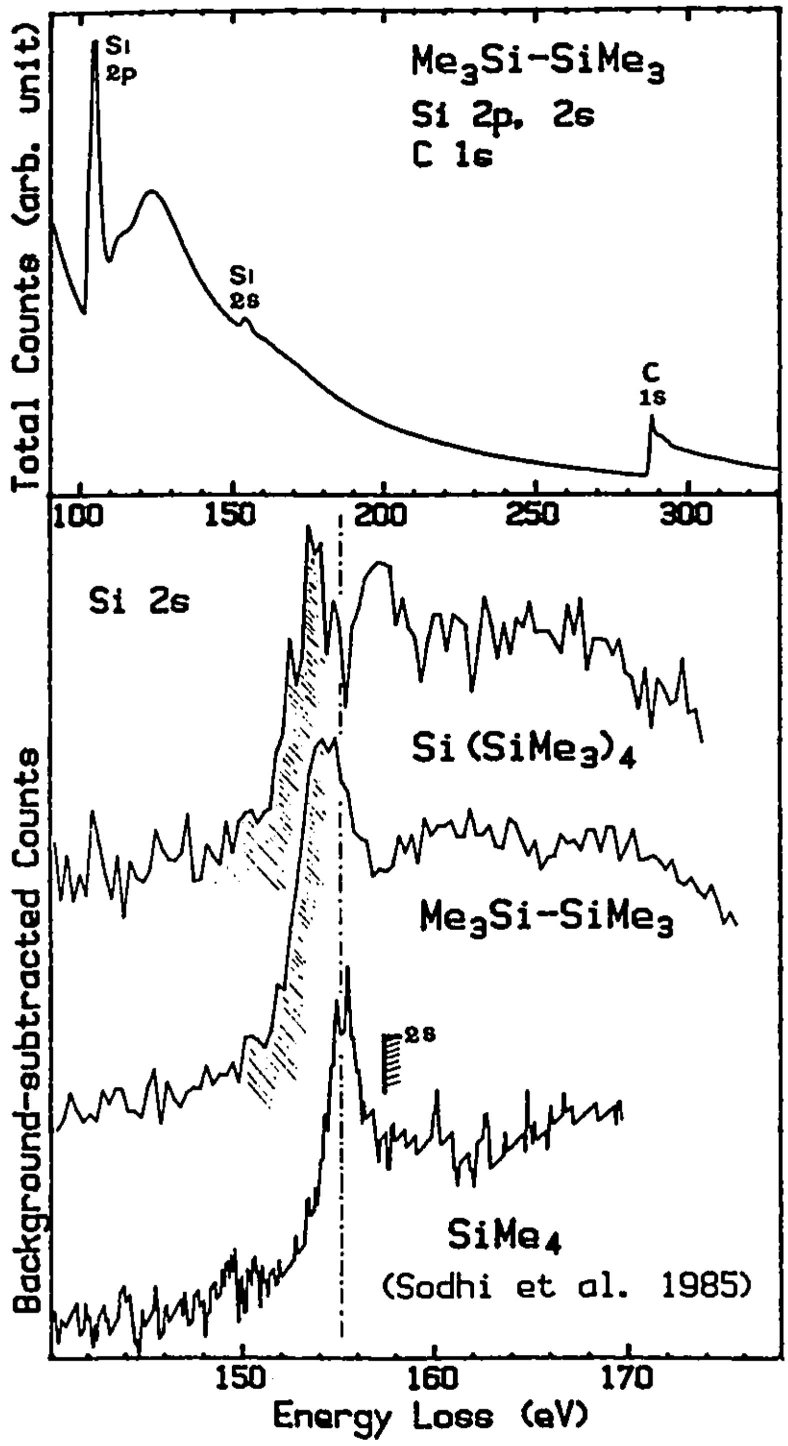

Fig. 7.3 (top) Full range spectrum containing Si 2p, 2s and C 1s edges of $(CH_3)_3Si\text{-}Si(CH_3)_3$. (bottom) Si 2s electron energy loss spectra of $Si[Si(CH_3)_3]_4$, $(CH_3)_3Si\text{-}Si(CH_3)_3$ (this work) and $Si(CH_3)_4$ (digitized from ref. 182). The shading indicates the additional resonant intensities relative to $Si(CH_3)_4$.

7.3. No attempt has been made to derive quantitative Si 2s oscillator strengths due to the poor statistics of these spectra. The values of the Si 2s ionization limits are usually estimated from the 2p thresholds, using an average Si 2p-2s separation of 51.2 eV.[182] Since there are no reports of the Si 2p XPS binding energies for the two polysilane species, further estimates of the Si 2s edges for them seem less significant. Therefore, the two Si 2s spectra of HDS and TTS remain unassigned here. However, even without detailed discussion, the Si 2s spectra, together with that of TMS, show trends consistent with the assignments of the Si 2p spectra. In both the HDS and TTS spectra, there is additional intensity below 155 eV, i.e., below the location of the most intense peak in the TMS spectrum which has been attributed to the Si 2s → σ^*(t_2 p-like) dipole-allowed transition.[182] The latter assignment has also been supported by the Si 1s photoabsorption spectrum.[190] These additional low-energy features in HDS and TTS are considered to be associated with Si 2p → σ^*(p-like) transitions, in particular, to reflect the presence of Si 3p character in the Si-Si σ^* MO. In other words, the virtual-valence Si-Si σ^* MO possesses not merely Si 3s but Si 3p character also.

§7.5 Summary

Si 2p, 2s and C 1s core excitation of HDS and TTS have been investigated by ISEELS. A number of resonances near the Si 2p and C 1s edges have been tentatively assigned. In particular a low-lying Si-Si σ^* resonance has been identified at 102.5 eV in the Si 2p spectra, about 4 eV below the Si $2p_{3/2}$ IP, by comparison with the Si 2p spectrum of TMS. This is consistent with the weak-bond model. Overall, the spectra are characterized mainly by some strong Rydberg transitions in the pre-edge region. Unlike the C 1s spectra, the Si 2p spectra reveal very intense Si 3d resonances beyond the ionization threshold. The energy-loss cross sections associated with Si 2s excitation were found to be much weaker than the corresponding Si 2p excitation, but the displayed trends of the Si 2s spectra were generally supportive of the occurrence of a low-lying Si-Si σ^* orbital in species containing a Si-Si bond.

Chapter 8

CONCLUDING REMARKS

Core excitation measurements using electron energy-loss spectroscopy have been applied to a wide range of gas-phase 3d transition-metal organometallic complexes (metal carbonyls, ferrocene and its derivatives, half-sandwich compounds) and organopolysilanes. The resulting data demonstrate that site-selective core excitation is a rather sensitive probe of the unoccupied MO levels and provides useful new insight into the electronic structure as well as the bonding mechanisms of these molecules. Combined with extended Hückel MO calculations within the equivalent ionic core virtual orbital (Z+1) model, the electron energy-loss technique has proven to be a state-of-the-art molecular spectroscopy.

For the metal carbonyls, the C 1s and O 1s spectra of the CO ligand show some major similarities to those of free CO. In particular, they are all characterized by two intense $1s \rightarrow \pi^*$ and $1s \rightarrow \sigma^*$ resonances, indicating that both C 1s and O 1s excitations in metal carbonyls are localized largely on just a single CO ligand. However, there exist also some significant differences between the spectra of the carbonyls and those of free CO, principally owing to greater orbital relaxation accompanying creation of a core hole in the organometallic complexes and the larger number of final states accessible. The red shift of the σ^* resonances has been related to C-O bond-length increases within the bond-length correlation model, while the intensity reduction of the π^* resonances reflects aspects of the metal-ligand bonding in these complexes, in particular the metal $3d \rightarrow$ CO π^* back-donation.

In the half-sandwich compounds, the C 1s spectra are found to be similar to a weighted sum of the C 1s spectra of species containing the individual ligands. This suggests that the virtual- valence orbitals of the ligands are relatively independent of those of the other ligands. Ligand-ligand interaction has been evaluated by quantitative discrepancies between the experiment and additivity simulation. In general the virtual

MOs associated with an unsaturated hydrocarbon ligand are more subject to perturbation by ligand-ligand interaction than those associated with a carbonyl ligand. C 1s excitation is found to be very sensitive to the ligand perturbation, a minor chemical modification introduced on the unsaturated hydrocarbon ligand. All of the O 1s spectra are rather similar, not only in energy but also in intensity, indicating that they all originate from a common $M(CO)_n$ group. However, both O 1s and C 1s (except metallocenes) spectra show a relative independence on the nature of the central metal atom.

It is very interesting that the metal 2p spectra are found to be surprisingly sensitive to the type of attached ligands and the nature of the metal-ligand bonding, but apparently insensitive to the molecular symmetry, chemical modification at remote sites on the ligands or even the d-count of the metal atoms. In particular, metal 2p excitation follows a certain pattern in a series and the real mechanism behind this pattern is still not fully understood. In some cases, EHMO calculations have been used to aid the analyses of these spectra. For the basic two-line pattern of the metal 2p spectra, EHMO suggests that the low-energy line is essentially pure metal-3d-localized resonances while the line of higher energy is associated principally with the M-C σ^* antibonding valence MOs. The calculated results signify also that the 2p spectra should be more influenced by the molecular symmetry than is actually observed. For the compounds with more ionic bonding character, the atomic multiplet model incorporating the crystal field theory[110] apparently affords a much more satisfactory prediction for the experiment. Overall, 2p inner-shell excitation at the metal atom furnishes information complimentary to that obtained from ligand 1s core excitation.

The metal 3p spectra are much less informative than the metal 2p spectra. This may be attributed to (a) the larger natural linewidth associated with the rapid final-state decay via autoionization to a continuum state or via Coster-Kronig processes, and (b) line overlap due to a small spin-orbit splitting. Nevertheless, the strong pre-edge structure can be identified broadly as 3p → *n*s, *n*d transitions converging on the 3p ionization thresholds, although detailed analyses of these lines have not been attempted.

In particular, 3p transitions into d-like final states are expected to be dominant in terms of the large orbital overlap and the consequent large electrostatic interaction between the 3p and 3d orbitals which leads to a localization of the 3d electron wave function in the final state. Thus, metal-3p core excitation is a useful means of probing the 3d character in the 3d transition-metal complexes.

No evidence for a σ^* resonance associated with metal-metal bond in 3d-transition-metal complexes was found in either ligand 1s or metal 2p/3p spectra of the dinuclear metal carbonyls. However, strong Si-Si σ^* resonances have been observed for two organopolysilane compounds. These results suggest that several metal-metal single σ bonds are necessary for a complex to have a detectible metal-metal σ^* resonance in its inner-shell spectra. Thus, in addition to multinuclear species having a single metal-metal σ^* bond, compounds with multiple metal-metal bonds, such as a triple or even a quadruple bond, should be interesting targets for future core-excitation studies related to the nature of metal-metal bonding.

REFERENCES

1. a) C.E. Brion, *Comments At. Mol. Phys.* **16**, 249, 1985; b) C.E. Brion, in "*Physics of Electronic and Atomic Collisions*", ed. S. Datz, North-Holland, Amsterdam, 1982, p 579; c) C.E. Brion, S. Daviel, R. Sodhi, A.P. Hitchcock, "*AIP Conference Proceedings No. 94, X-ray & Atomic Inner-shell Physics*", ed. B. Crasemann, American institute of Physics, New York, 1982, p 429.

2. A.P. Hitchcock, *J. Electron Spectrosc.* **25**, 245, 1982, updated to Nov-1991 (unpublished).

3. a) D.A. Shaw, D. Cvejanovic, G.C. King, F.H. Read, *J. Phys.* **B**, **17**, 1173, 1984; b) *ibid.* 2091, 1984; c) D.A. Shaw, G.C. King, F.H. Read, D. Cvejanovic, *J. Phys.* **B**, **15**, 1785, 1982.

4. G.R. Wight, C.E. Brion, M.J. van der Wiel, *J. Electron Spectrosc.* **1**, 457, 1972/3.

5. a) J.L. Dehmer, D. Dill, *Phys. Rev. Lett.* **35**, 213, 1975; b) J.L. Dehmer, D. Dill, *J. Chem. Phys.* **65**, 532?, 1976; c) J.L. Dehmer, D. Dill, A.C. Parr, in "*Photophysics and Photochemistry in the Vacuum Ultraviolet*", ed. S.P. McGlynn, G.L. Findley, R.H. Huebner, Reidel, Dordrecht, 1985, p 341, Ref. therein.

6. a) T.N. Rescigno, P.W. Langhoff, *Chem. Phys. Lett.* **51**, 65, 1977; b) T.N. Rescigno, C.F. Bender, B.V. McKoy, P.W. Langhoff, *J. Chem. Phys.* **68**, 970, 1978.

7. M.J. van der Wiel, in "*Electronic and Atomic Collisions*", ed. N. Oda and K. Takayanagi, North-Holland, Amsterdam, 1980, p 209.

8. M. Nakamura, S. Sasanuma, S. Sato, M Watanabe, H. Yamashita, Y. Iguchi, A. Ejiri, S. Nakai, S. Yamaguchi, T. Sagawa, Y. Nakai, T. Oshio, *Phys. Rev.* **178**, 80, 1969.

9. G.R. Wight, C.E. Brion, *Chem. Phys. Lett.* **26**, 607, 1974.

10. a) A.P. Hitchcock, G. Tourillon, W. Braun, *Can. J. Chem.* **67**, 1819, 1989; b) A.P. Hitchcock, G. Tourillon, R. Garret, G.P. Williams, C. Mahatsekake, C. Andrieu, *J. Phys. Chem.* **94**, 2327, 1990.

11. E. Rühl, A.P. Hitchcock, *J. Am. Chem. Soc.* **111**, 2614, 1989.

12. G. Cooper, K.H. Sze, C.E. Brion, *J. Am. Chem. Soc.* **111**, 5051, 1989.

13. E. Rühl, A.P. Hitchcock, *J. Am. Chem. Soc.* **111**, 5069, 1989.

14. A.P. Hitchcock, A.T. Wen, E. Rühl, *J. Electron Spectrosc.* **51**, 653, 1990.

15. F.A. Cotton, G. Wilkinson, "*Advanced Inorganic Chemistry*", 5th Ed. J. Wiley & Sons, New York, 1988, Ch 2, p 57-83; Ch 22, p 1021; Ch 26, p 1152.

16. a) C.H. Bartholomew, P.K. Agrawal, J.R. Katzer, *Adv. Catal.* **31**, 135, 1982; b) L. Moggi, A. Juris, D. Sandrini, M.F. Manfrin, *Rev. Chem. Intermed.* **4**, 171, 1981; c) C. Masters, "*Homogeneous Transition Metal Catalysis*", Chapman & Hall, New York, 1981.

17. a) R.M. Osgood, T.F. Doutsch, *Science*, **227**, 709, 1985; b) C. Mayer, G.J. Fisanik, T.S. Eichelberger, IV, *J. Appl. Phys.* **53**, 8462, 1982.

18. A.P. Hitchcock, A.T. Wen, E. Rühl, *Chem. Phys.* **147**, 51, 1990.

19. E. Rühl, A.T. Wen, A.P. Hitchcock, *J. Electron Spectrosc.* **57**, 137, 1991.

20. G. Cooper, K.H. Sze, C.E. Brion, *J. Am. Chem. Soc.* **112**, 4121, 1990.

21. a) N.F. Lane, *Rev. Mod. Phys.* **52**, 29, 1980; b) "*Symposium on Electron-Molecule Collision*", ed. I. Shimamura, M. Matsuzawa, Univ. of Tokyo, 1979.

22. H. Bethe, *Ann. Phys.* (Leipzig), **5**, (5), 325, 1930.

23. M. Inokuti, *Rev. Mod. Phys.* **43**, 297, 1971.

24. C.E. Brion, A. Hamnett, *Adv. Chem. Phys.* **45**, 1, 1981.

25. G.C. King, M Tronc, F.H. Read, R.C. Bradford, *J. Phys.* **B**, **10**, 2479, 1977.

26. D.A. Shaw, G.C. King, F.H. Read, *J. Phys.* **B**, **13**, L723, 1980.

27. Y. Jugnet, F.J. Himpsel, Ph. Avouris, E.E. Koch, *Phys. Rev. Lett.* **53**, 198, 1984.

28. A.A. Pavlychev, A.S. Vinogradov, *Opt. Spectrosc.* (USSR) **62**, 197, 1987.

29. W.H.E. Schwarz, L. Mensching, K.H. Hallmerier, R. Szargan, *Chem. Phys.* **82**, 57, 1983.

30. S.P. McGlynn, G.L. Findley, *J. Photochem.* **17**, 461, 1981.

31. J.A. Sheehy, T.J. Gil, C.L. Winstead, R.E. Farren, P.W. Langhoff, *J. Chem. Phys.* **91**, 1796, 1989.

32. W. Thiel, *J. Electron Spectrosc.* **31**, 151, 1983.

33. M.R. Hermann, P.W. Langhoff, *Chem. Phys. Lett.* **82**, 242, 1981.

34. P.W. Langhoff, A. Gerwer, C. Asaso, B.V. Mckoy, *Int. J. Quantum Chem.* **S13**, 645, 1979.

35. A.P. Hitchcock, C.E. Brion, G.R.J. Williams, P.W. Langhoff, *Chem. Phys.* **66**, 435, 1982.

36. F. Sette, J. Stöhr, A.P. Hitchcock, *J. Chem. Phys.* **81**, 4906, 1984.

37. D. Dill, A. Wallace, J. Siegel, J.L. Dehmer, *Phys. Rev. Lett.* **41**, 1230, 1978.

38. E.U. Condon, H. Odabasi, "*Atomic Structure*", Cambridge University Press, Cambridge, 1980.

39. R.S. Mulliken, *Accounts Chem. Rev.* **9**, 7, 1976.

40. A.P. Hitchcock, C.E. Brion, *J. Phys.* **B**, **14**, 4399, 1981.

41. A.P. Hitchcock, I. Ishii, *J. Electron Spectrosc.* **42**, 11, 1987.

42. A.P. Hitchcock, D.C. Newbury, I. Ishii, J. Stöhr, J.A. Horsley, R.D. Redwing, A.L. Johnson, F. Sette, *J. Chem. Phys.* **85**, 4849, 1986.

43. R.S. Mulliken, *J. Chim. Phys.* **46**, 497, 1949; **46**, 675, 1949.

44. M. Wolfsberg, L. Helmholtz, *J. Chem. Phys.* **20**, 837, 1952.

45. R. Hoffmann, *J. Chem. Phys.* **39**, 1963; *ibid.*, **40**, 2474, 1963.

46. M. Elian, R. Hoffmann, *Inorg. Chem.* **14**, 365, 1975.

47. J.W. Lauher, M. Elian, R.H. Summerville, R. Hoffmann, *J. Am. Chem. Soc.* **98**, 3219, 1976.

48. R.H. Summerville, R. Hoffmann, *J. Am. Chem. Soc.* **98**, 7240, 1976.

49. T.A. Albright, P. Hofmann, R. Hoffmann, *J. Am. Chem. Soc.* **99**, 7546, 1977.

50. S. Alvarez, "*Tables of Parameters for Extended Hückel Calculations*", Universitat-de-Bascelona Press, Barcelona, 1989.

51. E. Lindholm, L. Asbrink, "*Molecular Orbitals and Their Energies Studied by the Semiempirical HAM Method*", (Springer, Berlin, 1985) p 150.

52. I. Ishii, A.P. Hitchcock, *J. Chem. Phys.* **87**, 830, 1987.

53. J. Howell, A. Rossi, D. Wallace, K. Haraki, R. Hoffmann, "*Quantum Chemistry Program Exchange No.011*", Cornell/Indiana University.

54. V. Bellagamba, R. Ercoli, A. Gamba, G.B. Suffritti, *J. Organomet. Chem.* **190**, 381, 1980.

55. M. J-A. Prins, *Physica*, **1**, 1174, 1934.

56. W.H.E. Schwarz, *Angew. Chem. Internat. Edit.* **13**, 454, 1974.

57. W.H.E. Schwarz, *Chem. Phys.* **11**, 217, 1975.

58. W.H.E. Schwarz, R.J.Buenker, *Chem. Phys.* **13**, 153, 1976.

59. T. Steel, B.Sc. Thesis, McMaster University, 1982.

60. D.C. Newbury, M.Sc. Thesis, McMaster University, 1986.

61. A.P. Hitchcock, S. Beaulieu, T. Steel, J. Stöhr, F. Sette, *J. Chem. Phys.* **80**, 3927, 1984.

62. D.C. Newbury, I. Ishii, A.P. Hitchcock, *Can. J. Chem.* **64**, 1145, 1986.

63. D.W.O. Heddle, *J. Phys.* E. **4**, 589, 1971.

64. G.R. Wright, Ph.D. thesis, UBC, 1974.

65. A.P. Hitchcock, C.E. Brion, *J. Electron Spectrosc.* **13**, 193, 1978.

66. R.N. Sodhi, C.E. Brion, *J. Electron Spectrosc.* **34**, 363, 1984.

67. G.R. Wight, C.E. Brion, *J. Electron Spectrosc.* **4**, 313, 1974.

68. A.P. Hitchcock, A.T. Wen, S.W. Lee, J.T. Spencer, P.A. Dowben, *J. Am. Chem. Soc.*, to be submitted.

69. E.N. Lassettere, in "*Chemical Spectroscopy and Photochemistry in the Vacumm-Ultraviolet*", ed. C. Sandorfy, P.J. Ausloos, M.B. Robin, (Reidel, Boston, 1974) p 43.

70. R.D. Leapman, L.A. Grunes, P.J. Fejes, J. Sicox, "*EXAFS Spectroscopy*", ed. B.K. Teo, C. Joy (Plenum, New York, 1981).

71. R. McLaren, S.A.C. Clark, I. Ishii, A.P. Hitchcock, *Phys. Rev.* **A**, **36**, 1683, 1987.

72. B.L. Henke, P. Lee, J.T. Tanaka, R.L. Shimabukuro, B.K. Fujikawa, *At. Data Nucl. Data Tab.* **27**, 1, 1982.

73. W.F. Chen, G. Cooper, C.E. Brion, *Phys. Rev.* **A 44**, 186, 1991.

74. a) P.A. Dowben, D.C. Driscoll, R.S. Tate and N.M. Boag, *Organometallics* **7**, 305, 1988; b) J.D. Morrison, ed., "*Asymmetric Synthesis*", 2 Vols., Academic Press, New York (1984); c) J.K. Stille, *Mod. Synth. Methods*, 3, 1, 1983; d) J.T. Mague, *J. Organomet. Chem.* **242**, 241, 1983; e) S.G. Davies, "*Organotransition Metal Chemistry Application to Organic Synthesis*", (Oxford, Pergamon Press, 1982); e) C. Masters, "*Homogeneous Transition-Metal Catalysis*", (New York, Chapman and Hall, 1981); f) R. Mason, M.W. Roberts, *Inorg. Chim. Acta*, **50**, 53, 1981; g) C.K. Rofer-DePoorter, *Chem. Rev.* **81**, 447 1981; h) D. Forster, A. Herschman, D.E. Morris, *Catal. Rev.*, **23**, 89, 1981.

75. D. Outka and J. Stöhr, *J. Chem. Phys.* **88**, 3539, 1989.

76. W. Heijser, E.J. Baerends and P. Ros, *Faraday Symp. Royal Chem. Soc.* **14**, 211, 1980.

77. a) R. Benn, K. Cibura, P. Hofmann, K. Jonas and A. Rufinska, *Organometallics*, 4, 2214, 1985; b) P. Hofmann, *Ang. Chem. Int. Ed.* **16**, 536, 1977.

78. a) A. Modelli, G. Distefano, M. Guerra, D. Jones, *J. Am. Chem. Soc.* **109**, 4440, 1987; b) M. Guerra, D. Jones, G. Distefano, A. Foffani and A. Modelli, *J. Am. Chem. Soc.* **110**, 375, 1988; c) A. Modelli, A. Foffani, F. Scagnolari, S. Torroni, M. Guerra and D. Jones, *J. Am. Chem. Soc.* **111**, 6040, 1989; d) J.C. Giordan, J. H. Moore, J. A. Tossell and J. Weber, *J. Am. Chem. Soc.* **105**, 3431, 1983.

79. D.A. Brown, H.L. Clarke, N.J. Fitzpatrick, *J. Organomet. Chem.* **47**, C11, 1973.

80. L.B. Byers, L.F. Dahl, *Inorg. Chem.* **19**, 277, 1980.

81. F.M.F. de Groot, M. Grioni, J.C. Fuggle, J. Ghijsen, G.A. Sawatzky, H. Petersen, *Phys. Rev.* **B 40**, 5715, 1989.

82. A. Haaland, *Acc. Chem. Res.* **12**, 415, 1979.

83. B. Beagley, C.T. Parrott, V. Ulbrecht, G.G. Young, *J. Mol. Struct.* **52**, 47, 1979.

84. I. Kojima, A.K. Srivasta, E. Miyazaki, H. Adachi, *J. Chem. Phys.* **84**, 4445, 1986.

85. a) E.W. Plummer, W.K. Ford, W. Eberhardt, R.P. Messmer, H.J. Freund, *Surf. Sci.*, **158**, 58, 1985; b) W. Eberhardt, E.W. Plummer, C.T. Chen, W.K. Ford, *Aust. J. Chem.* **39**, 853, 1986; c) W. Eberhardt, C.T. Chen, W.K. Ford, E.W. Plummer, H. R. Moser, Springer Series in *Surface Science*, **4**, 50, 1985; d) R. Murphy, E.W. Plummer, C.T. Chen, W Eberhardt, R. Carr, *Phys. Rev.* **B**, 39, 7517, 1989.

86. a) B. Gumhalter, K. Wandelt, Ph. Avouris, *Phys. Rev.* **B 37**, 8048, 1988; b) W. Wurth, D. Coulman, A. Puschman, D. Menzel, E. Umbach, *Phys. Rev.* **B**, **41**, 12933, 1990

87. E.J. Baerends, P. Ros, *J. Electron Spectrosc.* **7**, 69, 1975.

88. J.C. Giordan, J.H. Morre, J.A. Tossell, *J. Am. Chem. Soc.* **103**, 6632, 1981.

89. I.H. Hillier, V.K. Saunders, *Mol. Phys.* **22**, 1025, 1971.

90. a) P.S. Bagus, C.J. Nelin, C.W. Bauschlicher, *J. Vac. Sci. Tech.* **A 2**, 905, 1985; b) Ph. Avouris, P.S. Bagus, A.R. Rossi, *J. Vac. Sci. Tech.* **B 3**, 1484, 1985.

91. I. Ishii, R. McLaren, A.P. Hitchcock, M.B. Robin, *J. Chem. Phys.* **87**, 4344, 1987.

92. W.L. Jolly, K.D. Bomben, C.J. Eyermann, *At. Data Nucl. Data Tables*, **31**, 433, 1984.

93. F.A. Cotton, "*Chemical Applications of Group Theory*", (Wiley, NY, 1971).

94. J.A. Horsley, J. Stöhr, A.P. Hitchcock, D.C. Newbury, A.L. Johnson and F. Sette, *J. Chem. Phys.* **83**, 6099, 1985.

95. W.H.E. Schwarz, T.C. Chang, U. Seeger and K.H. Huang, *Chem. Phys.* **117**, 73, 1987.

96. L.J. Medhurst, T.A. Ferrett, P.A. Heiman, D.W. Lindle, S.H. Liu and D.A. Shirley, *J. Chem. Phys.* **89**, 6096, 1988.

97. H.W. Cnen, W.L. Jolly, J. Kopf, T.H. Lee, *J. Am. Chem. Soc.* **101**, 2607, 1979.

98. G. van der Laan, G.A. Sawatzky, R. Karnatak and J.M. Esteva, *Phys. Rev.* **B** 3, 4253, 1986.

99. a) A.P. Hitchcock, *Physica Scripta*, T 31, 159, 1990; b) A.P. Hitchcock, *Proc. of Escola Latino-Americana de Fisica* (World Sci. Publ. Co.) 1991. in press.

100. J. Stöhr, "*NEXAFS Spectroscopy*" (Springer, Berlin, 1991)

101. D. Sondericker, Z. Fu, J. Bradley, W. Eberhardt, *J. Chem. Phys.* 92, 2203, 1990.

102. a) D. Guenzburger, E.M.B. Saitovitch, M.A. DePaoli, H. Manela, *J. Chem. Phys.* **80**, 735,1984; b) J.K. Olthoff, J.H. Moore, J.A. Tossell, J.C. Giordan, E.J. Baerends, *J. Chem. Phys.* **87**, 7001, 1987.

103. a) T.A. Albright, J.K. Burdett, M.H. Whangbo, "*Orbital Interactions in Chemistry*", (John Wiley & Sons, New York, 1985) p 368; b) M. Elian, R. Hoffmann, *Inorg. Chem.*, **14**, 1058, 1975.

104. R.V.G. Evens, M.W. Lister, *Trans. Faraday Soc.* **35**, 681, 1939.

105. F.A. Cotton, *Progress in Inorg. Chem.* **21**, 1, 1976.

106. a) M.J.S. Dewar, *Bull. Soc. Chim. Fr.*, C17, 1951; b) J. Chatt, L.A. Duncanson, *J. Chem. Soc.* 2939, 1953.

107. J.P. Connerade, *J. Phys.* **B 17** L165, 1984.

108. A.P. Hitchcock, J. Stöhr, *J. Chem. Phys.* **87**, 3253, 1987.

109. J. Waite, M.G. Papadopoulis, *J. Phys. Chem.* 95, 5426, 1991.

110. a) F.M.F. de Groot, J.C. Fuggle, B.T. Thole, G.A. Sawatzky, *Phys. Rev.* B 42, 5459, 1990; b) F.M.F. de Groot, J.C. Fuggle, B.T. Thole, G.A. Sawatzky, *Phys. Rev.* B 41, 928, 1990.

111. C.T. Chen, F. Sette, *Physica Scripta* T 31, 119, 1990.

112. D.A. Shirley, R.L. Martin, S.P. Kowalczyk, F.R. McFeeley, L. Ley, *Phys. Rev.* B 15, 544, 1977.

113. R.E. Dietz, E.G. McRae, Y. Taft, C.W. Caldwell, *Phys. Rev. Lett.* 33, 1372, 1974.

114. G. van der Laan, *J. Phys. Condensed Matter*, C 3, 7443, 1991.

115. M. Meyer, Th. Prescher, E. von Raven, M. Richter, E. Schmidt, B. Sonntag, H.E. Wetzel, *Z. Phys.* D 2, 347, 1986.

116. A.L. Johnson, W.K. Walter, M. Perez, D.A. Jigato, D. King, E. Norman, E. Rühl, C. Schmale, H. Baumgärtel, M.J. McGlinchey, A.P. Hitchcock, in prep.

117. a) D.A. Brown, N.J. Fitzpatrick, N.J. Mathews, *J. Organomet. Chem.* 88, C27, 1975; b) N.J. Fitzpatrick, J.M. Savariault, J.F. Labarre, *ibid.*, 127, 325, 1977.

118. B.E.R. Schilling, R. Hoffmann, D.L. Lichtenberger, *J. Am. Chem. Soc.* 101, 585, 1979.

119. M.F. Guest, I.H. Hillier, B.R. Higginson, D.R. Lloyd, *Mol. Phys.* 29, 113, 1975.

120. D.L. Lichtenberger, R.F. Fenske, *J. Am. Chem. Soc.* 98, 50, 1976.

121. A.C. Campbell, M.Sc. thesis, University of Arizona, 1980.

122. D.C. Calabro, J.L. Hubbard, C.H. Blevins II, A.C. Campbell, D.L. Lichtenberger, *J. Am. Chem. Soc.* 103, 6839, 1981.

123. D.L. Lichtenberger, G.E. Kellogg, *J. Am. Chem. Soc.* 108, 2560, 1986.

124. a) R. Cataliotti, A. Poletti, A. Santucci, *J. Mol. Struct.* 5, 215, 1970; b) J. Brunvoll, S.J. Cyvin, L. Schafer, *J. Organomet. Chem.* 36, 143, 1972.

125. B. Rees, P. Coppens, *Acta Cryst.* B29, 2515, 1973.

126. a)S.C. Avanzino, A.A. Bakke, H.W. Chen, C.J. Donahue, W.L. Jolly, T.H. Lee, A.J. Ricco, *Inorg. Chem.* 19, 1931, 1980; b) H.W. Chen, W.L. Jolly, S.F. Xiang, I.S. Butler, J. Sedman, *J. Electron Spectrosc.* 24, 121, 1981.

127. P. Powell, "*Principles of organometallic Chemistry*", 2nd ed., Champman & Hall, New York, 1988, p 208.

128. a) C. Cauletti, J.C. Green, M.R. Kelly, P. Powell, J. van Tilborg, J. Robbins, J. Smart, *J. Electron Spectrosc.* 19, 327, 1980; b) I. Fragala, T.J. Marks, P.J. Fagan, J.M. Manriquez, *ibid.*, 20, 249, 1980.

129. R. Crabtree, "*The organometallic chemistry of the transition metals*", John Wiley & Sons, New York, 1988, p 114, p 108.

130. J.C. Green, *Struct. Bonding*, 43, 37, 1981.

131. P.D. Burrow, A. Modelli, M. Guerra, K.D. Jordan, *Chem. Phys. Lett.* 18, 328, 1985.

132. R.D. Leapman, P. Rez, D.F. Mayers, *J. Chem. Phys*, 72, 1232.

133. A.P. Hitchcock, C.E. Brion, *J. Electron Spectrosc.* 17, 139, 1979.

134. J.A. Connor, in "*Transition Metal Cluster*", ed. B.F.G. Johnson, J. Wiley & Sons, New york, 1980, p 345.

135. a) L.I. Yin, I. Adler, T. Trang, M.H. Chen, D.A. Ringers, B.W. Crasemann, *Phys. Rev.* A9, 1070, 1974; *ibid.* A17, 1556, 1978; b) E.J. McGuire, *ibid.* A5, 1043, 1972.

136. O. Keski-Rahkonen, M. O. Krause, *At. Data Nucl. Data Tables*, 14, 139, 1974.

137. D.M.P. Mingos, "*Comprehensive Organometaliic Chemistry*", Vol. 3, Ch.1, 1982.

138. P.L. Pauson, T.L. Kealy, *Nature*, 168, 1039, 1951.

139. a) G. Wilkinson, P.L. Pauson, J.M. Birminham, F.A. Cotton, *J. Am. Chem. Soc.*, 75, 1011, 1953; b) G. Wilkinson, J.M. Birminham, *J. Am. Chem. Soc.* 76, 4281, 1954.

140. M. Bottrill, P.D. Gavens, J.W. Kelland, J. McMeeking, "*Comprehensive Organometallic Chemistry*", Pergamon, 1982, Vol. 3, Ch. 2, and Ref. therein.

141. V.I. Tel'noi, I.B. Rabinovich, V.D. Tikhonov, V.N. Latyaeva, L.I. Vyshinskaya, G.A. Razuvaev, *Dokl. Chem.* 174, 467, 1967.

142. P. Ganis, G. Allegra, *Atti. Accad. Nazl. Lincei. Rend. Cl. Sci. Fis. Mat. Nat.*[8]33, 304, 1962.

143. T.A. Albright, J.K. Burdett, M.H. Whangbo, "*Orbital Interactions in Chemistry*", Wiley, New York, 1985, p 280, p 381.

144. R. F. Fenske, D. D. Radtke, *Inorg. Chem.* 7. 479, 1968, and Ref. therein.

145. a) C.A.L. Becker, C.J. Ballhausen, I. Trabjerg, *Theoret. Chim. Acta.* 13, 355, 1969; b) C.A.L. Becker, J.P. Dahl, *Theor. Chim. Acta.* 14, 26, 1969.

146. C. Dijkgraaf, J.P.G. Rousseau, *Spectrochem. Acta*, 25A, 1831, 1969.

147. J.C.Green, M.L.H. Green, P.J. Joachim, A.F. Orchard, D.W. Turner, *Phil. Trans. Roy. Soc. Lond.* A. 268, 111, 1970.

148. A.A. Iverson. B. Russell, *Spectrochem. Acta.* 29A, 715, 1973.

149. T. Parameswaran, D.E. Ellis, *J. Chem. Phys.* 58, 2088, 1973.

150. B. Wallbank, J.S.H.Q. Perera, D.C. Frost, C.A. McDowell, *J. Chem. Phys.* 69, 5405, 1978.

151. R.J.H. Clark, "*Titanium*", in "*Comprehensive Inorganic Chemistry*", Pergamon, Oxford, 1973, p. 371.

152. M. BassO-Bert, P. Cassoux, F. Crasnier, D. Gervais, J-F. Labarre, P. de Loth, *J. Organomet. Chem.* 136, 201, 1977.

153. C. Dijkgraaf, J.P.G. Rousseau, *Spectrochem. Acta*, 25A, 1455, 1969.

154. M.B. Robin, "*Higher Excited States of Polyatomic Molecules*", Academic Press, 1975, Vol. II, p 277.

155. M.B. Robin, "*Higher Excited States of Polyatomic Molecules*", Academic Press, 1985, Vol. III, p 30.

156. A.F. Reid, D.E. Scaife, P.C. Wailes, *Spectrochim. Acta.* **20**, 1257, 1964.

157. K.H. Sze, C.E. Brion, A. Katrib, *Chem. Phys.* 132, 271, 1989.

158. a) A.P. Hitchcock, C.E. Brion, *J. Electron Spectrosc.* **14**, 41, 1978; b) *ibid.* **14**, 417, 1978; c) "*Giant Resonances in Atoms, Molecules, and Solids*", ed. J.P. Connerade, J.M. Esteva, R.C. Karnatak, Plenum, New York, 1987.

159. a) U. Fano, J.W. Cooper, *Rev. Mod. Phys.* **40**, 441, 1968; b) *ibid.* **41**, 724.

160. R.D. Leapman, L.A. Grunes, P.L. Fejes, *Phys. Rev.* **B 26**, 614, 1982.

161. L.A. Grunes, R.D. Leapman, C.N. Wilker, R. Hoffmann, A.B. Kunz, *Phys. Rev.* **B. 25**, 7157, 1982.

162. a) S. Larsson, *J. Electron Spectrosc.* **8**, 171, 1976; b) M. Braga, S. Larsson, *Int. J. Quantum Chem. Symp.* **11**, 61, 1977.

163. a) J.A. Tossell, *J. Electron Spectrosc.* **8**, 1, 1976; b) J.A. Tossell, *J. Electron Spectrosc.* **10**, 169, 1977.

164. M. Meyer, Th. Prescher, E.v. Raven, M. Richter, E. Schmidt, B. Sonntag, H.E. Wetzel, in "*Giant Resonances in Atoms, Molecules and Solids*", ed. J.P. Connerade, J.M. Esteva, R.C. Karnatak, Plenum, New York, 1987, p 251.

165. a) R. West, E. Carbery, *Science*, **189**, 179, 1975; b) L.F. Brough, R. West, *J. Am. Chem. Soc.* **103**, 3049, 1981; c) A. Herman, B. Dreczewski, W. Wojnowski, *Chem. Phys.* **98**, 475, 1985.

166. Y. Hasegawa, M. Imura, S. Yajima, *J. Mater. Sci.* **15**, 720, 1980.

167. a) G.D. Kubiak, D.A. Outka, C.M. Rohlfing, J.M. Zeigler, D.L. Windt, W.K. Waskiewicz, *J. Vac. Sci. Technol.* **B 8**, 1643, 1990; b) V.R. McCray, F. Sette, C.T. Chen, A.J. Lovinger, M.B. Robin, J. Stöhr, J.M. Zeigler, *J. Chem. Phys.* **88**, 5925, 1988.

168. B. Beagley, J.J. Monaghan, T.G. Hewitt, *J. Mol. Struct.* **8**, 401, 1971.

169. L.S. Bartell, F.B. Clippard Jr., T.L. Boates, *Inorg. Chem.* **9**, 2436, 1970.

170. H. Bock, W. Ensslin, *Angew. Chem. Int. Ed. Engl.* **10**, 404, 1971.

171. H. Bock, W. Ensslin, F. Feher, R. Freund, *J. Am. Chem. Soc.* **98**, 668, 1976.

172. C. Pitt, in "*Homoatomic Rings, Chains and Macromolecules of Main-Group Elements*", ed. A.L. Rheingold, Elsevier, Amsterdam, 1977, p 203.

173. J.M. Gaidis, P.R. Briggs, T.W. Shannon, *J. Phys. Chem.* **75**, 974, 1971.

174. R. Walsh, *Acc. Chem. Res.* **14**, 246, 1981.

175. M.B. Robin, "*High Excited States of Polyatomic Molecules*" (Academic, New York, 1974, 1975, 1985) Vol. I, II and III.

176. R.W. Bigelow, *Chem. Phys. Lett.* 126, 63, 1986.

177. a) K. Takeda, H. Teramae, N. Matsumoto, *J. Am. Chem. Soc.* **108**, 8186, 1986; b) K. Takeda, N. Matsumoto, M. Fukuchi, *Phys. Rev.* **B 30**, 5871, 1984.

178. K.A. Klingensmith, J.W. Downing, R.D. Miller, J. Michl, *J. Am. Chem. Soc.* 108, 7438, 1986.

179. C.G. Pitt, M.M. Bursey, P.F. Rogerson, *J. Am. Chem. Soc.* **107**, 519, 1985.

180. B.G. Ramsay, "*Electronic Transitions in Organometalloids*" (Academic, New York, 1969).

181. L.A. Harrah, J.M. Zeigler, *Mocromolecules*, **29**, 601, 1987.

182. R.N.S. Sodhi, S. Daviel, C.E. Brion, G.G.B. de Souza, *J. Electron Spectroc.* 35, 45, 1985.

183. P. Kelfve, B. Blomster, H. Siegbahn, K. Siegbahn, E. Sanhueza, O. Goscinski, *Phys. Scr.* 21, 75, 1980.

184. J.W. Davenport, *Phys. Rev. Letters*, **36**, 945, 1976.

185. W.H.E. Schwarz, *Chem. Phys.* **9**, 157, 1975.

186. E.A. Halevi, G. winkelhofer, M. Meisl, R. Janoschek, *J. Organomet. Chem.* 294, 151, 1985.

187. J.D. Bozek, K.H. Tan, G.M. Bancroft, J.S. Tse, *Chem. Phys. Letters*, **138**, 33, 1987.

188. J.D. Bozek, G.M. Bancroft, K.H. Tan, *Chem. Phys.* **145**, 131, 1990.

189. A.P. Hitchcock, M. Pocock, C.E. Brion, *Chem. Phys. Letters*, **49**, 125, 1977.

190. S. Bodeur, I. Nener, P. Millie, *Phys. Rev.* **A 34**, 2986, 1986.